UNIVERSIDAD DE CHILE
FACULTAD DE CIENCIAS FÍSICAS Y MATEMÁTICAS
DEPARTAMENTO DE ASTRONOMÍA

ORBITAL PARAMETERS AND MASS DETERMINATION OF VISUAL BINARY SYSTEMS

TESIS PARA OPTAR AL GRADO DE
MAGÍSTER EN CIENCIAS, MENCIÓN ASTRONOMÍA

MAXIMILIANO DIRK VEGA AGUILERA

PROFESOR GUÍA:
RENÉ MÉNDEZ BUSSARD

PROFESOR CO-GUÍA:
EDGARDO COSTA HECHENLEITNER

MIEMBROS DE LA COMISIÓN:
MÓNICA RUBIO LÓPEZ
CHRISTIAN MONI BIDIN
CÉSAR FUENTES GONZÁLEZ

Este trabajo ha sido parcialmente financiado por:
FONDECYT/ANID proyecto No. 1240049
FONDECYT/ANID proyecto No. 1190684
Fondo GEMINI/ANID proyecto No. 3223 AS0002, y
Vicerrectoria de Investigacion y Desarrollo (VID) de la Universidad de Chile No. ENL02/23

SANTIAGO DE CHILE
2024

Abstract

Determinación de Parámetros Orbitales y Masa de Sistemas Binarios Visuales

Determinar las masas estelares sigue siendo un desafío fundamental en astrofísica, y los sistemas estelares binarios ofrecen una oportunidad única para medir estas masas directamente por medio de las leyes de Kepler. Esta tesis tiene como objetivo mejorar la caracterización de los sistemas estelares binarios derivando en forma precisa elementos orbitales y estimaciones de masa por medio de una combinación de observaciones astrométricas y, en menor medida, de velocidad radial. El estudio se centra en una muestra de 16 binarias visuales, 8 binarias espectroscópicos de una sola línea y 2 binarias espectroscópicos de doble línea observados en el hemisferio sur. Las nuevas mediciones astrométricas fueron obtenidas utilizando la cámara Speckle HRCam del telescopio SOAR de 4.1 m y la cámara Speckle Zorro del telescopio Gemini de 8.1 m, ambos en Cerro Pachón. Las nuevas observaciones de velocidad radial fueron obtenidas con el espectrógrafo Echelle FEROS en el telescopio MPG de 2.2 m del Observatorio ESO/La Silla. Se emplearon métodos Bayesianos de Monte Carlo de Cadena de Markov para analizar los datos, obteniendo modelos estadísticos robustos y parámetros orbitales refinados. Este trabajo introduce 10 nuevas soluciones orbitales, aborda desafíos como una alta excentricidad e inclinaciones casi de canto, y examina discrepancias en las mediciones de paralaje. La integración de datos visuales y espectroscópicos resuelve eficazmente ambigüedades en el parámetro orbital Ω, contribuyendo a una comprensión más profunda de la dinámica estelar.

Orbital Parameters and Mass Determination of Visual Binary Systems

Determining stellar masses remains a fundamental challenge in astrophysics, and binary star systems offer a unique opportunity to measure these masses directly using Kepler's laws. This thesis aims to enhance the characterization of binary systems by deriving accurate orbital elements and mass estimates using a combination of radial velocity and, mainly, astrometric observations. The study focuses on a sample of 16 visual binaries, 8 single-lined spectroscopic binaries, and 2 double-lined spectroscopic binaries observed in the southern hemisphere. The new astrometric measurements were secured with the HRCam Speckle camera on the SOAR 4.1m telescope and the Zorro Speckle camera on the Gemini 8.1m telescope, both at Cerro Pachón. New radial velocity observations were obtained with the FEROS Echelle spectrograph on the 2.2m MPG telescope at the ESO/La Silla Observatory. Bayesian Markov Chain Monte Carlo methods were employed to analyze the data, yielding robust statistical models and refined orbital parameters. This work introduces 10 new orbital solutions, addresses challenges such as high eccentricity and nearly edge-on inclinations, and examines discrepancies in parallax measurements. The integration of visual and spectroscopic data effectively resolves ambiguities in orbital parameter Ω, contributing to a deeper understanding of stellar dynamics.

Porque para construir un mundo mejor,
primero hay que imaginarlo.

A mis padres.

Agradecimientos

Agradezco profundamente a todas las personas que me han acompañado durante este proceso, sin su presencia y apoyo esta tesis no habría visto la luz.

A mis padres, Marcelino y Janit, gracias por todo lo que me han dado, por su amor incondicional, su paciencia, y por ser siempre un pilar en mi vida. Sin su sacrificio y apoyo constante, no habría llegado hasta aquí.

A mis profesores guías, René y Edgardo, por sus consejos, guía, e infinita paciencia. Gracias por brindarme la oportunidad de participar en este proyecto y por permitirme crecer tanto a nivel profesional como personal.

A mis amigos, que con su compañía y apoyo me han acompañado durante todo este camino, haciéndolo más llevadero y enriquecedor.

Table of Content

List of Tables

List of Figures

Chapter 1

Introduction

According to the Vogt-Russell theorem (Kahler, 1972; Kippenhahn et al., 2013), the initial mass of a star of a given chemical composition is the most fundamental parameter that determines its internal structure and evolution.

Among the observable properties of a star, its luminosity is also dependent on its internal structure and, therefore, on its mass. This dependency is evidenced by the correlation between mass and luminosity, known as the mass-luminosity relation (MLR)(Eddington, 1924). The empirical version of the MLR has become one of the most powerful tools for testing stellar structure and evolutionary models.

Improving the observational MLR is challenging due to the difficulty of determining precise masses and distances. Moreover, the MLR also shows a statistical dispersion that cannot be explained solely by observational errors (Horch et al., 2015), suggesting the existence of an intrinsic dispersion resulting from differences in age or chemical composition of the stars.

Stellar masses can be determined by observing binary star systems and then applying Kepler's laws of motion (Pourbaix, 1994); which is currently the prime direct method for this purpose. This approach also requires measuring another quite elusive parameter: distance (van Altena and Lee, 1988), which is done through high-precision trigonometric parallax measurements.

Fortunately, the recent advent of Gaia (Gaia Collaboration et al., 2016) has significantly increased the accuracy of stellar parallaxes. For distances up to 250 pc, the uncertainty of a parallax measurement made by Gaia is less than 1%, which by current standards has essentially solved the distance dilemma.

Given that roughly half of the solar-type stars in the solar neighborhood belong to binary systems (Raghavan et al., 2010; Fuhrmann et al., 2017), it should be possible in principle to determine precise masses for a large number of stars. This has encouraged various new efforts to improve the MLR of the solar neighborhood, which is used as a starting point for all-sky catalogs of binary systems, like the Hipparcos catalog (HIP) and the Geneva-Copenhagen spectroscopic survey (GCS).

Since 2014 our team has been leading the study of visual binary systems in the southern hemisphere. Our survey combines interferometric observations being secured with the HRCam@SOAR and Zorro@GS Speckle cameras at Cerro Pachón, Chile; and spectroscopic observations being made with the FEROS Echelle spectrograph on the MPI/ESO 2.2m telescope at La Silla, Chile (Mendez et al., 2018).

Next in this chapter, we present the objective of this thesis and a theoretical framework to provide context to the work done. In Chapter 2, we describe the sample and instruments used to obtain the new data points. In Chapter 3, we present the results in tables, along with the methodology employed. Then, in Chapter 4, we discuss all the systems studied. Finally, in Chapter 5, we draw our conclusions. In Appendix , we present the figures for all our objects.

1.1 Objective

The primary objective of this thesis is to improve the characterization of binary star systems by deriving accurate orbital elements and, where possible, mass estimates using a combination of astrometric and radial velocity (RV) data. This work aims to contribute to the understanding of stellar dynamics by applying Bayesian Markov Chain Monte Carlo (MCMC) methods to generate robust statistical models. Additionally, this study aims to lay the groundwork for addressing discrepancies in parallax measurements and refining the MLR through future analysis of newly observed systems, to advance our understanding of stellar structure and evolution.

1.2 Theoretical Framework

Binary star systems are pairs of stars that orbit around a common center of mass due to their mutual gravitational attraction. These systems are fundamental as they allow us to determine stellar masses through the study of the orbit by applying Kepler's laws of motion. These systems can be classified into different types depending on the observation technique employed. Among these are Visual Binaries, where the relative positions of both components are directly observable, Astrometric Binaries, and Spectroscopic Binaries. In visual binaries, the position of the fainter secondary star is measured relative to the brighter primary star, with observations capturing the projection of the system's orbit into the plane of the sky, as seen by the observer. This projection is known as the apparent orbit and is critical for understanding the motion and interaction within the system.

1.2.1 Keplerian Orbits of Visual Binary Systems

The motion of binary star systems can be described by Kepler's laws, which govern the elliptical trajectories of celestial bodies in a gravitational two-body system. The specific geometry of a binary star's orbit is characterized by seven orbital parameters[1]:

- **Period** (P): The time it takes for the stars to complete one full orbit around their common center of mass.
- **Epoch of Periastron Passage** (T): The specific time at which the star passes closest to its companion, marking the periastron, or the point of the orbit nearest to the other star.
- **Eccentricity** (e): A measure of the deviation of the orbit from a perfect circle, with e = 0 representing a circular orbit and e = 1 representing a parabolic trajectory.
- **Semi-Major Axis** (a): The longest radius of the elliptical orbit, representing the average distance between the two stars over one complete orbit.
- **Argument of Periastron** (ω): The angle measured from the ascending node to the periastron in the true orbit, indicating the orientation of the ellipse within its orbital plane.
- **Longitude of the Ascending Node** (Ω): The angle measured from a reference direction (typically from North to East) to the ascending node, indicating the orientation of the orbit's plane relative to the plane of the sky.
- **Inclination** (i): The angle between the plane of the sky and the plane of the orbit, indicating how tilted the orbit is with respect to the line of sight from the observer.

These parameters collectively describe the shape, size, and orientation of the orbit, as well as the motion of the stars' positions within that orbit. In Figure 1.1[2], the angle ν is also illustrated. This angle corresponds to the true anomaly, which is the position angle of the secondary star with respect to the primary, measured from the periastron in the direction of the orbital motion.

Kepler's third law states that the square of the orbital period P is proportional to the cube of the semi-major axis a of the orbit, with the constant of proportionality being related to the total mass $M_1 + M_2$ of the two stars in the system. Mathematically, this can be expressed as:

$$P^2 = \frac{4\pi^2}{G(M_1 + M_2)} a^3, \tag{1.1}$$

where M_1 and M_2 are the masses of the two stars and G is the universal gravitational constant. This relationship implies that by knowing the orbital period and the semi-major axis, we can determine the total mass of the binary system. This is particularly valuable in astrophysics, where direct measurements of stellar masses are challenging. To use this law to obtain the total mass, we first need to know a with his physical unit and not angular. For this, we need to know the distance to the system.

---

[1] Also called the Campbell elements.

[2] Image by Lasunncty, CC-BY-SA-3.0.

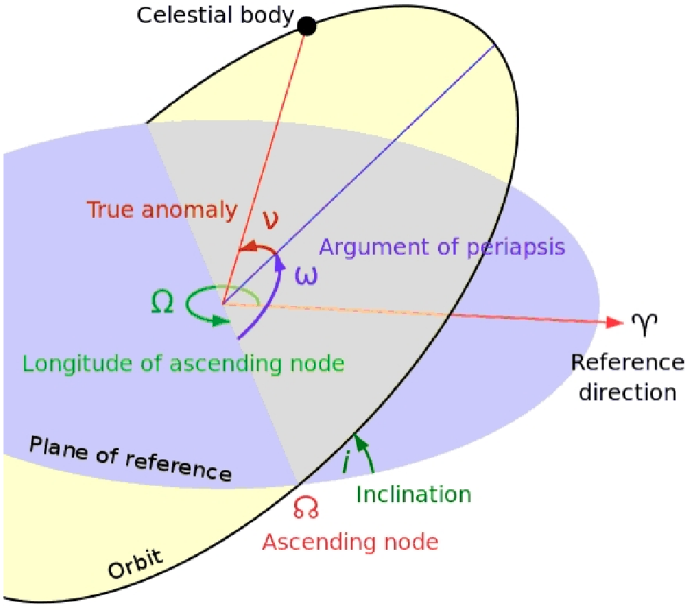

Figure 1.1: Diagram illustrating orbital parameters: true anomaly (ν), argument of periastron (ω), longitude of the ascending node (Ω), and inclination (i).

Parallax is the apparent shift in the position of a star when observed from two different points in Earth's orbit around the Sun, separated by six months. This effect is used to measure the distance to stars. The parallax angle π is inversely proportional to the distance d to the star:

$$\mathrm{d} = \frac{1}{\pi}, \tag{1.2}$$

where d is the distance to the star in parsecs and π is known as the parallax angle in arcseconds.

The relative motion of the stars in the system is defined by their Keplerian orbit, where the mean anomaly M at a given time t is related to the eccentric anomaly E by Kepler's equation:

$$M = 2\pi\frac{(t-T)}{(P)} = E - \mathrm{e}\sin(E). \tag{1.3}$$

Given that there is no analytical solution to Kepler's equation, the Newton-Raphson numerical method is employed to solve for the eccentric anomaly E. The Newton-Raphson method is an iterative technique used to find the roots of a function, which means solving equations of the form $f(x) = 0$. In the context of this work, it is used to solve Kepler's equation, $M = E - \mathrm{e}\sin(E)$, for the eccentric anomaly E, given the mean anomaly M and eccentricity e. The method starts with an initial guess for E and refines this guess iteratively using the formula $E_{n+1} = E_n - \frac{f(E_n)}{f'(E_n)}$, where $f(E_n)$ represents the difference between the two sides of Kepler's equation. The process continues until the difference between successive

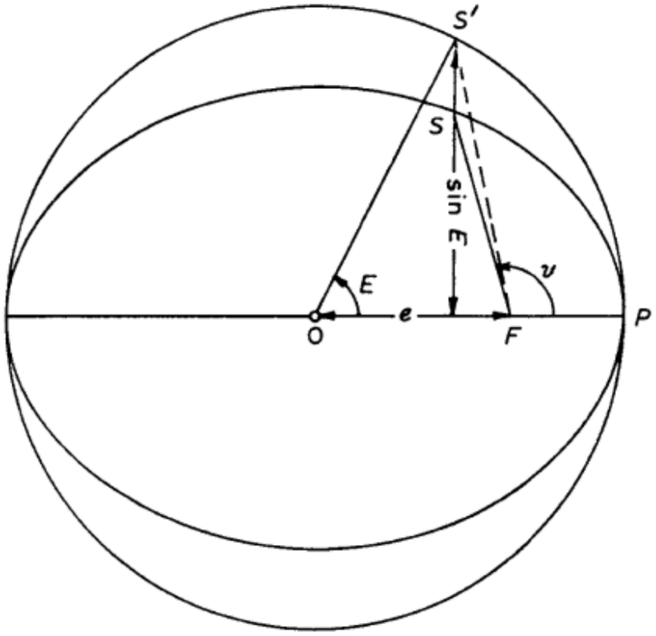

Figure 1.2: Kepler's problem. S indicates the position of the secondary star in the true orbit ellipse with eccentricity e, where F is the focus of the ellipse, indicating the position of the primary star. S' represents the projection on the auxiliary circle. ν is the true anomaly, E corresponds to the eccentric anomaly, and P marks the position of periastron.

approximations is smaller than a predefined threshold, ensuring that E is found to a desired accuracy. Once we solve E, we can compute the true anomaly ν:

$$\tan\left(\frac{\nu}{2}\right) = \sqrt{\frac{1+\mathrm{e}}{1-\mathrm{e}}}\tan\left(\frac{E}{2}\right) \tag{1.4}$$

As was said before, the true anomaly ν represents the angle between the direction of periastron and the current position of the star as seen from the focus of the ellipse, where the primary star is located, see Figure 1.2[3]. Once ν is determined, the radial distance r from the primary star to its companion can be calculated using the following equation:

$$r = \frac{a(1-\mathrm{e}^2)}{1+\mathrm{e}\cos(\nu)}. \tag{1.5}$$

The observed motion of binary stars on the plane of the sky is known as the apparent orbit, see Figure 1.1. This is a projection of the true orbit onto the sky plane, and its analysis involves converting the orbital parameters into the Thiele-Innes constants A, B, F, and G, which are defined as:

---

[3] Image from Principles of Astrometry, Van De Kamp (1967).

$$
\begin{aligned}
A &= a\left(\cos(\omega)\cos(\Omega) - \sin(\omega)\sin(\Omega)\cos(\mathrm{i})\right), \\
B &= a\left(\cos(\omega)\sin(\Omega) + \sin(\omega)\cos(\Omega)\cos(\mathrm{i})\right), \\
F &= a\left(-\sin(\omega)\cos(\Omega) - \cos(\omega)\sin(\Omega)\cos(\mathrm{i})\right), \\
G &= a\left(-\sin(\omega)\sin(\Omega) + \cos(\omega)\cos(\Omega)\cos(\mathrm{i})\right).
\end{aligned}
\tag{1.6}
$$

These constants facilitate the transformation from the orbital parameters to the observable positions X and Y of the stars, which are functions of the eccentric anomaly E and are given by:

$$
\begin{aligned}
X &= B\cos(E) - F\sqrt{1-\mathrm{e}^2}\,\sin(E), \\
Y &= A\cos(E) - G\sqrt{1-\mathrm{e}^2}\,\sin(E).
\end{aligned}
\tag{1.7}
$$

However, it is important to note that the Thiele-Innes representation can be ambiguous. Different combinations of the angles ω, Ω, and i may produce the same set of Thiele-Innes constants for a given value of the semi-major axis a. Despite this potential ambiguity, the Thiele-Innes constants remain a popular choice among astronomers because they enable straightforward calculations of the apparent orbit, particularly in algorithms that leverage the linear relationship between these constants and the observed positional coordinates (x, y).

Equivalently, the positions X and Y on the apparent orbit can be calculated directly using the true anomaly ν, obtained from the eccentric anomaly E in Equation 1.4, and r is the radial distance given by Equation 1.5. The position coordinates are then expressed as:

$$
\begin{aligned}
X &= r\left(\cos(\nu)\cos(\Omega) - \sin(\nu)\sin(\Omega)\cos(\mathrm{i})\right), \\
Y &= r\left(\cos(\nu)\sin(\Omega) + \sin(\nu)\cos(\Omega)\cos(\mathrm{i})\right),
\end{aligned}
\tag{1.8}
$$

1.2.2 Radial Velocity Observations and Mass Determination

In addition to astrometric observations, the study of binary systems often involves measuring the RVs of the components. These RV measurements are based on the Doppler effect, where the motion of a star towards or away from the observer causes a shift in the wavelength of the star's light (see Figure 1.3[4]). As the star moves toward the observer, its light shifts to shorter wavelengths (blue shift), and as it moves away, its light shifts to longer wavelengths (red shift). By analyzing these shifts in the spectral lines of the stars, the RVs can be accurately determined.

In the case of double-lined spectroscopic binaries (SB2), the spectral lines of both stars are measurable, allowing for the determination of the RV curves for both components. The RV V of each star can be modeled as:

$$
V = V_0 + K\left[\cos(\omega+\nu) + \mathrm{e}\cos(\omega)\right], \tag{1.9}
$$

---

[4] Image edited from ESO Press photo 22e/07, April 2007.

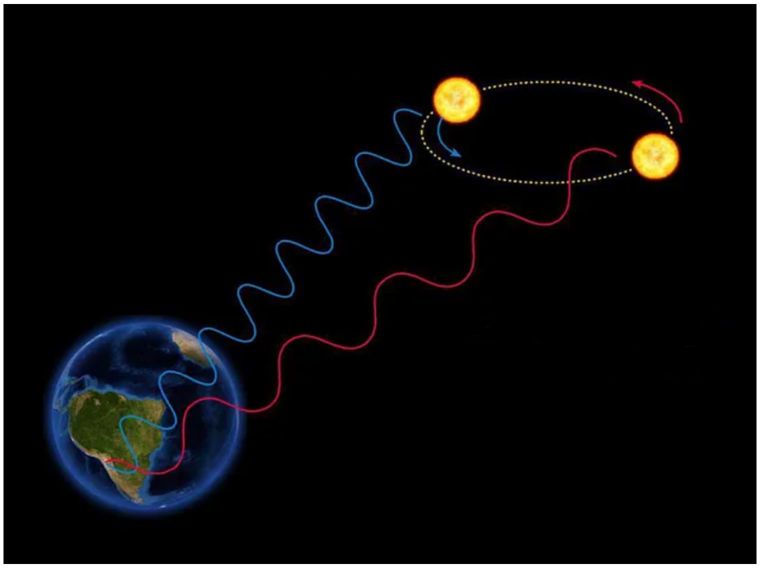

Figure 1.3: Doppler effect in a binary star system: the star moving towards Earth shows a blue shift (shorter wavelength), while the star moving away shows a red shift (longer wavelength).

where V_0 is the systemic velocity[5], K is the amplitude of the RV curve, and ν is the true anomaly. The amplitudes K_1 and K_2 for the primary and companion stars are given by:

$$\begin{aligned} K_1 &= \frac{2\pi a \sin(\mathrm{i})}{P\sqrt{1-\mathrm{e}^2}} \frac{q}{1+q}, \\ K_2 &= \frac{2\pi a \sin(\mathrm{i})}{P\sqrt{1-\mathrm{e}^2}} \frac{1}{1+q}, \end{aligned} \tag{1.10}$$

where $q = \frac{M_2}{M_1}$ is the mass ratio between the secondary and primary star[6]. The analysis of these RV curves, combined with the astrometric data, allows for the determination of the masses of the individual components.

By combining astrometric and spectroscopic observations with the parallax measurement, we can determine the masses of the individual stars in the binary system. The total mass M_1+M_2 can be derived from Kepler's third law, while the individual masses can be estimated from mass ratio $q = \frac{M_2}{M_1}$. The relationship between the RVs and the orbital parameters allows us to solve for the mass ratio:

$$\frac{K_1}{K_2} = \frac{M_2}{M_1} = q \tag{1.11}$$

where K_1 and K_2 are the RV amplitudes of the primary and secondary stars, respectively.

---

[5] A.K.A. velocity of the center of mass (V_{CoM}).

[6] We also denote M_P as the more massive primary star and M_S as the secondary star.

Chapter 2

Observations

2.1 Binary System Sample Selection

The initial sample studied in this work was selected from a list of systems with new astrometric observations, secured as part of our monitoring program of southern binaries described in Mendez et al. (2017), with the HRCam[1] (Tokovinin et al., 2010) and Zorro[2] (Howell and Furlan, 2022) Speckle cameras on the SOAR 4.1 m and Gemini 8.1 m telescopes at Cerro Pachón, respectively.

HRCam observations deliver a precision of 3-5 mas in angular separation for objects brighter than $V \sim 12$ magnitude (Mendez et al., 2017), while Zorro observations have a better precision (1 mas). Our Speckle observations were reduced using standard interferometry techniques. Calibration binary systems were observed each night to ensure the consistency of our measurements (Tokovinin et al., 2010; Tokovinin, 2018).

We then checked the Sixth Catalog of Orbits of Visual Binary Stars (Orb6)[3], maintained by the US Naval Observatory (USNO)[4], and the 9th Catalog of Spectroscopic Binary Orbits (SB9; Pourbaix, D. et al. (2004))[5], to search for previous orbital results for the objects in our list. When that was the case, we then compiled the historical astrometric measurements and orbital parameters from the Washington Double Star Catalog (WDS; Mason et al. (2001); Hartkopf et al. (2001)) and RV data from the SB9 catalog. The historical data from WDS was kindly provided by Dr. Brian Mason of the USNO.

A first analysis of the systems selected was made using a versatile IDL-driven interactive code, ORBIT, developed by A. Tokovinin (2016, 1992)[6]. This code employs a parametric χ^2 minimization approach using the Levenberg-Marquardt algorithm to obtain an initial solution for the orbit. Objects with sufficient data points were then selected for further analysis using

---

[1] See `https://noirlab.edu/science/programs/ctio/instruments/visitor-instruments/HRCam`.

[2] See `https://www.gemini.edu/instrumentation/alopeke-zorro`.

[3] Available at `http://www.astro.gsu.edu/wds/orb6.html`.

[4] Available at `https://www.cnmoc.usff.navy.mil/usno/`.

[5] Available at `https://sb9.astro.ulb.ac.be/`.

[6] The code and user manual can be downloaded from `https://zenodo.org/records/61119`.

MCMC methods.

Our final sample consists of 2 double-lined spectroscopic binaries (SB2), 8 single-lined spectroscopic binaries (SB1)[7], of which 4 are first-time reports of orbital parameters, and 16 visual binaries, with 6 having their orbital parameters reported for the first time. We must emphasize that, as a result of our selection process, our final sample is very heterogeneous and it should not be considered complete or representative of these systems in any astrophysical sense. From this point of view, this work's main contribution is adding new orbits and mass ratios (when possible).

As a part of our on-going survey of spectroscopic binaries being carried out with the FEROS Echelle spectrograph (Kaufer et al., 1999) on the 2.2m MPG telescope at the ESO/La Silla Observatory[8], we also secured high resolution spectra, leading to high precision radial velocities measurements, for our SB2 and SB1 systems. FEROS spectra were reduced using the CERES pipeline (Brahm et al., 2017), which provides consistent and accurate (better than 0.1 km s^{-1}) RV measurements.

When both available, the processed astrometric and RV data were then combined to perform a joint MCMC analysis of the orbital elements. This combined approach allows for a more accurate determination of the orbital parameters, including the orbital parallax for SB2 systems, which provides an independent measure of distance.

Basic properties available in the literature for our final sample of systems are presented in Table 2.1. The first three columns provide the WDS name, the corresponding Hipparcos number and the discoverer designation for each system. The fourth and fifth columns present parallax results from the Hipparcos (Π_H) and Gaia eDR3 (Π_G) catalogs, respectively. The sixth column gives the Reduced Unit Weight Error (RUWE) listed in Gaia eDR3, which is an indicator of the quality of Gaia's astrometric solution. The next three columns show the apparent V magnitudes of the systems listed in SIMBAD (Wenger et al., 2000) and the individual magnitudes of the primary (V_P) and secondary (V_S) components as recorded in the WDS database. The tenth and eleventh columns give the estimated masses for the primary (M_P) and secondary (M_S) stars, respectively, provided in the Abushattal et al. (2020) mass-absolute Magnitude calibration tables. Finally, the last column gives spectral type information, sourced from both the WDS and SIMBAD databases.

---

[7] Some have only one RV observation, so it can not be considered a proper SB1.

[8] See `https://www.eso.org/sci/facilities/lasilla/instruments/feros.html`

Table 2.1: Object identification

WDS name	HIP number	Discoverer designation	Π_H[a] [mas]	Π_G[b] [mas]	RUWE[b]	V_{Simbad}[c]	V_P[d]	V_S[d]	M_P[e] [$M_\odot$]	M_S[e] [$M_\odot$]	Sp Type[cd] WDS/Simbad
00462−2214	3606	RST4155	10.66 ± 1.02	9.2071 ± 0.3270[f]	−−	9.01	9.76	10.03	1.11 ± 0.04	1.07 ± 0.04	G0V
01117+0835	5593	HDS 158	7.23 ± 1.38	10.1184 ± 0.2448	13.077633	9.25	9.54	11.3	1.11 ± 0.04	0.85 ± 0.03	G5
01376−0924	7580	KUI 7	24.76 ± 0.90	22.9702 ± 0.6299	20.701488	6.24	6.8	7.2	1.39 ± 0.05	1.23 ± 0.05	F7V/F8.5V
02057−2423	9774	WSI 71Aa,Ab	21.44 ± 1.43	21.0892 ± 0.0879	3.0044014	−−	9.27	9.50	0.93 ± 0.04	0.85 ± 0.03	G9V
02572−2458	13768	BEU 4Ca,Cb	38.35 ± 1.24	40.9861 ± 0.4288	20.025099	6.281	8.24	9.3	0.85 ± 0.03	0.67 ± 0.03	K2V
03347−0451	−−	TSN 127	−−	37.8198 ± 0.6105	26.910942	13.033	10.7	11.6	0.56 ± 0.02	0.48 ± 0.02	M3.87
03489+1143	17826	A 831	6.53 ± 1.08	2.8884 ± 0.5923	19.209284	8.21	8.54	10	1.54 ± 0.05	1.11 ± 0.04	F0/F1+F8
05286−4548	25641	HDS 723	6.19 ± 0.89	5.7574 ± 0.0161	1.7343152	9.14	9.8	10.31	1.39 ± 0.05	1.23 ± 0.05	F3/F5V
05474−1032	27341	MCA 22	4.88 ± 0.73	2.1898 ± 0.6359	23.098963	6.09	6.34	7.79	9.57 ± 3.35	2.5 ± 0.11	A4V/A2IV
07548−6613	38645	TOK 830	11.26 ± 0.76	11.7234 ± 0.0704	5.856625	9.26	9.8	9.8	1.05 ± 0.04	1.05 ± 0.04	G6/8V
12018−3439	58669	I 215AB	17.87 ± 0.77	11.6897 ± 0.8228[f]	−−	6.955	7.27	8.48	1.71 ± 0.05	1.35 ± 0.05	G0V
13138−6756	64545	HDS1853	8.54 ± 1.07	6.1995 ± 0.1882	12.189999	8.98	9.29	10.92	1.50 ± 0.05	1.07 ± 0.04	F6V
14025−2440	68587	B 263AB	16.02 ± 1.19	13.3967 ± 0.2046	9.356615	8.15	8.42	10.59	1.23 ± 0.05	0.85 ± 0.03	G3V
14152−6739	69643	DON 652	19.38 ± 0.73	20.4052 ± 0.0842	4.338634	7.64	7.7	11.2	1.23 ± 0.05	0.67 ± 0.03	F8/G0V
14567−6247	73129	FIN 372	2.16 ± 0.29	4.19729 ± 0.77394	8.955013	5.11	5.9	5.9	5.04 ± 0.78	4.26 ± 1.15	B4V/B2III
15317+0053	76031	TOK 48	19.67 ± 0.89	23.5633 ± 1.2061[f]	−−	7.42	7.8	8.9	1.11 ± 0.04	0.93 ± 0.04	G0V
16016−7843	78505	HDS2259	17.13 ± 0.64	17.7971 ± 0.2789	8.651914	8.01	8.43	9.79	1.11 ± 0.04	0.89 ± 0.04	G3V
16035−5747	78662	SEE 258AB	25.39 ± 1.25	−−	−−	4.67	5.2	5.76	1.58 ± 0.06	1.31 ± 0.05	A7IV/A5IV
16434−2819	81874	LSC 67	7.36 ± 0.81	6.908 ± 0.048	1.9636867	8.13	8.7	9.1	1.60 ± 0.05	1.50 ± 0.05	F2V
17157−0949	84430 AB	A 2592AB	4.90 ± 0.94	2.74544 ± 0.85725[f]	−−	7.04	7.15	10.4	4.40 ± 0.42	1.81 ± 0.06	F7V/F5V
17157−0949	84430 BaBb	TOK 53Ba,Bb	4.90 ± 0.94	2.74544 ± 0.85725[f]	−−	7.04	9.69	10.6	2.00 ± 0.06	1.64 ± 0.05	F9IV/F5V
17349+1234	86032	MCY 4	67.13 ± 1.06	−−	−−	2.07	2.1	5	2.02 ± 0.18	1.20 ± 0.05	A5III/A5IV
20306+1349	101181	HDS2932	10.96 ± 0.87	9.1483 ± 0.2843	13.141935	8.02	8.61	9.23	1.54 ± 0.05	1.23 ± 0.05	F8
22302−5345	−−	TSN 204	−−	64.3577 ± 0.3893	17.299686	−−	13.1	14.2	0.31 ± 0.02	0.14 ± 0.02	M4.5
23133−4937	114626	I 1467	3.91 ± 0.61	5.5518 ± 0.1545	7.164579	6.808	7.06	9.7	2.70 ± 0.48	1.54 ± 0.05	G8/K0III
23167−1534	114919	HU 399	1.28 ± 1.41	5.1587 ± 0.1496	9.8933325	8.95	9.56	10.31	1.54 ± 0.05	1.29 ± 0.05	G3V/G0

---

a. From the Hipparcos mission.
b. From the GAIAeDR3.
c. From the SIMBAD database.
d. From WDS database.
e. From Abushatal.
f. From the GAIAeDR2.

Chapter 3

Results

To calculate the orbital elements, we used a Bayesian MCMC code whose implementation is described in detail in Mendez et al. (2017) and Claveria et al. (2019). This approach allowed us to exploit advantages that are inherent to these methods; that is (i) provide realistic confidence limits for the derived orbital elements, and (ii) generate posterior probability density functions (PDF) for each orbital element, as well as for the masses derived and for the self-consistent orbital parallax (when RV data are available).

Because MCMC methods tend to converge faster and be more reliably when the algorithm is initialized from a point close to the global minimum, we first employed the ORBIT code, which uses a parametric χ^2 minimization approach, to obtain initial parameters that "feed" our MCMC code. The ORBIT code is particularly useful for providing a prior solution, which is crucial for those objects without previous orbital results.

When applying our MCMC code to the objects listed in Table 2.1, we differentiated them in three groups based on the data at hand: (i) visual binaries: only astrometric data available (ii) SB1 binaries: astrometric data available plus RV data for 1 component, and (iii) SB2 binaries: astrometric data available plus RV data for both components. For each object (see tables in the next sections 3.1, 3.2, and 3.3), we provide two sets of numbers for the orbital elements: the upper rows indicate the maximum likelihood (ML) value resulting from the MCMC simulation, while the lower row indicates the median value of the posterior PDF of the MCMC simulation, as well as the upper (third) quartile (Q75) and the lower (first) quartile (Q25) of the distribution, in the form of a superscript and subscript, respectively.

In situations characterized by highly dispersed and asymmetric probability densities, the expected value rarely provides a meaningful estimate of the parameters, typically yielding orbits that are not in good agreement with the observations. Maximum likelihood (ML) and maximum a posteriori (MAP) estimates, defined as the values that maximize the likelihood function and the posterior distribution, respectively (Gelman et al., 2013), are preferred in those situations. In this work, the likelihood functions assume a Gaussian observation model, and the priors are just uniform densities within a certain interval (e.g., the prior of eccentricity p(e) is 1 in [0, 1) and 0 out of that range). In orbits with good orbital coverage, the expected value approximately coincides with the MAP/ML estimates (Mendez et al., 2021).

In the next sections, we present and discuss the results of our MCMC fit for our visual, SB1, and SB2 systems. Figures of orbits, RV curves, posterior distribution of parameters, corner plots with parameter correlations, and residuals O-C for all objects studied in this work, can be found in Appendix .

3.1 Visual binaries

Orbital parameters for 16 visual binary systems were derived; they are presented in Table 3.1. The first column provides the WDS name and the Hipparcos number for each system. The subsequent columns detail the orbital elements: period (P) and epoch of periastron passage (T), in years; eccentricity (e) and semi-major axis (a), in arcseconds; the argument of periastron (ω), the longitude of the ascending node (Ω), and the inclination (i) of the orbital plane relative to the line of sight, in degrees; total mass of the system (M_T) in $M_\odot$ and in the last column the reference for the orbit. We report first orbital parameters for 6 systems, thus contributing new data to the field.

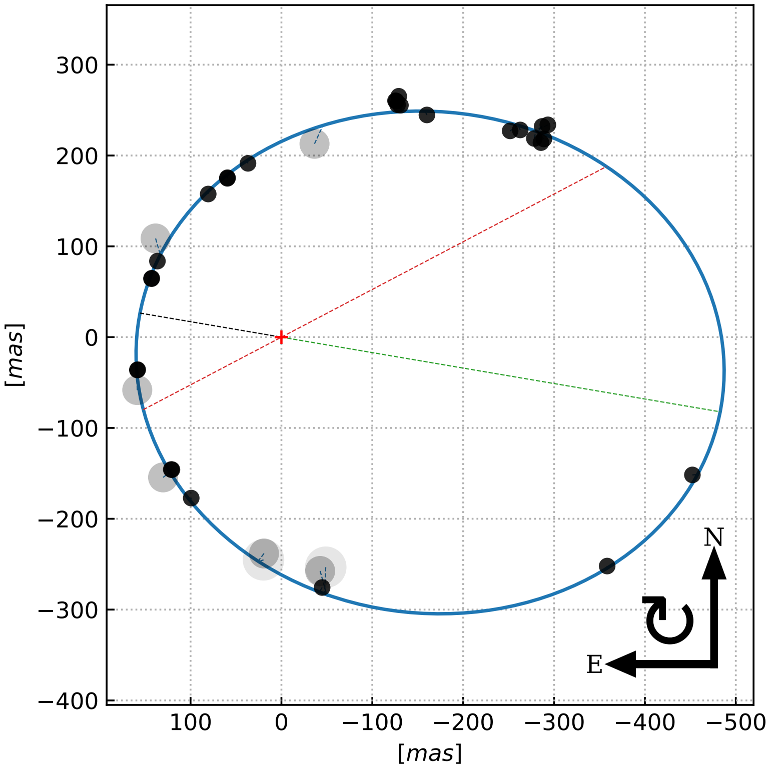

Figure 3.1: Orbit of the visual system HIP 78662.

In the orbit plots, such as in Figure 3.1 for the visual binary HIP 78662, the blue ellipse represents the orbit calculated using the maximum a-posteriori parameter values, the dashed red line the line of nodes, and the dashed black and green lines indicate the positions of the periastron and apoastron, respectively. The lower-right corner of the orbit plot includes the North-East directions and the sense of motion.

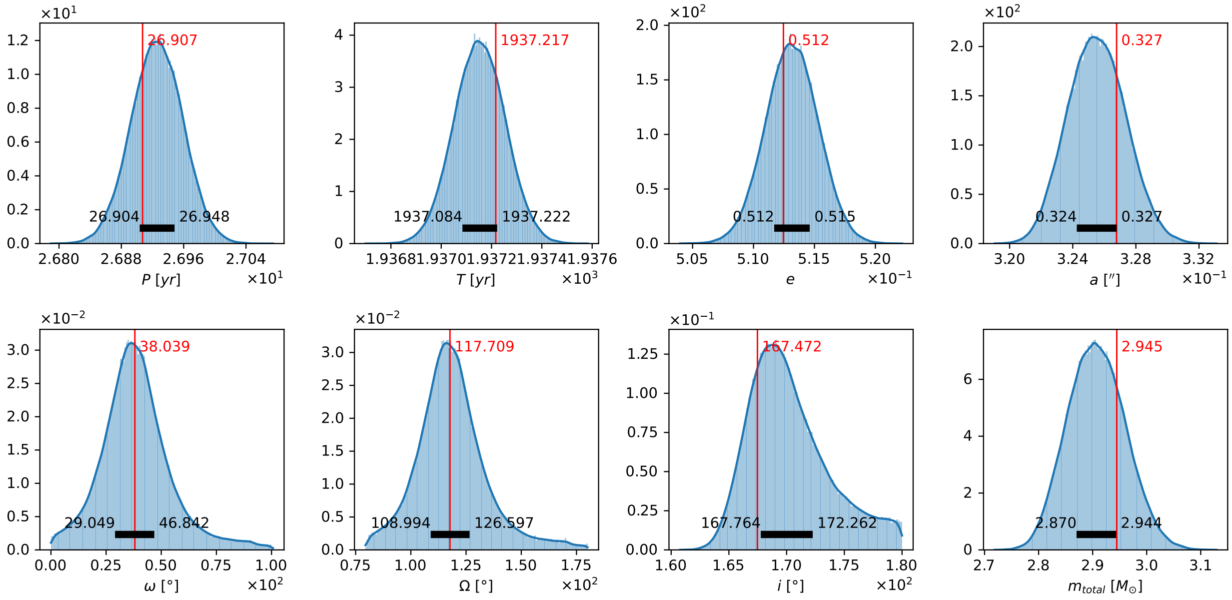

Figure 3.2: Marginal posterior distribution of parameters of the visual system HIP 78662.

Figure 3.2 shows an example of a marginal posterior distribution of orbital parameters estimated with our MCMC method, specifically for the visual binary HIP 78662. In these plots, the vertical red line indicates the MAP estimator, while the horizontal black bar shows the range between Q25 and Q75 of the distribution, providing a visual representation of the uncertainties associated with each parameter. Note that not all distributions have a Gaussian shape, this highlights the importance of reporting a confidence interval using the quartiles.

Figure 3.3 shows an example corner plot, with the pairwise marginal posterior distributions of the parameters, specifically for the visual binary HIP 78662. Each panel in the corner plot represents a pair of parameters. Diagonal panels display the marginal posterior distribution of each parameter, while the off-diagonal panels provide insights into potential correlations between pairs of parameters.

3.2 SB1 binaries

Table 3.2 presents the extended orbital elements for the 8 SB1 systems in our sample. The first two columns list the WDS name and the Hipparcos number, followed by the orbital parameters: P, T, e, a, ω, Ω, and i; the systemic velocity (V_{CoM}) and the amplitude of the RV curve (K_1 or K_2). The last column references the source of the orbital data.

Table 3.3 presents the parallaxes and individual component masses for the SB1 binaries. The first column lists the WDS name and Hipparcos number. The second column gives the parallax (π) values from Hipparcos, while the third column those from Gaia eDR3. The fourth column presents a tentative orbital parallax (π_{orb}), which is derived from the orbital analysis. The fifth column presents the mass ratio (M_S/M_P). The sixth and seventh columns give the masses of the primary (M_P) and secondary (M_S) components, expressed in solar

Table 3.1: Orbital elements of our visual binaries.

WDS name **HIP number**	P [yr]	T [yr]	e	a [arcsec]	ω [°]	Ω [°]	i [°]	M$_T$ [M$_\odot$]	Orbit reference
00462−2214 3606	50.34 $50.02^{+0.90}_{-0.87}$	1953.46 $1953.86^{+0.91}_{-0.94}$	0.275 $0.274^{+0.016}_{-0.017}$	0.1680 $0.1658^{+0.0035}_{-0.0034}$	148.8 $147.4^{+2.8}_{-2.7}$	179.2 $177.8^{+3.8}_{-4.1}$	141.5 $142.6^{+2.5}_{-2.3}$	2.40 $2.33^{+0.11}_{-0.11}$	Tok2020e
03347−0451 −−	3.911 $3.953^{+0.089}_{-0.082}$	2021.904 $2021.875^{+0.028}_{-0.023}$	0.524 $0.559^{+0.031}_{-0.031}$	0.0927 $0.0902^{+0.0027}_{-0.0026}$	177.0 $174.5^{+9.5}_{-12}$	175.7 $174.4^{+7.4}_{-9.6}$	142.6 $149.7^{+10}_{-6.8}$	0.962 $0.864^{+0.11}_{-0.091}$	NEW
03489+1143 17826	186 253^{+73}_{-48}	2231 2299^{+65}_{-49}	0.557 $0.461^{+0.088}_{-0.077}$	0.398 $0.428^{+0.045}_{-0.024}$	40 358^{+29}_{-36}	154.3 $164.2^{+8.1}_{-8.8}$	57.1 $53.0^{+4.4}_{-4.5}$	6.51 $4.03^{+1.5}_{-0.78}$	USN2002
05474−1032 27341	32.21 $32.13^{+0.27}_{-0.26}$	1973.40 $1972.98^{+0.32}_{-0.32}$	0.9818 $0.9588^{+0.0067}_{-0.0054}$	0.1490 $0.0947^{+0.010}_{-0.0027}$	78 65^{+21}_{-30}	43 52^{+28}_{-25}	55 23^{+13}_{-12}	27.6 $7.1^{+2.5}_{-0.6}$	Doc2022d
14152−6739 69643	123.4 $126.7^{+6.6}_{-6.1}$	2023.94 $2024.09^{+0.33}_{-0.34}$	0.896 $0.882^{+0.027}_{-0.024}$	0.655 $0.650^{+0.025}_{-0.015}$	19.9 $14.7^{+9.1}_{-7.2}$	84.0 $84.9^{+1.2}_{-1.7}$	79.92 $80.13^{+0.61}_{-0.64}$	2.53 $2.28^{+0.52}_{-0.27}$	Tok2018b
14567−6247 73129	38.11 $38.18^{+0.39}_{-0.37}$	1993.83 $1993.71^{+0.29}_{-0.3}$	0.284 $0.279^{+0.014}_{-0.013}$	0.088 $0.087^{+0.002}_{-0.002}$	242.6 $243.3^{+4.6}_{-5.2}$	41.4 $42.2^{+5}_{-4.9}$	146.4 $148.1^{+3.5}_{-3.1}$	6.34 $6.10^{+0.41}_{-0.39}$	Msn2010c
16016−7843 78505	60.5 $58.8^{+6.0}_{-5.1}$	2003.9 $2003.3^{+1.3}_{-1.6}$	0.769 $0.738^{+0.088}_{-0.086}$	0.347 $0.335^{+0.041}_{-0.017}$	41 36^{+12}_{-13}	156.81 $156.99^{+0.23}_{-0.29}$	88.93 $89.12^{+0.64}_{-0.65}$	2.02 $2.08^{+0.26}_{-0.16}$	NEW
16035−5747 78662	26.907 $26.926^{+0.022}_{-0.022}$	1937.217 $1937.153^{+0.069}_{-0.069}$	0.5125 $0.5131^{+0.0015}_{-0.0014}$	0.3268 $0.3255^{+0.0013}_{-0.0013}$	38.0 $37.7^{+9.2}_{-8.7}$	117.7 $117.5^{+9.1}_{-8.5}$	167.5 $169.7^{+2.6}_{-1.9}$	2.945 $2.906^{+0.037}_{-0.036}$	Tok2015c
16434−2819 81874	15.0 $14.3^{+2.9}_{-1.6}$	1939.9 $1943.8^{+8.1}_{-14}$	0.857 $0.859^{+0.046}_{-0.046}$	0.146 $0.144^{+0.043}_{-0.024}$	277.9 $277.1^{+4.1}_{-2.9}$	108.7 $108.8^{+1.4}_{-1.4}$	95.1 $95.3^{+1.2}_{-1.2}$	42 40^{+33}_{-14}	NEW
17157−0949 84430 AB	114.3 $113.1^{+4.7}_{-4.1}$	1904 $1905.5^{+5.0}_{-5.6}$	0.279 $0.275^{+0.014}_{-0.012}$	0.3207 $0.3193^{+0.0067}_{-0.0057}$	298.7 $300.4^{+7.0}_{-7.1}$	32.4 $33.0^{+2.3}_{-2.4}$	140.89 $140.63^{+1.0}_{-0.97}$	21.45 $21.67^{+0.58}_{-0.56}$	Tok2021b
17157−0949 84430 BaBb	5.203 $5.207^{+0.036}_{-0.036}$	2010.749 $2010.68^{+0.10}_{-0.093}$	0.432 $0.386^{+0.027}_{-0.025}$	0.0322 $0.03007^{+0.0012}_{-0.00097}$	78 70^{+25}_{-25}	79 70^{+30}_{-24}	146.3 $161.6^{+9.2}_{-9.2}$	10.5 $8.53^{+1.1}_{-0.82}$	Tok2021b
17349+1234 86032	8.5369 $8.5384^{+0.0041}_{-0.0041}$	1986.557 $1986.555^{+0.019}_{-0.018}$	0.8976 $0.8979^{+0.0027}_{-0.0026}$	0.4319 $0.4317^{+0.0027}_{-0.0026}$	343.8 $344.0^{+1.4}_{-1.4}$	55.47 $55.57^{+0.55}_{-0.55}$	115.68 $115.63^{+0.66}_{-0.64}$	3.655 $3.648^{+0.069}_{-0.065}$	CIA2021c
20306+1349 101181	29.47 $29.62^{+0.77}_{-0.71}$	2005.62 $2005.73^{+0.15}_{-0.15}$	0.901 $0.894^{+0.018}_{-0.016}$	0.171 $0.160^{+0.018}_{-0.013}$	294.1 $295.8^{+3.1}_{-3.3}$	170.2 $170.8^{+1.5}_{-1.5}$	75.7 $74.2^{+2.2}_{-2.2}$	4.35 $3.54^{+1.4}_{-0.83}$	Doc2021e
22302−5345 −−	6.3 $7.3^{+1.8}_{-1.1}$	2016.4 $2015.2^{+1.3}_{-2}$	0.328 $0.355^{+0.05}_{-0.035}$	0.1375 $0.1427^{+0.0098}_{-0.0054}$	211 192^{+21}_{-19}	90.7 $91.6^{+1.9}_{-1.6}$	108.5 $110.5^{+2.5}_{-2.3}$	0.247 $0.199^{+0.056}_{-0.042}$	NEW
23133−4937 114626	129.3 $129.3^{+4.3}_{-4.2}$	1866.6 $1868.0^{+4.5}_{-4.7}$	0.835 $0.790^{+0.053}_{-0.044}$	0.766 $0.649^{+0.12}_{-0.078}$	106.7 $110.7^{+4.6}_{-4.7}$	167.48 $167.49^{+0.89}_{-0.89}$	92.98 $93.81^{+0.89}_{-0.88}$	160 95^{+65}_{-30}	NEW
23167−1534 114919	660 610^{+240}_{-140}	2012.46 $2012.43^{+0.65}_{-0.77}$	0.857 $0.852^{+0.031}_{-0.031}$	0.550 $0.534^{+0.12}_{-0.076}$	326.3 $326.6^{+3.9}_{-4.1}$	143.5 $143.9^{+2.0}_{-2.1}$	72.8 $73.5^{+2.8}_{-2.9}$	2.82 $2.96^{+0.40}_{-0.34}$	NEW

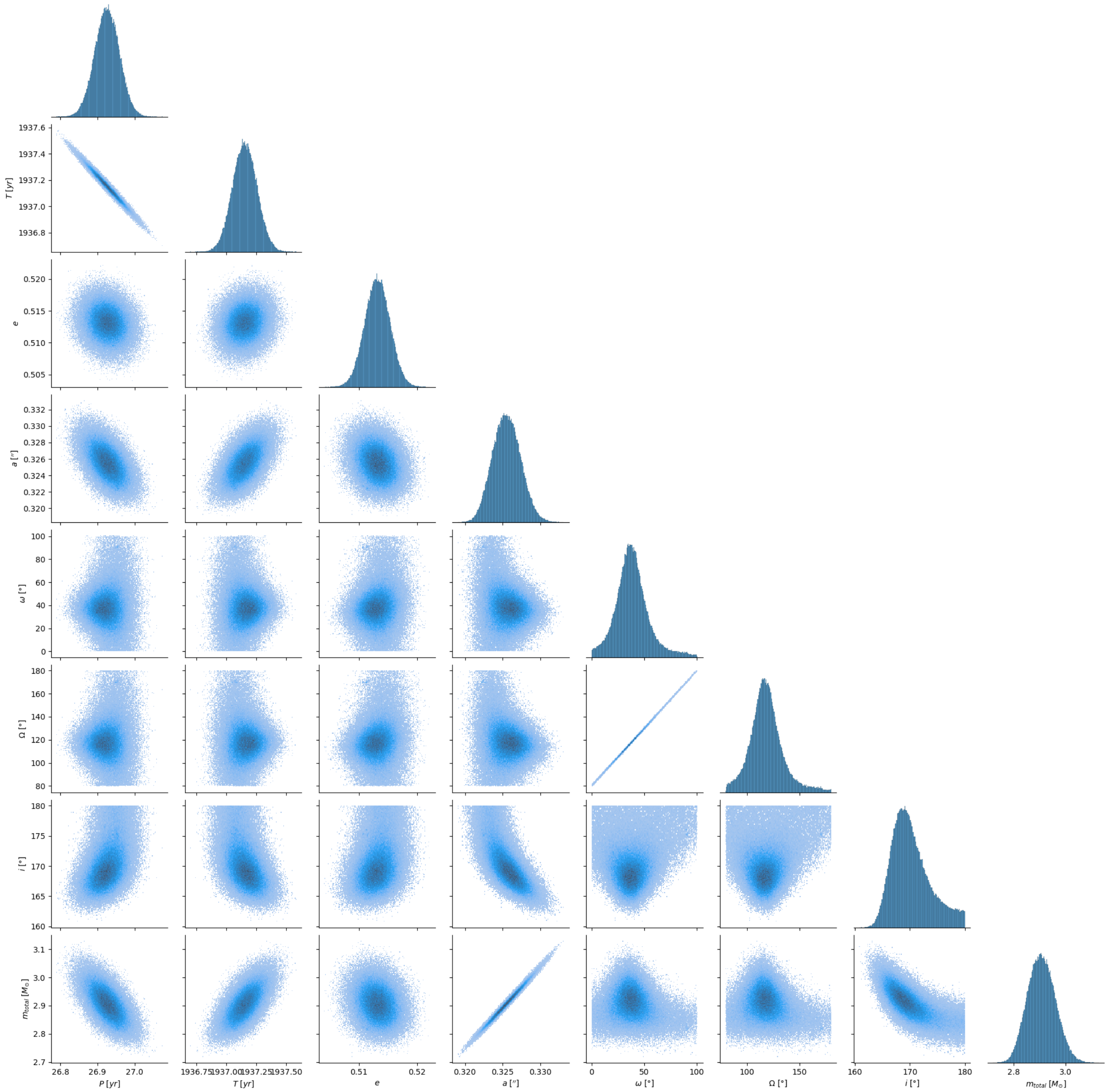

Figure 3.3: Pair marginal posterior distribution of parameters of the visual system HIP 78662.

masses. We report first time results for 4 of these systems.

Figure 3.4 shows an example orbit (left panel)/RV phase curve (right panel) plot, specifically for the SB1 system HIP 38645. The features in the orbit plot are the equivalent of those shown in the example orbit plot for visual binaries detailed previously. In the RV curve plot, the blue curve represents the radial velocity, and the dashed black line indicates the systemic velocity.

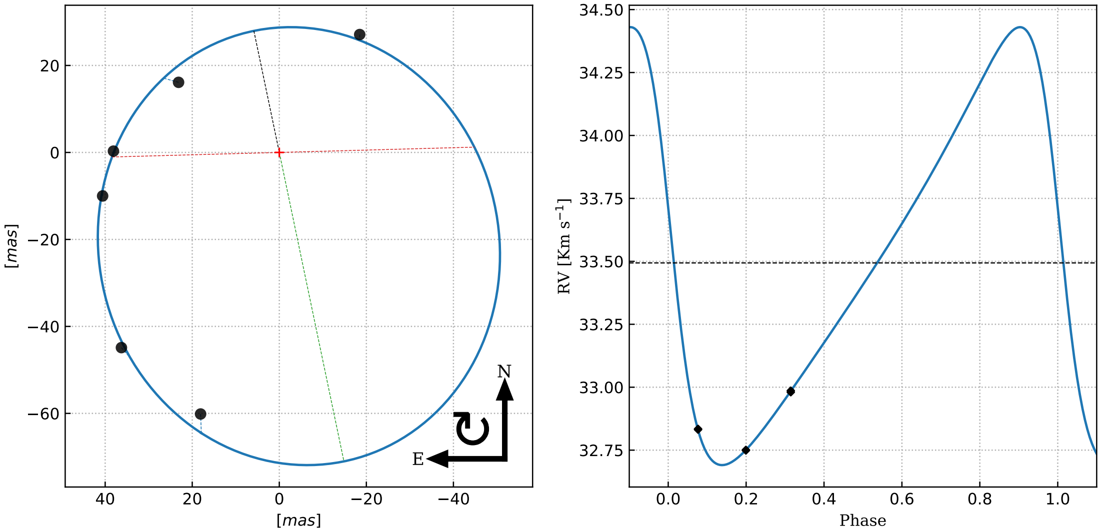

Figure 3.4: Orbit and RV curve of the SB1 system HIP 38645.

3.3 SB2 binaries

In Table 3.4, we present the extended orbital elements for the two SB2 systems in our sample. In the upper part of the table, the first column provides the WDS name and the Hipparcos number; and the next columns the source of the values presented and the orbital elements P, T, e, a, ω, Ω, and i. In the lower part of the table, the first two columns are the same as in the upper part, followed by V_{CoM}, K_1, and K_2. The last column references the source of the orbital data previously reported in the literature. Table 3.5 is analog to Table 3.3.

Figures 3.5 and 3.6 illustrates the orbit (left panel) and the RV phase curve (right panel) for our two SB2 binaries; HIP 7580 and HIP 9774 AaAb. The features in the orbit panel are analogous to those in the orbit plots for visual and SB1 systems. The features in the RV panel are analogous to those in our SB1 example, but now the blue curve represents the primary star, and the red curve the secondary star.

In all the figures, orbit and RV phase, the data points are depicted with varying sizes and fill styles to indicate different ranges of uncertainties. Smaller, filled points correspond to measurements of high precision, often from our recent observations. In contrast, larger, partially filled or empty points represent data with higher uncertainties, which often correspond

Table 3.2: Extended orbital elements for our SB1 binaries.

WDS name **HIP number**	P [yr]	T [yr]	e	a [arcsec]	ω [°]	Ω [°]	i [°]	V_{CoM} [km s^{-1}]	K_* [km s^{-1}]	Orbit reference
01117+0835 5593	59.6 $60.1^{+9.9}_{-6.3}$	2024.34 $2024.38^{+0.28}_{-0.25}$	0.699 $0.685^{+0.051}_{-0.051}$	0.238 $0.240^{+0.029}_{-0.019}$	145 145^{+10}_{-13}	136.46 $136.11^{+0.63}_{-0.75}$	78.5 $78.9^{+1.5}_{-1.7}$	51.4 $51.0^{+1.6}_{-1.6}$	11.62[b] $11.44^{+1.1}_{-0.95}$	NEW
02572−2458 13768	1.51664 $1.51687^{+0.00040}_{-0.00048}$	1982.8437 $1982.8391^{+0.010}_{-0.0083}$	0.5560 $0.5549^{+0.0076}_{-0.0076}$	0.06103 $0.06139^{+0.00075}_{-0.00074}$	78.8 $77.4^{+3.9}_{-3.5}$	97.3 $95.8^{+3.9}_{-3.5}$	174.7 $174.65^{+0.43}_{-0.48}$	49.894 $49.894^{+0.039}_{-0.039}$	1.461[a] $1.499^{+0.073}_{-0.073}$	Tok2015c
05286−4548 25641	39.0 $40.1^{+1.8}_{-1.4}$	2016.78 $2016.88^{+0.15}_{-0.14}$	0.913 $0.919^{+0.015}_{-0.014}$	0.117 $0.112^{+0.013}_{-0.010}$	304.3 $304.2^{+4.9}_{-5.1}$	323.3 $322.5^{+3.9}_{-4.4}$	113.7 $115.2^{+4.1}_{-3.8}$	50.2 $51.0^{+1.4}_{-1.7}$	25.5[b] $22.1^{+8.8}_{-6.5}$	NEW
07548−6613 38645	7.5 $7.7^{+1.5}_{-1.0}$	2021.674 $2021.679^{+0.090}_{-0.096}$	0.435 $0.442^{+0.047}_{-0.040}$	0.0511 $0.0509^{+0.0053}_{-0.0037}$	79.9 $80.7^{+4.1}_{-3.8}$	92 93^{+10}_{-10}	171.8 $169.0^{+4.5}_{-8.5}$	33.49 $33.5^{+0.21}_{-0.15}$	0.87[a] $0.88^{+0.25}_{-0.17}$	NEW
12018−3439 58669	190.7 $188.1^{+5.5}_{-5.0}$	2015.03 $2015.32^{+0.48}_{-0.49}$	0.4192 $0.4171^{+0.0072}_{-0.0066}$	0.906 $0.895^{+0.020}_{-0.018}$	261.7 $263.2^{+2.4}_{-2.4}$	268.74 $268.78^{+0.22}_{-0.22}$	110.8 $110.97^{+0.37}_{-0.37}$	-4.210 $-4.228^{+0.0.72}_{-0.074}$	2.04[a] $2.02^{+0.15}_{-0.15}$	Tok2015a
13138−6756 64545	34.6 $37.7^{+1.1}_{-1.0}$	2023.164 $2023.132^{+0.021}_{-0.029}$	0.884 $0.794^{+0.023}_{-0.018}$	0.1925 $0.1314^{+0.011}_{-0.0076}$	237.4 $218.6^{+5.3}_{-4.7}$	303.4 $304.4^{+2.5}_{-2.5}$	107.5 $121.6^{+3.6}_{-4.0}$	66.5 $43.0^{+5.3}_{-4.2}$	51.0[b] $18.6^{+5.4}_{-3.6}$	NEW
14025−2440 68587	207 202^{+17}_{-14}	2011.18 $2011.30^{+0.42}_{-0.43}$	0.536 $0.528^{+0.024}_{-0.022}$	0.605 $0.594^{+0.033}_{-0.028}$	240.4 $241.1^{+3.6}_{-3.5}$	201.1 $201.0^{+1.6}_{-1.6}$	50.0 $49.8^{+1.1}_{-1.1}$	13.51 $13.48^{+0.19}_{-0.19}$	3.0[b] $3.0^{+0.2}_{-0.2}$	Tok2020e
15317+0053 76031	1.70355 $1.70359^{+0.00027}_{-0.00027}$	2004.3203 $2004.32090^{+0.00060}_{-0.00080}$	0.478 $0.472^{+0.010}_{-0.010}$	0.03943 $0.03931^{+0.00058}_{-0.00058}$	359.39 $359.60^{+0.23}_{-0.38}$	325.0 $325.1^{+1.0}_{-1.0}$	163.1 $163.2^{+1.2}_{-1.4}$	4.29 $4.27^{+0.10}_{-0.10}$	7.97[b] $7.89^{+0.16}_{-0.16}$	Tok2016e

---

a. K_1.

b. K_2.

Table 3.3: Parallaxes and individual component masses for our SB1 sample.

WDS name **HIP number**	Hipparcos [mas]	GAIA eDR3 [mas]	π_{orb} [mas]	$M_{\rm S}/M_{\rm P}$ $M_\odot$	$M_{\rm P}$ $M_\odot$	$M_{\rm S}$ $M_\odot$
01117+0835 5593	7.23 ± 1.38	10.1184 ± 0.2448	10.11 $10.09^{+0.16}_{-0.16}$	0.389 $0.383^{+0.038}_{-0.034}$	2.65 $2.73^{+0.25}_{-0.23}$	1.030 $1.046^{+0.027}_{-0.027}$
02572−2458 13768	38.35 ± 1.24	40.9861 ± 0.4288	41.02 $40.96^{+0.29}_{-0.29}$	0.818 $0.835^{+0.092}_{-0.088}$	0.788 $0.798^{+0.02}_{-0.02}$	0.644 $0.666^{+0.065}_{-0.064}$
05286−4548 25641	6.19 ± 0.89	5.7574 ± 0.0161	5.758 $5.757^{+0.011}_{-0.011}$	0.37 $2.05^{+1.3}_{-0.79}$	4.0 $3.1^{+1.9}_{-1.2}$	1.491 $1.495^{+0.034}_{-0.034}$
07548−6613 38645	11.26 ± 0.76	11.7234 ± 0.0704	11.706 $11.721^{+0.047}_{-0.047}$	0.47 $0.34^{+0.17}_{-0.10}$	0.9954 $1.005^{+0.027}_{-0.027}$	0.47 $0.34^{+0.17}_{-0.10}$
12018−3439 58669	17.87 ± 0.77	$11.6897 \pm 0.8228^{\textbf{eDR2}}$	22.22 $22.24^{+0.22}_{-0.22}$	0.453 $0.447^{+0.043}_{-0.041}$	1.281 $1.275^{+0.025}_{-0.025}$	0.580 $0.569^{+0.053}_{-0.051}$
13138−6756 64545	8.54 ± 1.07	6.1995 ± 0.1882	6.27 $6.19^{+0.13}_{-0.13}$	0.0585 $0.251^{+0.089}_{-0.075}$	23 $5.4^{+2.3}_{-1.4}$	1.338 $1.347^{+0.033}_{-0.034}$
14025−2440 68587	16.02 ± 1.19	13.3967 ± 0.2046	13.39 $13.37^{+0.14}_{-0.14}$	0.969 $0.969^{+0.10}_{-0.087}$	1.094 $1.099^{+0.097}_{-0.092}$	1.060 $1.066^{+0.027}_{-0.027}$
15317+0053 76031	19.67 ± 0.89	$23.5633 \pm 1.2061^{\textbf{eDR2}}$	18.65 $18.56^{+0.52}_{-0.53}$	0.536 $0.535^{+0.077}_{-0.068}$	2.12 $2.13^{+0.30}_{-0.26}$	1.136 $1.141^{+0.027}_{-0.027}$

to historic data collected in earlier epochs. This visual distinction allows for an intuitive assessment of the reliability of the data points used in the orbital and RV analyses and show how the quality of the data may influence the fitting of the orbital elements and the overall confidence in the derived parameters.

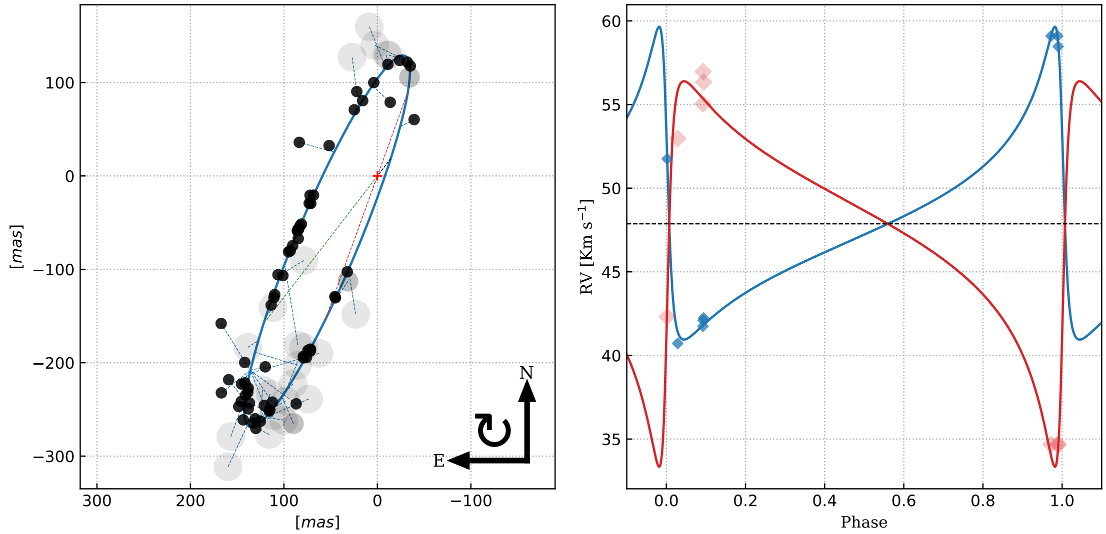

Figure 3.5: Orbit and RV curve of the SB2 system HIP 7580.

3.4 O−C Analysis

An analysis of the Observed−Calculated (O−C) residuals allows to identify and discard data points that exhibit a dispersion beyond a 3 sigma difference. Given that most of the systems under study have a limited set data points, this filtering was applied only in the case of HIP 7580 which has a substantial amount of data available. For this system, the extensive

Table 3.4: Extended orbital elements for our SB2 binaries.

WDS name **HIP number**	Source	P [yr]	T [yr]	e	a [arcsec]	ω [°]	Ω [°]	i [°]
01376−0924	MCMC prior	28.978	1960.937	0.7904	0.3230	70.78	340.1	96.383
7580		$28.980^{+0.020}_{-0.021}$	$1960.937^{+0.022}_{-0.022}$	$0.7900^{+0.0026}_{-0.0026}$	$0.3228^{+0.0018}_{-0.0018}$	$70.81^{+0.17}_{-0.17}$	$340.15^{+0.17}_{-0.17}$	$96.410^{+0.089}_{-0.089}$
	MCMC no-prior	28.982	1960.938	0.7933	0.3248	70.98	340.11	96.351
		$28.984^{+0.021}_{-0.021}$	$1960.937^{+0.022}_{-0.022}$	$0.7922^{+0.0028}_{-0.0028}$	$0.3244^{+0.0020}_{-0.0019}$	$70.95^{+0.18}_{-0.19}$	$340.17^{+0.17}_{-0.18}$	$96.369^{+0.092}_{-0.090}$
	ORB6	28.83 ± 0.25	1989.915 ± 0.021	0.748 ± 0.005	0.292 ± 0.009	248.8 ± 0.3	161.1 ± 1.7	97.4 ± 0.2
	SB9	10540 ± 281.236[d]	47864.7 ± 4.25091[d]	0.797569 ± 0.0066	–	71.5979 ± 0.67	–	–
02057−2423	MCMC prior	2.5809	1998.0115	0.7682	0.04789	289.04	137.8	65.86
9774 AaAb		$2.5812^{+0.0022}_{-0.0021}$	$1998.0100^{+0.0069}_{-0.0071}$	$0.7715^{+0.0044}_{-0.0044}$	$0.04779^{+0.00036}_{-0.00037}$	$289.13^{+0.45}_{-0.44}$	$137.7^{+1.4}_{-1.4}$	$65.97^{+0.80}_{-0.80}$
	MCMC no-prior	2.5799	1998.0122	0.7759	0.0549	288.96	132.2	72.0
		$2.5805^{+0.0021}_{-0.0020}$	$1998.0108^{+0.0064}_{-0.0067}$	$0.7755^{+0.0043}_{-0.0042}$	$0.0553^{+0.0013}_{-0.0013}$	$288.97^{+0.43}_{-0.43}$	$132.8^{+1.5}_{-1.5}$	$72.0^{+1.0}_{-1.1}$
	ORB6	2.582 ± 0.003	2010.917 ± 0.015	0.769 ± 0.015	0.048 ± 0.003	287.9 ± 1.5	127.2 ± 4.6	75.9 ± 4
	SB9	944.2 ± 1.1[d]	55530.0563 ± 2.5[d]	0.769 ± 0.015	–	287.9 ± 1.5	–	–

WDS name **HIP number**	Source	V_{CoM} [km s^{-1}]	K_1 [km s^{-1}]	K_2 [km s^{-1}]	Orbit reference
01376−0924	MCMC prior	47.867	9.354	11.53	This paper
7580		$47.834^{+0.079}_{-0.078}$	$9.343^{+0.087}_{-0.087}$	$11.6^{+0.31}_{-0.31}$	
	MCMC no-prior	47.827	9.315	11.26	This paper
		$47.82^{+0.078}_{-0.079}$	$9.311^{+0.088}_{-0.088}$	$11.11^{+0.39}_{-0.39}$	
	ORB6	–	–	–	Tok1993
	SB9	47.8417 ± 0.12	9.3279 ± 0.23	11.203 ± 0.56	PBX 2000
02057−2423	MCMC prior	40.744	18.45	18.85	This paper
9774 AaAb		$40.763^{+0.063}_{-0.062}$	$18.48^{+0.23}_{-0.21}$	$18.99^{+0.23}_{-0.22}$	
	MCMC no-prior	40.755	18.67	19.20	This paper
		$40.766^{+0.062}_{-0.062}$	$18.63^{+0.22}_{-0.21}$	$19.16^{+0.23}_{-0.22}$	
	ORB6	–	–	–	Tok2014b
	SB9	40.66 ± 0.12	18.52 ± 0.5	19.1 ± 0.5	TOK 2015

Table 3.5: Parallaxes and individual component masses for our SB2 sample.

WDS name **HIP number**	Hipparcos [mas]	GAIA eDR3 [mas]	π_{orb} [mas]	$M_{\mathrm{S}}/M_{\mathrm{P}}$ $M_{\odot}$	M_{P} $M_{\odot}$	M_{S} $M_{\odot}$
01376−0924	24.76 ± 0.90	22.9702 ± 0.6299	25.8	0.812	1.291	1.047
7580 **Prior**			$25.69^{+0.42}_{-0.41}$	$0.805^{+0.024}_{-0.023}$	$1.310^{+0.073}_{-0.070}$	$1.055^{+0.036}_{-0.035}$
01376−0924			26.48	0.827	1.202	0.994
7580 **No-Prior**			$26.59^{+0.62}_{-0.60}$	$0.838^{+0.031}_{-0.029}$	$1.177^{+0.092}_{-0.088}$	$0.986^{+0.047}_{-0.045}$
02057−2423	21.44 ± 1.43	21.0892 ± 0.0879	21.122	0.9787	0.884	0.865
9774 AaAb **Prior**			$21.119^{+0.059}_{-0.059}$	$0.9728^{+0.0083}_{-0.0081}$	$0.882^{+0.020}_{-0.020}$	$0.858^{+0.020}_{-0.020}$
02057−2423			25.21	0.9720	0.785	0.763
9774 AaAb **No-Prior**			$25.45^{+0.66}_{-0.67}$	$0.9724^{+0.0082}_{-0.0082}$	$0.783^{+0.020}_{-0.019}$	$0.762^{+0.020}_{-0.019}$

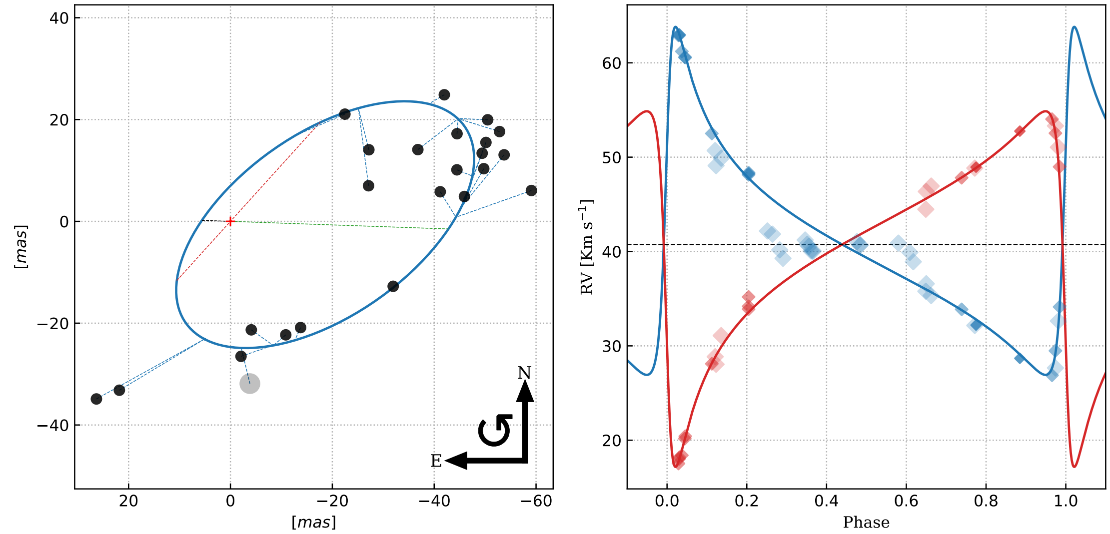

Figure 3.6: Orbit and RV curve of the SB2 system HIP 9774 AaAb.

dataset available allowed for a rigorous examination, ensuring that outliers were identified and excluded, thereby enhancing the reliability of the derived orbital parameters and mass estimates.

In the case of systems with fewer data points, despite that some observations do lie beyond the 3 sigma threshold, they were not egregiously out of line. In general, the observations of these systems with limited data points are more recent and of higher quality. Retaining these points was deemed appropriate to optimize the use of available observations, while maintaining the integrity of the analysis.

Figure 3.7 is an example residual plot, specifically for our SB2 system HIP 7580, showing the O−C residuals for the position angle θ, the separation ρ, and the RV of the primary and secondary component, V_p and V_S respectively. These residuals are plotted against both epoch (left panels) and orbital phase (right panels).

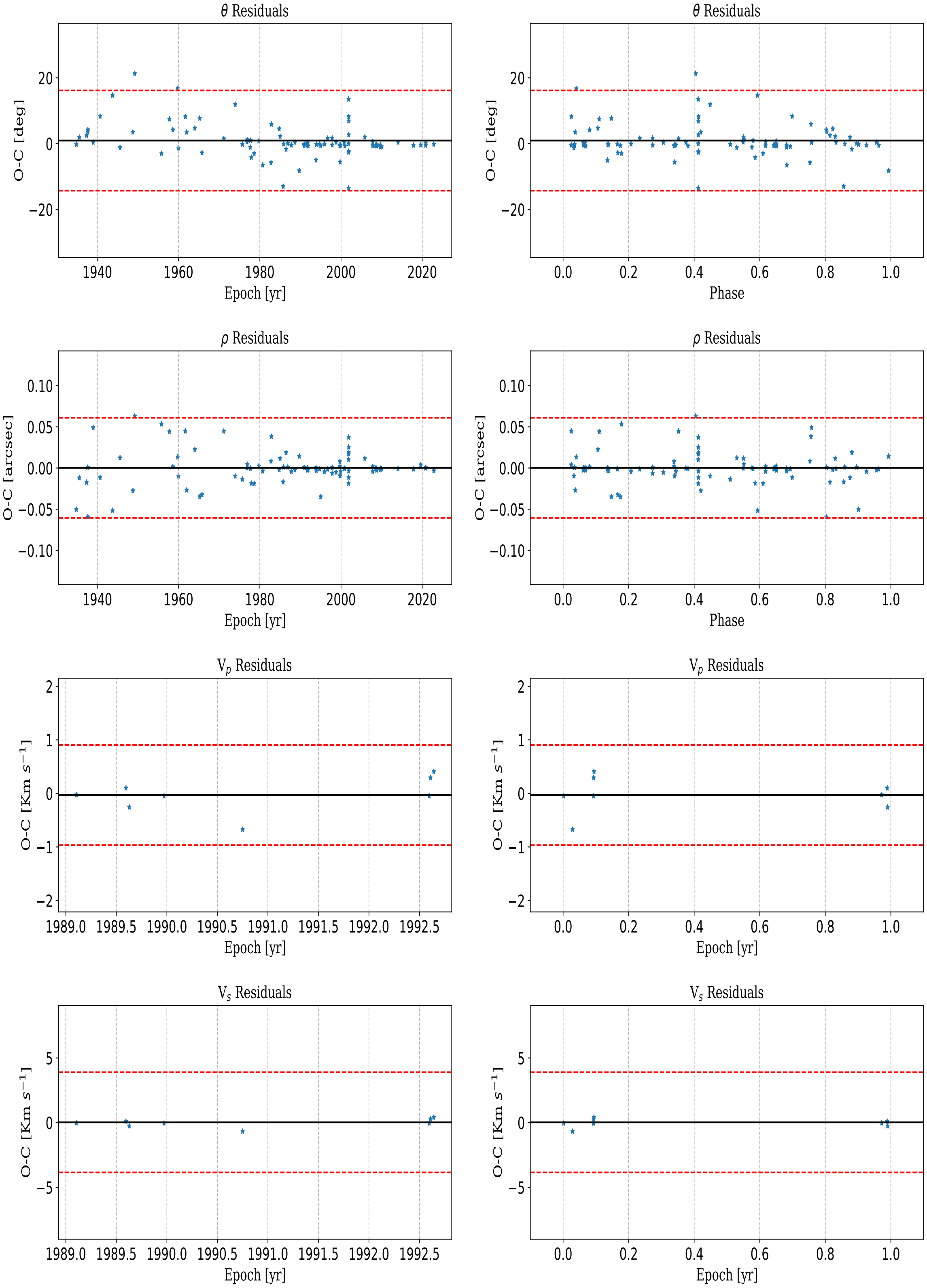

Figure 3.7: Residuals from O−C after point cleaning of the SB2 system HIP 7580.

Chapter 4

Discussion

4.1 Comments on Individual Objects

Here we provide some details about the orbital solutions obtained, along with a discussion of the mass and parallax determinations (where applicable), for each of our systems. These comments aim to highlight key aspects of each system, including the strengths and potential limitations of the data available for them. Additionally, we identify areas where further observations could enhance the accuracy of the derived parameters, particularly in cases where the current data may not fully constrain the system's dynamics.

WDS00462−2214=HIP 3606: Our latest observations with HRCam cover about one third of the orbit. The only available Hipparcos data point lies in the opposite part of the orbit covered by high-precision observations, which allowed for a good orbit determination. The total mass calculated for this system is consistent with the masses estimated from mass and absolute magnitude relations. RV observations for this object are highly recommended to obtain a self-consistent orbital parallax and individual masses.

WDS01117+0835=HIP 5593: Ours is the first orbit calculated for this relatively high-inclination system. The orbit has been half-covered and the latest observations were made near the periastron, which allowed for a good orbit determination. We also incorporated a testimonial RV point in our solution. The marginal posterior distribution of the parameters narrow down the constraint range, but they are non-Gaussian, and the parameters exhibit correlations. There is a significant discrepancy of 2.88 mas between the parallax values given by Hipparcos and Gaia (together with a high RUWE), which renders the parallax unreliable.

WDS01376−0924=HIP 7580: This SB2 system has good orbit coverage and a strategic RV observation made near periastron, where the components are too close to be easily observed (see Figure 3.5). Our solutions, with and without parallax prior, are self-consistent, but there is a discrepancy of 0.68 mas between them (see Table 3.5). This discrepancy in the parallax leads to different results for the masses, despite the good orbit solution. Our combined solution improves the error margins of the results reported in ORB6 and SB9. New

RV observations are necessary to reduce the uncertainty on the orbital parallax, and thus refine the individual masses.

WDS02057−2423=HIP 9774 AaAb: This SB2 system is a compact, so visual observations near periastron are difficult. Fortunately, the RV curve of this object is well covered (see Figure 3.6). The solutions with and without prior parallax are self-consistent, with only a slight variation in π and a. This is a multiple system, so measurements of the parallax tend to be biased. Treating this object as a hierarchical multiple system is recommended.

WDS02572−2458=HIP 13768: This SB1 system has a good observational coverage of both the orbit and the RV curve, providing a strong foundation for determining the orbital parameters. Its orbit is nearly face-on, with an inclination of 174° and a period of 1.5 years. The face-on nature of the orbit, while advantageous in some respects, makes it challenging to accurately constraining certain parameters. Most parameters exhibit a low correlation, indicating a reliable solution in general. However, ω and Ω are the worst constrained, reflecting the difficulty to precisely determine these angles because of the system's orientation.

WDS03347−0451: Ours is the first orbit calculated for this system. With a period close to 4 years, the 6 observations available cover a significant portion of the orbit, resulting in a good initial fit of the orbital parameters. However, more observations are needed to improve precision and decouple the angular parameters.

WDS03489+1143=HIP 17826: This is a long-period system. Its orbit is only half covered and there are no observation close to the periastron. Our solution reports the range of uncertainty of the parameters. New observations closer to the periastron will allow to restrain T, and therefore, P.

WDS05286−4548=HIP 25641: Ours is the first orbit reported for this SB1 system. It is highly eccentric (e = 0.91) and has a period close to 40 years. The Hipparcos data point is off the curve and we do not have observations nearby. Only one RV observation is available. More RV points are necessary to validate the results obtained with this single data point and resolve the correlation between parameters.

WDS05474−1032=HIP 27341: This system has a high eccentricity (e = 0.95) and has a period of approximately 30 years. The available data points only cover the apoastron zone, which, along with the high eccentricity, causes difficulties to obtain a good fit of the orbital parameters.

WDS07548−6613=HIP 38645: Ours is the first orbit calculated for this system, which has a period of 7.5 years. Observations cover about one half of the orbit and we have three RV observations in a critical part of the curve (see Figure 3.4), which greatly aided the fitting process. For a first report the parameters are well constrained, but correlations are seen between some of the parameters. Further observations will help to refine these results.

WDS12018−3439=HIP 58669: This system, with a period close to 190 years, has been observed since 1897, covering about 3/4 of the orbit. The three RV observations we have included allowed us to resolve the ambiguity in Ω. The orbital parameters are well constrained, but still correlations between them are seen. The Gaia DR2 parallax (11.6 mas) is in discrepancy with the 17.8 mas reported by Hipparcos. Our tentative solution, using the Gaia parallax as a prior, gives an orbital parallax of 22.2 mas. Extended observations of the RV curve for both components will allow for a more reliable orbital parallax estimation.

WDS13138−6756=HIP 64545: This system has a period of $P = 37.7$ years and the observations cover about a fourth of the orbit. The Hipparcos data point, located opposite to the most recent observations, is highly beneficial for the fitting process. Ours is the first orbit report for this system, and includes a single RV data point. More RV observations are necessary to validate the results obtained from this initial data point and decouple the parameters.

WDS14025−2440=HIP 68587: With a period of over 200 years, this is the second longest period system in our sample. This object has been continuously observed from 2014 to 2022 with HRCam@SOAR and Zorro@GS, which have beautifully mapped a orbit segment near the periastron. The previous solution by Tok2020e proposed $\omega = 65.5°$ and $\Omega = 19.8°$; the single RV point now available resolved the ambiguity of the ascending node, giving $\Omega = 201.1°$ and $\omega = 240.4°$. More RV observations are necessary to validate the results obtained from this initial data point.

WDS14152−6739=HIP 69643: The high eccentricity, close to 0.9, and the relatively high inclination, around 80°, make this system tricky to study. It has a period of over 120 years, but it is near periastron, so recent interferometric and spectroscopic observations have been very valuable. New data will help to resolve the correlations seen between the parameters.

WDS14567−6247=HIP 73129: This system, with a period close to 40 years, has been observed continuously. The good distribution of orbital observations, has made possible to constrain the orbital parameters effectively. However, while the orbital parameters seem well constrained, the total mass, estimated to be about 6 $M_\odot$, disagrees with the expected mass of the system according to the tables of Abushattal (about 9 $M_\odot$). It is cataloged as a multiple system in the Multiple Star Catalog (MSC)[1] of Tokovinin, A. A. (1997), which could explain the high RUWE (8.9), and cause a misestimation of parallax leading to a misestimation of the mass.

WDS15317+0053=HIP 76031: This relatively compact SB1 system, with a period of 1.7 years, has half of its orbit observed and a fully covered RV curve, to which our FEROS RV observations fit perfectly. Ours is the first combined solution for this system.

WDS16016−7843=HIP 78505: Ours is the first attempt to solve the orbit of this system. Several attempts were made to include RV data; however, due to the lack of sufficient points, fitting additional parameters led to convergence problems in the resulting fit. All tentative solutions suggest a system with a period of 80 years, an almost edge-on inclination (89°) and a high eccentricity (near 0.9), making this system particularly challenging to solve. Ultimately, we opted to fit the system using only astrometric data. In this case, the estimated inclination

---

[1] `https://www.ctio.noirlab.edu/~atokovin/stars/`.

remains close to 90°, but the eccentricity is now estimated to be lower than 0.8. More RV points are necessary to attempt a combined solution.

WDS16035−5747=HIP 78662: This system, with a period of 26.9 years, has a good distribution of orbital observations, allowing for a well-constrained set of orbital parameters. New RV data will help to resolve the correlation seen between Ω and ω.

WDS16434−2819=HIP 81874: Ours is the first orbit report for this system. The 95° inclination makes it difficult to obtain a good fit with only astrometric data. Additionally, the closeness between the primary star and the periastron makes it difficult to obtain good observations in that zone. RV observations are crucial.

WDS17157−0949=HIP 84430 AB: The outer orbit of this triple system has a period of 114 years. Observations cover half of the orbit, including the region near periastron. Although the parameters are generally well constrained, correlations between them persist, suggesting the need for additional observations to further refine the orbital solution.

WDS17157−0949=HIP 84430 BaBb: The inner orbit of this triple system has a period of 5.2 years. Despite good coverage of the orbit, the angular parameters still exhibit ambiguities and strong correlations between them, making it difficult to achieve a fully reliable solution.

There is a discrepancy between the parallaxes reported by Hipparcos and Gaia DR2 for this triple system, which highlights the difficulties to accurately determine its distance. A hierarchical study of this system would be valuable to better understand its complex dynamics and to resolve these discrepancies more effectively.

WDS17349+1234=HIP 86032: This system, with a period of 8.5 years, has a highly eccentric (e = 0.89) orbit. The orbital parameters are well constrained, but there are correlations between the parameters. Observations closer to the periastron are recommended.

WDS20306+1349=HIP 101181: This system, with a high eccentricity close to 0.9, has a period of 29 years. The proximity of the primary star to the periastron makes astrometric observations in this zone difficult. While the parameters are well constrained, correlation between them are seen. RV observations for this system are recommended.

WDS22302−5345: Ours is the first orbit report for this nearby (less than 20 pc) M-dwarf system, which has a period of about 7 years. The observations cover about half of the orbit, with a pair near periastron. The marginal post distribution of the parameters is not perfectly Gaussian and there is a correlation between the parameters, but they are relatively well constrained.

WDS23133−4937=HIP 114626: Ours is the first attempt to determine the orbital parameters of this system. Our results indicate a pronounced inclination of 92°, making this system a challenge to work with. The marginal posterior distribution of the parameters appears to have a good behavior; however, the total mass estimate does not make sense. More high-precision observations are needed.

WDS23167−1534=HIP 114919: This is the system with the longest period in our sample. Thanks to historical observations covering about a third of the orbit, and high-precision observations near the periastron, we were able to present this first orbit report. The total mass estimate, close to 3 $M_{\odot}$, is in line with the expected value from Abushattal's tables. This consistency enhances the reliability of our solution and highlights the importance of observations near the periastron.

4.2 Comments on Our SB1 Sample

Although we have 8 objects considered as SB1, only HIP 13768 and HIP 76031 have sufficient RV data points to be reliably classified as such. HIP 38645 has 3 observations that effectively cover the inflection point in the radial velocity curve, which aids in better determining the orbital parameters and reliably resolves the ambiguity in Ω for this system. HIP 58669 also has 3 points, but they are concentrated in the same section of the orbit, limiting the information they provide on their own. However, the visual orbit is well observed, allowing for a useful application of the radial velocity data.

In the system HIP 68587, as previously mentioned, the RV point enables us to resolve the ambiguity in Ω (and consequently in ω) relative to the visual orbit reported by Tok2020e. During our MCMC analysis, we also addressed the SB1 systems using only the available astrometric data. Despite the lack of points, the SB1 solutions for HIP 25641 and HIP 38645 successfully resolved the ambiguity, changing in 180° the values of Ω and ω with respect our solutions, even with HIP 25641 presenting a single RV observation. For the other systems, the RV observations confirmed the values obtained from the astrometric solution.

When incorporating RV data into the orbital analysis, it becomes necessary to fit three additional parameters, however, when only a single RV point, or very few, is available, this sparse data may not sufficiently constrain these parameters. This limitation can result in an overfitting of the RV data, potentially leading to less accurate orbital solutions than those derived using astrometric data alone. In such cases, the inclusion of minimal RV data points might not offer a significant advantage and may even complicate the solution, making the purely astrometric fit more reliable.

Chapter 5

Conclusion

This thesis presents a comprehensive analysis of a sample of 26 binary star systems, focused on deriving accurate orbital elements and mass estimates using a combination of astrometric and radial velocity data. Key results of this study include the determination of 10 new orbital solutions, for systems that previously lacked a detailed analysis.

This study highlights the challenges faced when characterizing binary star systems. In particular, systems with high eccentricity or nearly edge-on inclinations continue to present difficulties in obtaining precise orbital solutions. The combination of both visual and spectroscopic data has proven to be a powerful approach to resolve ambiguities in orbital parameters, such as the inclination and Ω, which are often hard to determine, even with a single RV observation. Additionally, discrepancies in parallax measurements from different sources underscores the need for further refinement of observational techniques and data analysis methods.

Successful application of Bayesian MCMC methods has allowed for the determination of posterior probability density functions for the orbital parameters, providing realistic confidence intervals that reflect the true uncertainties in the derived values.

Ongoing research by our group in the area of the present work includes continued observations, particularly in critical regions of the orbit, such as near periastron or lacking previous coverage, that are essential for a further refinement of the orbital parameters and addressing existing uncertainties.

The methodologies developed and used in this study are being applied by our group to a much larger sample of systems, contributing to the underlying effort to refine the MLR, and, in general, to a better understanding of the fundamentals of stellar astrophysics.

All the results presented in this thesis will be part of a publication by Dirk et al. (2024, in preparation).

Acknowledgments

We extend our deepest gratitude to Camila Caballero for her invaluable assistance in reducing and providing the new FEROS data utilized in this thesis. Additionally, we would like to sincerely thank Professor Mónica Rubio for generously allocating funds from her FONDECYT project No 1190684, which provided crucial support during the completion of this work.

Based in part on observations obtained at the Southern Astrophysical Research (SOAR) telescope, which is a joint project of the Ministério da Ciência, Tecnologia, e Inovaçãoes (MCTI) da República Federativa do Brasil, the U.S. National Optical Astronomy Observatory (NOAO), the University of North Carolina at Chapel Hill (UNC), and Michigan State University (MSU).

Some of the Observations in the thesis made use of the High-Resolution Imaging instrument Zorro. Zorro was funded by the NASA Exoplanet Exploration Program and built at the NASA Ames Research Center by Steve B. Howell, Nic Scott, Elliott P. Horch, and Emmett Quigley. Zorro was mounted on the Gemini South telescope of the international Gemini Observatory, a program of NSF NOIRLab, which is managed by the Association of Universities for Research in Astronomy (AURA) under a cooperative agreement with the U.S. National Science Foundation. on behalf of the Gemini partnership: the U.S. National Science Foundation (United States), National Research Council (Canada), Agencia Nacional de Investigación y Desarrollo (Chile), Ministerio de Ciencia, Tecnología e Innovación (Argentina), Ministério da Ciência, Tecnologia, Inovações e Comunicações (Brazil), and Korea Astronomy and Space Science Institute (Republic of Korea).

We acknowledge support from the Chilean Gemini Time Allocation Committee for programs GS-2019A-Q-110, GS-2019A-Q-311, GS-2019B-Q-116, GS-2019B-Q-223, GS-2020A-Q-116, GS-2020B-Q-142, GS-2021A-Q-141, GS-2021B-Q-145, GS-2022A-Q-150, GS-2022B-Q-143, and GS-2023A-Q-142. We acknowledge support from the Chilean National Time Allocation Committee under programs CN2018A-1, CN2019A-2, CN2019B-13, CN2020A-19, CN2020B-10, CN2021B-17, CN2022A-11, CN2022B-14, CN2023A-7, CN-2024A-4, and CN-2024B-5 for SOAR and CN2019A-19, CN2019B-12, CN2020A-1, CN2022A-1, CN2022B-8, CN2023A-5, CN2023B-1, CN2024A-5 and CN2024B-3 for FEROS.

We acknowldege support from FONDECYT/ANID grant No. 1240049 and Fondo GEMINI/ANID, grant No. 3223 AS0002.

Bibliography

Abushattal, A. A., Docobo, J. A., and Campo, P. P. (2020). The Most Probable 3D Orbit for Spectroscopic Binaries. AJ, 159(1):28.

Argyle, R. W. (2012). *Observing and Measuring Visual Double Stars.*

Brahm, R., Jordán, A., and Espinoza, N. (2017). Ceres: A set of automated routines for echelle spectra. *Publications of the Astronomical Society of the Pacific*, 129(973):034002.

Claveria, R. M., Mendez, R. A., Silva, J. F., and Orchard, M. E. (2019). Visual binary stars with partially missing data: Introducing multiple imputation in astrometric analysis. *Publications of the Astronomical Society of the Pacific*, 131(1002):084502.

Docobo, J. A., Campo, P. P., Gómez, J., Méndez, R. A., and Costa, E. (2023). A study of eight visual-spectroscopic southern binaries using recent soar observations. *The Astronomical Journal*, 166(5):211.

Eddington, A. S. (1924). On the relation between the masses and luminosities of the stars. MNRAS, 84:308–332.

Fuhrmann, K., Chini, R., Kaderhandt, L., and Chen, Z. (2017). Multiplicity among Solar-type Stars. ApJ, 836(1):139.

Gaia Collaboration, Prusti, T., de Bruijne, J. H. J., and Brown, A. G. A., e. a. (2016). The Gaia mission. A&A, 595:A1.

Gardner, T., Monnier, J. D., Fekel, F. C., Williamson, M., Baron, F., Hinkley, S., Ireland, M., Kraus, A. L., Kraus, S., Roettenbacher, R. M., Schaefer, G., Sturmann, J., Sturmann, L., and ten Brummelaar, T. (2021). Establishing α Oph as a Prototype Rotator: Precision Orbit with New Keck, CHARA, and RV Observations. ApJ, 921(1):41.

Gelman, A., Carlin, J. B., Stern, H. S., Dunson, D. B., Vehtari, A., and Rubin, D. B. (2013). *Bayesian Data Analysis.* Chapman and Hall/CRC.

Green, R. M. (1985). *Spherical Astronomy.*

Hartkopf, W. I., Mason, B. D., and Worley, C. E. (2001). The 2001 US Naval Observatory Double Star CD-ROM. II. The Fifth Catalog of Orbits of Visual Binary Stars. AJ, 122(6):3472–3479.

Horch, E. P., van Altena, W. F., Demarque, P., Howell, S. B., Everett, M. E., Ciardi, D. R., Teske, J. K., Henry, T. J., and Winters, J. G. (2015). Observations of Binary Stars with the Differential Speckle Survey Instrument. V. Toward an Empirical Metal-Poor Mass-Luminosity Relation. AJ, 149(5):151.

Howell, S. B. and Furlan, E. (2022). Speckle Interferometric Observations With the Gemini 8-m Telescopes: Signal-to-Noise Calculations and Observational Results. *Frontiers in Astronomy and Space Sciences*, 9:871163.

Kahler, H. (1972). The Local Vogt-Russell Theorem. A&A, 20:105.

Kaufer, A., Stahl, O., Tubbesing, S., Nørregaard, P., Avila, G., Francois, P., Pasquini, L., and Pizzella, A. (1999). Commissioning FEROS, the new high-resolution spectrograph at La-Silla. *The Messenger*, 95:8–12.

Kippenhahn, R., Weigert, A., and Weiss, A. (2013). *Stellar Structure and Evolution.*

Mason, B. D., Hartkopf, W. I., and Tokovinin, A. (2010). Binary Star Orbits. IV. Orbits of 18 Southern Interferometric Pairs. AJ, 140(3):735–743.

Mason, B. D., Wycoff, G. L., Hartkopf, W. I., Douglass, G. G., and Worley, C. E. (2001). The 2001 US Naval Observatory Double Star CD-ROM. I. The Washington Double Star Catalog. AJ, 122(6):3466–3471.

Mendez, R. A., Claveria, R. M., Orchard, M. E., and Silva, J. F. (2017). Orbits for 18 Visual Binaries and Two Double-line Spectroscopic Binaries Observed with HRCAM on the CTIO SOAR 4 m Telescope, Using a New Bayesian Orbit Code Based on Markov Chain Monte Carlo. AJ, 154(5):187.

Mendez, R. A., Clavería, R. M., and Costa, E. (2021). Orbits and masses of binaries from speckle interferometry at soar*. *The Astronomical Journal*, 161(4):155.

Mendez, R. A., Tokovinin, A., and Horch, E. (2018). A Speckle survey of Southern Hipparcos Visual Doubles and Geneva-Copenhagen Spectroscopic Binaries. In *Revista Mexicana de Astronomia y Astrofisica Conference Series*, volume 50 of *Revista Mexicana de Astronomia y Astrofisica Conference Series*, pages 56–57.

Murray, C. D. and Dermott, S. F. (2000). *Solar System Dynamics.*

Pourbaix, D. (1994). A trial-and-error approach to the determination of the orbital parameters of visual binaries. A&A, 290:682–691.

Pourbaix, D. (2000). Resolved double-lined spectroscopic binaries: A neglected source of hypothesis-free parallaxes and stellar masses. A&AS, 145:215–222.

Pourbaix, D., Tokovinin, A. A., Batten, A. H., Fekel, F. C., Hartkopf, W. I., Levato, H., Morrell, N. I., Torres, G., and Udry, S. (2004). S_{B^9}: The ninth catalogue of spectroscopic binary orbits. *AA*, 424(2):727–732.

Raghavan, D., McAlister, H. A., Henry, T. J., Latham, D. W., Marcy, G. W., Mason, B. D., Gies, D. R., White, R. J., and Ten Brummelaar, T. A. (2010). VizieR Online Data Catalog: A survey of stellar families (Raghavan+, 2010). *VizieR Online Data Catalog*, page J/ApJS/190/1.

Seymour, D. M., Mason, B. D., Hartkopf, W. I., and Wycoff, G. L. (2002). Binary Star Orbits. II. Preliminary First Orbits for 117 Systems. AJ, 123(2):1023–1038.

Smart, W. M. and Green, R. M. (1977). *Textbook on Spherical Astronomy.*

Tokovinin, A. (1992). Speckle Spectroscopic Studies of Late-Type Stars. In McAlister, H. A. and Hartkopf, W. I., editors, *IAU Colloq. 135: Complementary Approaches to Double and Multiple Star Research*, volume 32 of *Astronomical Society of the Pacific Conference Series*, page 573.

Tokovinin, A. (2016). New Orbits Based on Speckle Interferometry at SOAR. AJ, 152(5):138.

Tokovinin, A. (2016). ORBIT: IDL software for visual, spectroscopic, and combined orbits.

Tokovinin, A. (2018). Ten Years of Speckle Interferometry at SOAR. PASP, 130(985):035002.

Tokovinin, A. (2021). Inner and Outer Orbits in 13 Resolved Hierarchical Stellar Systems. AJ, 161(3):144.

Tokovinin, A., Gorynya, N. A., and Morrell, N. I. (2014). The quadruple system ADS 1652. MNRAS, 443(4):3082–3089.

Tokovinin, A., Mason, B. D., and Hartkopf, W. I. (2010). Speckle interferometry at the blanco and soar telescopes in 2008 and 2009. *The Astronomical Journal*, 139(2):743.

Tokovinin, A., Mason, B. D., and Hartkopf, W. I. (2010). Speckle Interferometry at the Blanco and SOAR Telescopes in 2008 and 2009. AJ, 139(2):743–756.

Tokovinin, A., Mason, B. D., Hartkopf, W. I., Mendez, R. A., and Horch, E. P. (2015a). Speckle Interferometry at SOAR in 2014. AJ, 150(2):50.

Tokovinin, A., Mason, B. D., Mendez, R. A., Costa, E., and Horch, E. P. (2020). Speckle Interferometry at SOAR in 2019. AJ, 160(1):7.

Tokovinin, A., Pribulla, T., and Fischer, D. (2015b). Radial Velocities of Southern Visual Multiple Stars. AJ, 149(1):8.

Tokovinin, A. A. (1993). —. *Astronomy Letters*, 19:73.

Tokovinin, A. A. (1997). Msc - a catalogue of physical multiple stars*. *Astron. Astrophys. Suppl. Ser.*, 124(1):75–84.

van Altena, W. F. and Lee, J. T. (1988). The mass-luminosity relationship for solar-type stars. In Rolfe, E. J., editor, *Seismology of the Sun and Sun-Like Stars*, volume 286 of *ESA Special Publication*, pages 649–651.

Van De Kamp, P. (1967). *Principles of astrometry.*

Wenger, M., Ochsenbein, F., Egret, D., Dubois, P., Bonnarel, F., Borde, S., Genova, F., Jasniewicz, G., Laloë, S., Lesteven, S., and Monier, R. (2000). The SIMBAD astronomical database. The CDS reference database for astronomical objects. A&AS, 143:9–22.

ANNEXES

Annex A

Visual Binaries

WDS00462−2214=HIP 3606

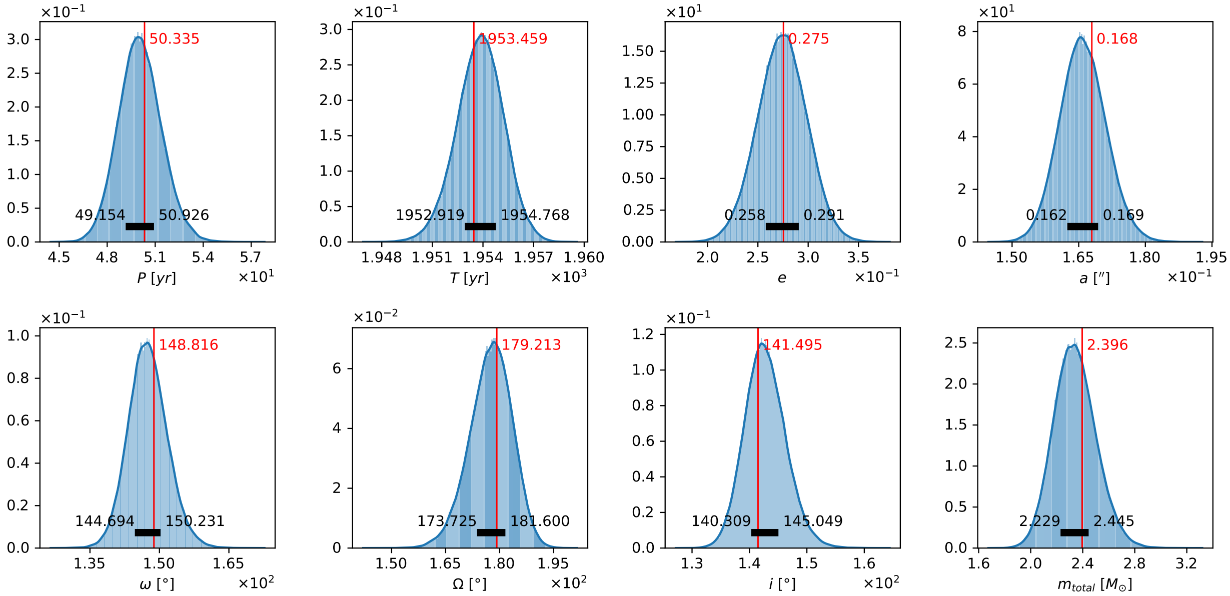

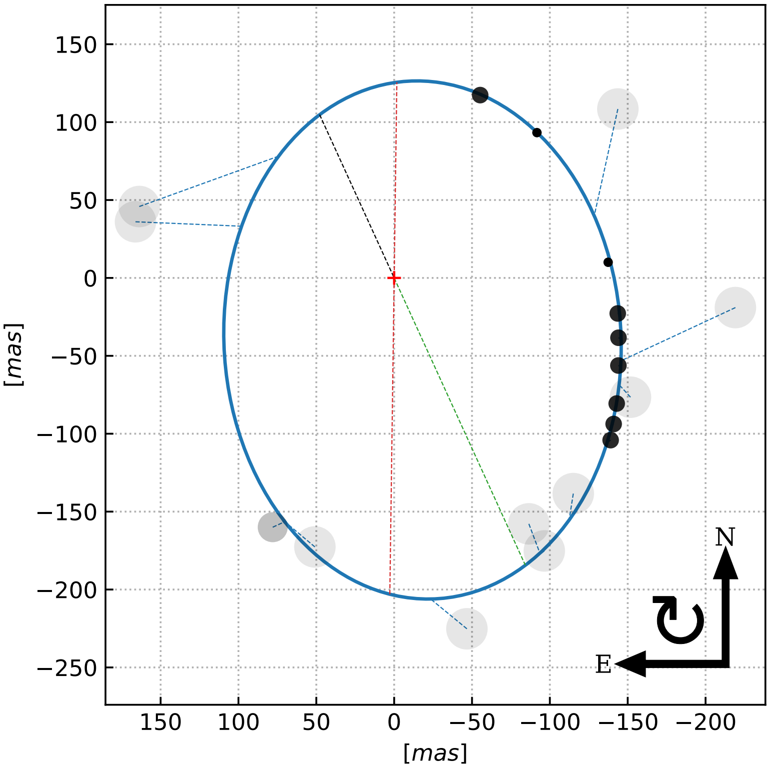
150
100
50
0
−50
−100
−150
−200
−250
[mas]
150
100
50
0
−50
−100
−150
−200
[mas]
N
E

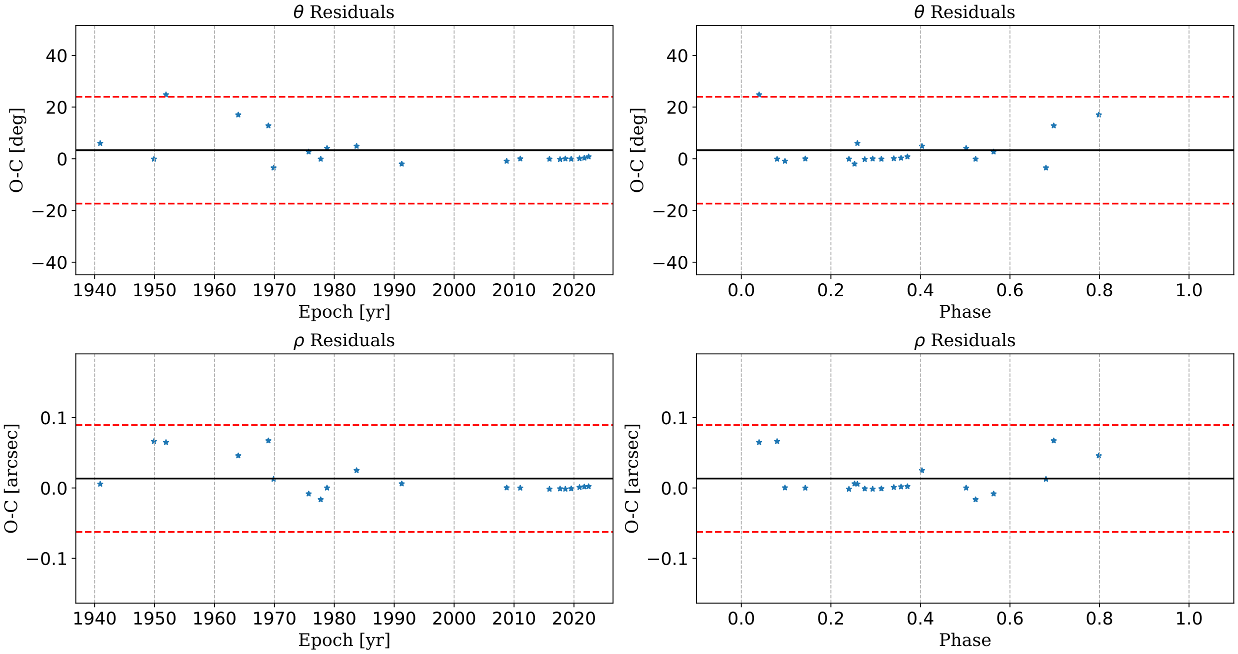
θ Residuals
O-C [deg]
40
20
0
−20
−40
1940
1950
1960
1970
1980
1990
2000
2010
2020
Epoch [yr]
θ Residuals
O-C [deg]
0.0
0.2
0.4
0.6
0.8
1.0
Phase
ρ Residuals
O-C [arcsec]
0.1
0.0
−0.1
Epoch [yr]
ρ Residuals
O-C [arcsec]
Phase

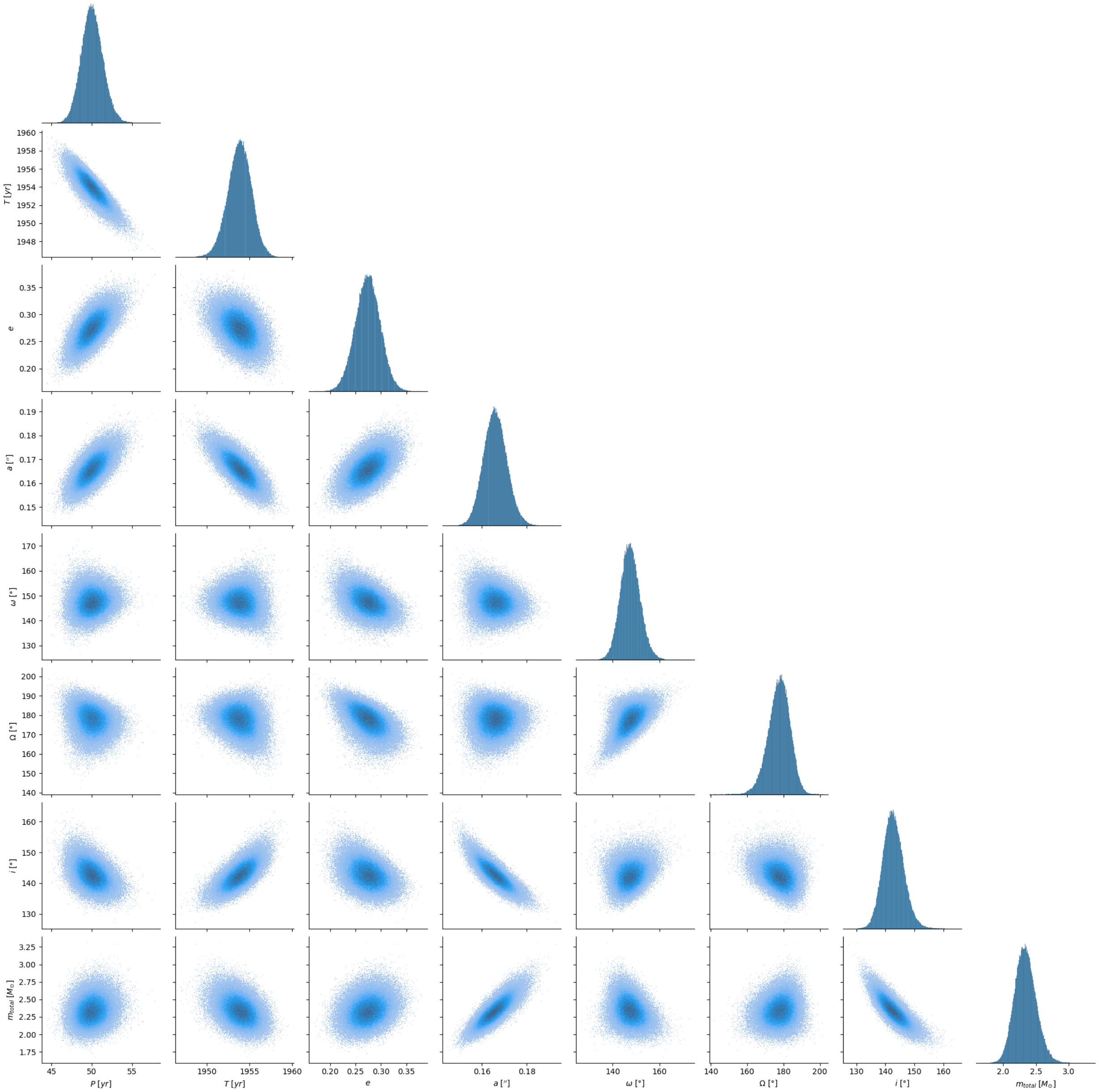
1960
1958
1956
1954
1952
1950
1948
$T\ [yr]$
0.35
0.30
0.25
0.20
e
0.19
0.18
0.17
0.16
0.15
$a\ ['']$
170
160
150
140
130
$\omega\ [°]$
200
190
180
170
160
150
140
$\Omega\ [°]$
160
150
140
130
$i\ [°]$
3.25
3.00
2.75
2.50
2.25
2.00
1.75
$m_{total}\ [M_\odot]$
45
50
55
$P\ [yr]$
1950
1955
1960
$T\ [yr]$
0.20
0.25
0.30
0.35
e
0.16
0.18
$a\ ['']$
140
160
$\omega\ [°]$
140
160
180
200
$\Omega\ [°]$
130
140
150
160
$i\ [°]$
2.0
2.5
3.0
$m_{total}\ [M_\odot]$

WDS03347−0451

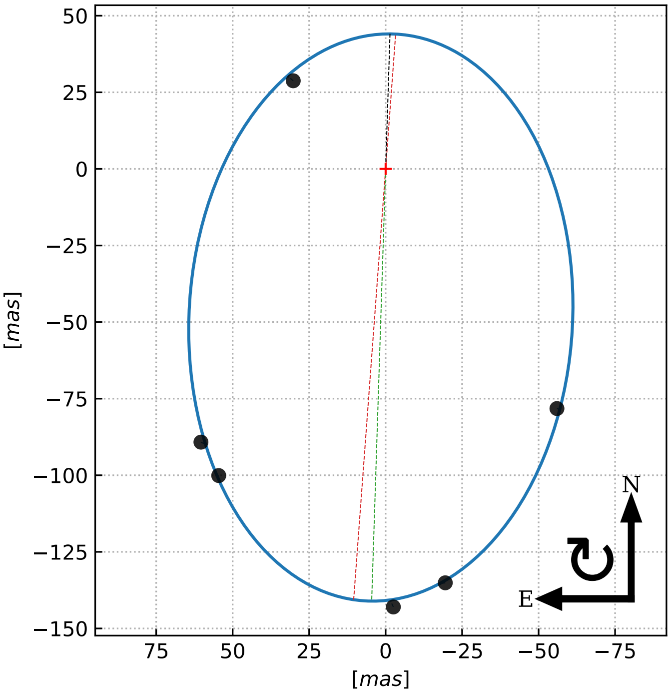

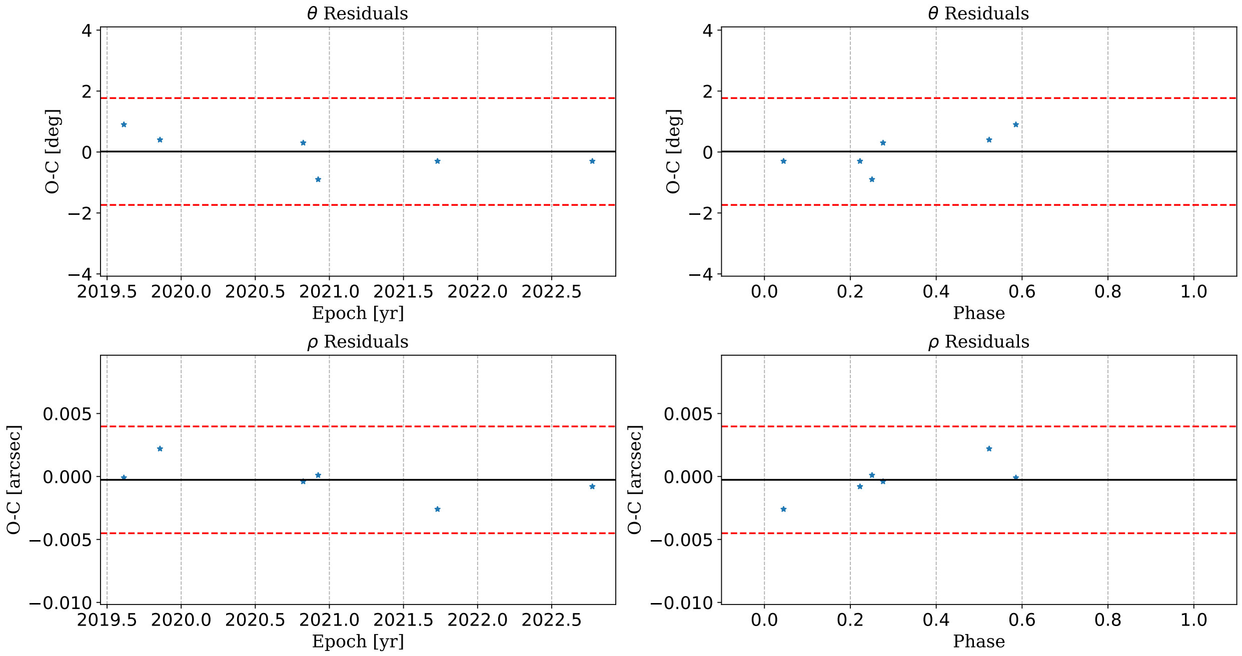

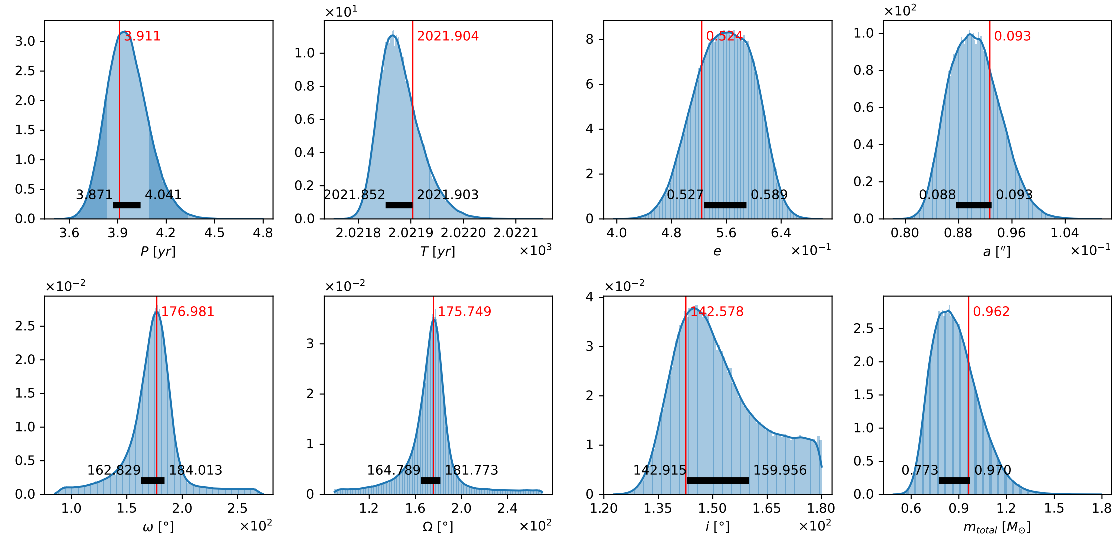

3.911
3.871
4.041
P [yr]
×10¹
2021.904
2021.852
2021.903
T [yr]
×10³
0.524
0.527
0.589
e
×10⁻¹
×10²
0.093
0.088
0.093
a ["]
×10⁻¹
×10⁻²
176.981
162.829
184.013
ω [°]
×10²
×10⁻²
175.749
164.789
181.773
Ω [°]
×10²
×10⁻²
142.578
142.915
159.956
i [°]
×10²
0.962
0.773
0.970
m_total [M_⊙]

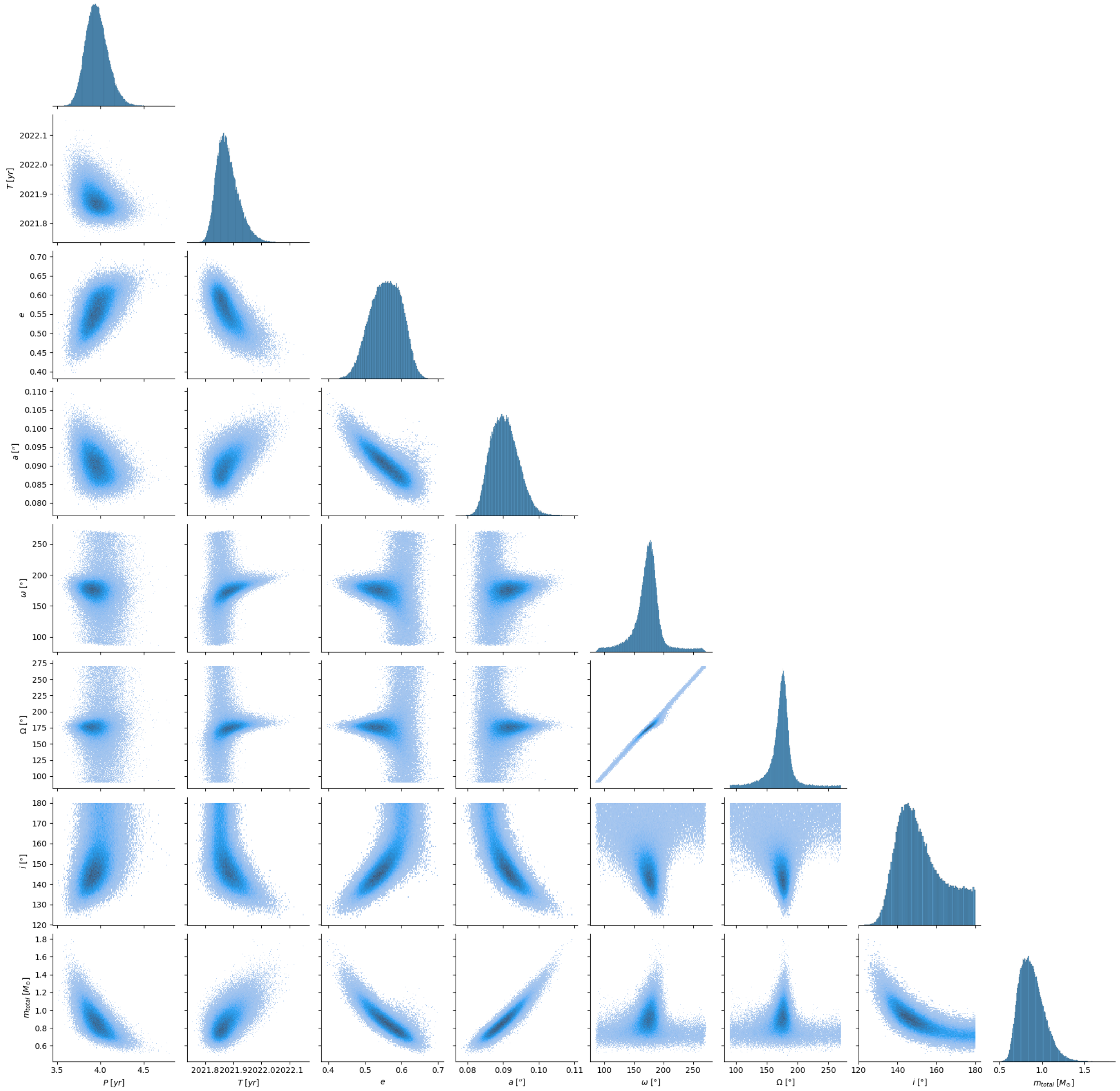

T [yr]
e
a ["]
ω [°]
Ω [°]
i [°]
m_total [M_⊙]
P [yr]
T [yr]
e
a ["]
ω [°]
Ω [°]
i [°]
m_total [M_⊙]

WDS03489+1143=HIP 17826

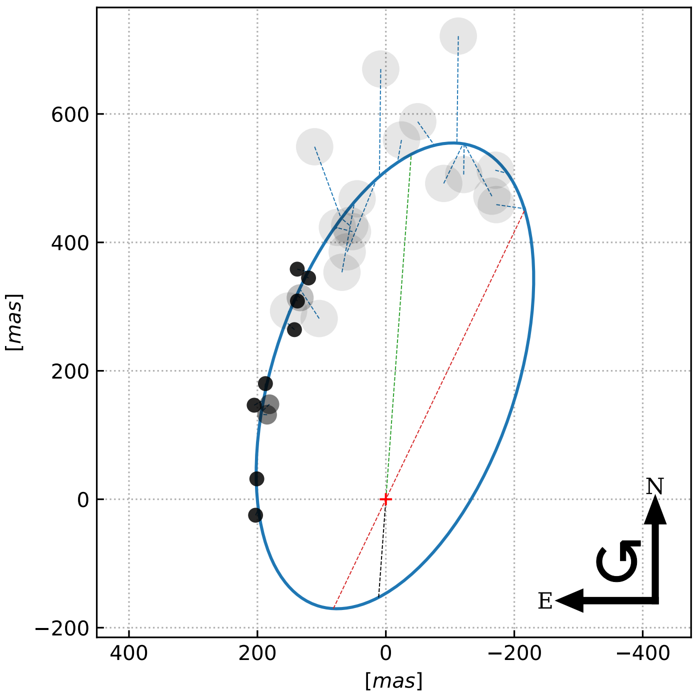

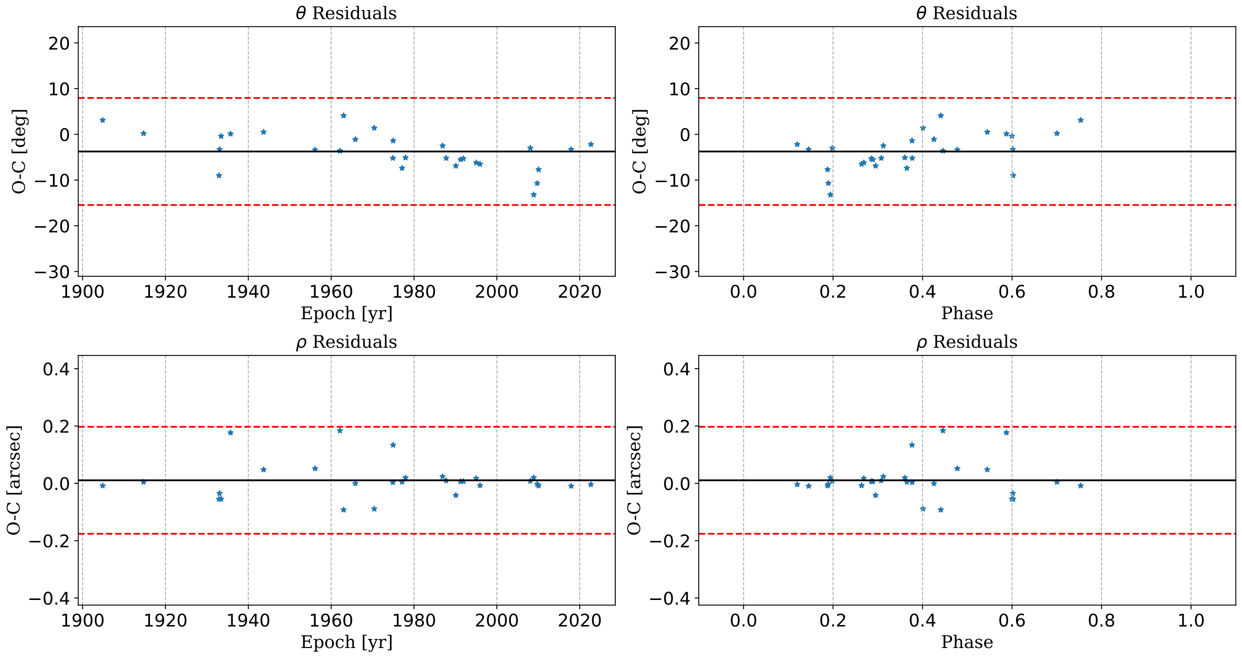

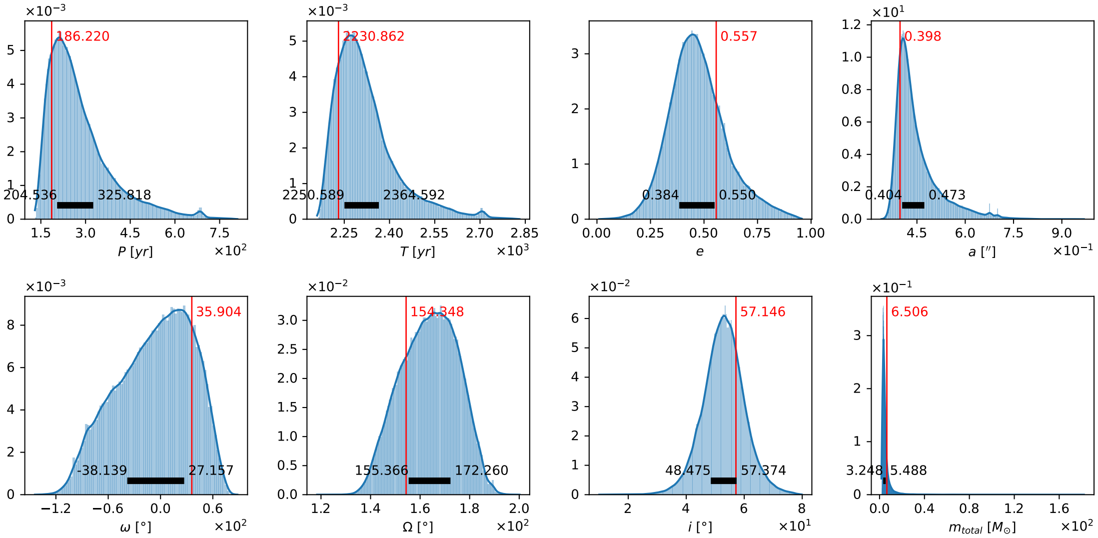

×10−3
186.220
204.536
325.818
P [yr]
×10²
×10−3
2230.862
2250.589
2364.592
T [yr]
×10³
0.557
0.384
0.550
e
×10¹
0.398
0.404
0.473
a ["]
×10−1
×10−3
35.904
-38.139
27.157
ω [°]
×10²
×10−2
154.348
155.366
172.260
Ω [°]
×10²
×10−2
57.146
48.475
57.374
i [°]
×10¹
×10−1
6.506
3.248
5.488
m_total [M_⊙]
×10²

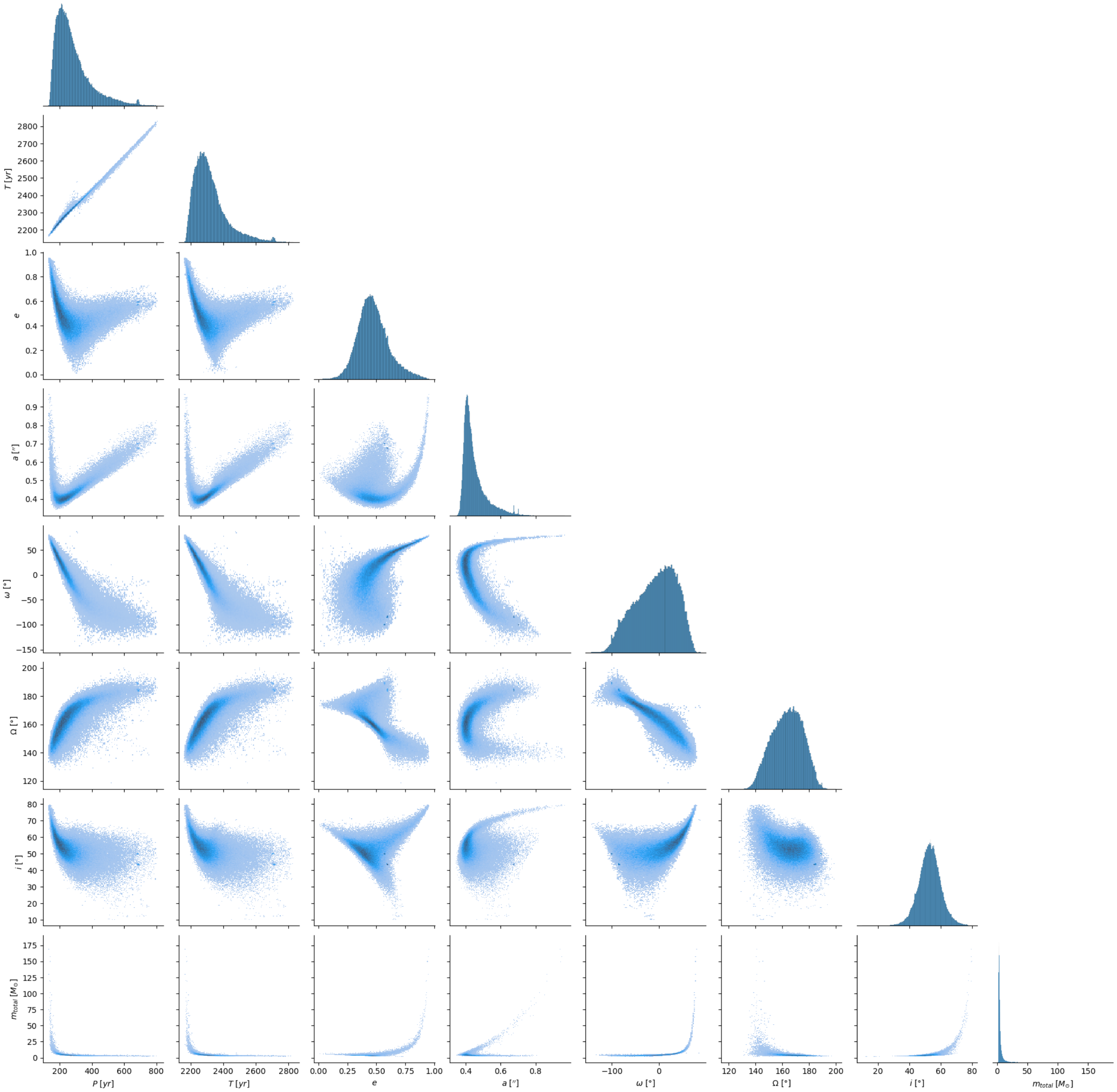

T [yr]
e
a ["]
ω [°]
Ω [°]
i [°]
m_total [M_⊙]
P [yr]
T [yr]
e
a ["]
ω [°]
Ω [°]
i [°]
m_total [M_⊙]

WDS05474−1032=HIP 27341

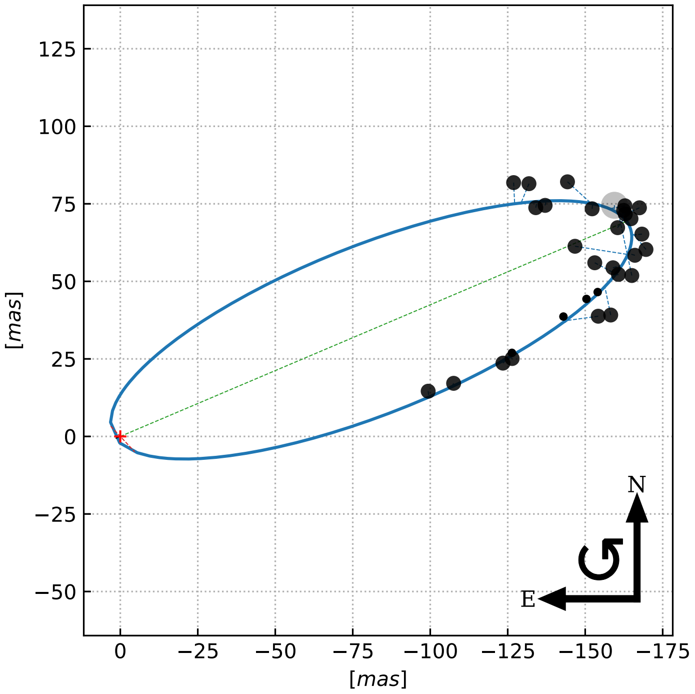

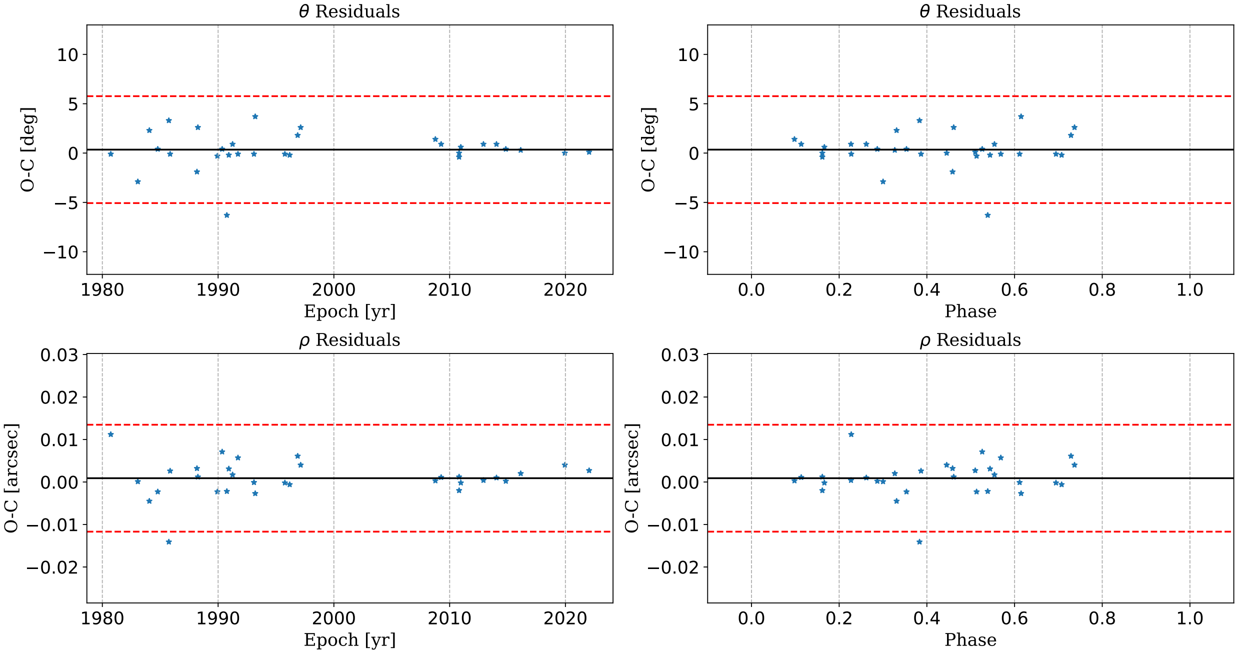

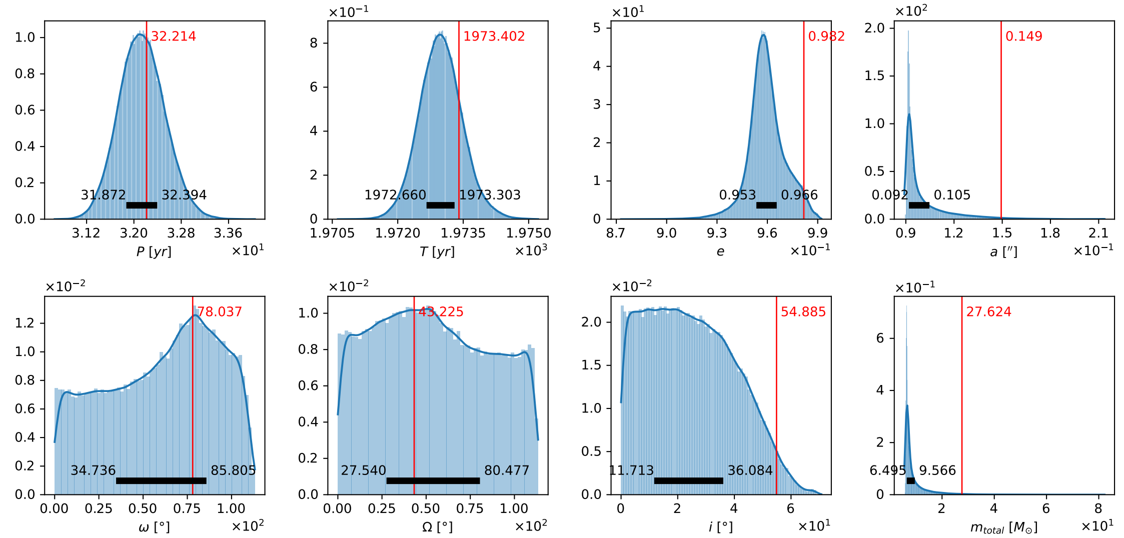
32.214
31.872
32.394
P [yr]
×10¹
1973.402
1972.660
1973.303
T [yr]
×10³
×10⁻¹
0.982
0.953
0.966
e
×10¹
×10⁻¹
0.149
0.092
0.105
a ["]
×10²
×10⁻¹
78.037
34.736
85.805
ω [°]
×10⁻²
×10²
43.225
27.540
80.477
Ω [°]
×10⁻²
×10²
54.885
11.713
36.084
i [°]
×10⁻²
×10¹
27.624
6.495
9.566
m_total [M_⊙]
×10⁻¹
×10¹

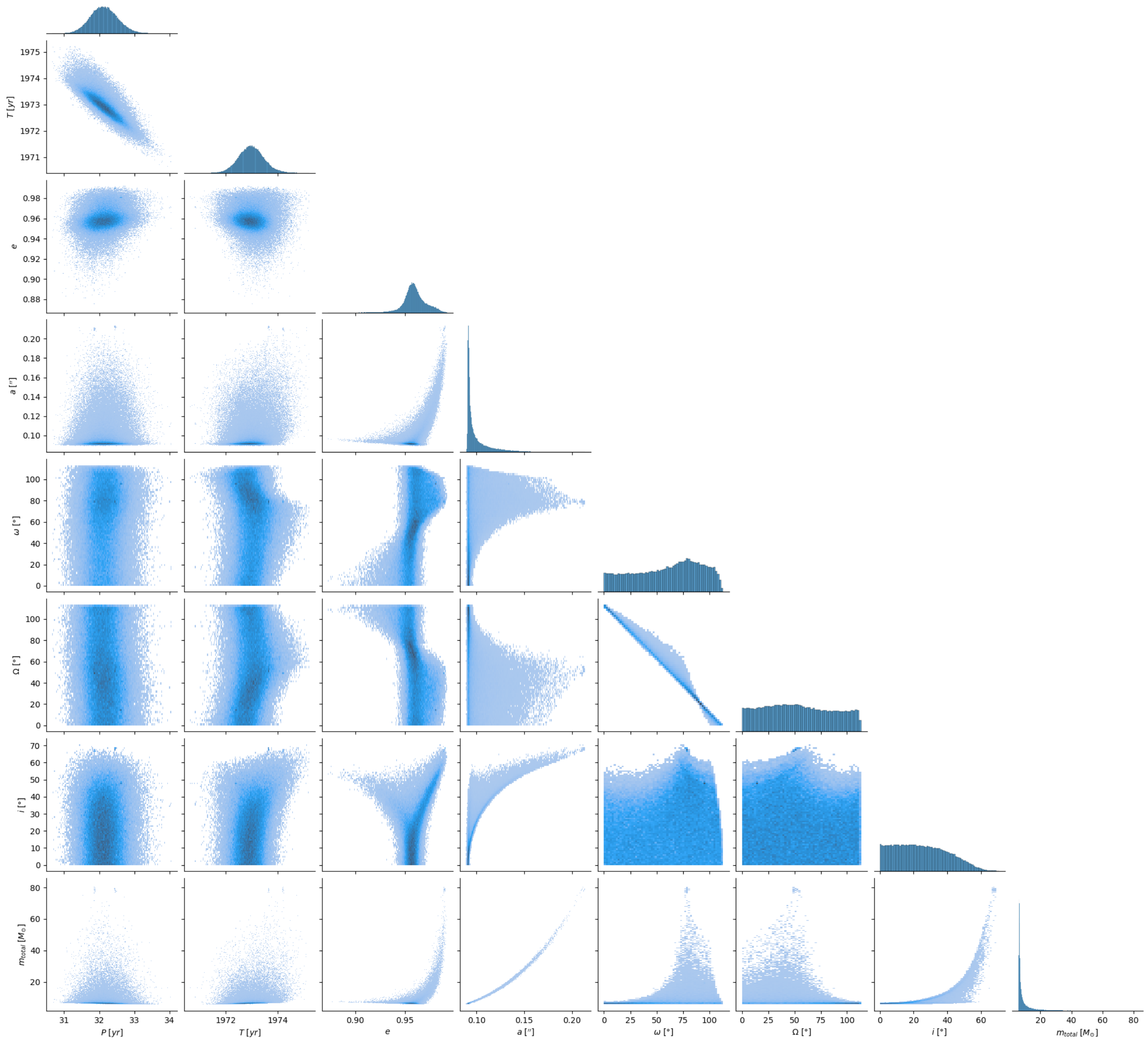
T [yr]
e
a ["]
ω [°]
Ω [°]
i [°]
m_total [M_⊙]
P [yr]
T [yr]
e
a ["]
ω [°]
Ω [°]
i [°]
m_total [M_⊙]

WDS14152−6739=HIP 69643

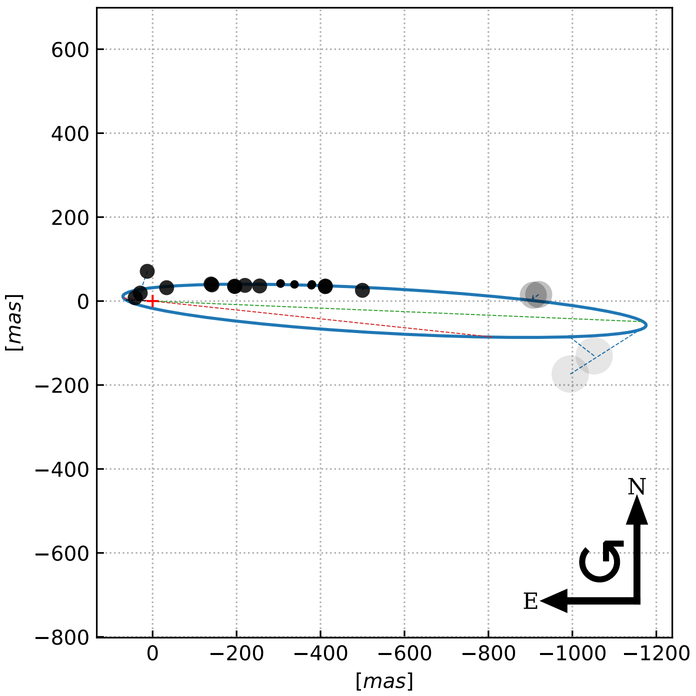

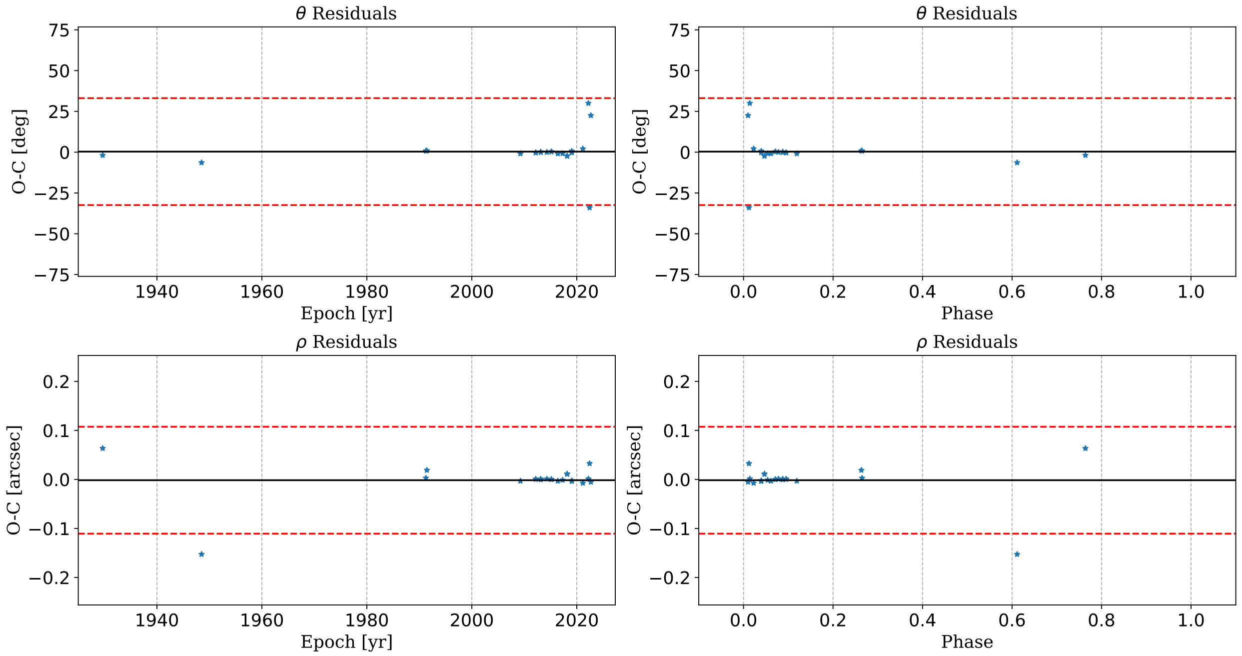

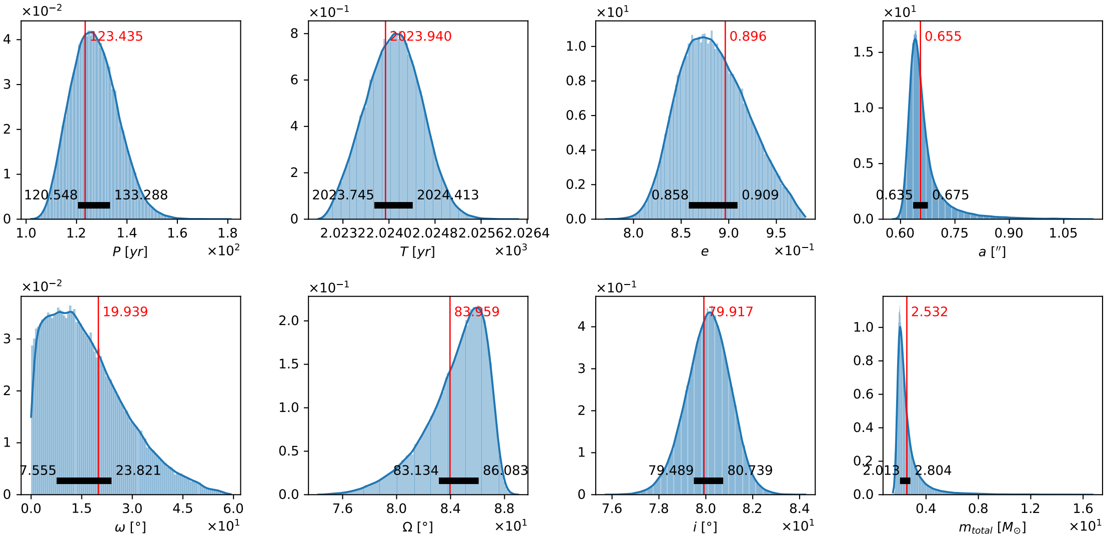
123.435
120.548
133.288
P [yr]
×10^2
×10^-2
2023.940
2023.745
2024.413
T [yr]
×10^3
×10^-1
0.896
0.858
0.909
e
×10^-1
×10^1
0.655
0.635
0.675
a ["]
×10^1
19.939
7.555
23.821
ω [°]
×10^1
×10^-2
83.959
83.134
86.083
Ω [°]
×10^1
×10^-1
79.917
79.489
80.739
i [°]
×10^1
×10^-1
2.532
2.013
2.804
m_total [M_⊙]
×10^1

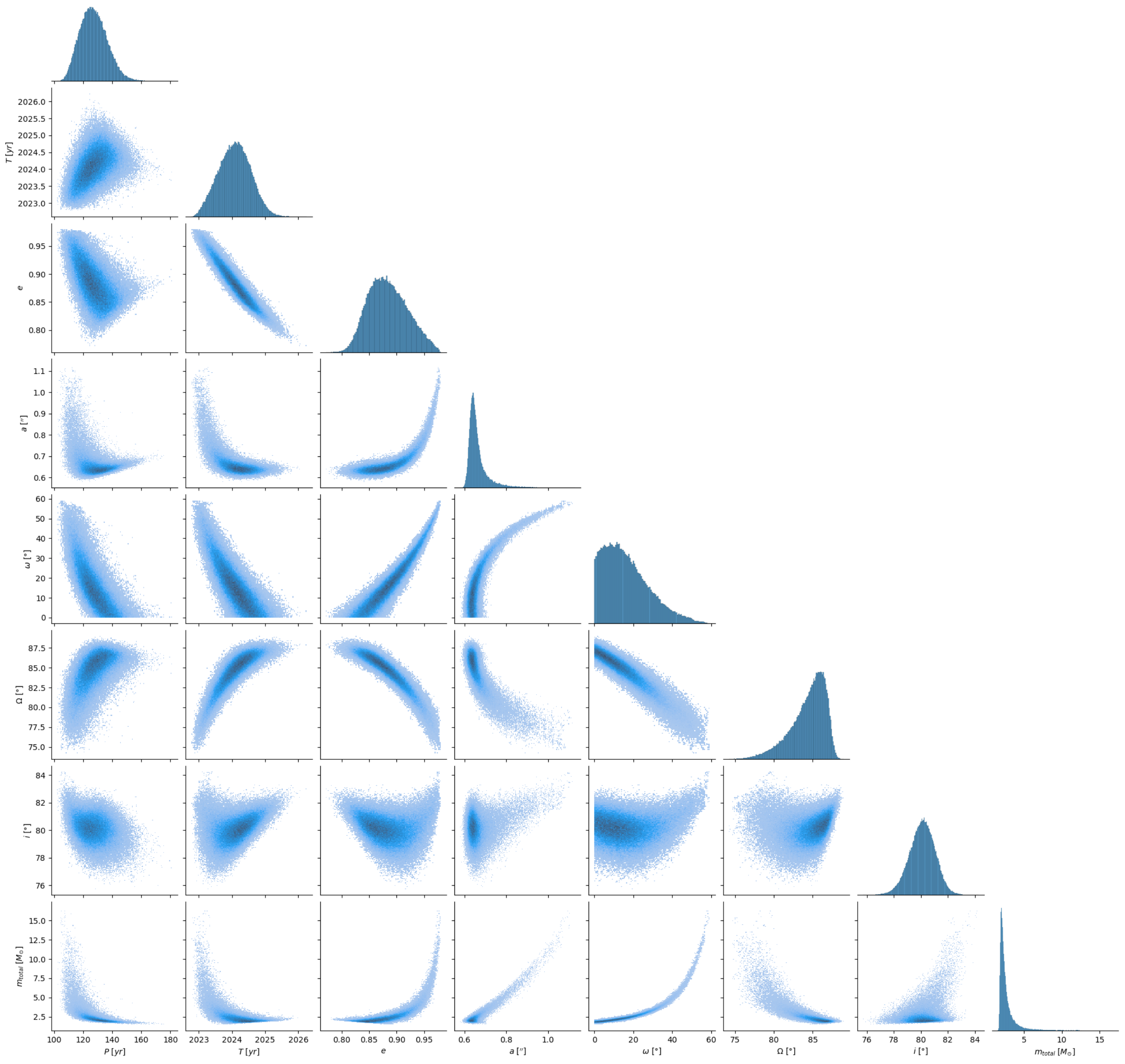
T [yr]
e
a ["]
ω [°]
Ω [°]
i [°]
m_total [M_⊙]
P [yr]
T [yr]
e
a ["]
ω [°]
Ω [°]
i [°]
m_total [M_⊙]

WDS14567−6247=HIP 73129

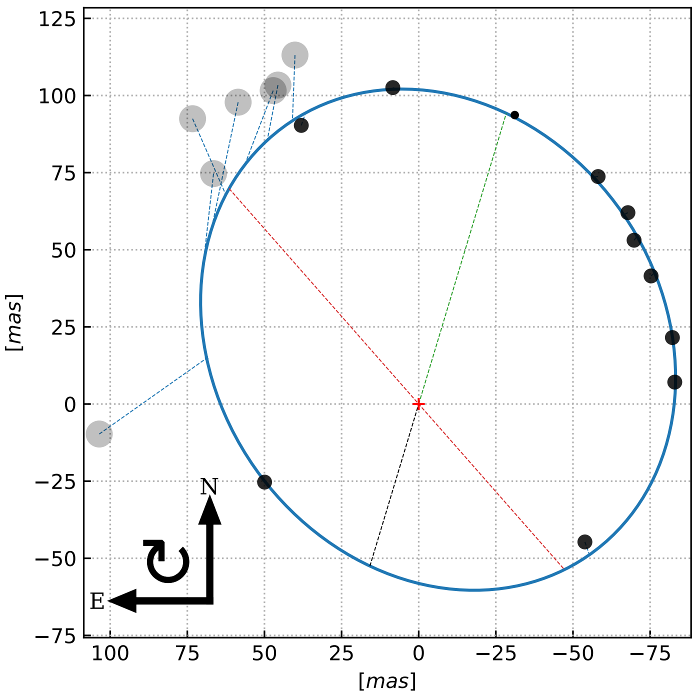

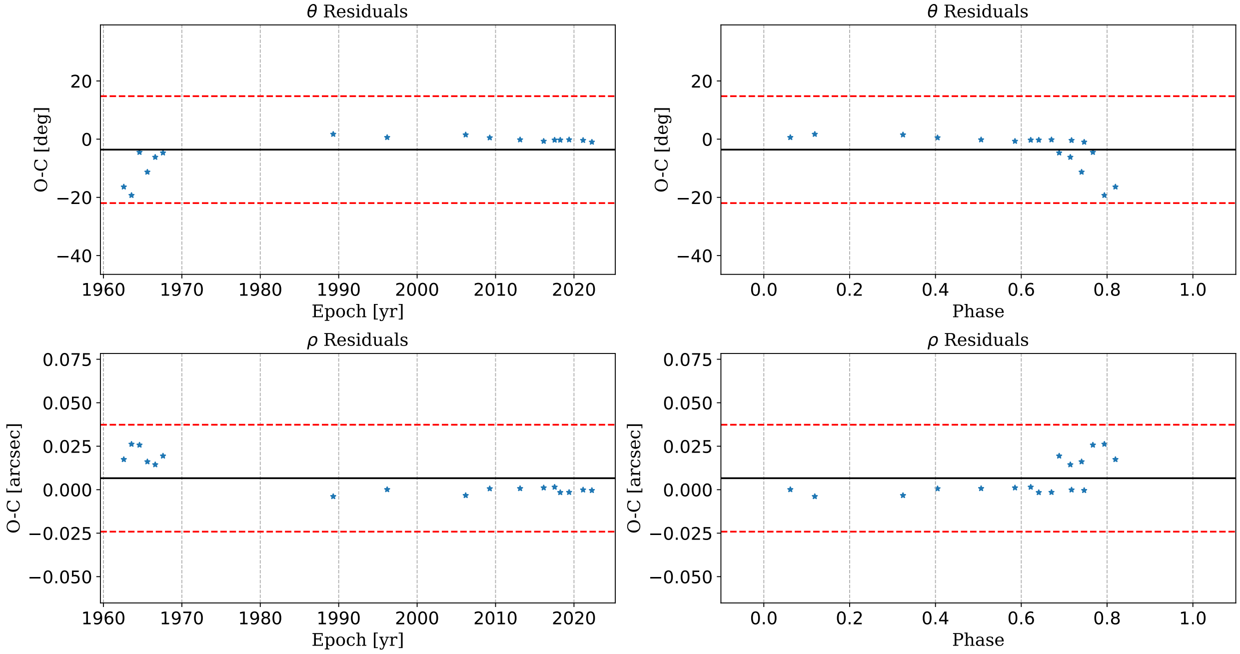

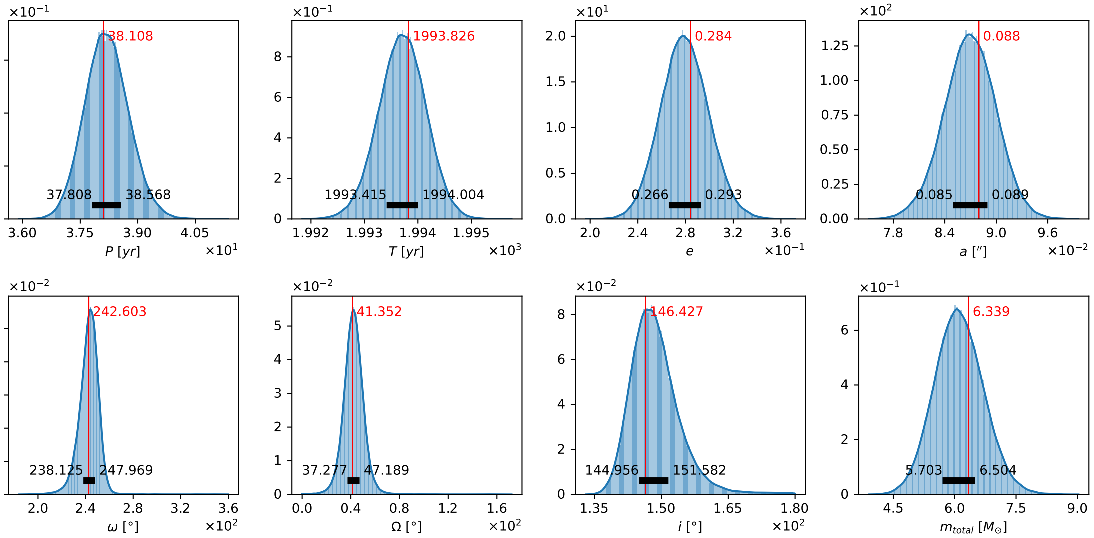
×10⁻¹
38.108
37.808
38.568
P [yr]
×10¹
3.60
3.75
3.90
4.05
×10⁻¹
1993.826
1993.415
1994.004
T [yr]
×10³
1.992
1.993
1.994
1.995
×10¹
0.284
0.266
0.293
e
×10⁻¹
2.0
2.4
2.8
3.2
3.6
×10²
0.088
0.085
0.089
a ["]
×10⁻²
7.8
8.4
9.0
9.6
×10⁻²
242.603
238.125
247.969
ω [°]
×10²
2.0
2.4
2.8
3.2
3.6
×10⁻²
41.352
37.277
47.189
Ω [°]
×10²
0.0
0.4
0.8
1.2
1.6
×10⁻²
146.427
144.956
151.582
i [°]
×10²
1.35
1.50
1.65
1.80
×10⁻¹
6.339
5.703
6.504
m_total [M_⊙]
4.5
6.0
7.5
9.0

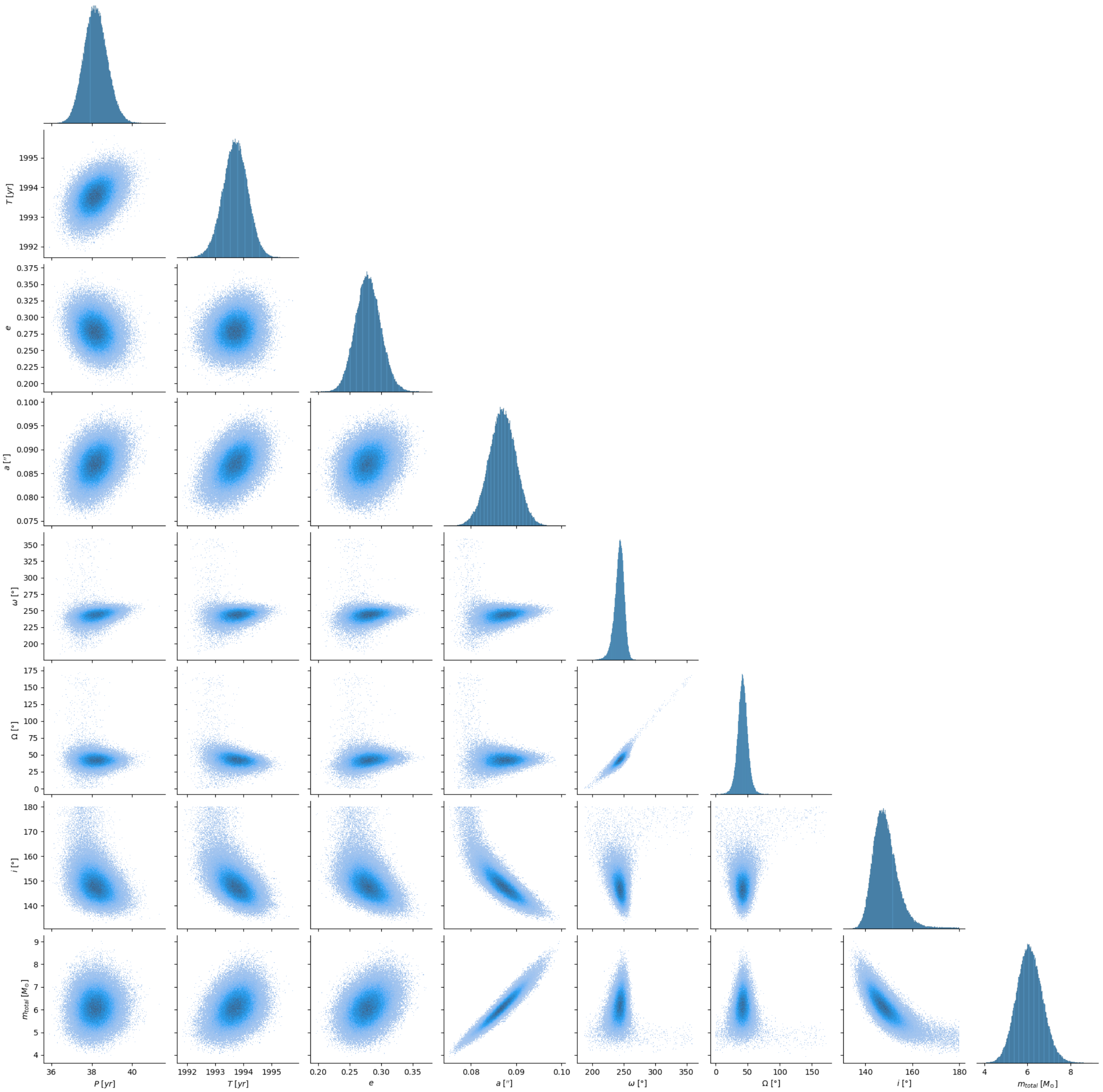
T [yr]
e
a ["]
ω [°]
Ω [°]
i [°]
m_total [M_⊙]
P [yr]
T [yr]
e
a ["]
ω [°]
Ω [°]
i [°]
m_total [M_⊙]
36
38
40
1992
1993
1994
1995
0.20
0.25
0.30
0.35
0.08
0.09
0.10
200
250
300
350
0
50
100
150
140
160
180
4
6
8

WDS16016−7843=HIP 78505

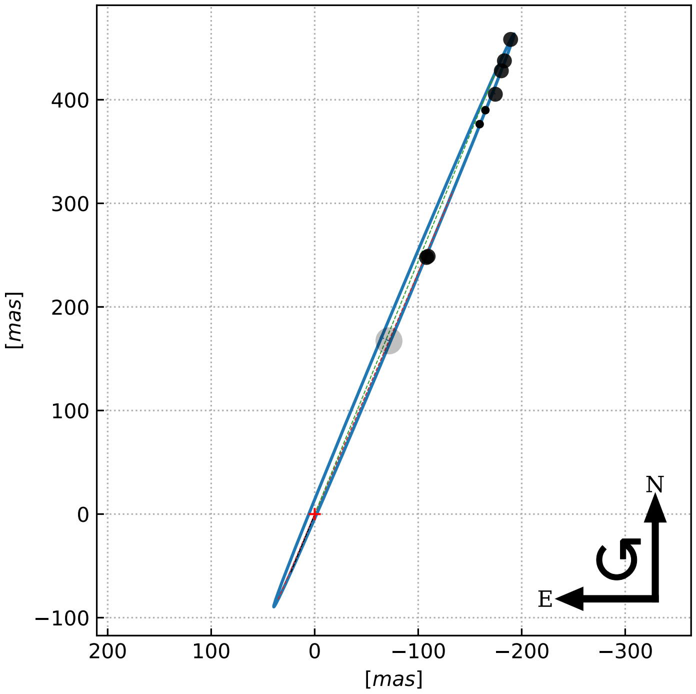

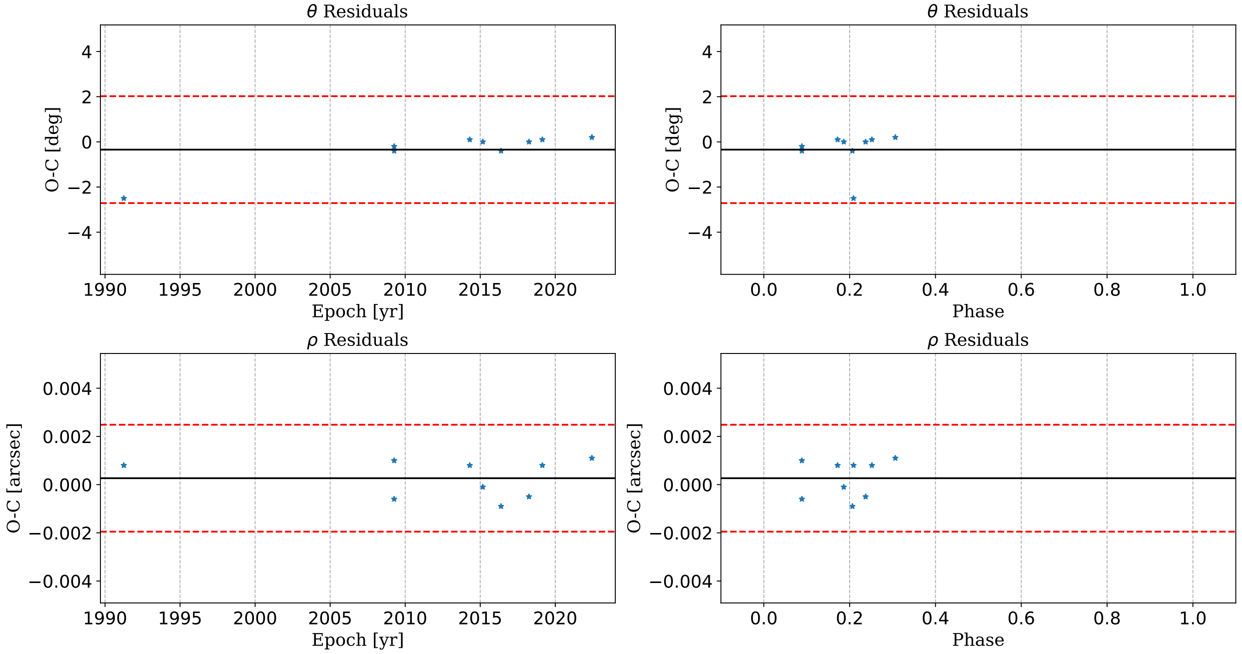

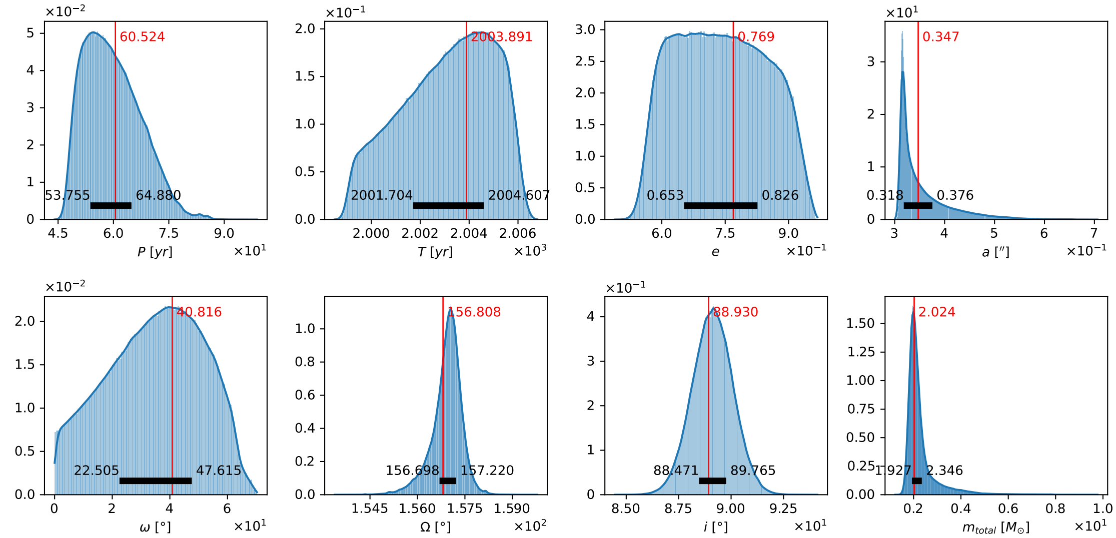

×10−2
60.524
53.755
64.880
P [yr]
×10¹
×10−1
2003.891
2001.704
2004.607
T [yr]
×10³
0.769
0.653
0.826
e
×10−1
×10¹
0.347
0.318
0.376
a ["]
×10−1
×10−2
40.816
22.505
47.615
ω [°]
×10¹
156.808
156.698
157.220
Ω [°]
×10²
×10−1
88.930
88.471
89.765
i [°]
×10¹
2.024
1.927
2.346
m_total [M_⊙]
×10¹

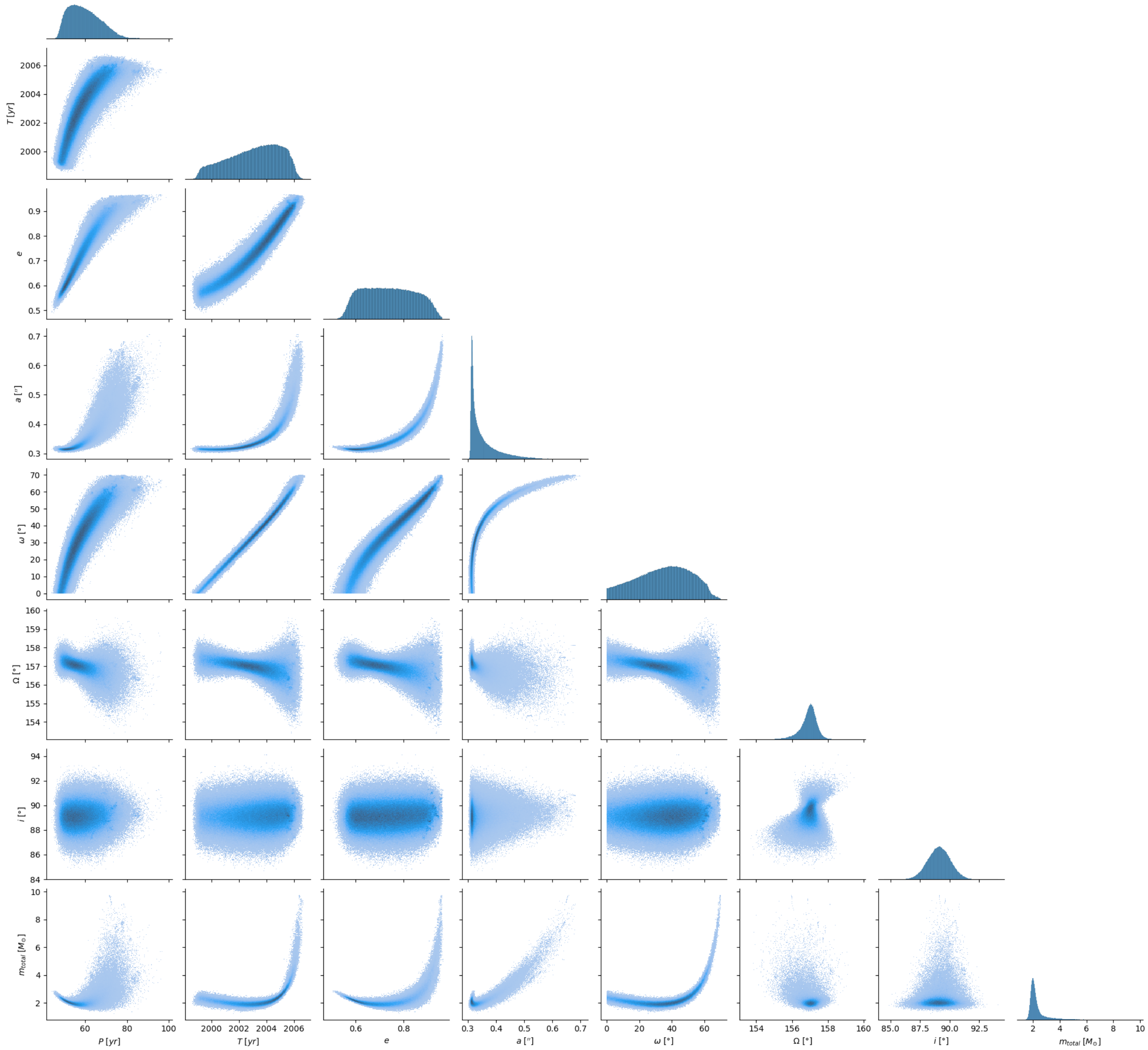

T [yr]
e
a ["]
ω [°]
Ω [°]
i [°]
m_total [M_⊙]
P [yr]
T [yr]
e
a ["]
ω [°]
Ω [°]
i [°]
m_total [M_⊙]

WDS16035−5747=HIP 78662

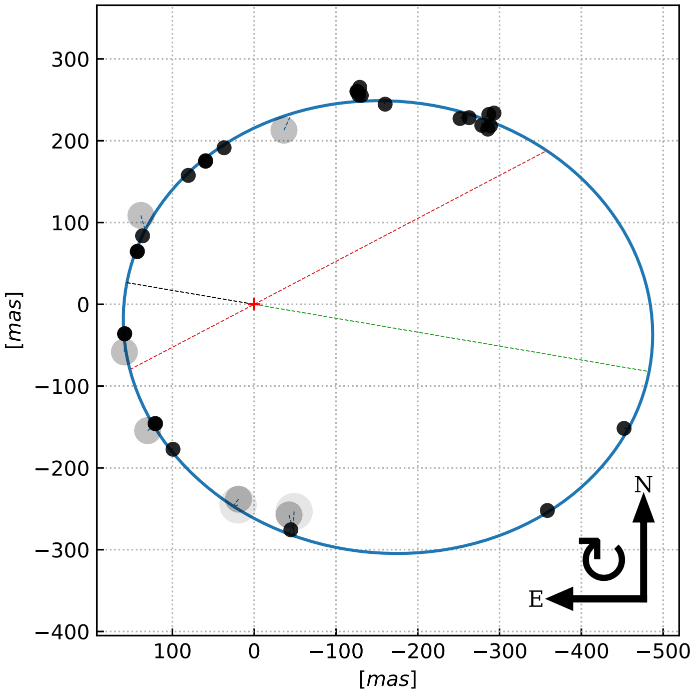

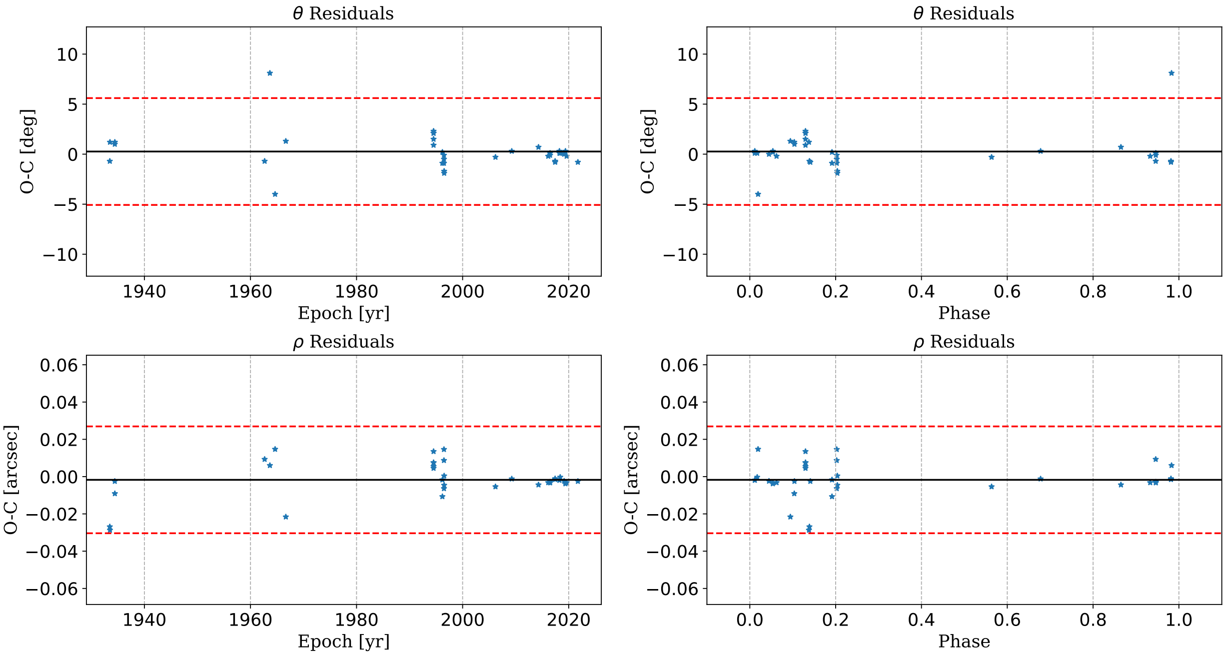

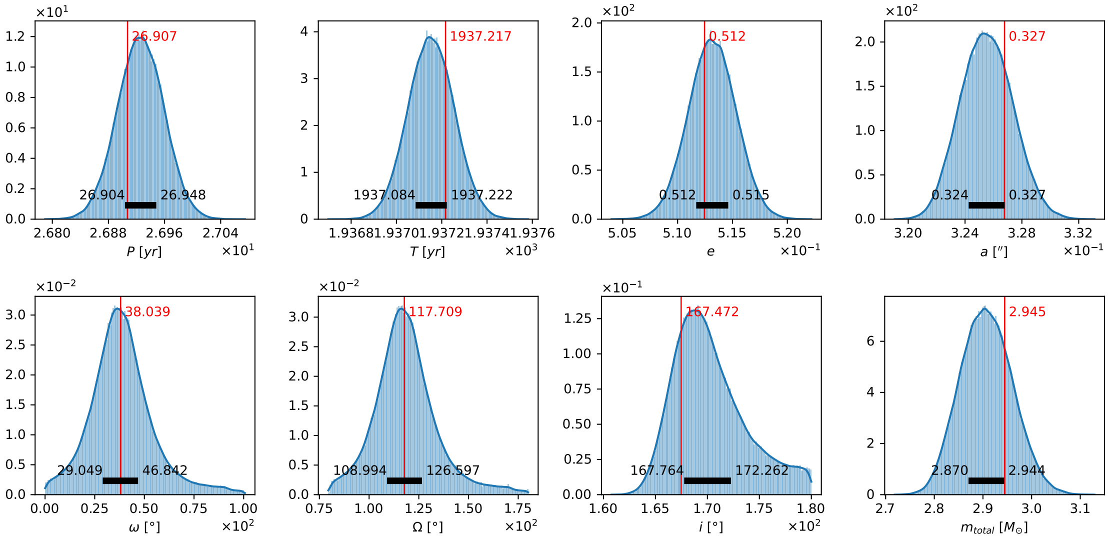
×10^1
1.2
1.0
0.8
0.6
0.4
0.2
0.0
26.907
26.904
26.948
2.680
2.688
2.696
2.704
P [yr]
×10^1
4
3
2
1
0
1937.217
1937.084
1937.222
1.93681.93701.93721.93741.9376
T [yr]
×10^3
×10^2
2.0
1.5
1.0
0.5
0.0
0.512
0.512
0.515
5.05
5.10
5.15
5.20
e
×10^−1
×10^2
2.0
1.5
1.0
0.5
0.0
0.327
0.324
0.327
3.20
3.24
3.28
3.32
a ['']
×10^−1
×10^−2
3.0
2.5
2.0
1.5
1.0
0.5
0.0
38.039
29.049
46.842
0.00
0.25
0.50
0.75
1.00
ω [°]
×10^2
×10^−2
3.0
2.5
2.0
1.5
1.0
0.5
0.0
117.709
108.994
126.597
0.75
1.00
1.25
1.50
1.75
Ω [°]
×10^2
×10^−1
1.25
1.00
0.75
0.50
0.25
0.00
167.472
167.764
172.262
1.60
1.65
1.70
1.75
1.80
i [°]
×10^2
6
4
2
0
2.945
2.870
2.944
2.7
2.8
2.9
3.0
3.1
m_total [M⊙]

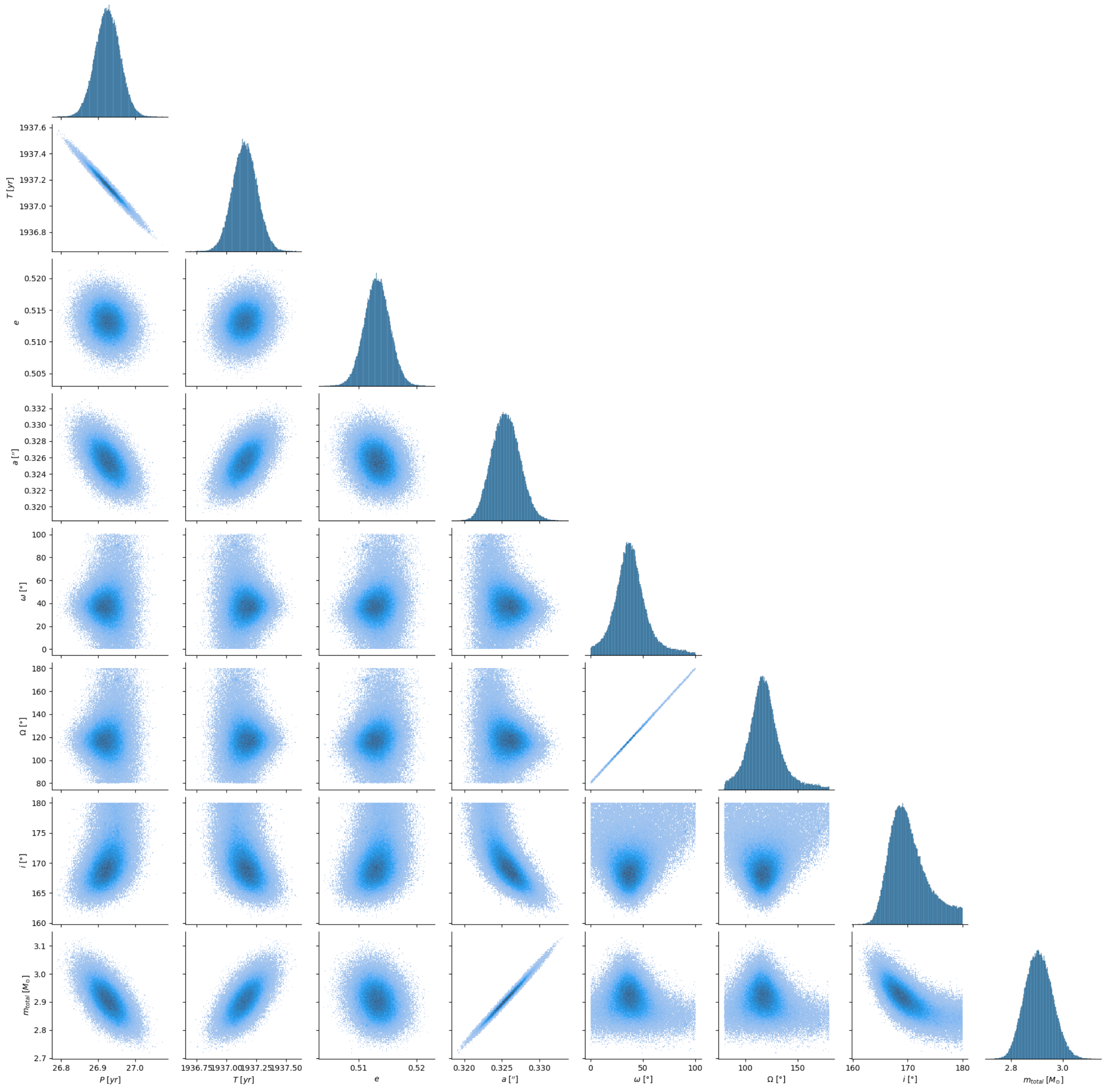
T [yr]
1937.6
1937.4
1937.2
1937.0
1936.8
e
0.520
0.515
0.510
0.505
a ['']
0.332
0.330
0.328
0.326
0.324
0.322
0.320
ω [°]
100
80
60
40
20
0
Ω [°]
180
160
140
120
100
80
i [°]
180
175
170
165
160
m_total [M⊙]
3.1
3.0
2.9
2.8
2.7
26.8
26.9
27.0
P [yr]
1936.75
1937.00
1937.25
1937.50
T [yr]
0.51
0.52
e
0.320
0.325
0.330
a ['']
0
50
100
ω [°]
100
150
Ω [°]
160
170
180
i [°]
2.8
3.0
m_total [M⊙]

WDS16434−2819=HIP 81874

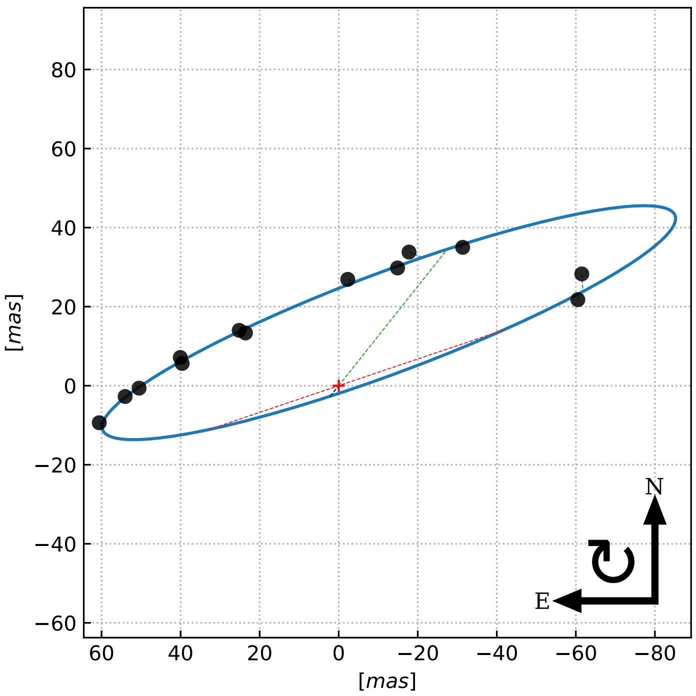

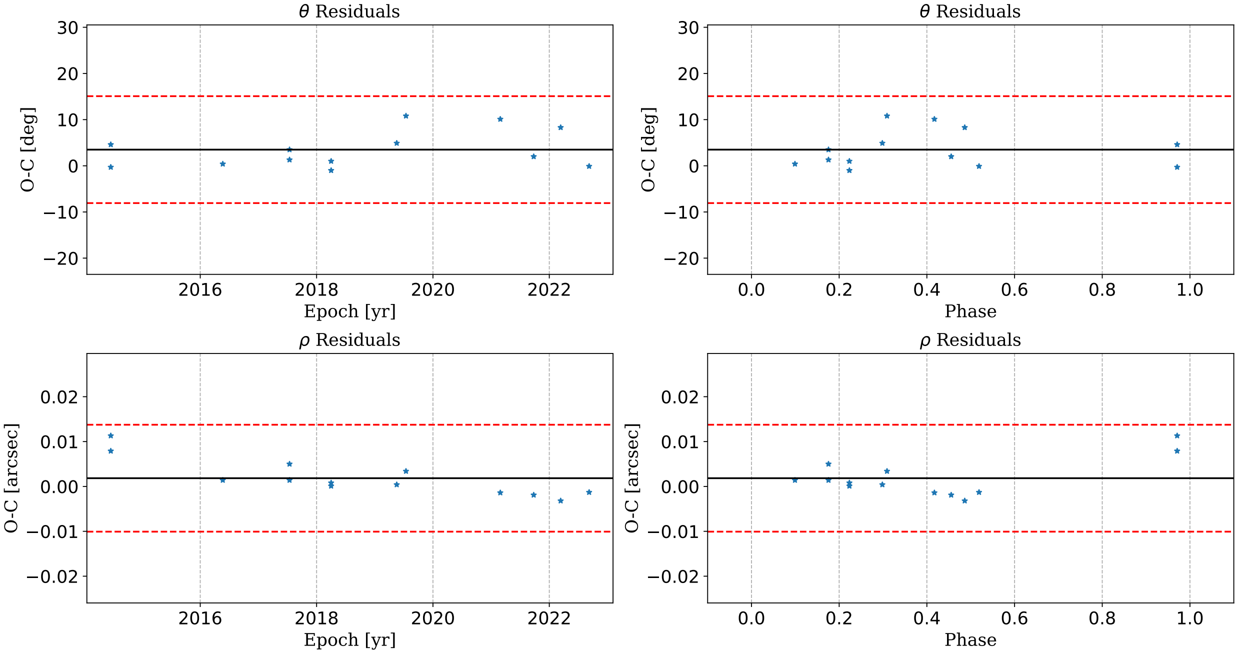

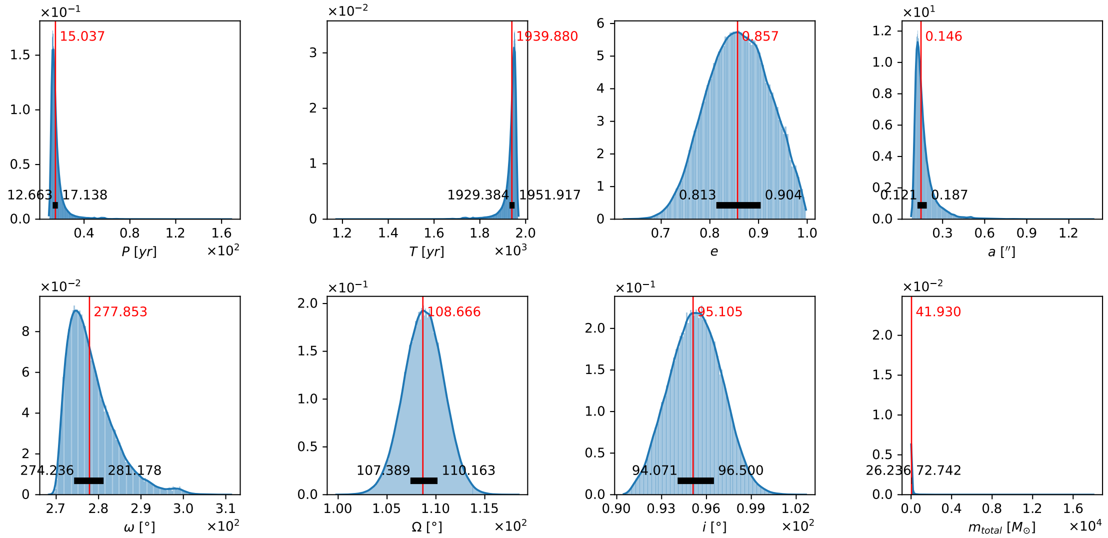

15.037
12.663
17.138
P [yr]
×10^2
1939.880
1929.384
1951.917
T [yr]
×10^3
0.857
0.813
0.904
e
0.146
0.121
0.187
a ["]
×10^1
277.853
274.236
281.178
ω [°]
×10^2
108.666
107.389
110.163
Ω [°]
×10^2
95.105
94.071
96.500
i [°]
×10^2
41.930
26.236
72.742
m_total [M_⊙]
×10^4

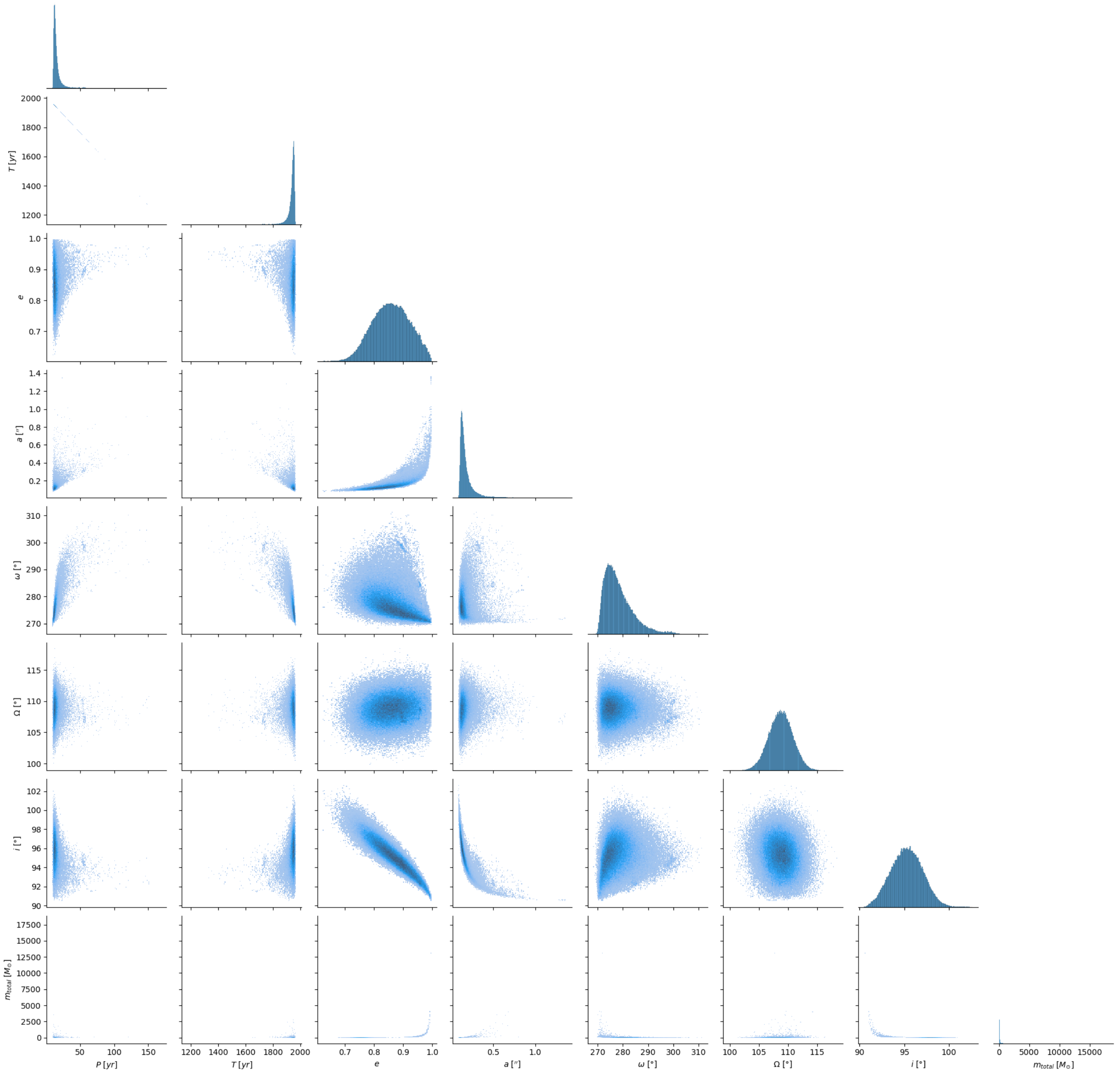

P [yr]
T [yr]
e
a ["]
ω [°]
Ω [°]
i [°]
m_total [M_⊙]

WDS17157−0949=HIP 84430 AB

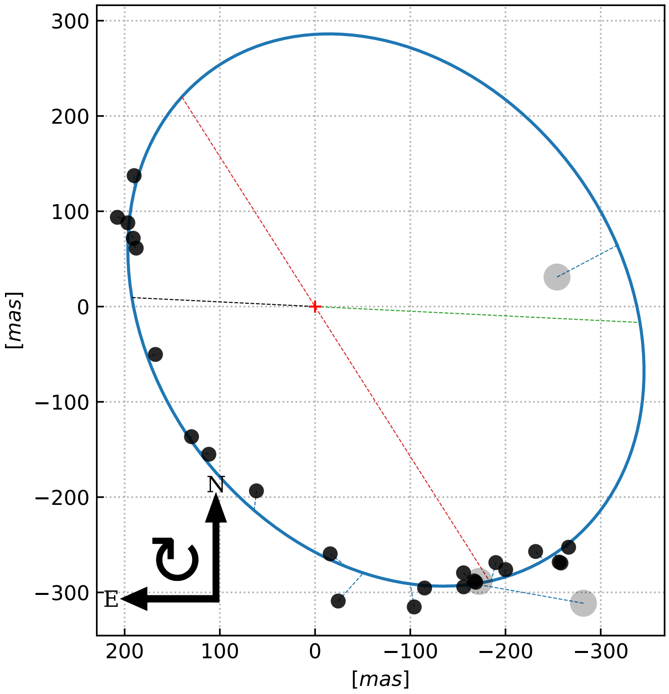

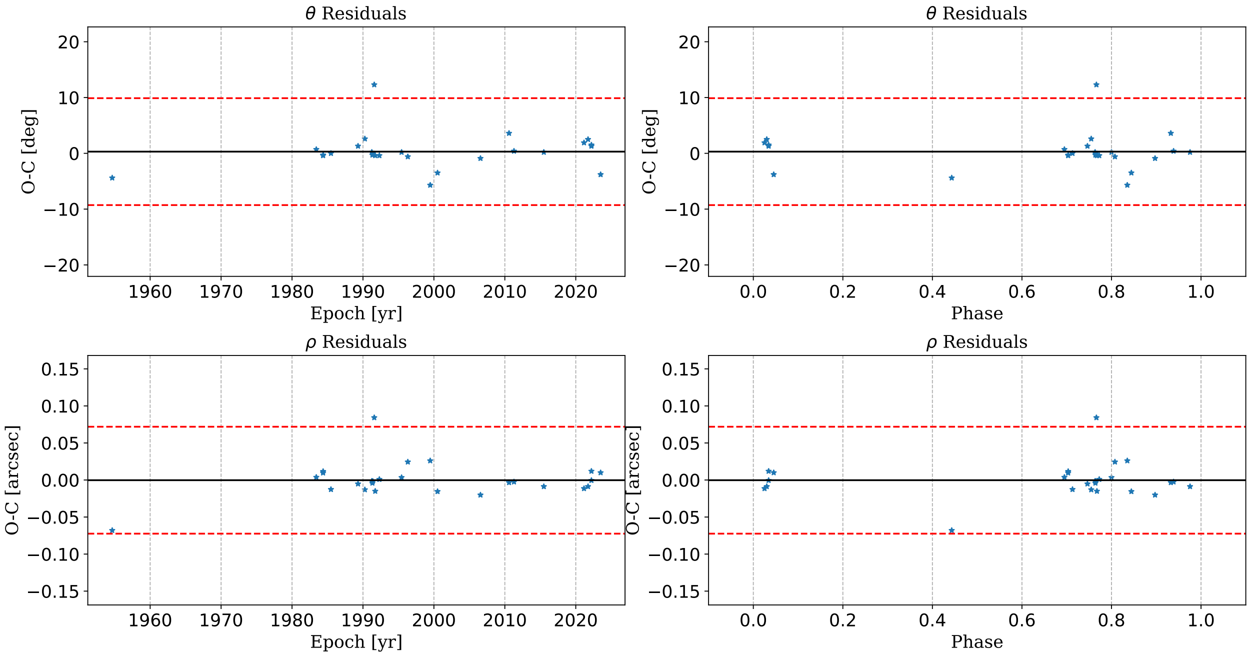

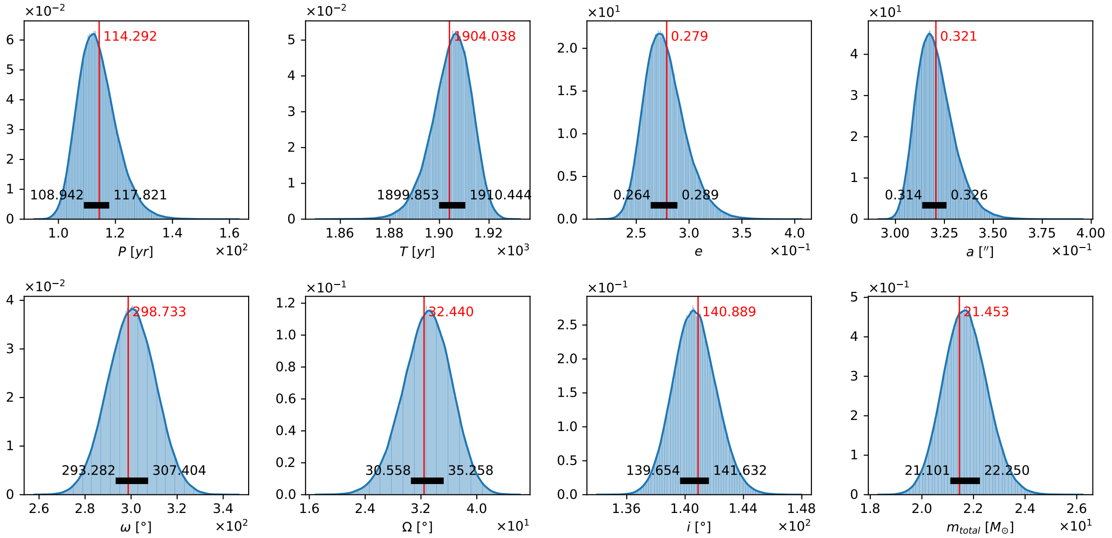
×10⁻²
114.292
108.942
117.821
P [yr]
×10²
1904.038
1899.853
1910.444
T [yr]
×10³
×10¹
0.279
0.264
0.289
e
×10⁻¹
0.321
0.314
0.326
a ["]
298.733
293.282
307.404
ω [°]
32.440
30.558
35.258
Ω [°]
140.889
139.654
141.632
i [°]
21.453
21.101
22.250
m_total [M_⊙]

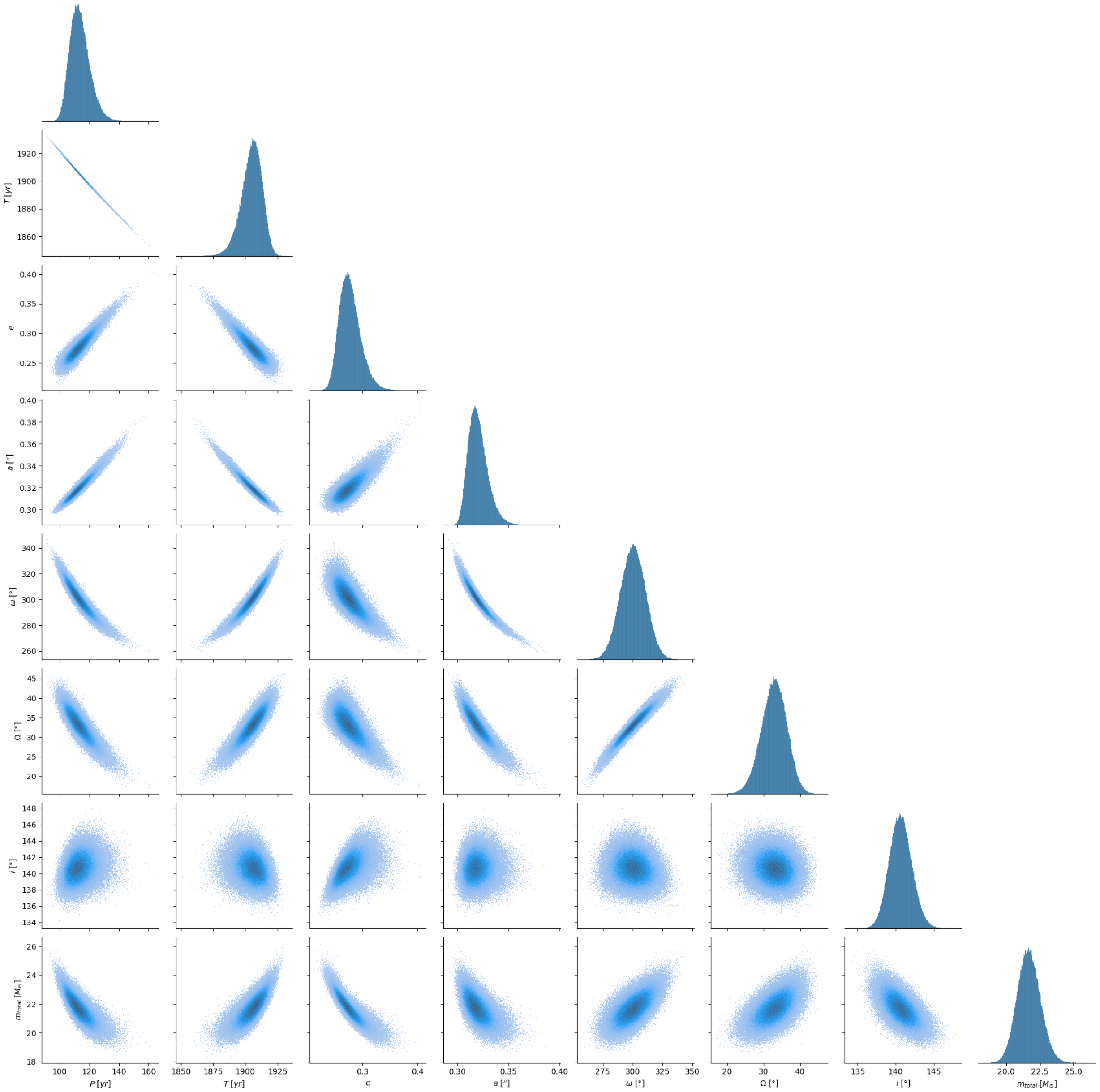
T [yr]
e
a ["]
ω [°]
Ω [°]
i [°]
m_total [M_⊙]
P [yr]
T [yr]
e
a ["]
ω [°]
Ω [°]
i [°]
m_total [M_⊙]

WDS17157−0949=HIP 84430 BaBb

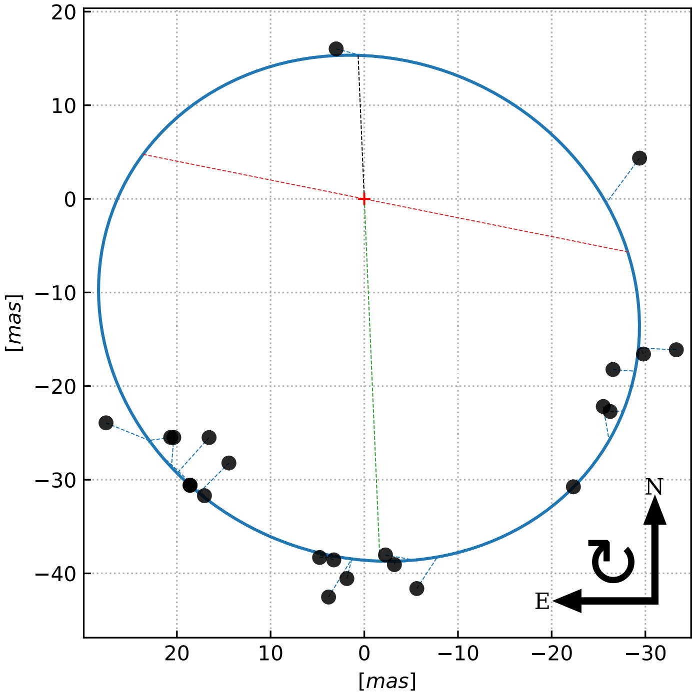

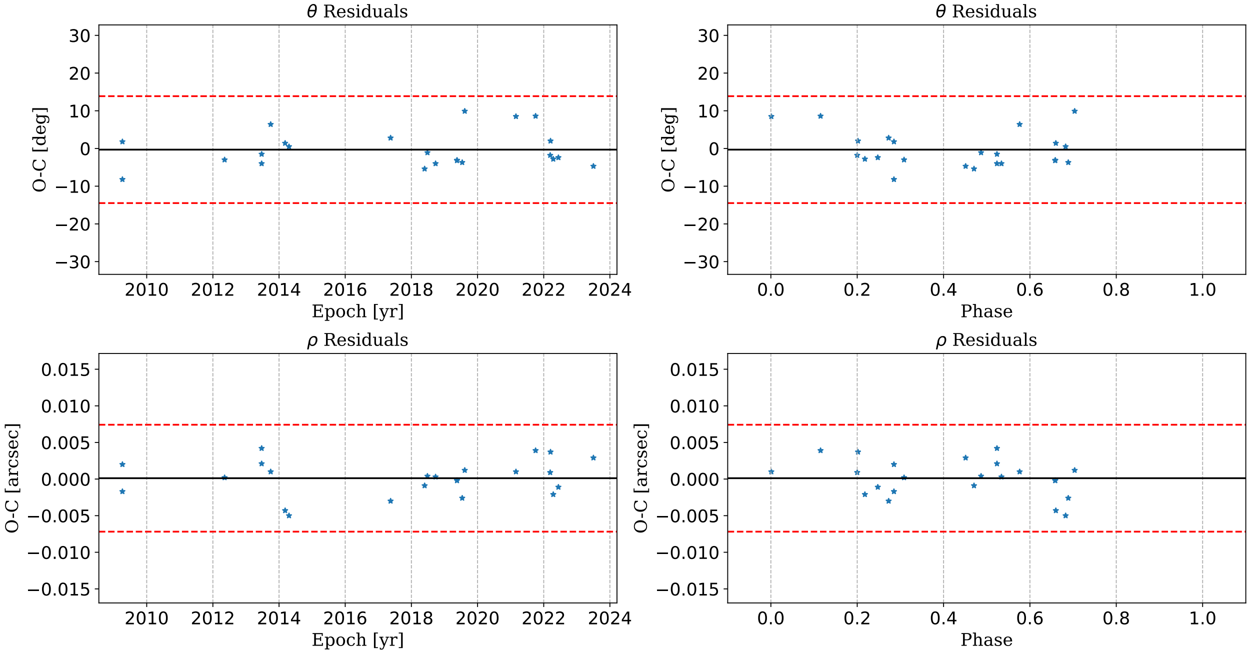

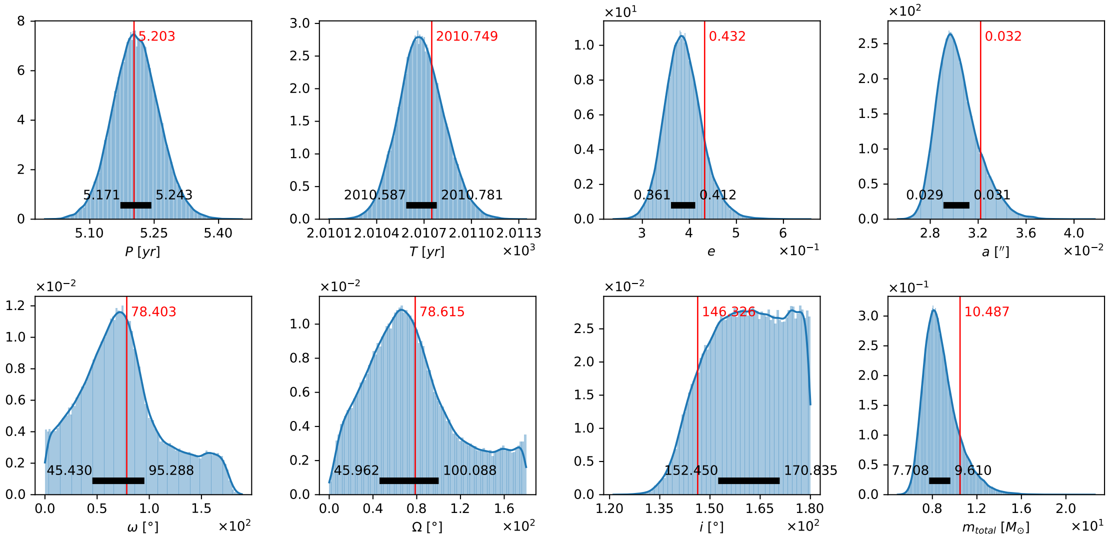

5.203
5.171
5.243
P [yr]
2010.749
2010.587
2010.781
T [yr]
×10^3
×10^1
0.432
0.361
0.412
e
×10^-1
×10^2
0.032
0.029
0.031
a ["]
×10^-2
×10^-2
78.403
45.430
95.288
ω [°]
×10^2
×10^-2
78.615
45.962
100.088
Ω [°]
×10^2
×10^-2
146.326
152.450
170.835
i [°]
×10^2
×10^-1
10.487
7.708
9.610
m_total [M_⊙]
×10^1

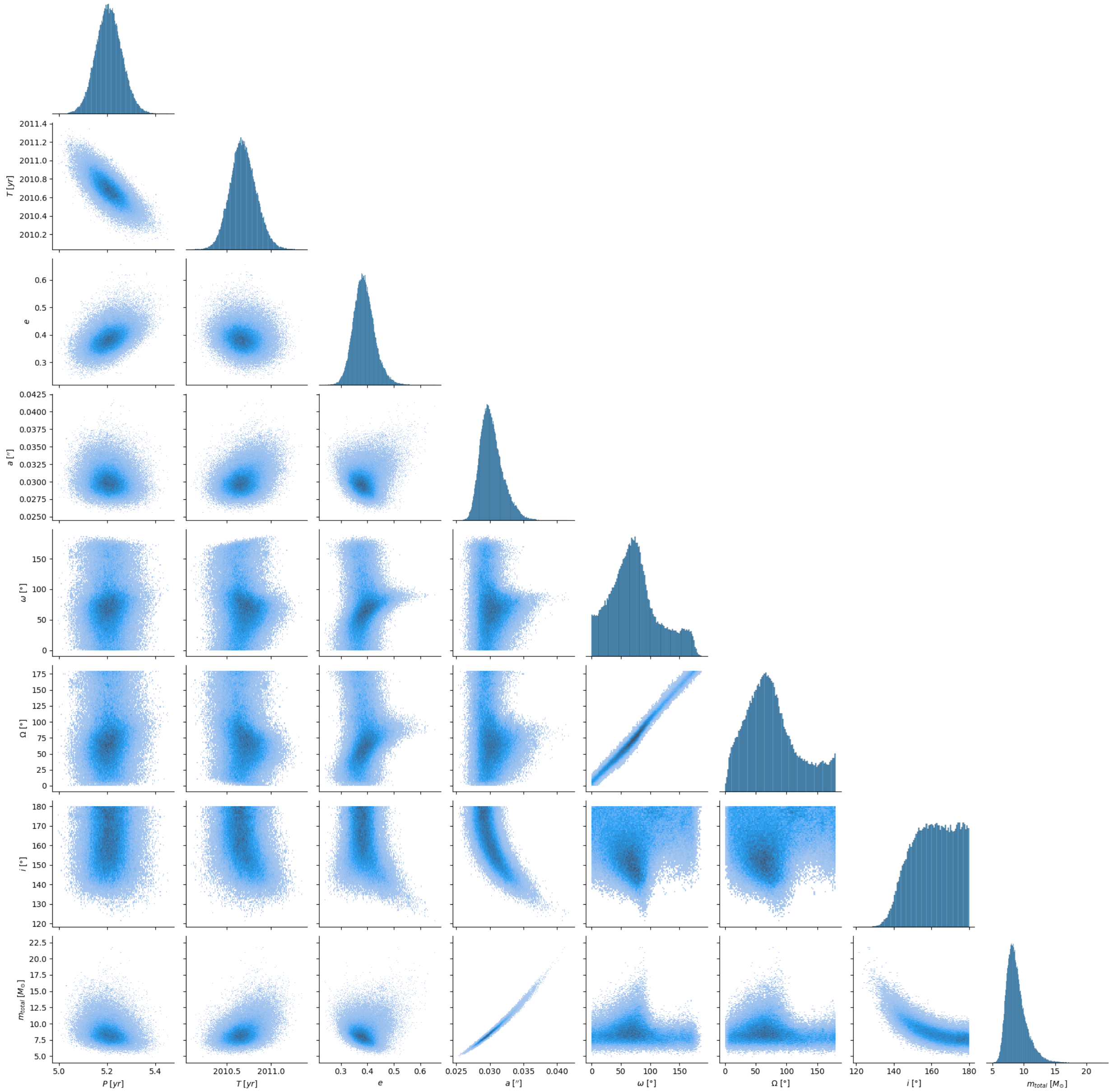

T [yr]
e
a ["]
ω [°]
Ω [°]
i [°]
m_total [M_⊙]
P [yr]
T [yr]
e
a ["]
ω [°]
Ω [°]
i [°]
m_total [M_⊙]

WDS17349+1234=HIP 86032

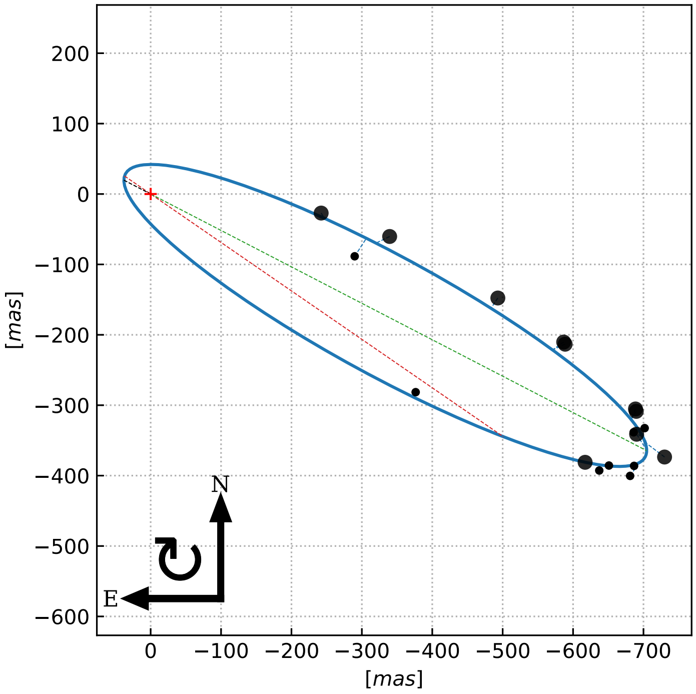

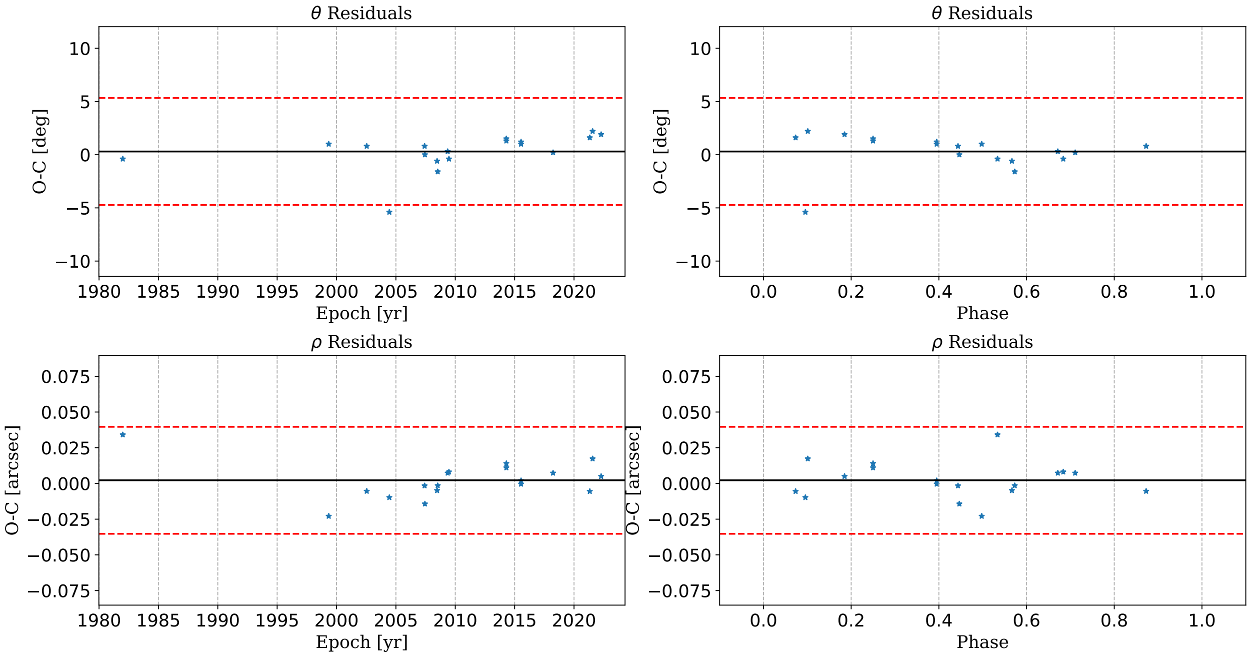

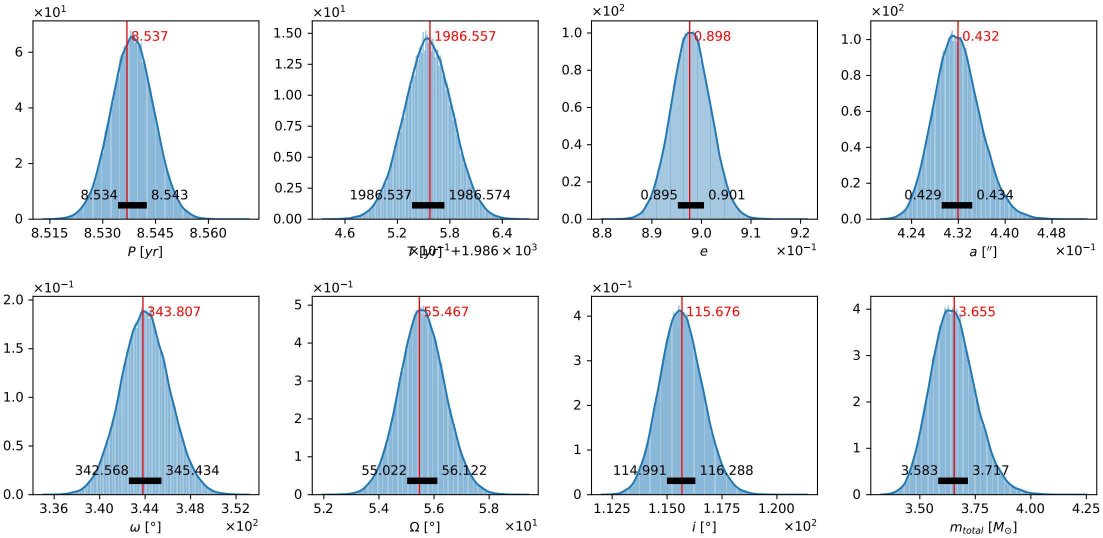
8.537
8.534
8.543
P [yr]
1986.557
1986.537
1986.574
T [yr] +1.986 × 10^3
0.898
0.895
0.901
e
0.432
0.429
0.434
a ["]
343.807
342.568
345.434
ω [°]
55.467
55.022
56.122
Ω [°]
115.676
114.991
116.288
i [°]
3.655
3.583
3.717
m_total [M_⊙]

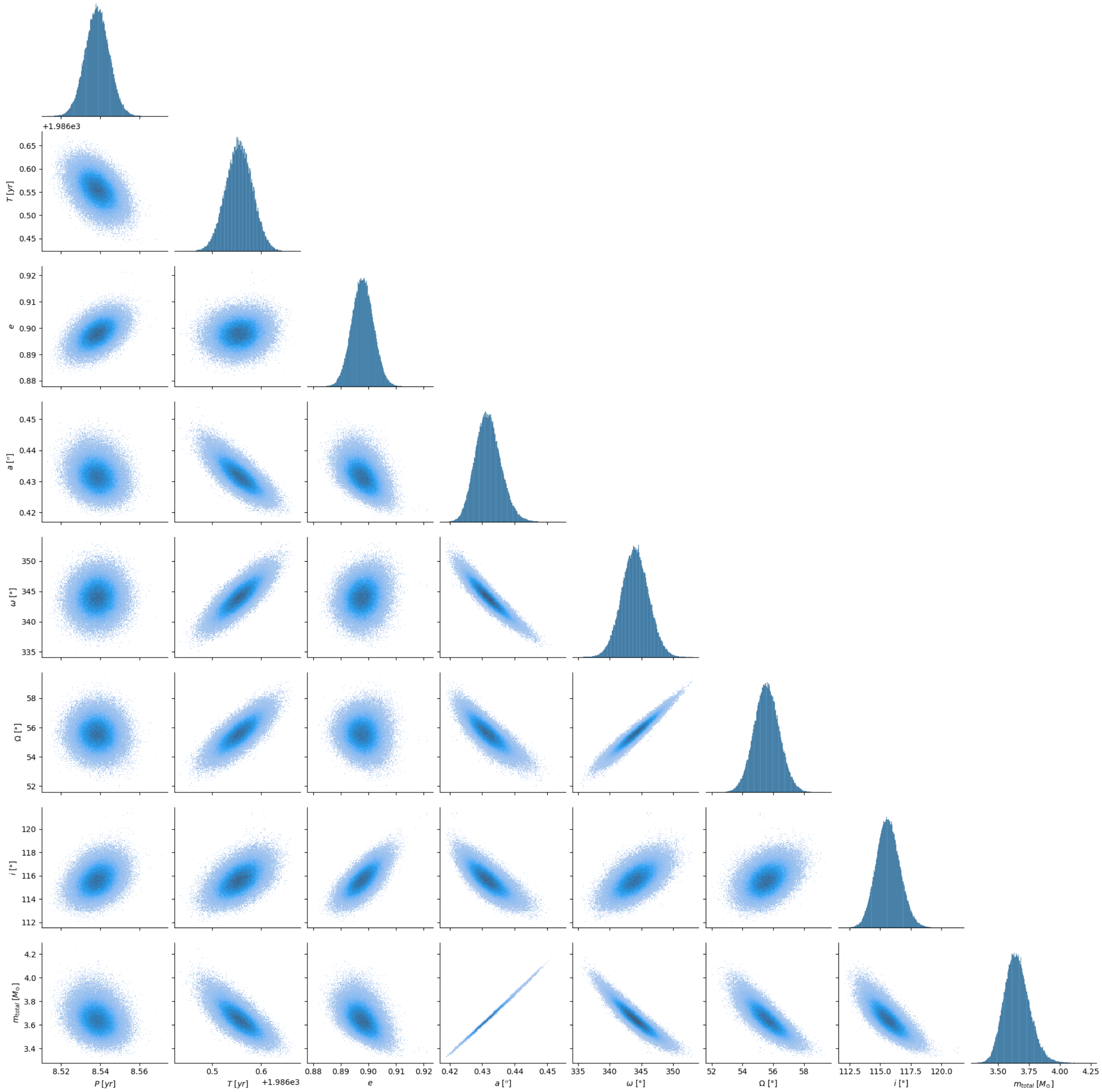
P [yr]
T [yr] +1.986e3
e
a ["]
ω [°]
Ω [°]
i [°]
m_total [M_⊙]

WDS20306+1349=HIP 101181

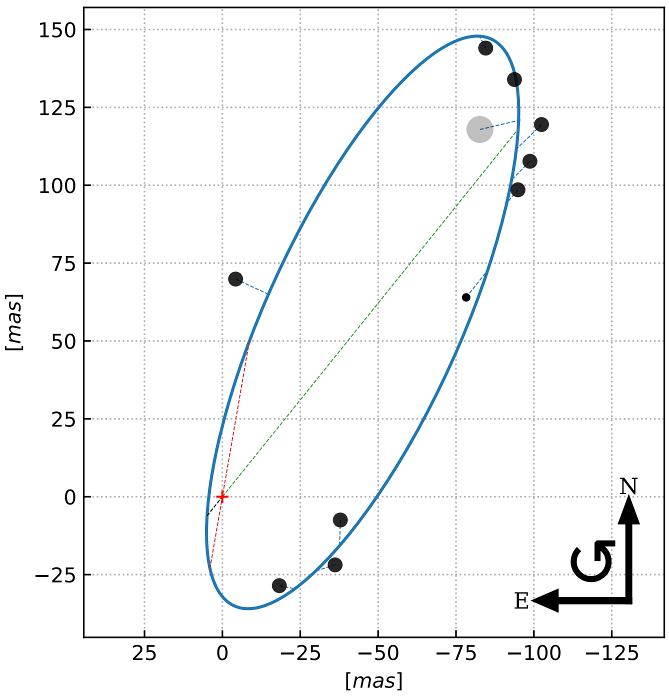

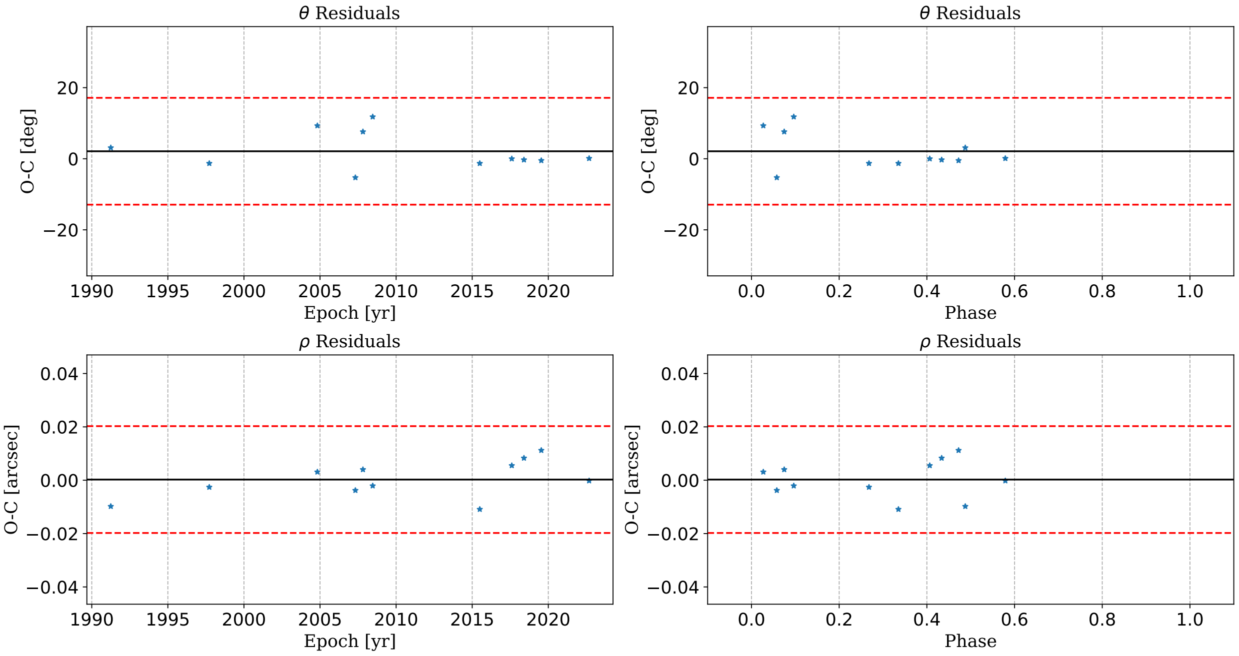

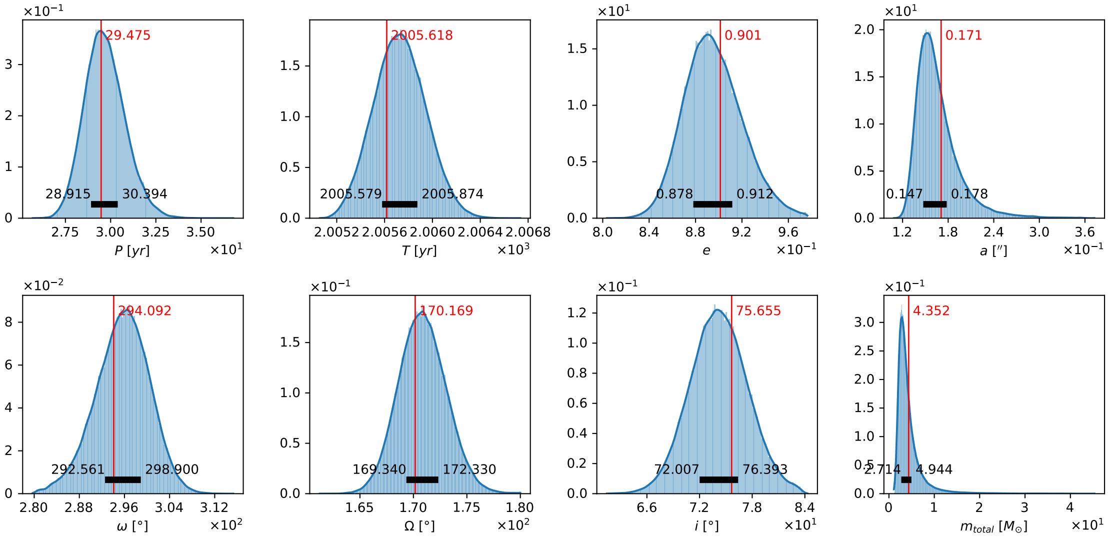
×10⁻¹
29.475
28.915
30.394
P [yr]
×10¹
2005.618
2005.579
2005.874
T [yr]
×10³
×10¹
0.901
0.878
0.912
e
×10⁻¹
×10¹
0.171
0.147
0.178
a ["]
×10⁻¹
×10⁻²
294.092
292.561
298.900
ω [°]
×10²
×10⁻¹
170.169
169.340
172.330
Ω [°]
×10²
×10⁻¹
75.655
72.007
76.393
i [°]
×10¹
×10⁻¹
4.352
2.714
4.944
m_total [M_⊙]
×10¹

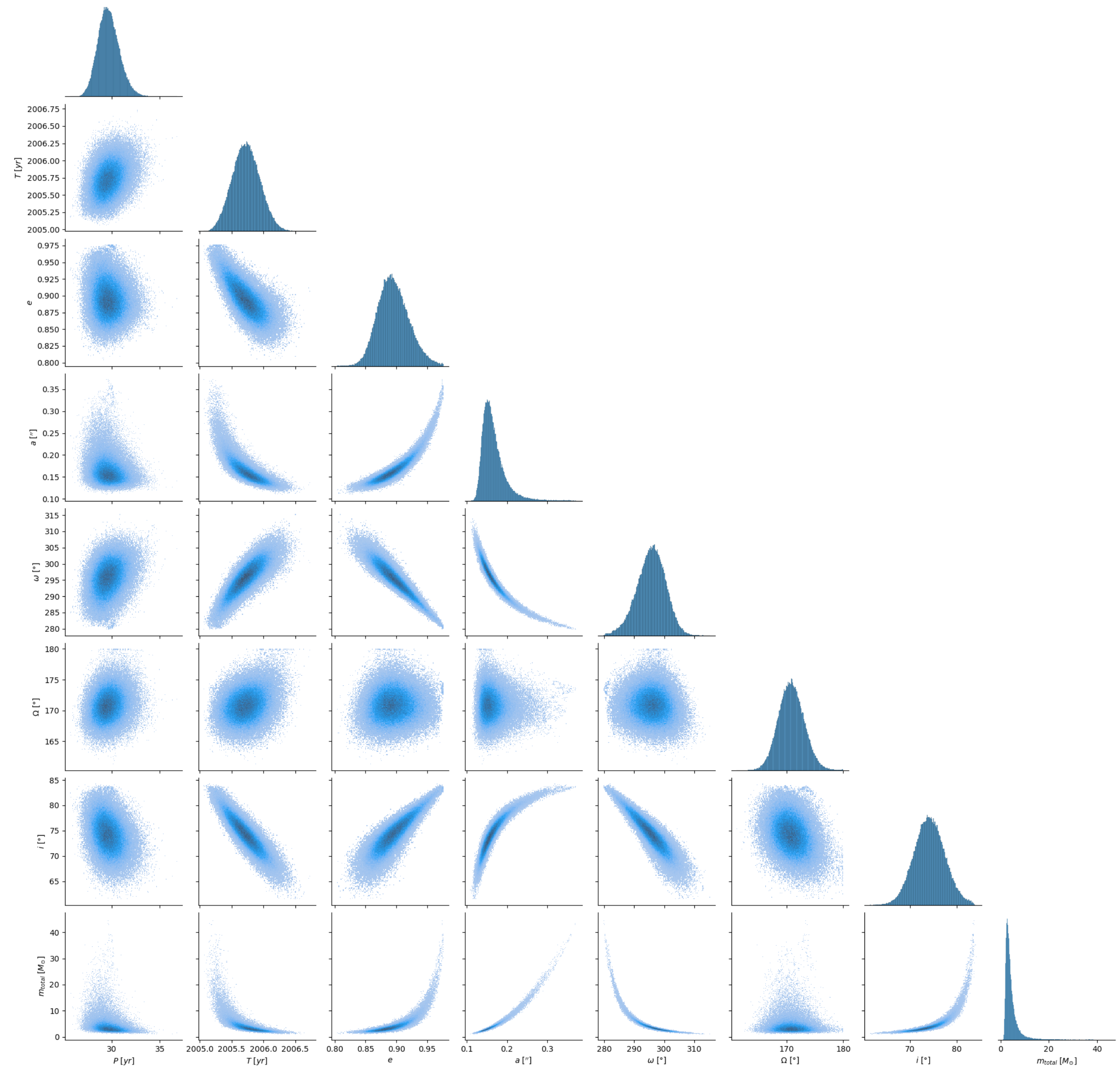
T [yr]
e
a ["]
ω [°]
Ω [°]
i [°]
m_total [M_⊙]
P [yr]
T [yr]
e
a ["]
ω [°]
Ω [°]
i [°]
m_total [M_⊙]

WDS22302−5345

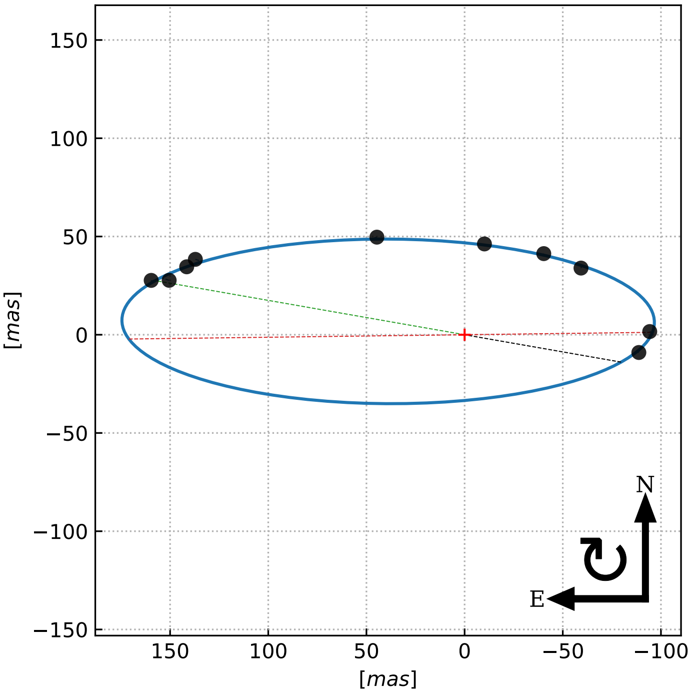

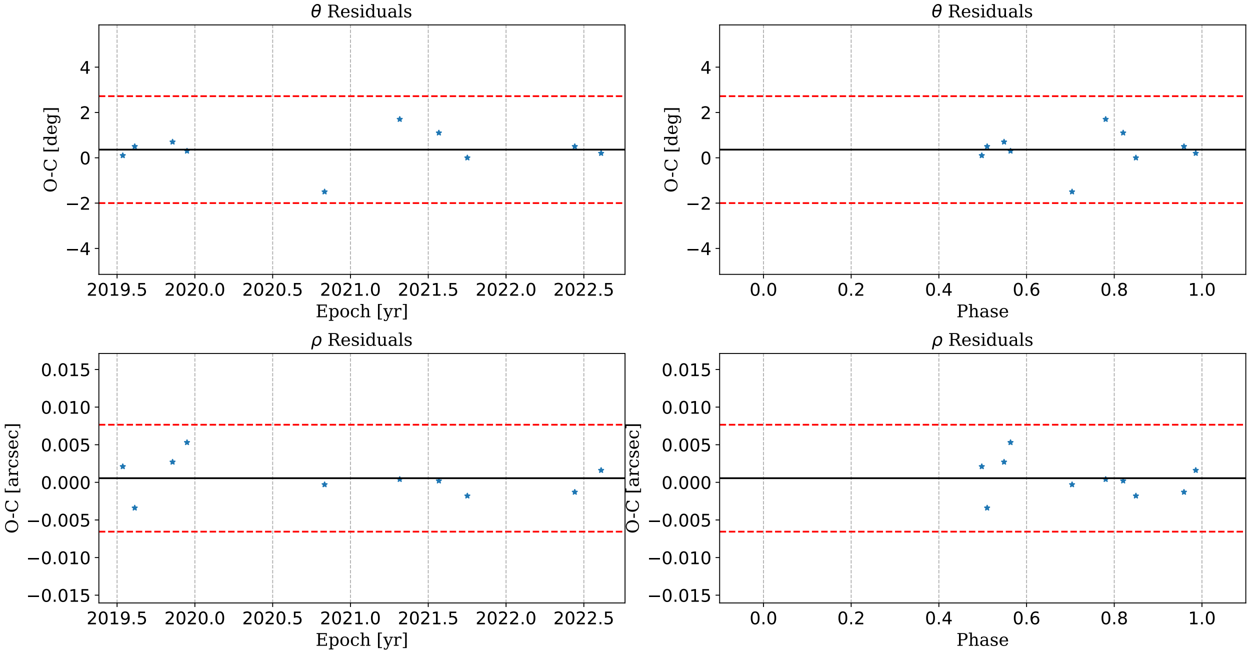

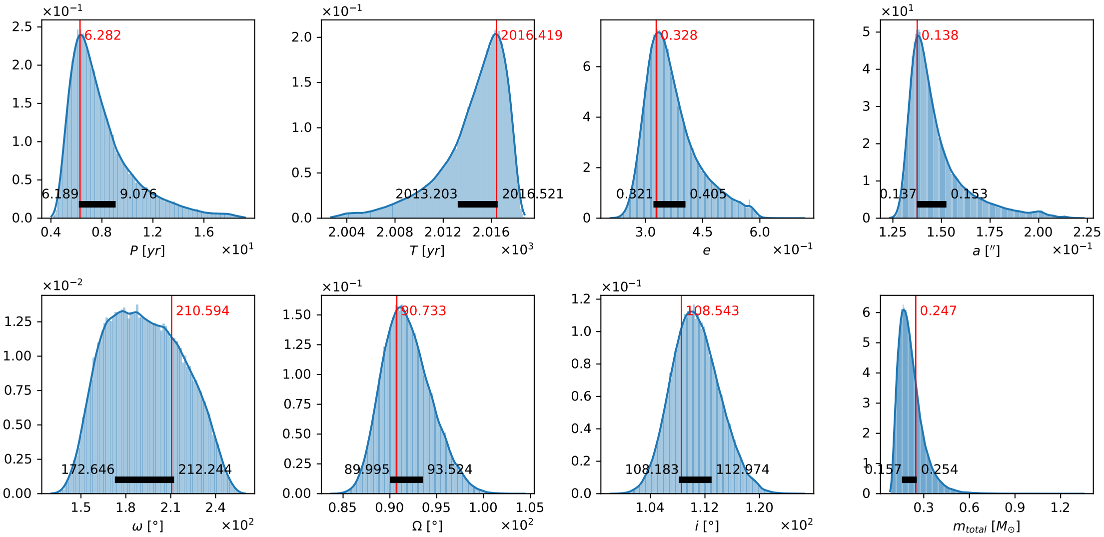
×10⁻¹
6.282
6.189
9.076
P [yr]
×10¹
2016.419
2013.203
2016.521
T [yr]
×10³
0.328
0.321
0.405
e
×10⁻¹
×10¹
0.138
0.137
0.153
a ["]
×10⁻¹
×10⁻²
210.594
172.646
212.244
ω [°]
×10²
90.733
89.995
93.524
Ω [°]
×10²
108.543
108.183
112.974
i [°]
×10²
0.247
0.157
0.254
m_total [M_⊙]

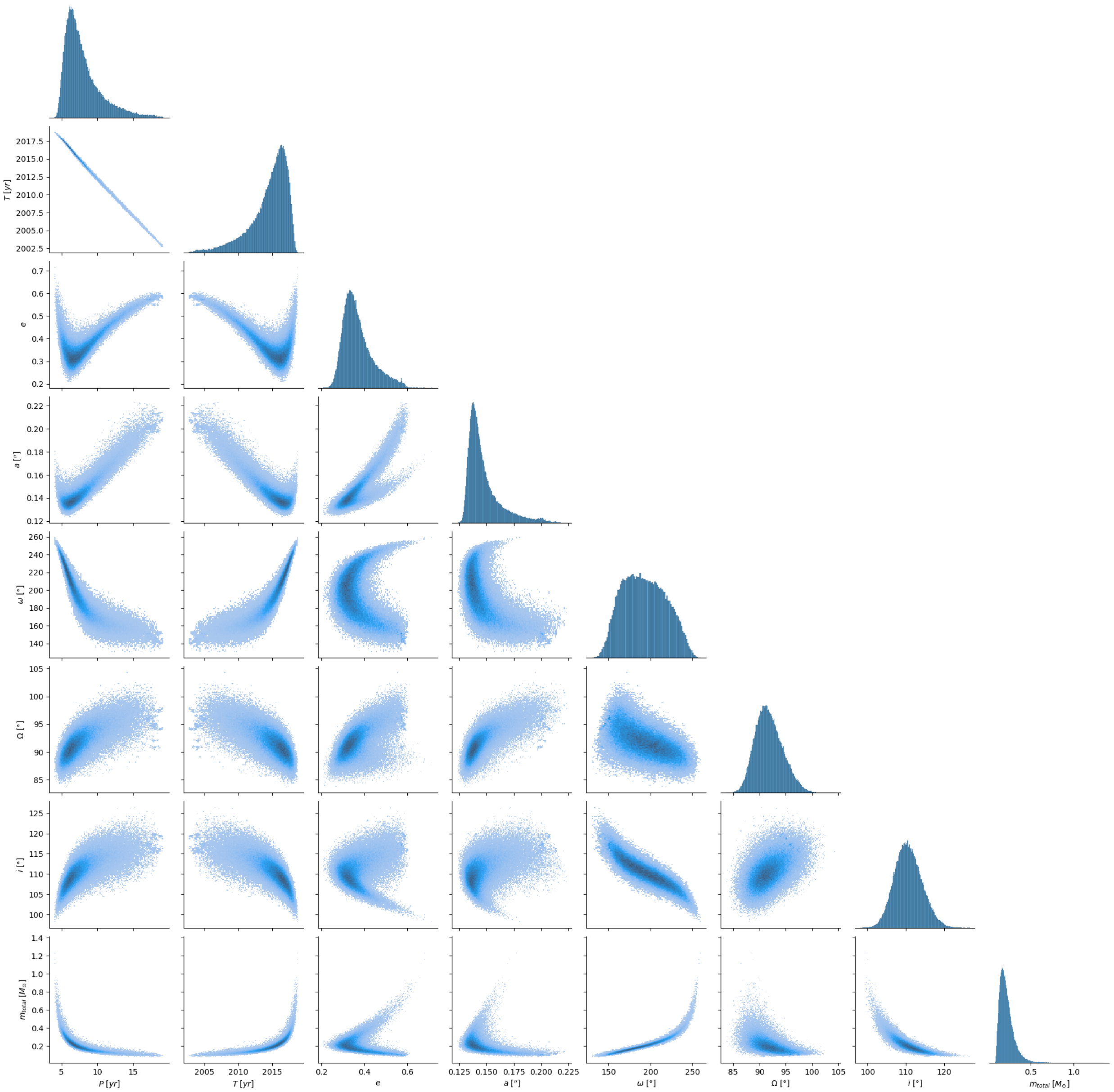
T [yr]
e
a ["]
ω [°]
Ω [°]
i [°]
m_total [M_⊙]
P [yr]
T [yr]
e
a ["]
ω [°]
Ω [°]
i [°]
m_total [M_⊙]

WDS23133−4937=HIP 114626

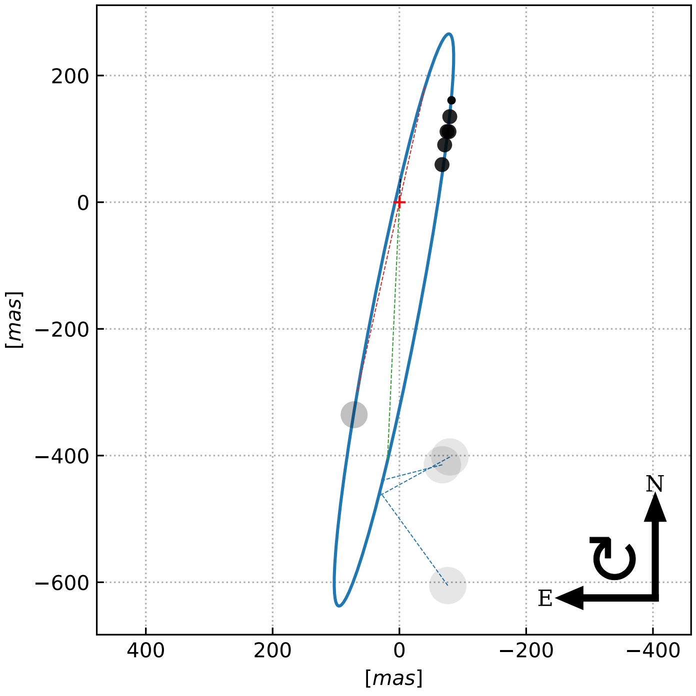

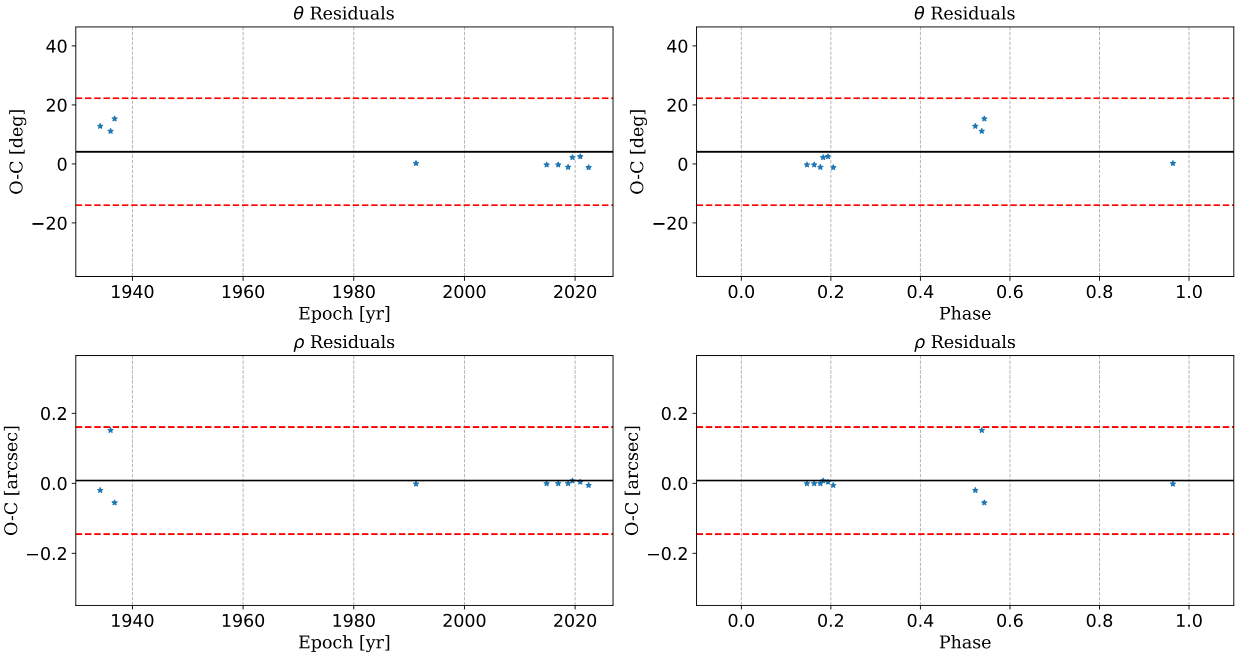

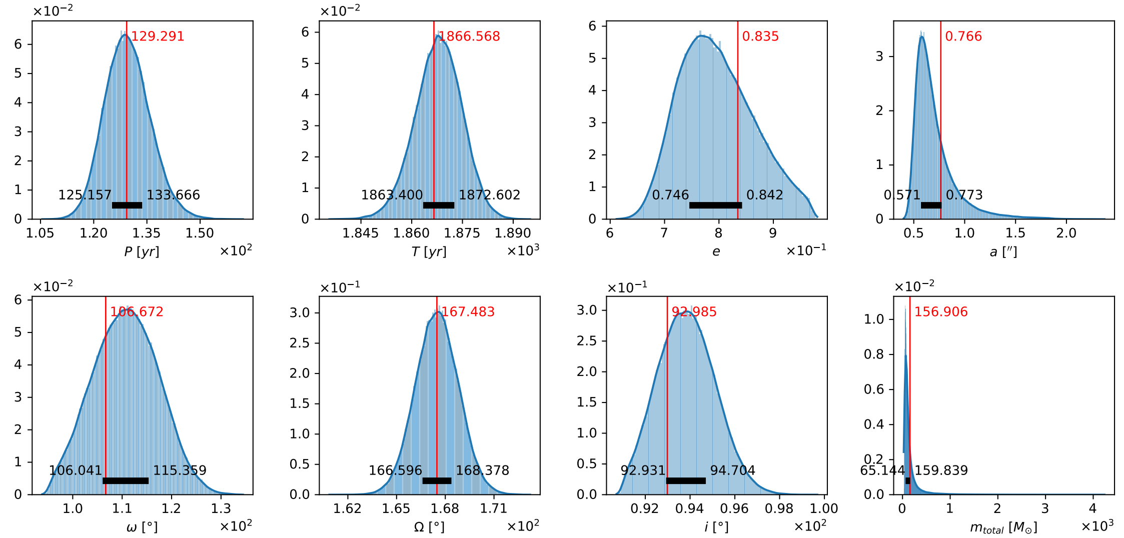

129.291
125.157
133.666
P [yr]
$\times10^{2}$
1866.568
1863.400
1872.602
T [yr]
$\times10^{3}$
0.835
0.746
0.842
e
$\times10^{-1}$
0.766
0.571
0.773
a ['']
106.672
106.041
115.359
ω [°]
167.483
166.596
168.378
Ω [°]
92.985
92.931
94.704
i [°]
156.906
65.144
159.839
m_{total} [$M_\odot$]
$\times10^{3}$

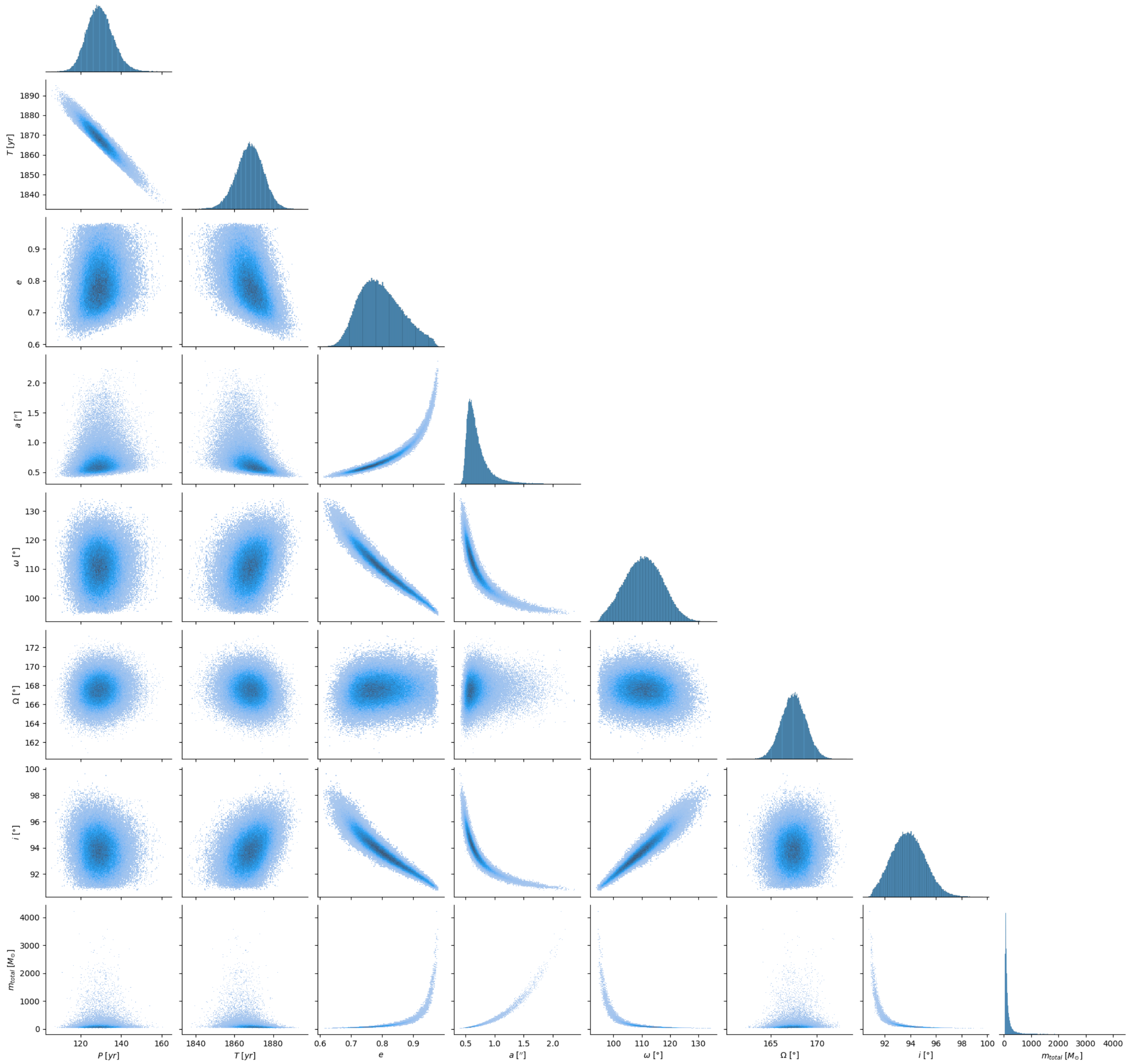

P [yr]
T [yr]
e
a ['']
ω [°]
Ω [°]
i [°]
m_{total} [$M_\odot$]

WDS23167−1534=HIP 114919

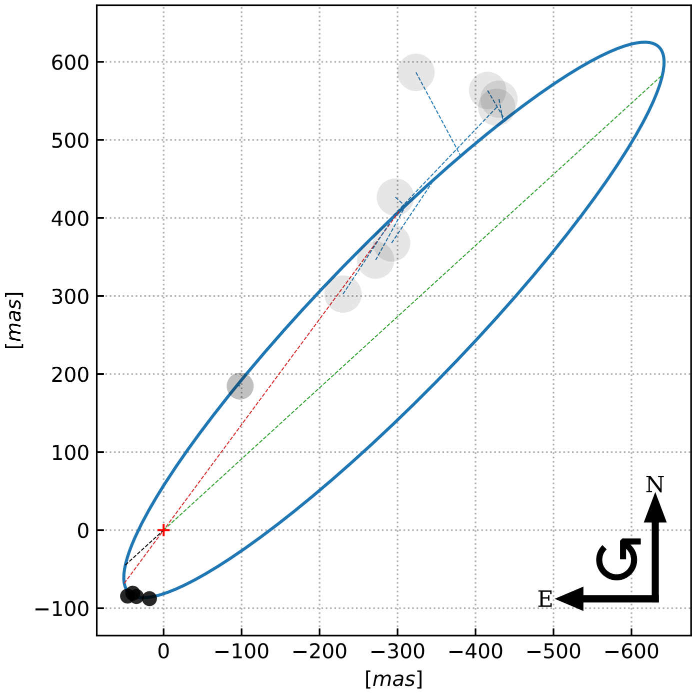

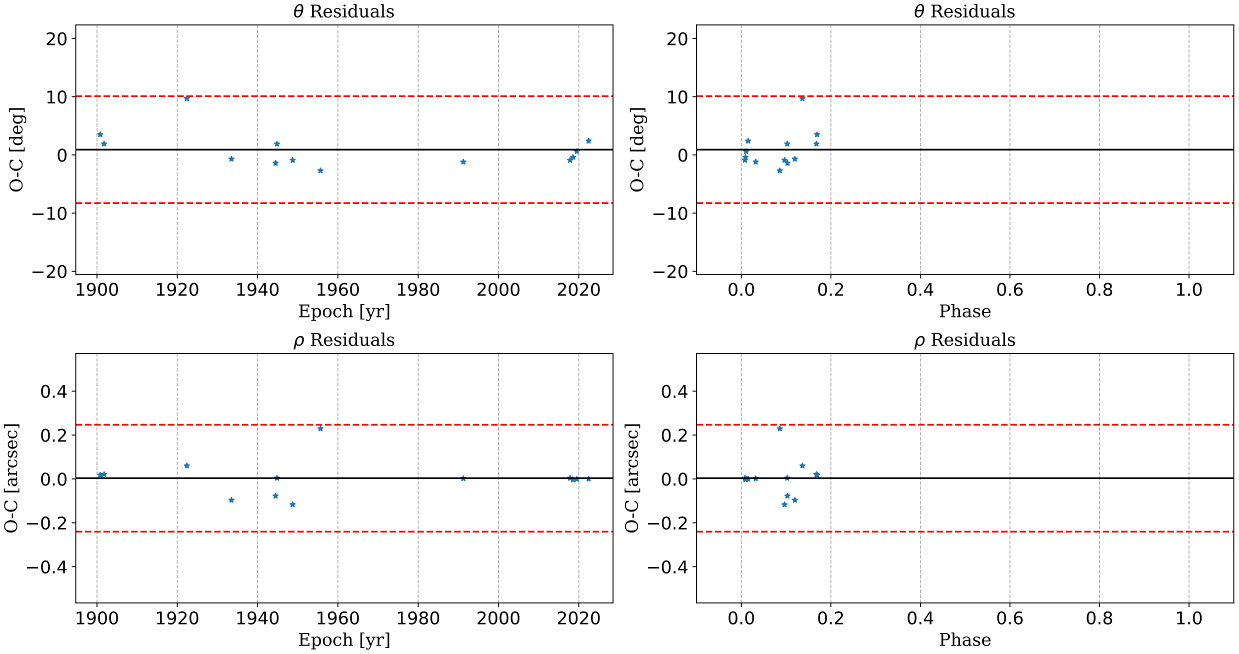

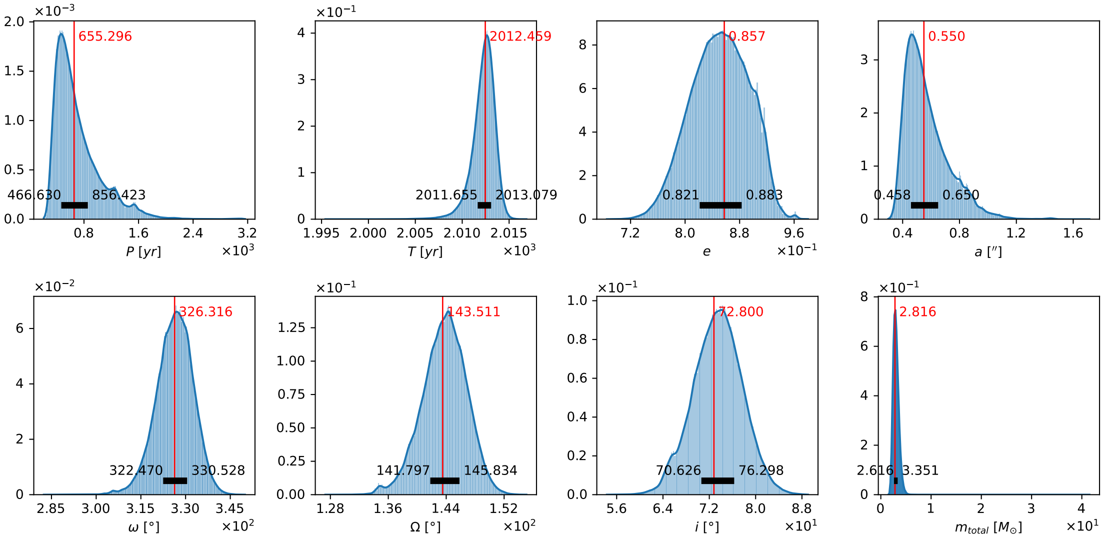
×10⁻³
655.296
466.630
856.423
P [yr]
×10³
×10⁻¹
2012.459
2011.655
2013.079
T [yr]
×10³
0.857
0.821
0.883
e
×10⁻¹
0.550
0.458
0.650
a ["]
×10⁻²
326.316
322.470
330.528
ω [°]
×10²
×10⁻¹
143.511
141.797
145.834
Ω [°]
×10²
×10⁻¹
72.800
70.626
76.298
i [°]
×10¹
×10⁻¹
2.816
2.616
3.351
m_total [M_⊙]
×10¹

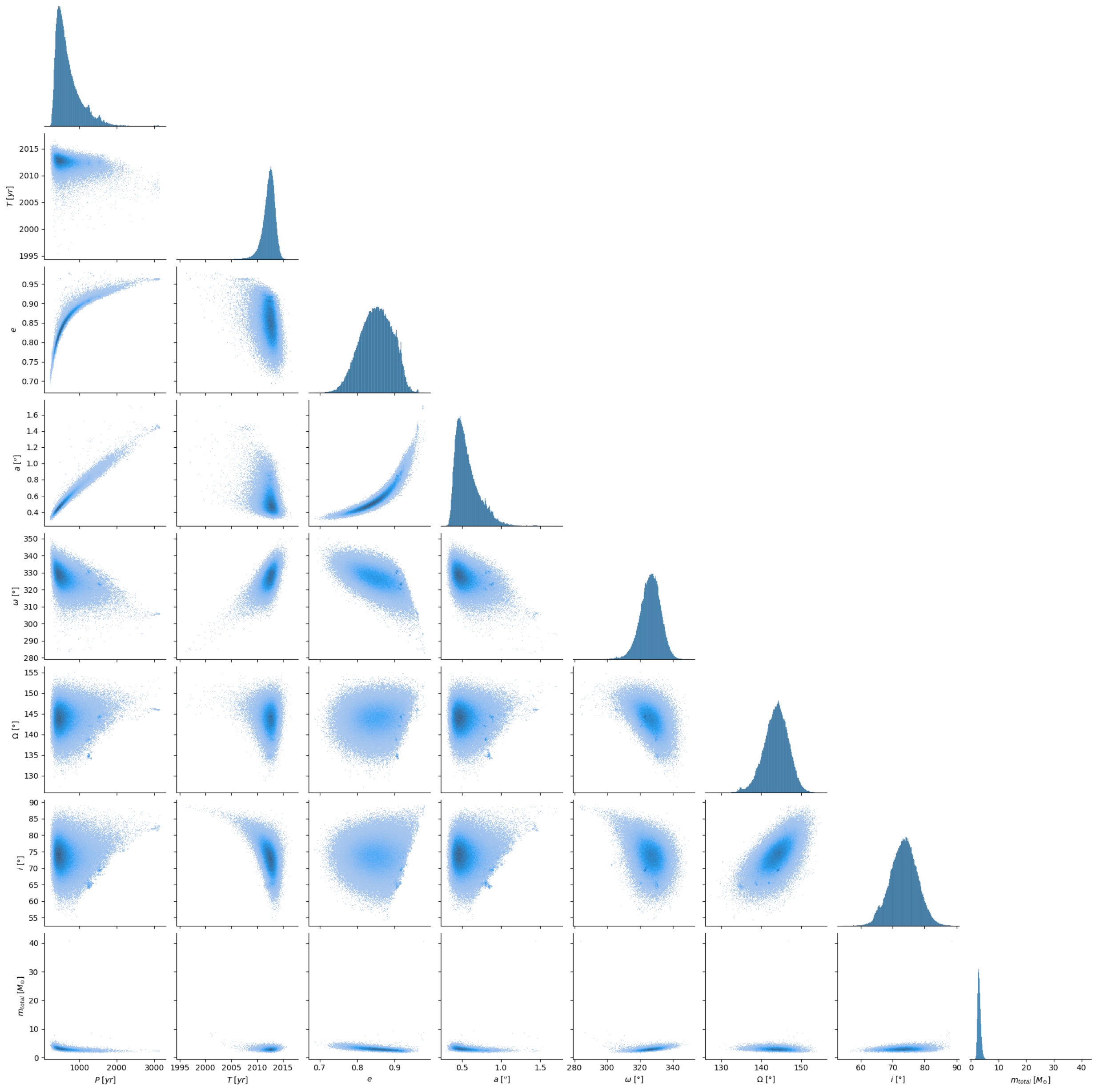
T [yr]
e
a ["]
ω [°]
Ω [°]
i [°]
m_total [M_⊙]
P [yr]
T [yr]
e
a ["]
ω [°]
Ω [°]
i [°]
m_total [M_⊙]

Single-lined Spectroscopic Binaries (SB1)

WDS01117+0835=HIP 5593

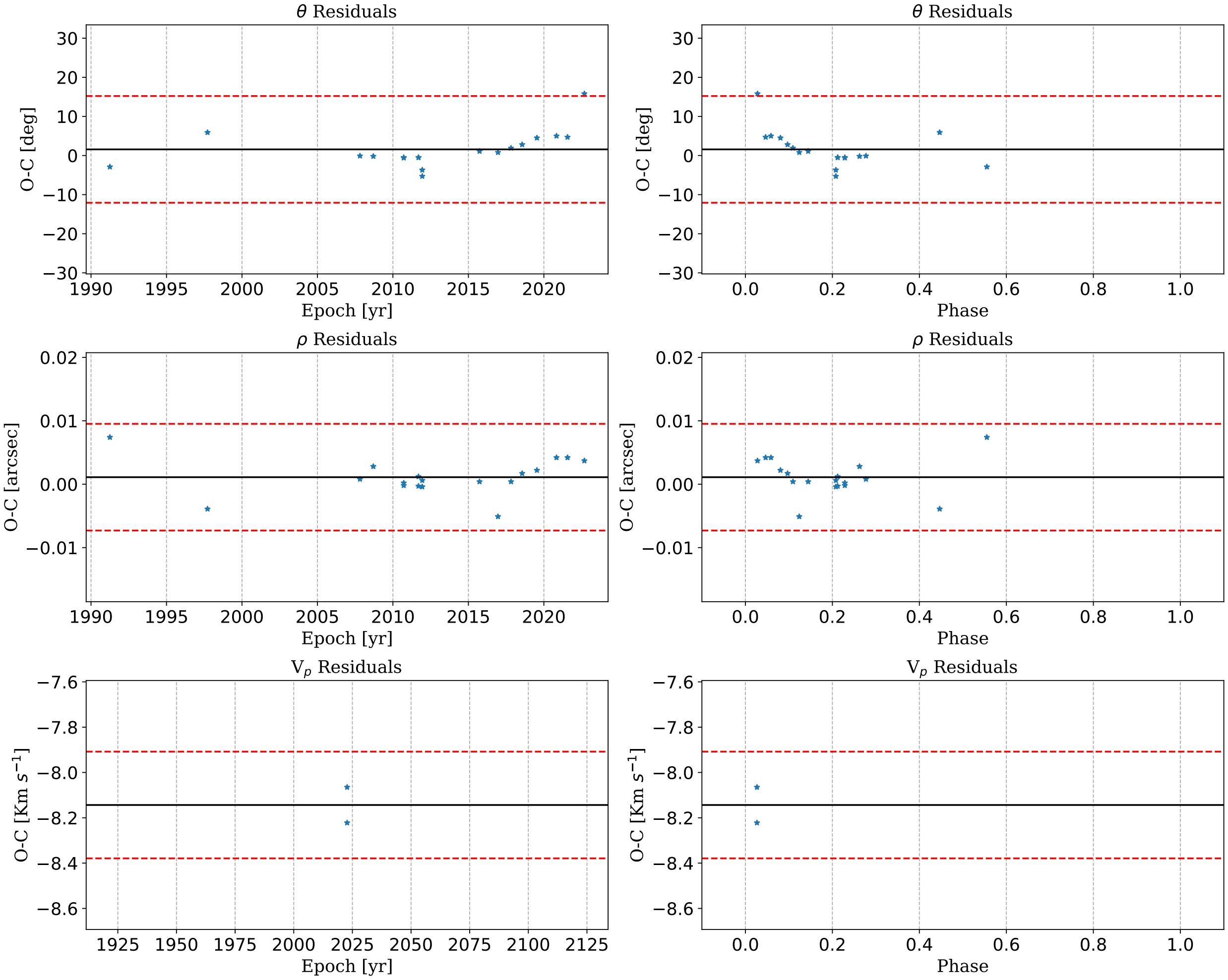

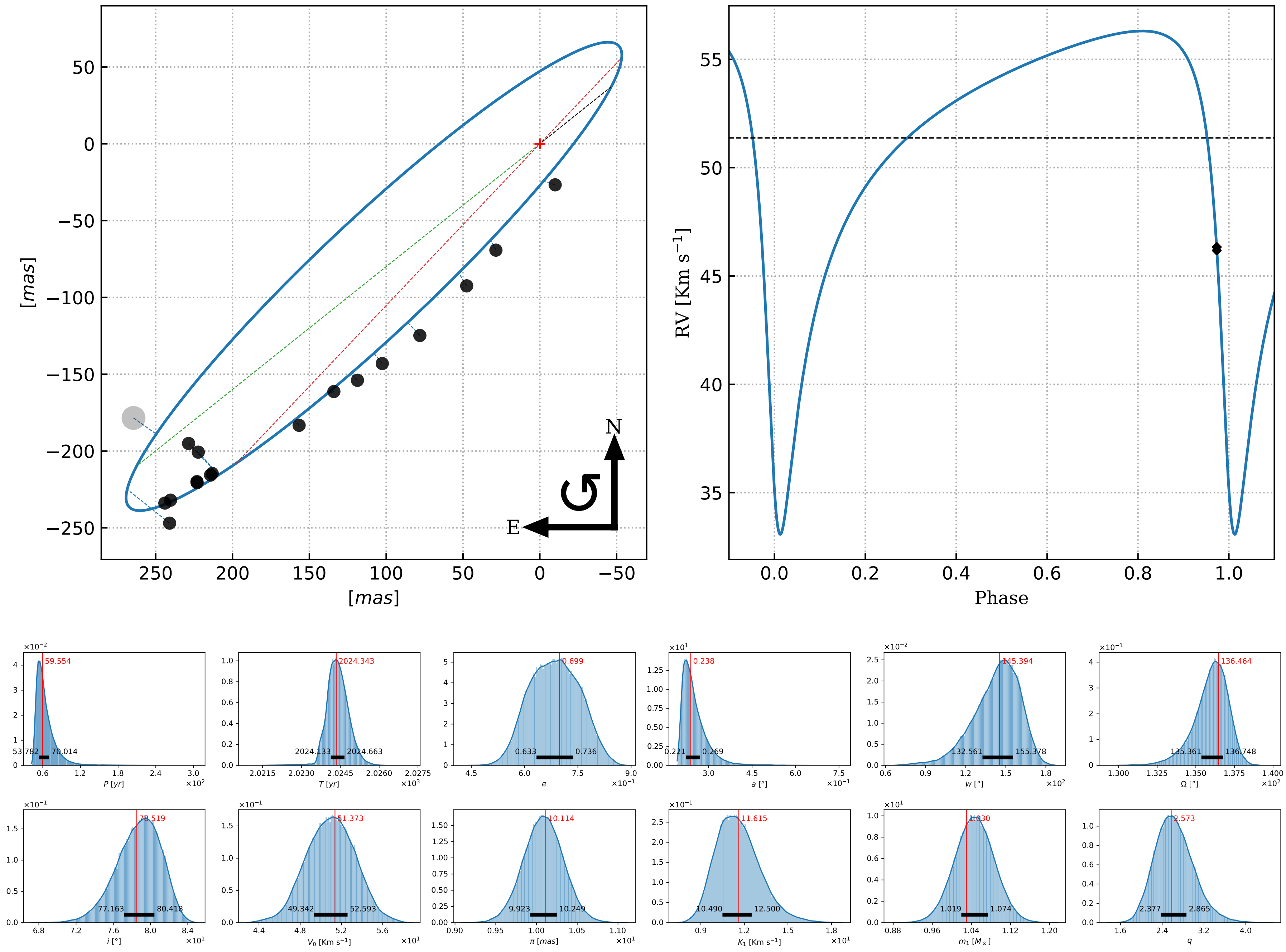
[mas]
[mas]
N
E
RV [Km s^{-1}]
Phase
59.554
53.782
70.014
P [yr]
2024.343
2024.133
2024.663
T [yr]
0.699
0.633
0.736
e
0.238
0.221
0.269
a ["]
145.394
132.561
155.378
w [°]
136.464
135.361
136.748
Ω [°]
78.519
77.163
80.418
i [°]
51.373
49.342
52.593
V$_0$ [Km s^{-1}]
10.114
9.923
10.249
π [mas]
11.615
10.490
12.500
K$_1$ [Km s^{-1}]
1.030
1.019
1.074
m$_1$ [M$_\odot$]
2.573
2.377
2.865
q

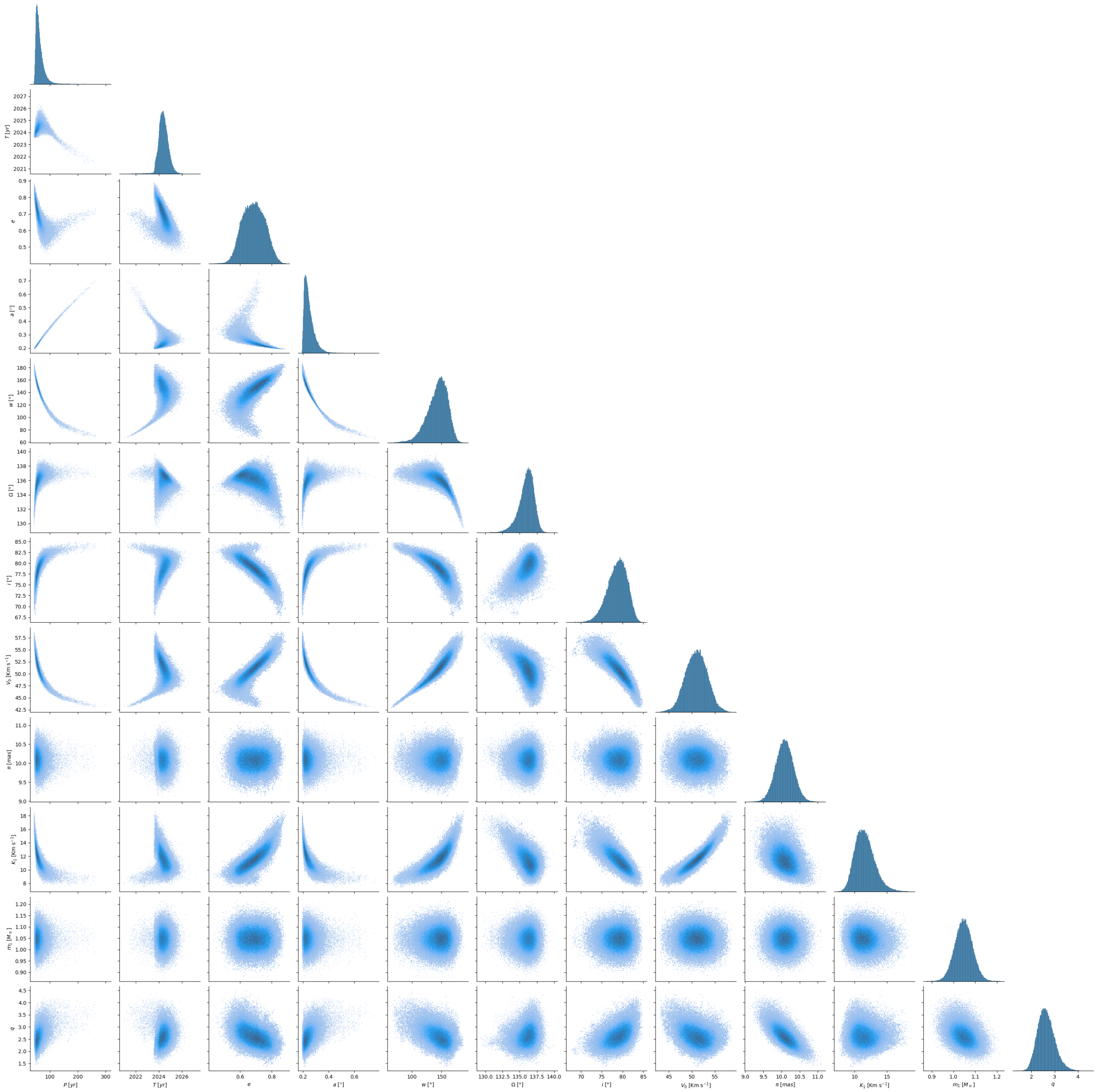

$T\ [yr]$
e
$a\ ['']$
$w\ [^\circ]$
$\Omega\ [^\circ]$
$i\ [^\circ]$
$V_0\ [\mathrm{Km\,s^{-1}}]$
$\pi\ [mas]$
$K_1\ [\mathrm{Km\,s^{-1}}]$
$m_1\ [M_\odot]$
q
$P\ [yr]$
$T\ [yr]$
e
$a\ ['']$
$w\ [^\circ]$
$\Omega\ [^\circ]$
$i\ [^\circ]$
$V_0\ [\mathrm{Km\,s^{-1}}]$
$\pi\ [mas]$
$K_1\ [\mathrm{Km\,s^{-1}}]$
$m_1\ [M_\odot]$
q

WDS02572−2458=HIP 13768

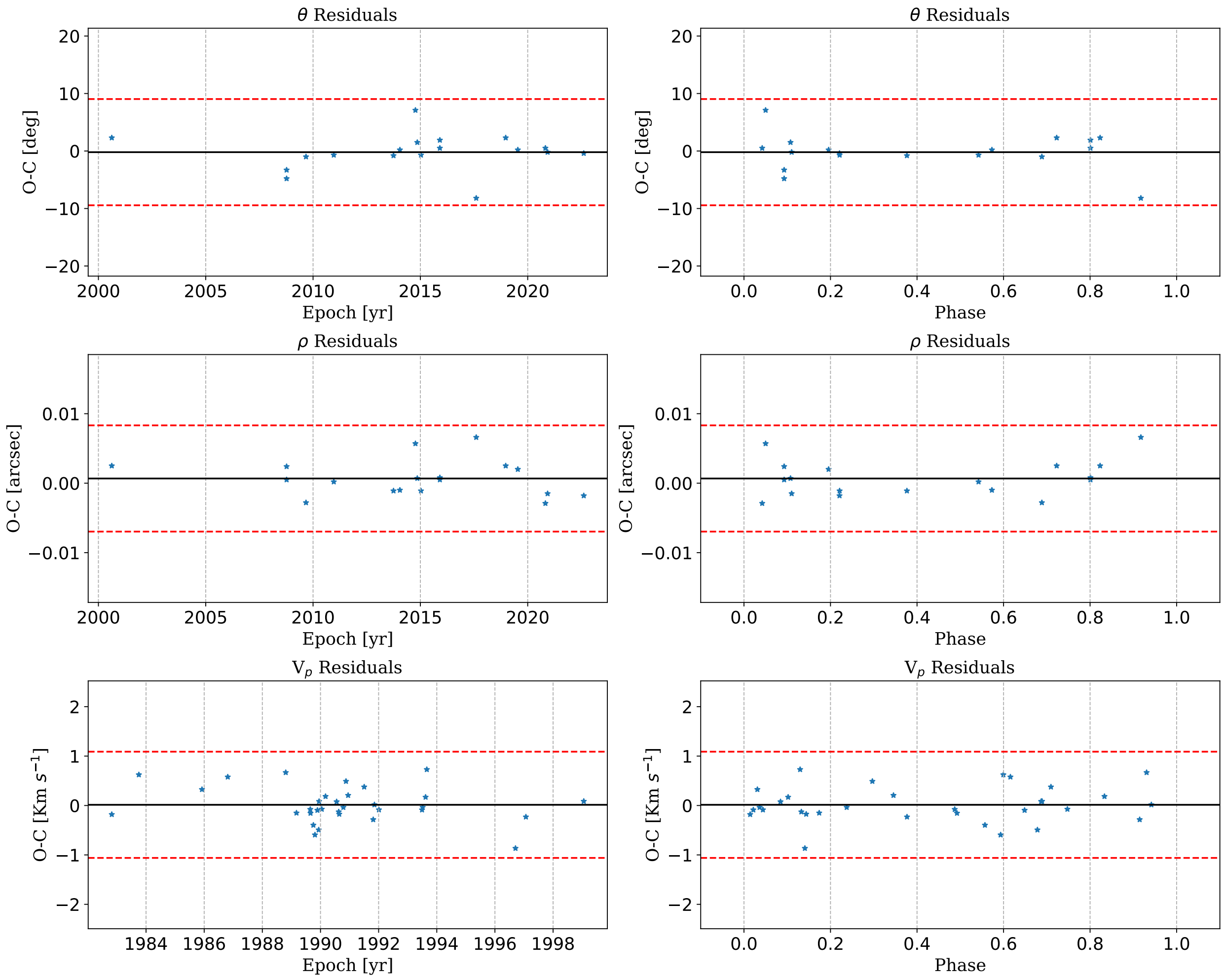

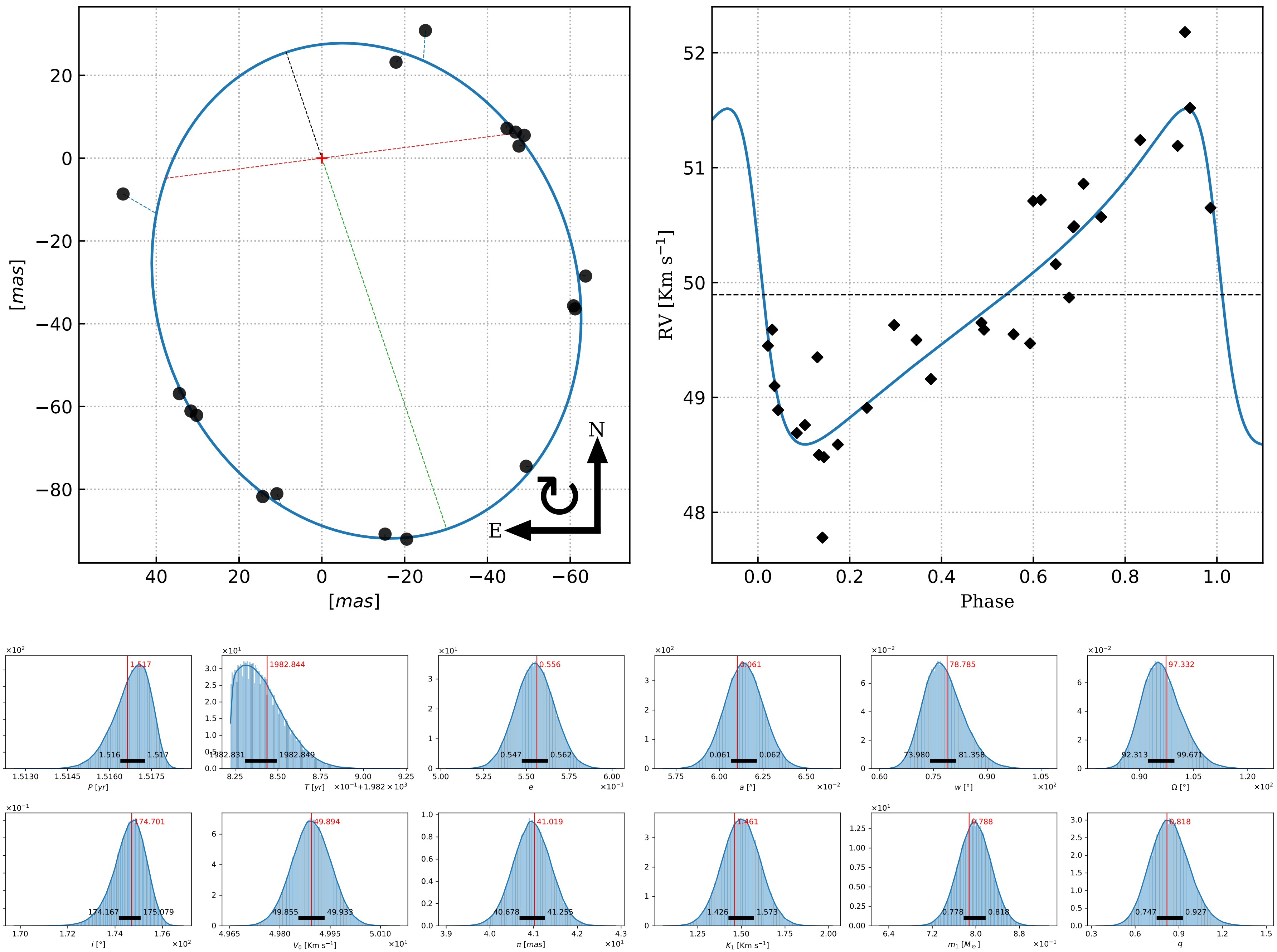[mas]
[mas]
20
0
−20
−40
−60
−80
40
20
0
−20
−40
−60
N
E
RV [Km s^{-1}]
52
51
50
49
48
0.0
0.2
0.4
0.6
0.8
1.0
Phase
1.517
1.516
1.517
P [yr]
1982.844
1982.831
1982.849
T [yr] ×10^{-1}+1.982×10^{3}
0.556
0.547
0.562
e
0.061
0.061
0.062
a ["]
78.785
73.980
81.358
w [°]
97.332
92.313
99.671
Ω [°]
174.701
174.167
175.079
i [°]
49.894
49.855
49.933
V$_0$ [Km s^{-1}]
41.019
40.678
41.255
π [mas]
1.461
1.426
1.573
K$_1$ [Km s^{-1}]
0.788
0.778
0.818
m$_1$ [M$_\odot$]
0.818
0.747
0.927
q

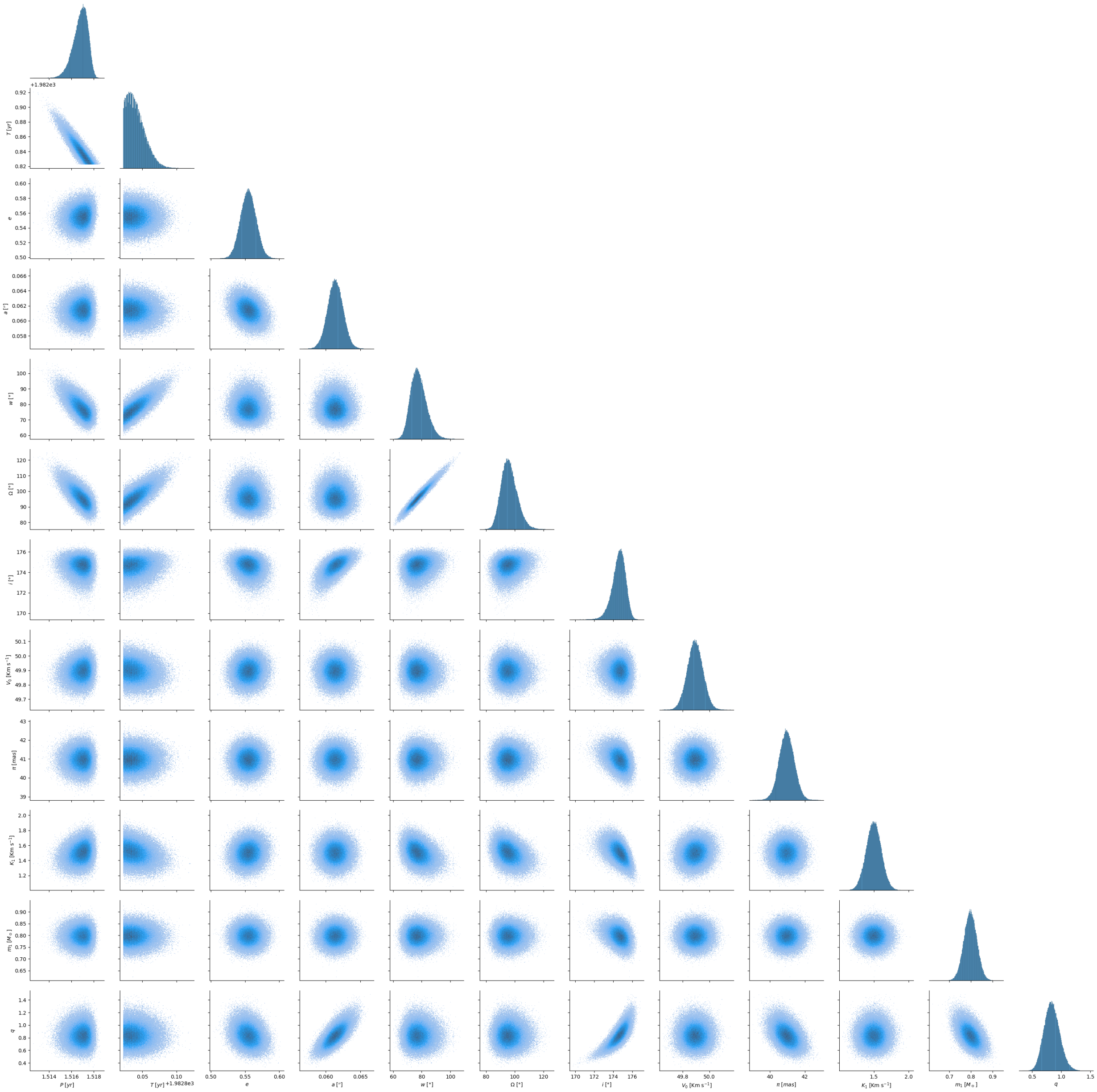
+1.982e3
T [yr]
0.92
0.90
0.88
0.86
0.84
0.82
e
0.60
0.58
0.56
0.54
0.52
0.50
a ["]
0.066
0.064
0.062
0.060
0.058
w [°]
100
90
80
70
60
Ω [°]
120
110
100
90
80
i [°]
176
174
172
170
V_0 [Km s^{-1}]
50.1
50.0
49.9
49.8
49.7
π [mas]
43
42
41
40
39
K_1 [Km s^{-1}]
2.0
1.8
1.6
1.4
1.2
m_1 [$M_\odot$]
0.90
0.85
0.80
0.75
0.70
0.65
q
1.4
1.2
1.0
0.8
0.6
0.4
1.514
1.516
1.518
P [yr]
0.05
0.10
T [yr] +1.9828e3
0.50
0.55
0.60
e
0.060
0.065
a ["]
60
80
100
w [°]
80
100
120
Ω [°]
170
172
174
176
i [°]
49.8
50.0
V_0 [Km s^{-1}]
40
42
π [mas]
1.5
2.0
K_1 [Km s^{-1}]
0.7
0.8
0.9
m_1 [$M_\odot$]
0.5
1.0
1.5
q

WDS05286−4548=HIP 25641

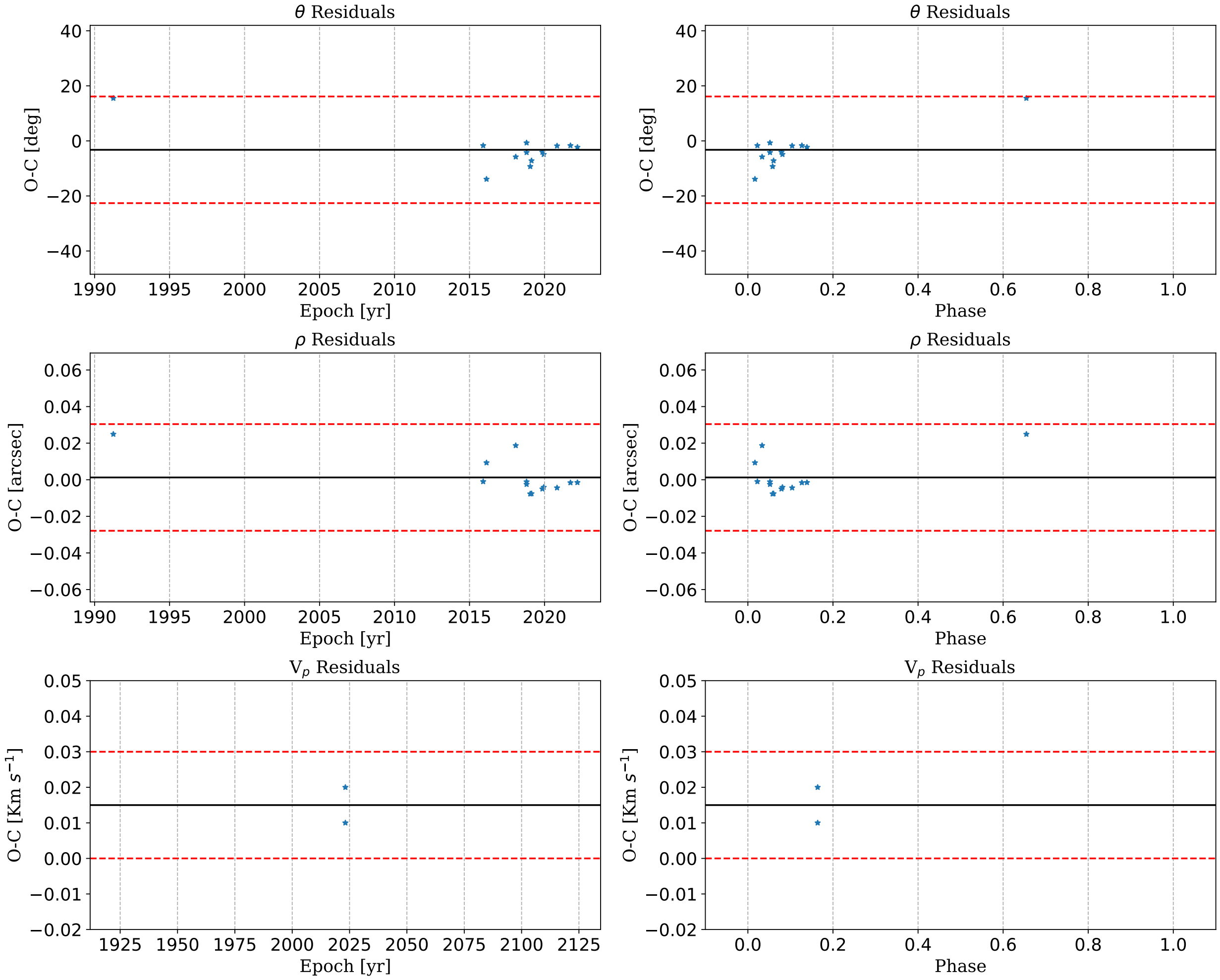

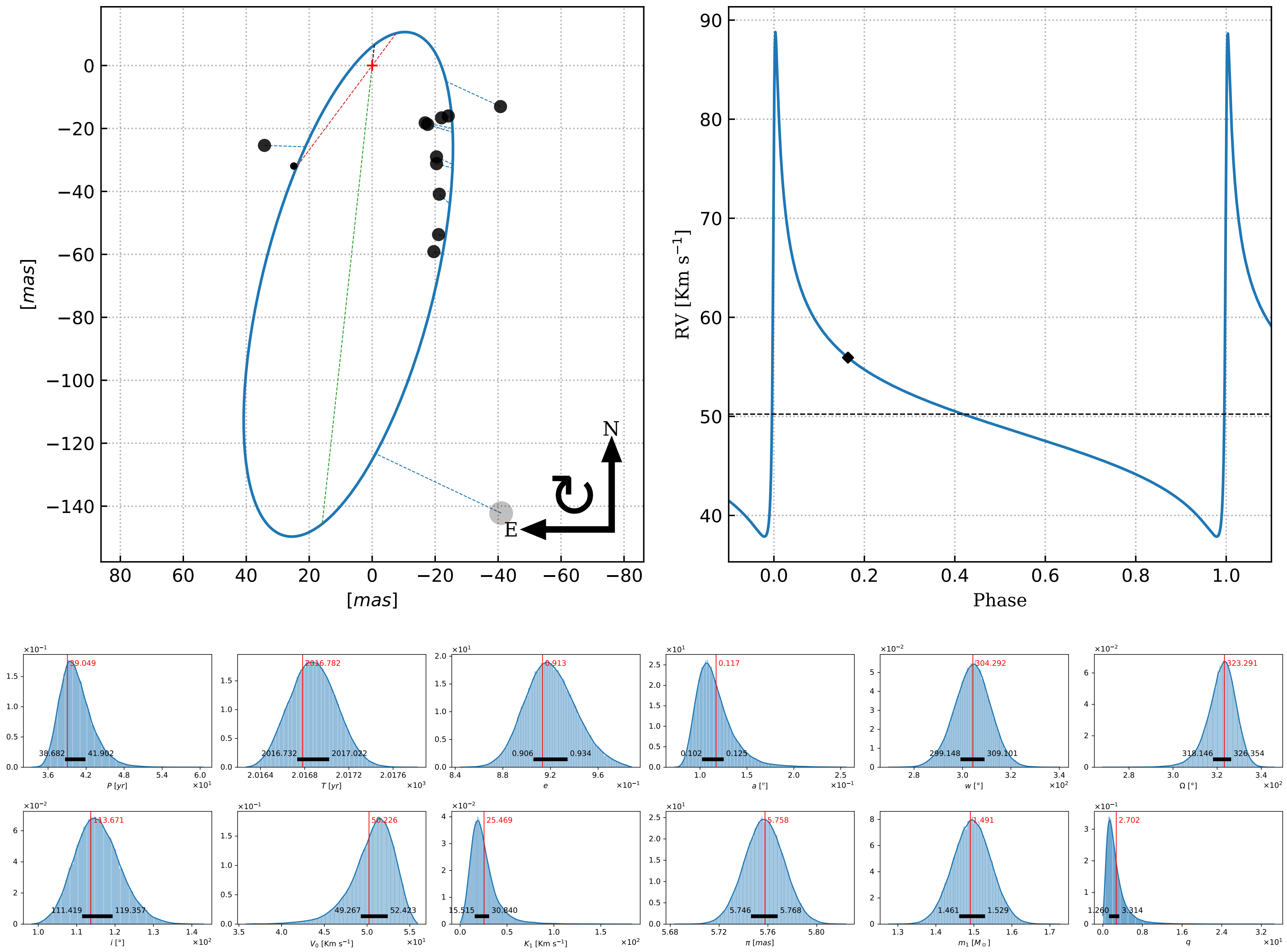
[mas]
[mas]
0
−20
−40
−60
−80
−100
−120
−140
80
60
40
20
0
−20
−40
−60
−80
N
E
RV [Km s^{-1}]
Phase
90
80
70
60
50
40
0.0
0.2
0.4
0.6
0.8
1.0
39.049
38.682
41.902
P [yr]
2016.782
2016.732
2017.022
T [yr]
0.913
0.906
0.934
e
0.117
0.102
0.125
a ["]
304.292
299.148
309.101
w [°]
323.291
318.146
326.354
Ω [°]
113.671
111.419
119.357
i [°]
50.226
49.267
52.423
V$_0$ [Km s^{-1}]
25.469
15.515
30.840
K$_1$ [Km s^{-1}]
5.758
5.746
5.768
π [mas]
1.491
1.461
1.529
m$_1$ [M$_\odot$]
2.702
1.260
3.314
q

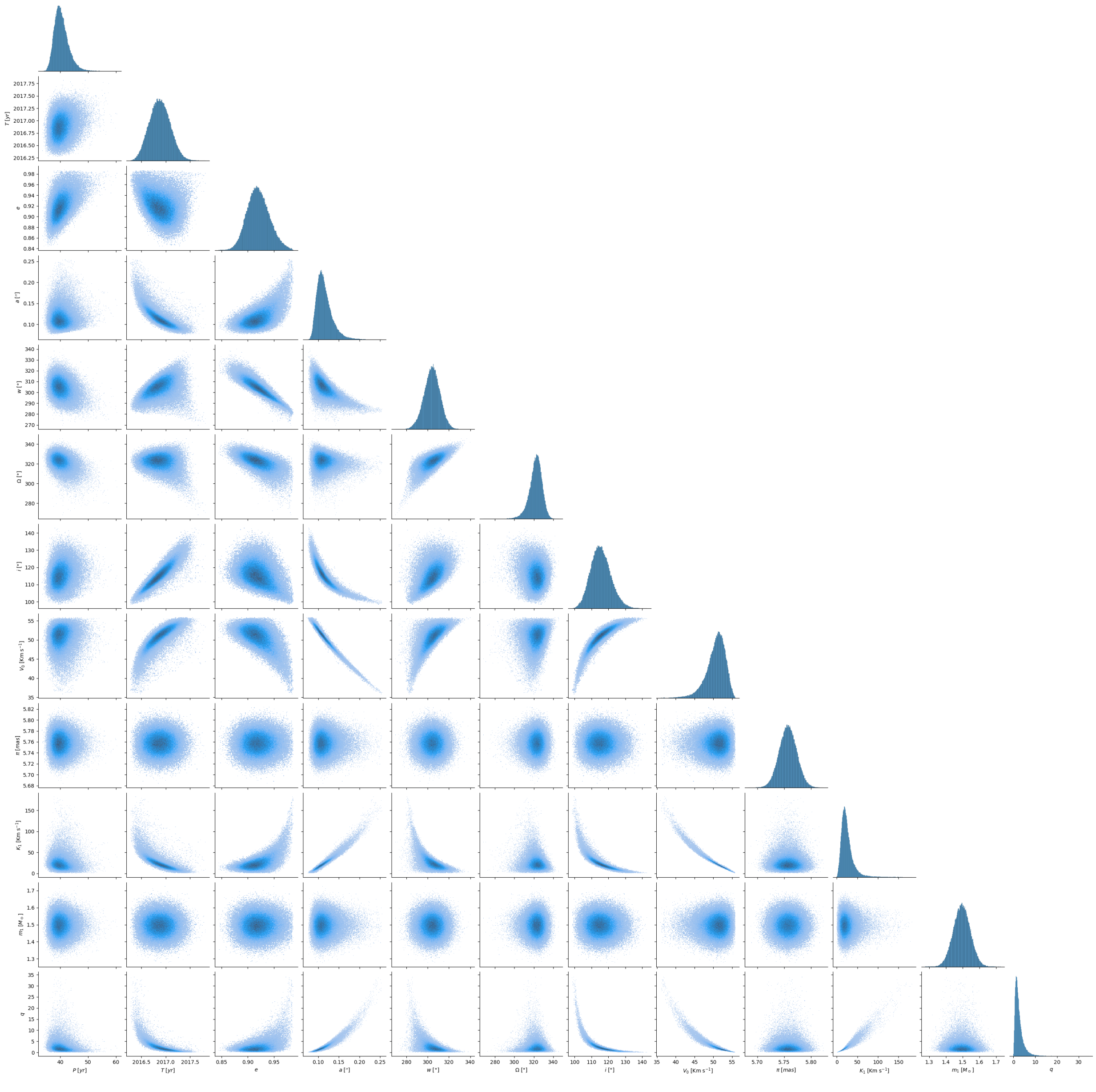
$T\,[yr]$
e
$a\,['']$
$w\,[°]$
$\Omega\,[°]$
$i\,[°]$
$V_0\,[\mathrm{Km\,s^{-1}}]$
$\pi\,[mas]$
$K_1\,[\mathrm{Km\,s^{-1}}]$
$m_1\,[M_\odot]$
q
$P\,[yr]$
$T\,[yr]$
e
$a\,['']$
$w\,[°]$
$\Omega\,[°]$
$i\,[°]$
$V_0\,[\mathrm{Km\,s^{-1}}]$
$\pi\,[mas]$
$K_1\,[\mathrm{Km\,s^{-1}}]$
$m_1\,[M_\odot]$
q

WDS07548−6613=HIP 38645

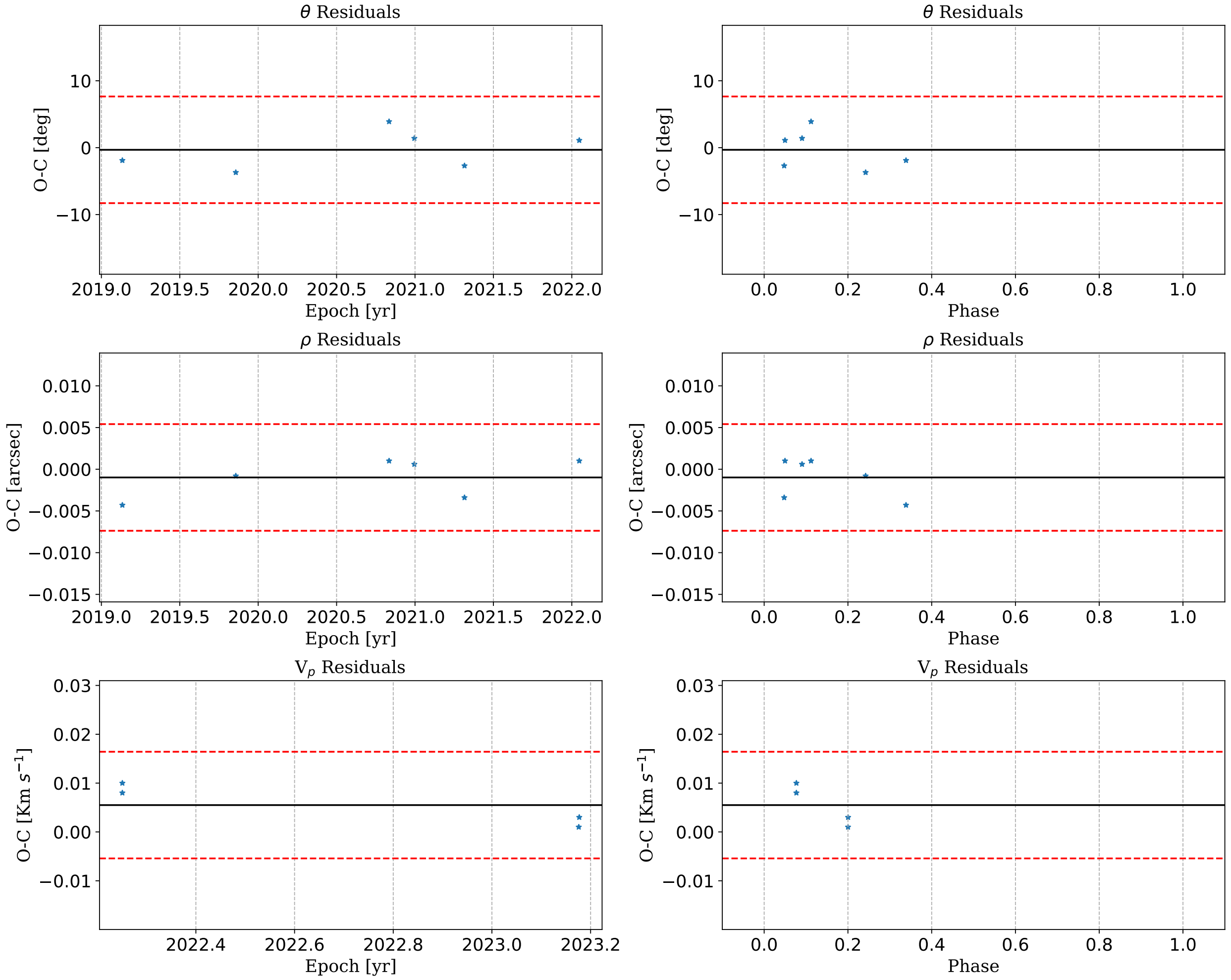

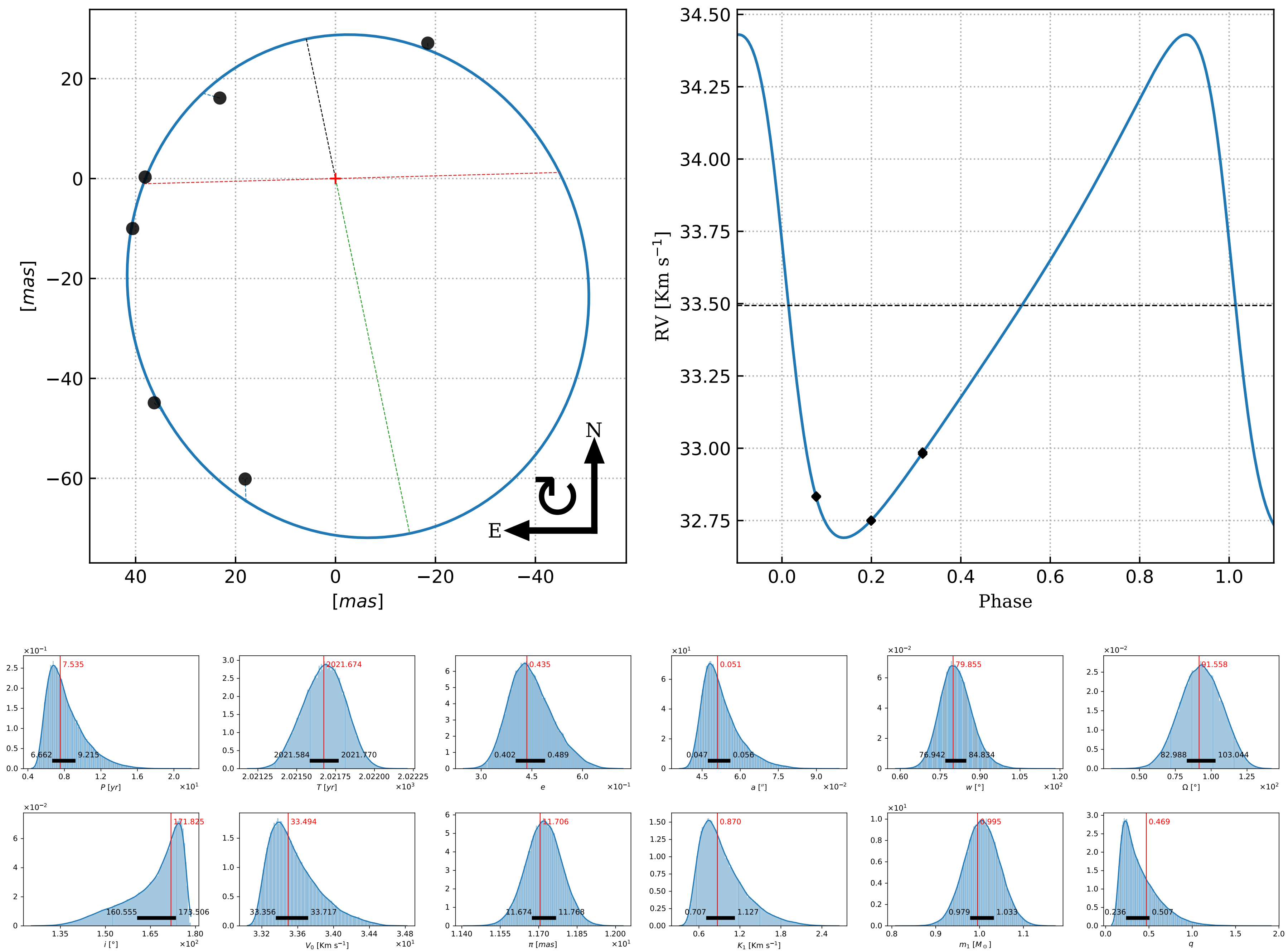
N
E
[mas]
[mas]
20
0
−20
−40
−60
40
20
0
−20
−40
RV [Km s^{-1}]
Phase
34.50
34.25
34.00
33.75
33.50
33.25
33.00
32.75
0.0
0.2
0.4
0.6
0.8
1.0
7.535
6.662
9.215
P [yr]
2021.674
2021.584
2021.770
T [yr]
0.435
0.402
0.489
e
0.051
0.047
0.056
a ["]
79.855
76.942
84.834
w [°]
91.558
82.988
103.044
Ω [°]
171.825
160.555
173.506
i [°]
33.494
33.356
33.717
V_0 [Km s^{-1}]
11.706
11.674
11.768
π [mas]
0.870
0.707
1.127
K_1 [Km s^{-1}]
0.995
0.979
1.033
m_1 [$M_\odot$]
0.469
0.236
0.507
q

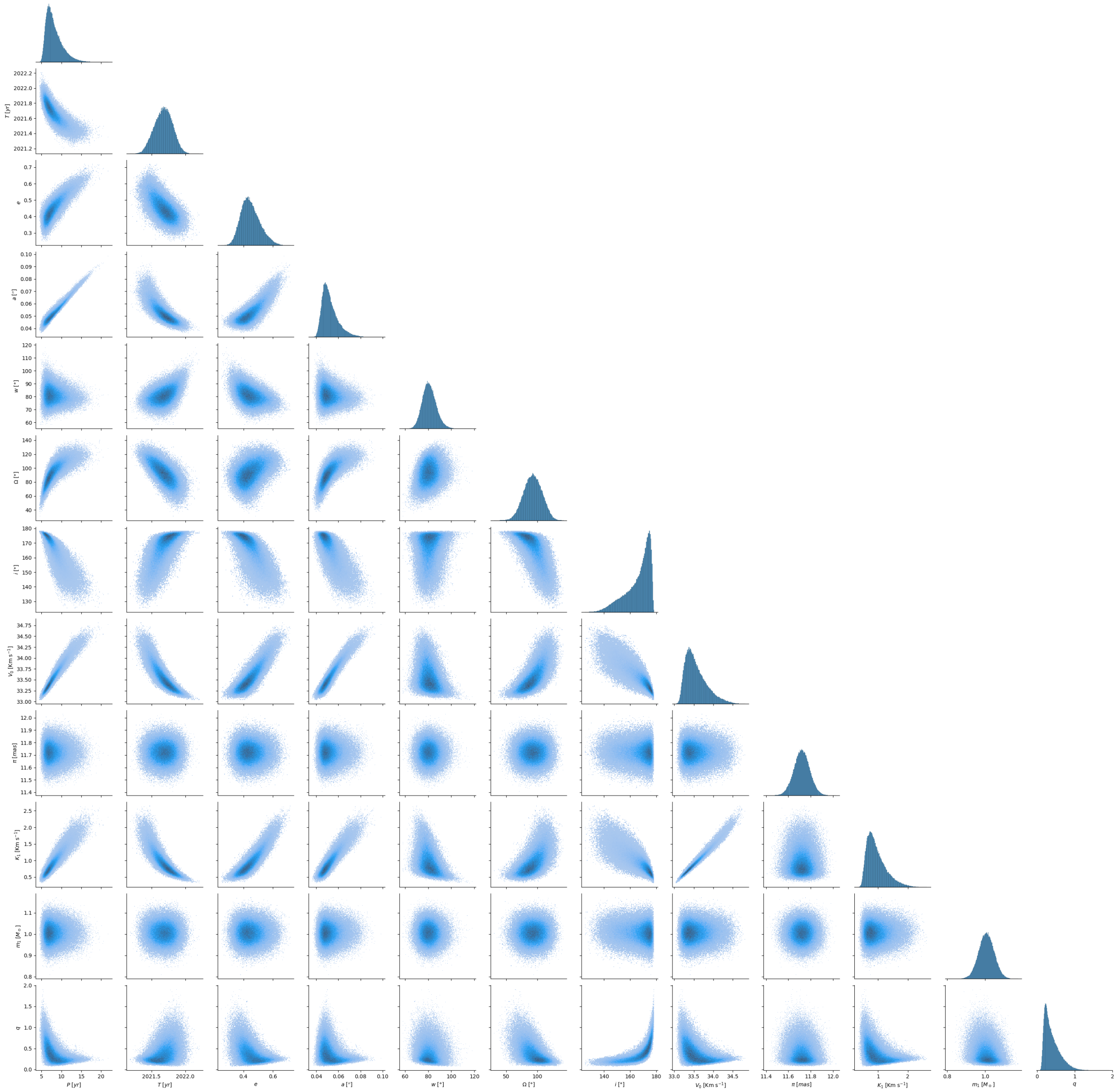
T [yr]
2022.2
2022.0
2021.8
2021.6
2021.4
2021.2
e
0.7
0.6
0.5
0.4
0.3
a ["]
0.10
0.09
0.08
0.07
0.06
0.05
0.04
w [°]
120
110
100
90
80
70
60
Ω [°]
140
120
100
80
60
40
i [°]
180
170
160
150
140
130
V₀ [Km s⁻¹]
34.75
34.50
34.25
34.00
33.75
33.50
33.25
33.00
π [mas]
12.0
11.9
11.8
11.7
11.6
11.5
11.4
K₁ [Km s⁻¹]
2.5
2.0
1.5
1.0
0.5
m₁ [M☉]
1.1
1.0
0.9
0.8
q
2.0
1.5
1.0
0.5
0.0
5
10
15
20
P [yr]
2021.5
2022.0
T [yr]
0.4
0.6
e
0.04
0.06
0.08
0.10
a ["]
60
80
100
120
w [°]
50
100
Ω [°]
140
160
180
i [°]
33.0
33.5
34.0
34.5
V₀ [Km s⁻¹]
11.4
11.6
11.8
12.0
π [mas]
1
2
K₁ [Km s⁻¹]
0.8
1.0
m₁ [M☉]
0
1
2
q

WDS12018−3439=HIP 58669

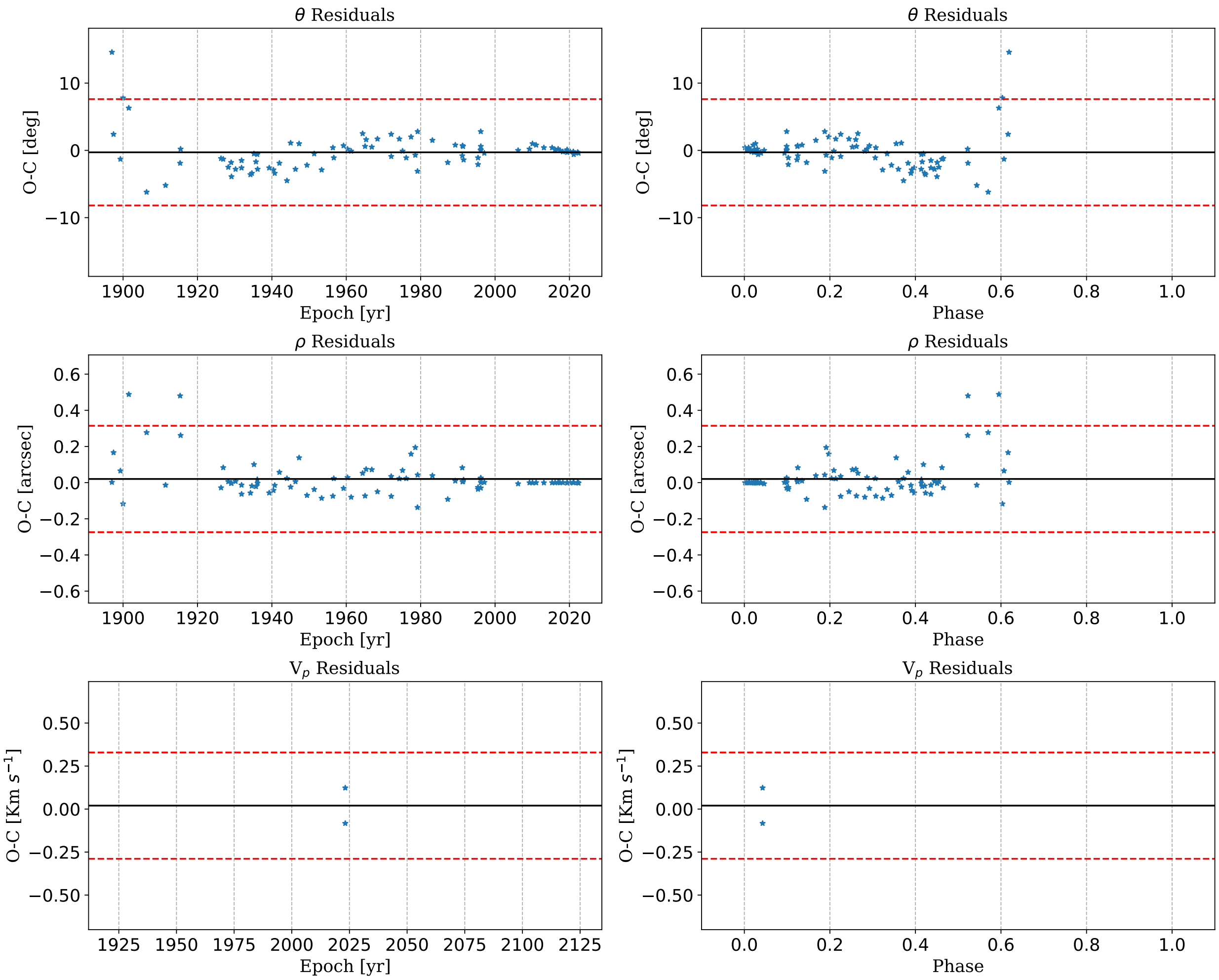

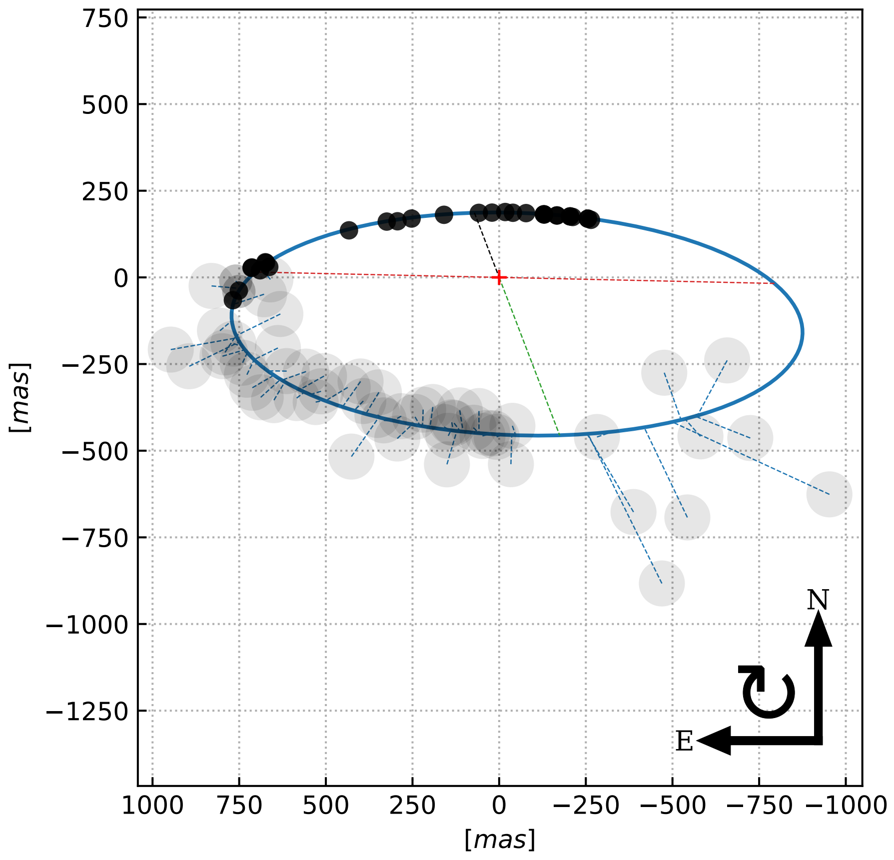
750
500
250
0
−250
−500
−750
−1000
−1250
[mas]
1000
750
500
250
0
−250
−500
−750
−1000
[mas]
N
E

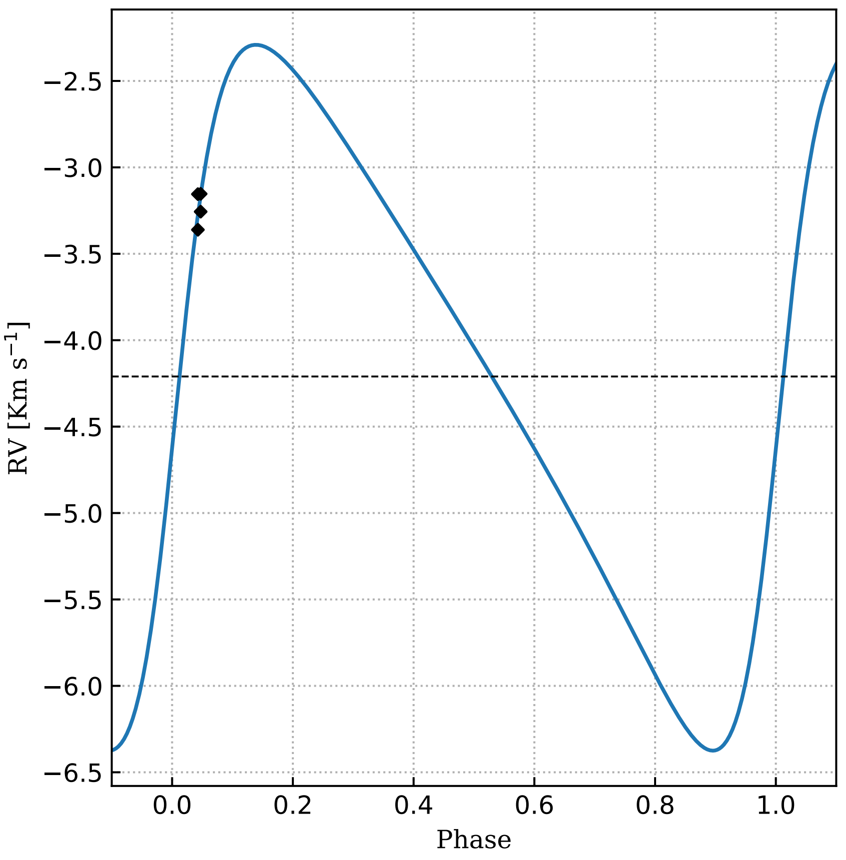
−2.5
−3.0
−3.5
−4.0
−4.5
−5.0
−5.5
−6.0
−6.5
RV [Km s−1]
0.0
0.2
0.4
0.6
0.8
1.0
Phase

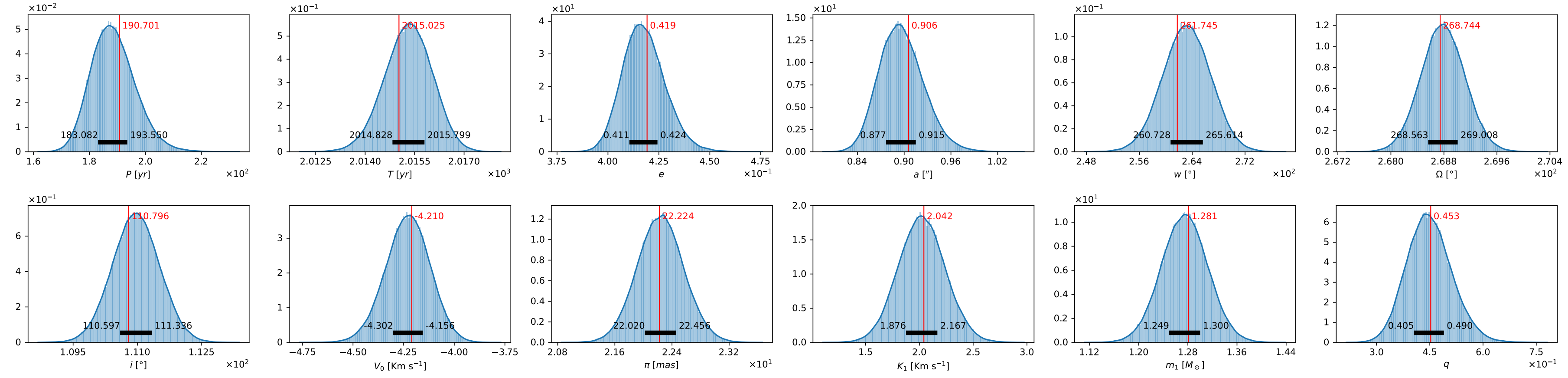
×10−2
190.701
183.082
193.550
P [yr]
×10²
×10−1
2015.025
2014.828
2015.799
T [yr]
×10³
×10¹
0.419
0.411
0.424
e
×10−1
×10¹
0.906
0.877
0.915
a ['']
×10−1
261.745
260.728
265.614
w [°]
×10²
268.744
268.563
269.008
Ω [°]
×10²
×10−1
110.796
110.597
111.336
i [°]
×10²
-4.210
-4.302
-4.156
V0 [Km s−1]
22.224
22.020
22.456
π [mas]
×10¹
2.042
1.876
2.167
K1 [Km s−1]
×10¹
1.281
1.249
1.300
m1 [M⊙]
0.453
0.405
0.490
q
×10−1

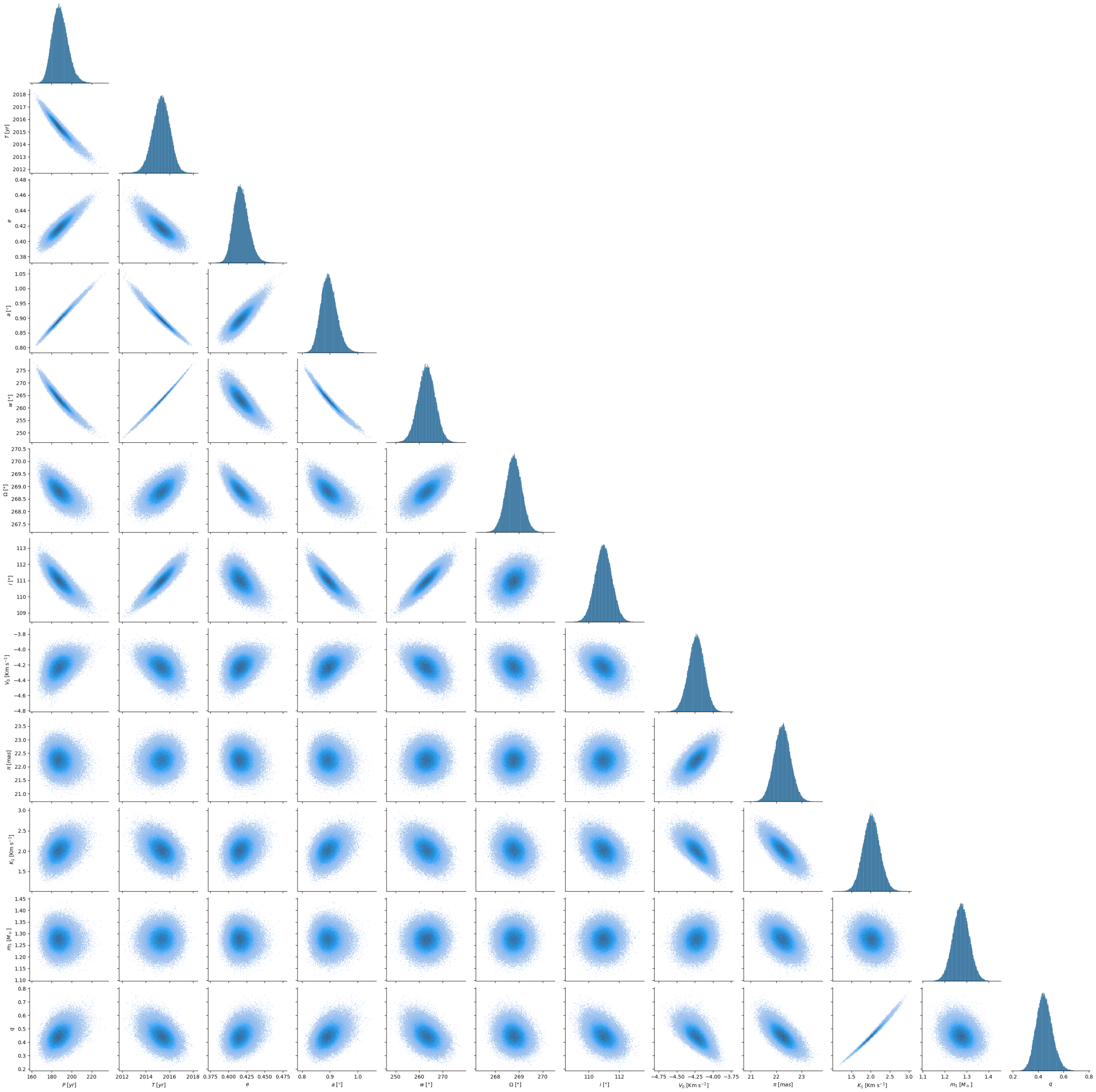
T [yr]
2018
2017
2016
2015
2014
2013
2012
e
0.48
0.46
0.44
0.42
0.40
0.38
a ["]
1.05
1.00
0.95
0.90
0.85
0.80
w [°]
275
270
265
260
255
250
Ω [°]
270.5
270.0
269.5
269.0
268.5
268.0
267.5
i [°]
113
112
111
110
109
V_0 [Km s^{-1}]
−3.8
−4.0
−4.2
−4.4
−4.6
−4.8
π [mas]
23.5
23.0
22.5
22.0
21.5
21.0
K_1 [Km s^{-1}]
3.0
2.5
2.0
1.5
m_1 [$M_\odot$]
1.45
1.40
1.35
1.30
1.25
1.20
1.15
1.10
q
0.8
0.7
0.6
0.5
0.4
0.3
0.2
160
180
200
220
P [yr]
2012
2014
2016
2018
T [yr]
0.375
0.400
0.425
0.450
0.475
e
0.8
0.9
1.0
a ["]
250
260
270
w [°]
268
269
270
Ω [°]
110
112
i [°]
−4.75
−4.50
−4.25
−4.00
−3.75
V_0 [Km s^{-1}]
21
22
23
π [mas]
1.5
2.0
2.5
3.0
K_1 [Km s^{-1}]
1.1
1.2
1.3
1.4
m_1 [$M_\odot$]
0.2
0.4
0.6
0.8
q

WDS13138−6756=HIP 64545

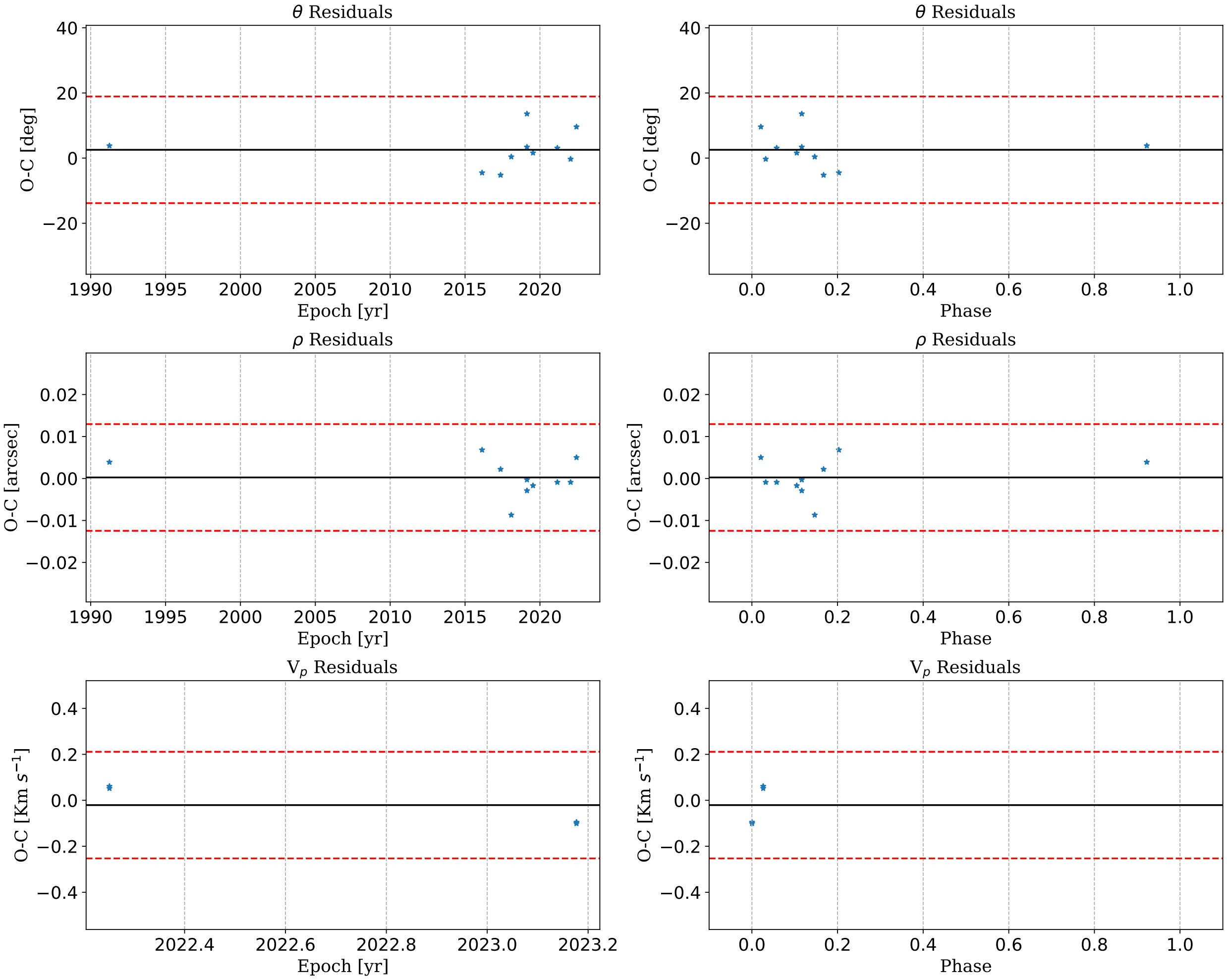

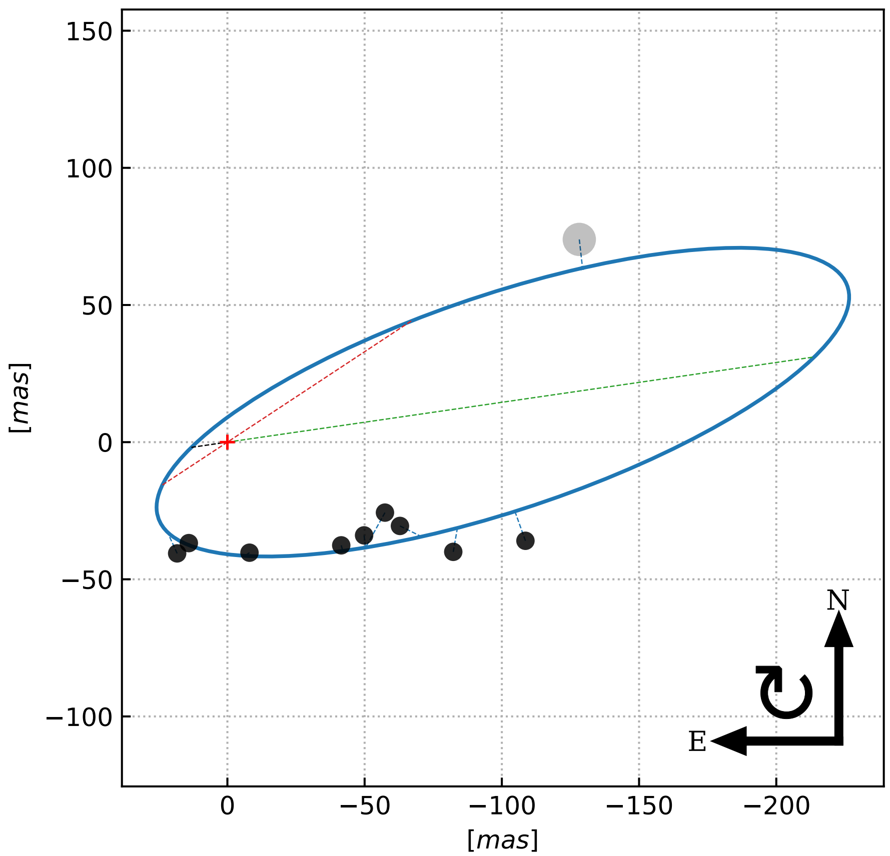
150
100
50
0
−50
−100
[mas]
0
−50
−100
−150
−200
[mas]
N
E

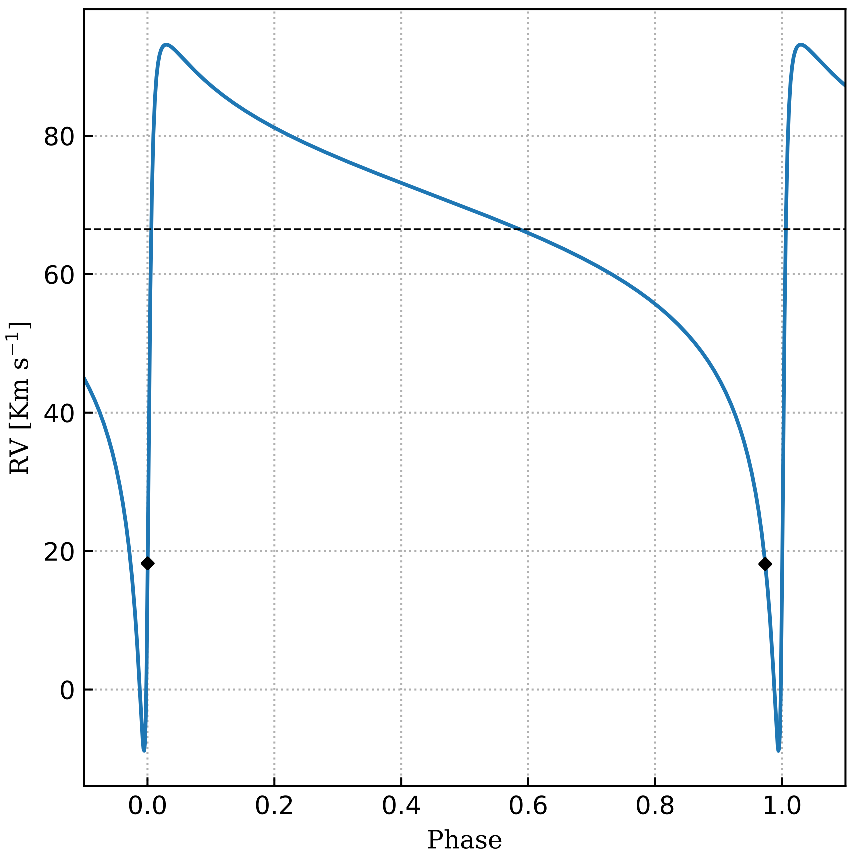
80
60
40
20
0
RV [Km s^{-1}]
0.0
0.2
0.4
0.6
0.8
1.0
Phase

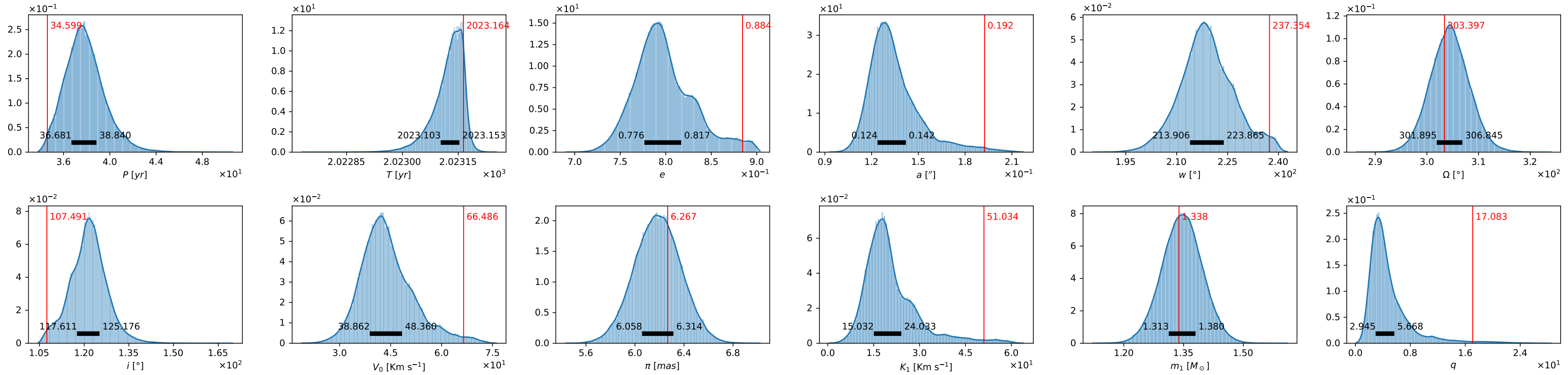
34.599
36.681
38.840
P [yr]
×10¹
2023.164
2023.103
2023.153
T [yr]
×10³
0.884
0.776
0.817
e
×10⁻¹
0.192
0.124
0.142
a ["]
×10⁻¹
237.354
213.906
223.865
w [°]
×10²
303.397
301.895
306.845
Ω [°]
×10²
107.491
117.611
125.176
i [°]
×10²
66.486
38.862
48.360
V₀ [Km s⁻¹]
×10¹
6.267
6.058
6.314
π [mas]
51.034
15.032
24.033
K₁ [Km s⁻¹]
×10¹
1.338
1.313
1.380
m₁ [M☉]
17.083
2.945
5.668
q
×10¹

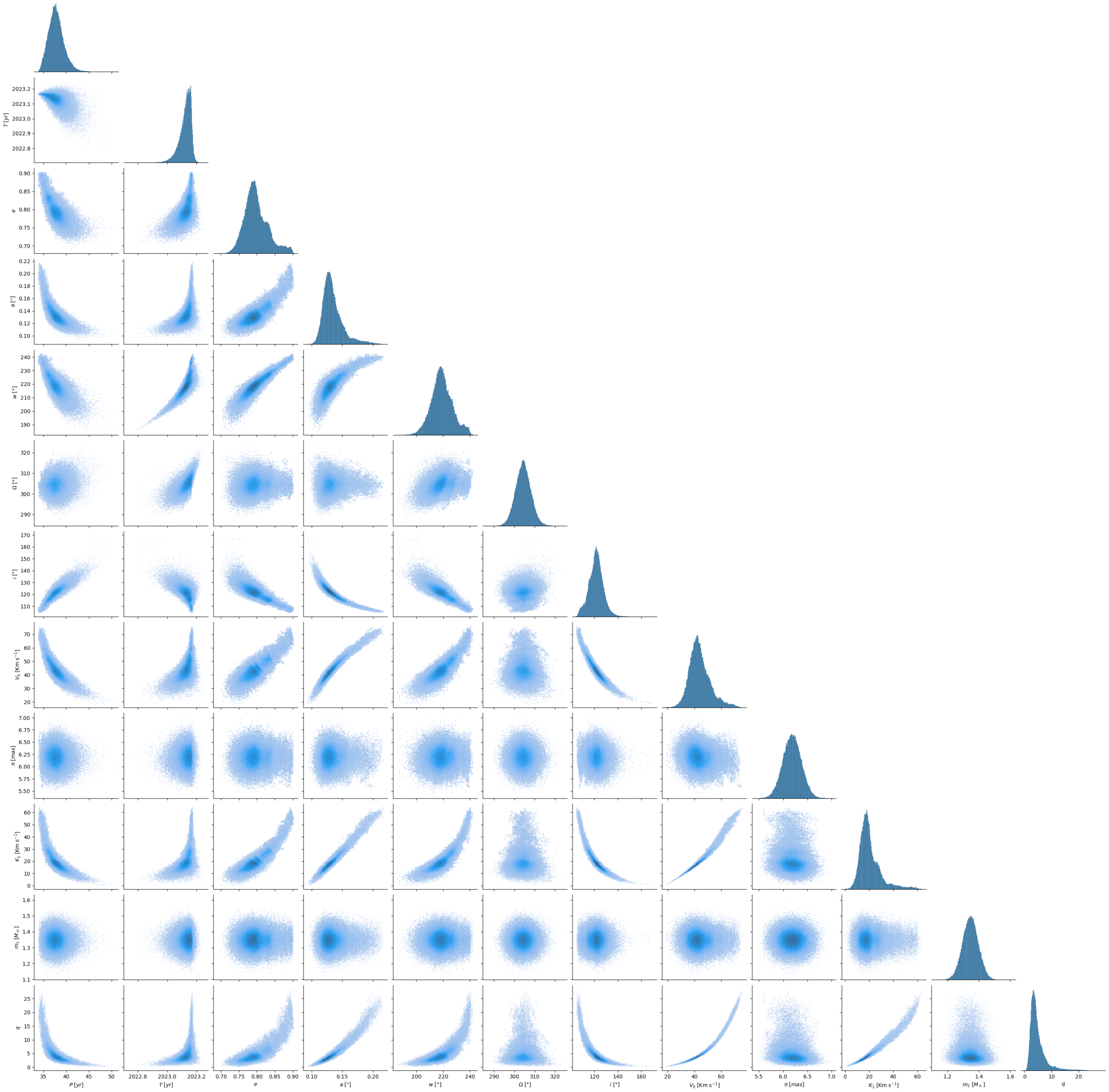
T [yr]
e
a ["]
w [°]
Ω [°]
i [°]
V_0 [Km s^-1]
π [mas]
K_1 [Km s^-1]
m_1 [M_⊙]
q
P [yr]
T [yr]
e
a ["]
w [°]
Ω [°]
i [°]
V_0 [Km s^-1]
π [mas]
K_1 [Km s^-1]
m_1 [M_⊙]
q

WDS14025−2440=HIP 68587

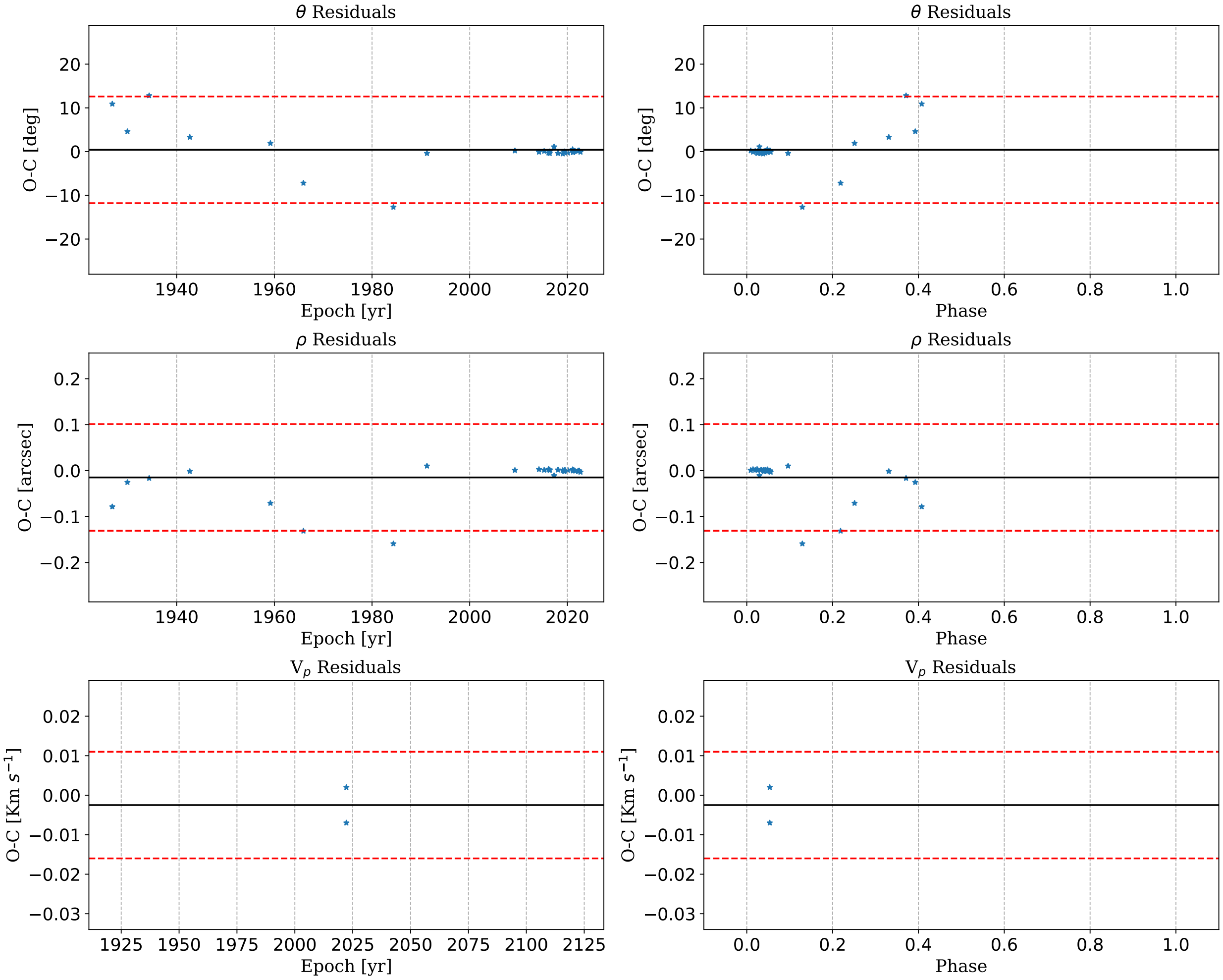

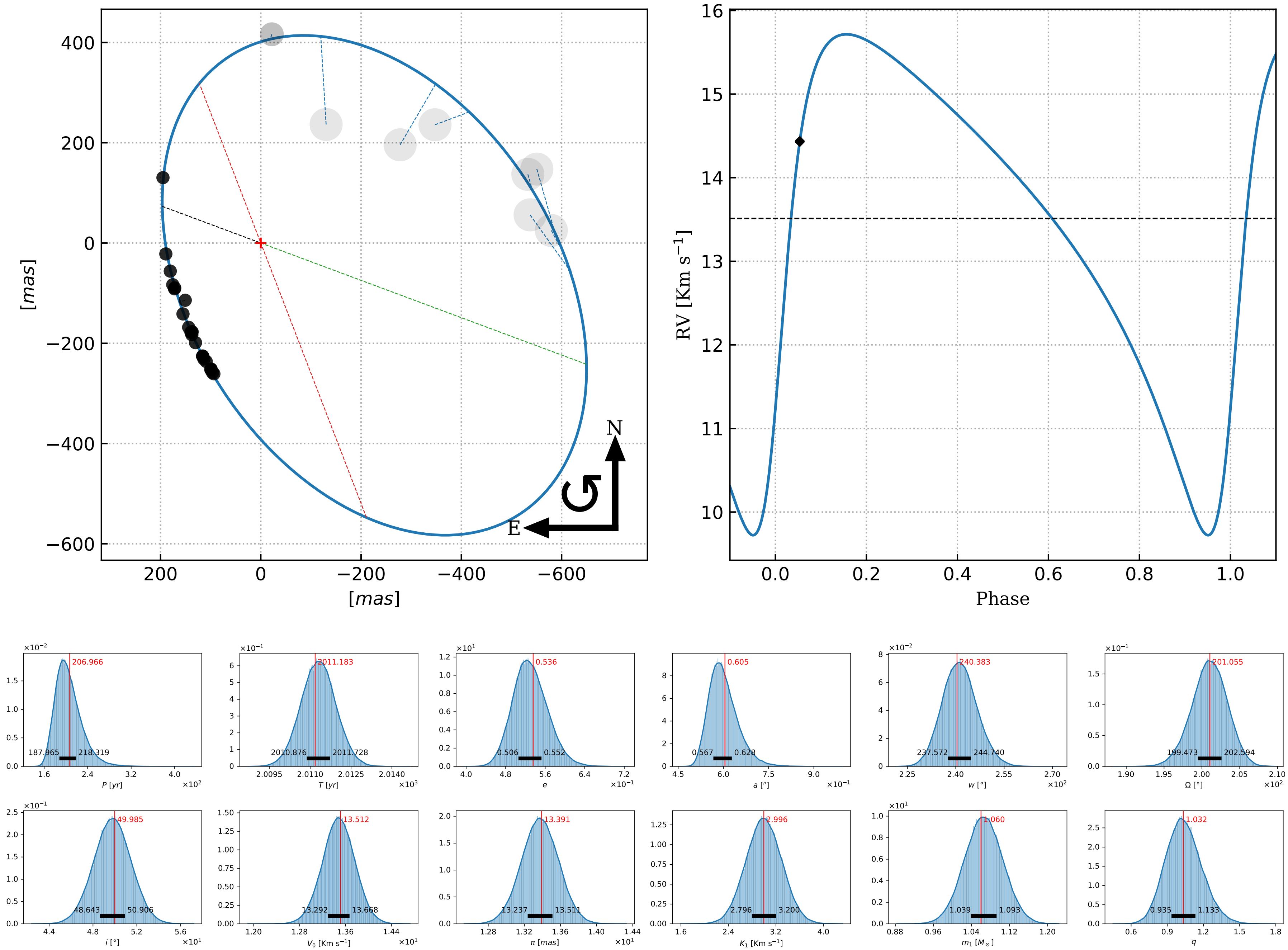
[mas]
N
E
RV [Km s^{-1}]
Phase
206.966
187.965
218.319
P [yr]
2011.183
2010.876
2011.728
T [yr]
0.536
0.506
0.552
e
0.605
0.567
0.628
a ["]
240.383
237.572
244.740
w [°]
201.055
199.473
202.594
Ω [°]
49.985
48.643
50.906
i [°]
13.512
13.292
13.668
V_0 [Km s^{-1}]
13.391
13.237
13.511
π [mas]
2.996
2.796
3.200
K_1 [Km s^{-1}]
1.060
1.039
1.093
m_1 [$M_\odot$]
1.032
0.935
1.133
q

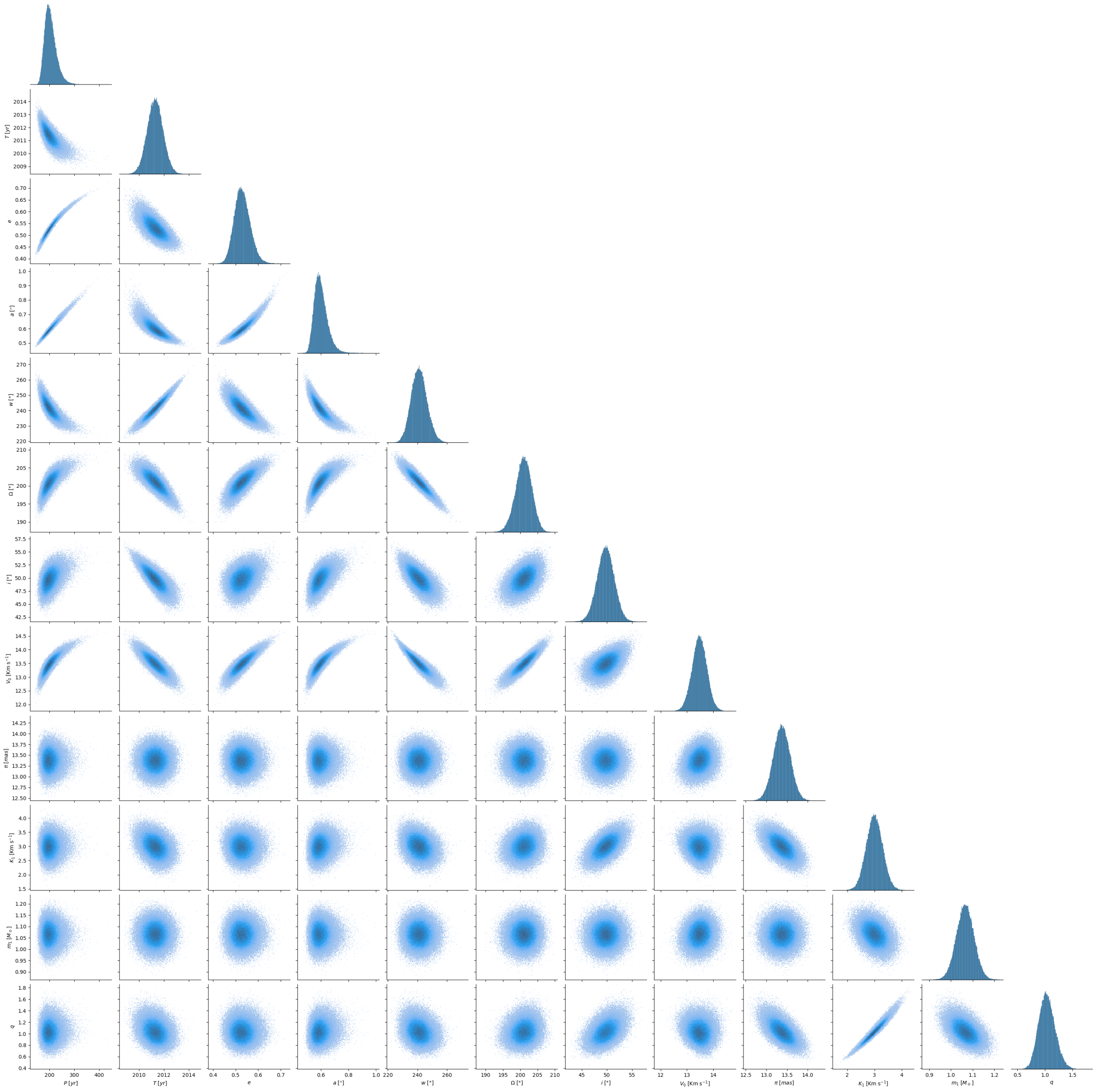$T\,[yr]$
e
$a\,['']$
$w\,[°]$
$\Omega\,[°]$
$i\,[°]$
$V_0\,[\mathrm{Km\,s^{-1}}]$
$\pi\,[mas]$
$K_1\,[\mathrm{Km\,s^{-1}}]$
$m_1\,[M_\odot]$
q
$P\,[yr]$

WDS15317+0053=HIP 76031

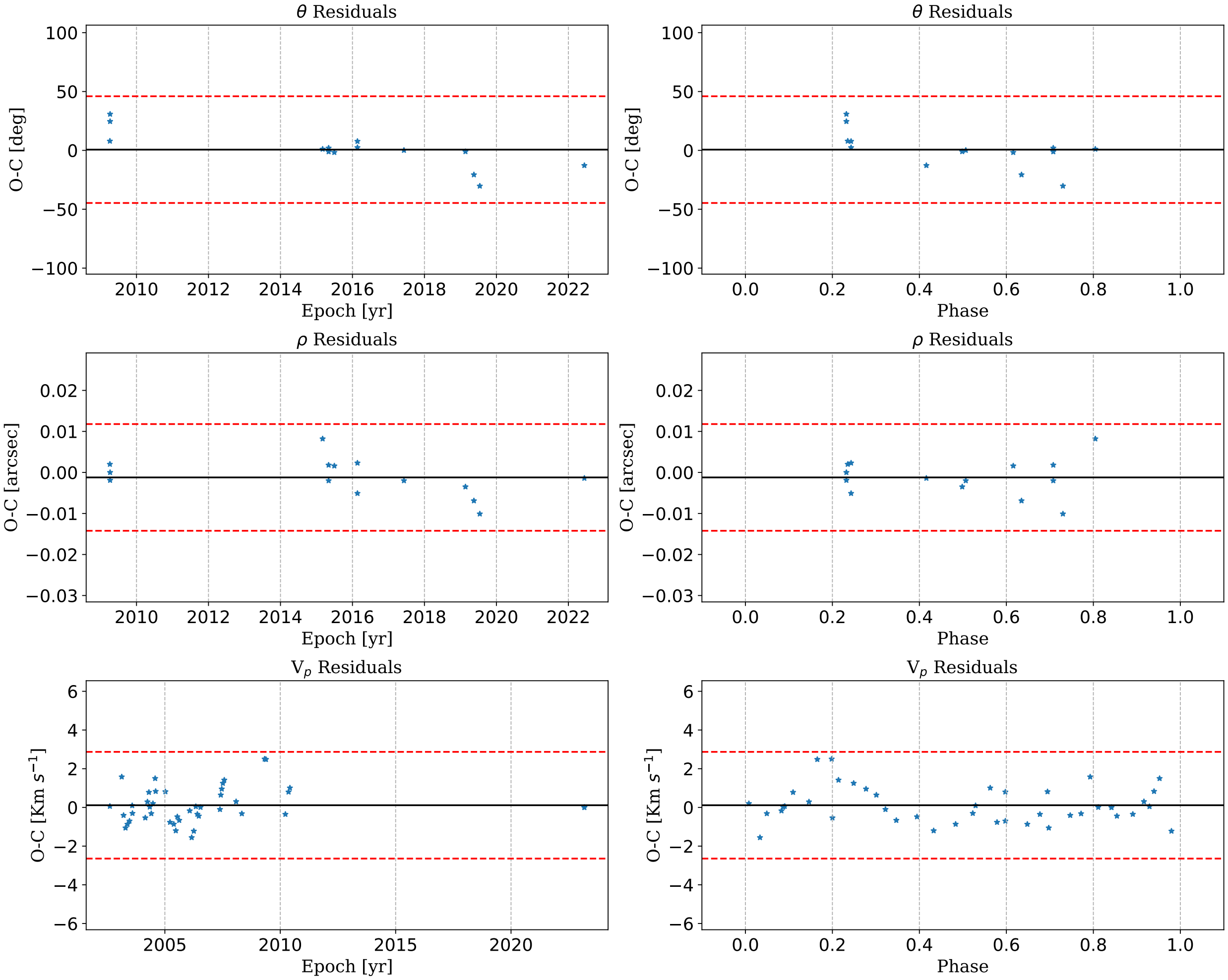

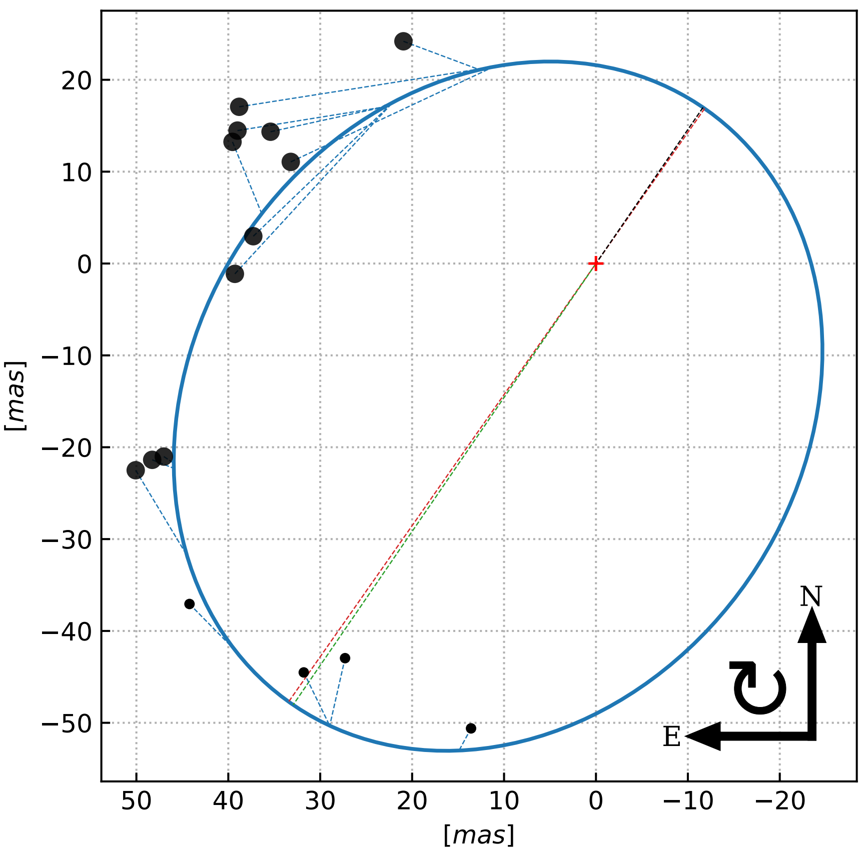
[mas]
[mas]
N
E
20
10
0
−10
−20
−30
−40
−50
50
40
30
20
10
0
−10
−20

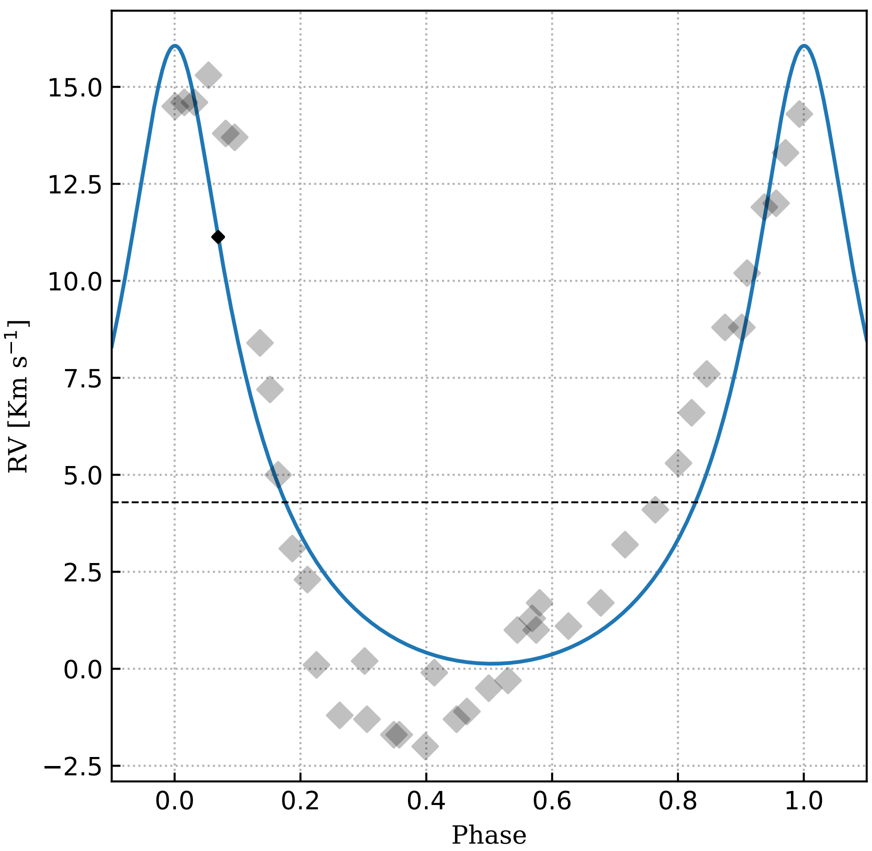
RV [Km s^{-1}]
Phase
15.0
12.5
10.0
7.5
5.0
2.5
0.0
−2.5
0.0
0.2
0.4
0.6
0.8
1.0

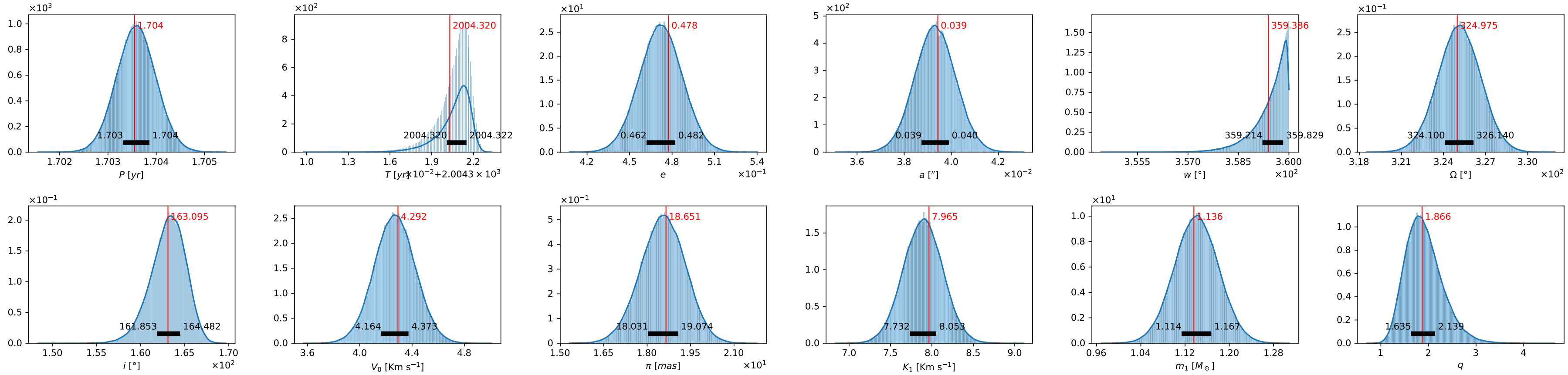
×10³
1.704
1.703
1.704
P [yr]
×10²
2004.320
2004.320
2004.322
T [yr]×10⁻²+2.0043×10³
×10¹
0.478
0.462
0.482
e
×10⁻¹
×10²
0.039
0.039
0.040
a ["]
×10⁻²
359.336
359.214
359.829
w [°]
×10²
×10⁻¹
324.975
324.100
326.140
Ω [°]
×10²
×10⁻¹
163.095
161.853
164.482
i [°]
×10²
4.292
4.164
4.373
V₀ [Km s⁻¹]
×10⁻¹
18.651
18.031
19.074
π [mas]
×10¹
7.965
7.732
8.053
K₁ [Km s⁻¹]
×10¹
1.136
1.114
1.167
m₁ [M☉]
1.866
1.635
2.139
q

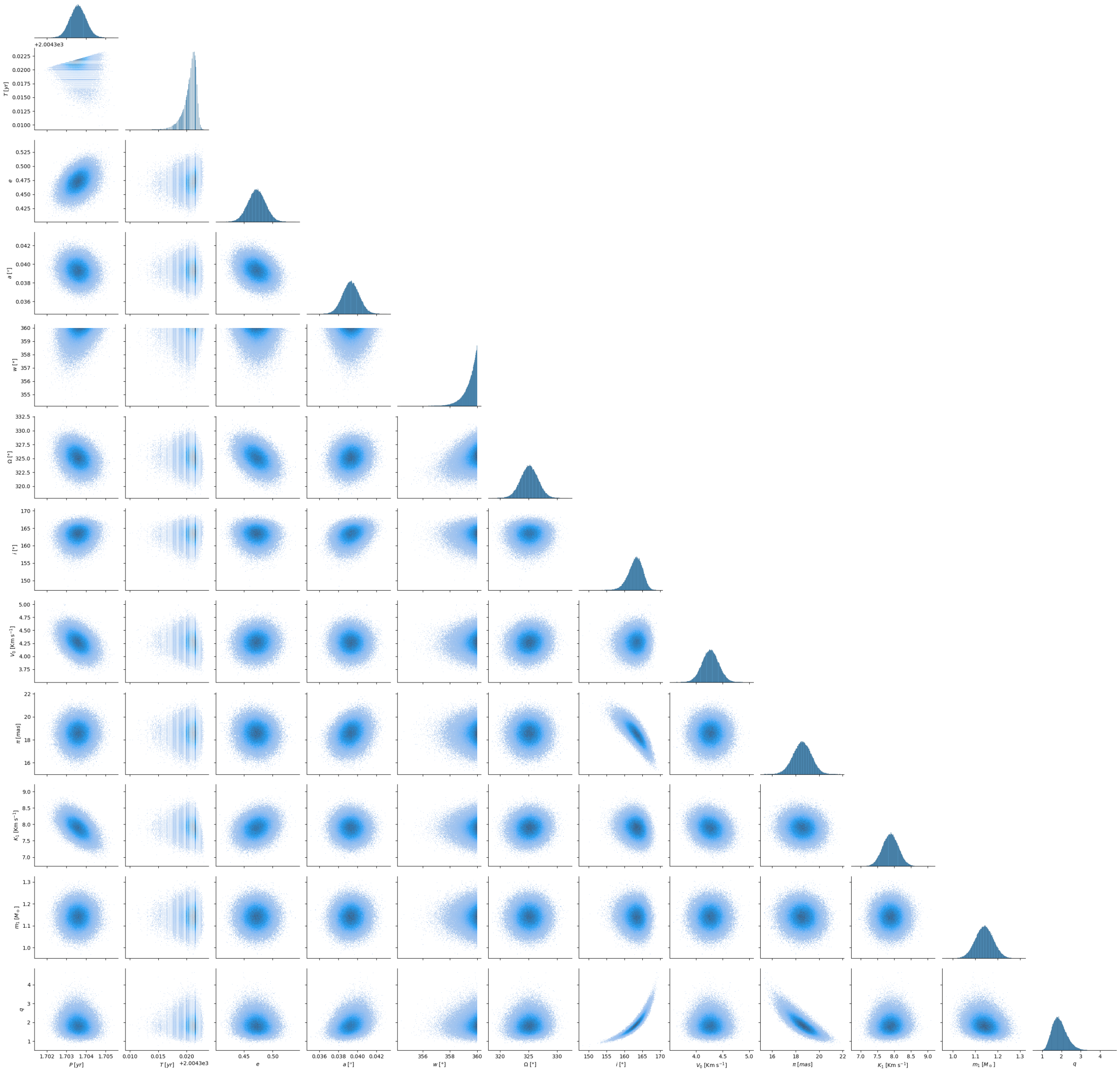
+2.0043e3
T [yr]
0.0225
0.0200
0.0175
0.0150
0.0125
0.0100
e
0.525
0.500
0.475
0.450
0.425
a ["]
0.042
0.040
0.038
0.036
w [°]
360
359
358
357
356
355
Ω [°]
332.5
330.0
327.5
325.0
322.5
320.0
i [°]
170
165
160
155
150
V_0 [Km s^{-1}]
5.00
4.75
4.50
4.25
4.00
3.75
π [mas]
22
20
18
16
K_1 [Km s^{-1}]
9.0
8.5
8.0
7.5
7.0
m_1 [$M_\odot$]
1.3
1.2
1.1
1.0
q
4
3
2
1
1.702 1.703 1.704 1.705
P [yr]
0.010 0.015 0.020 +2.0043e3
T [yr]
0.45 0.50
e
0.036 0.038 0.040 0.042
a ["]
356 358 360
w [°]
320 325 330
Ω [°]
150 155 160 165 170
i [°]
4.0 4.5 5.0
V_0 [Km s^{-1}]
16 18 20 22
π [mas]
7.0 7.5 8.0 8.5 9.0
K_1 [Km s^{-1}]
1.0 1.1 1.2 1.3
m_1 [$M_\odot$]
1 2 3 4
q

Double-lined Spectroscopic Binaries (SB2)

WDS01376−0924=HIP 7580 | No-prior Solution

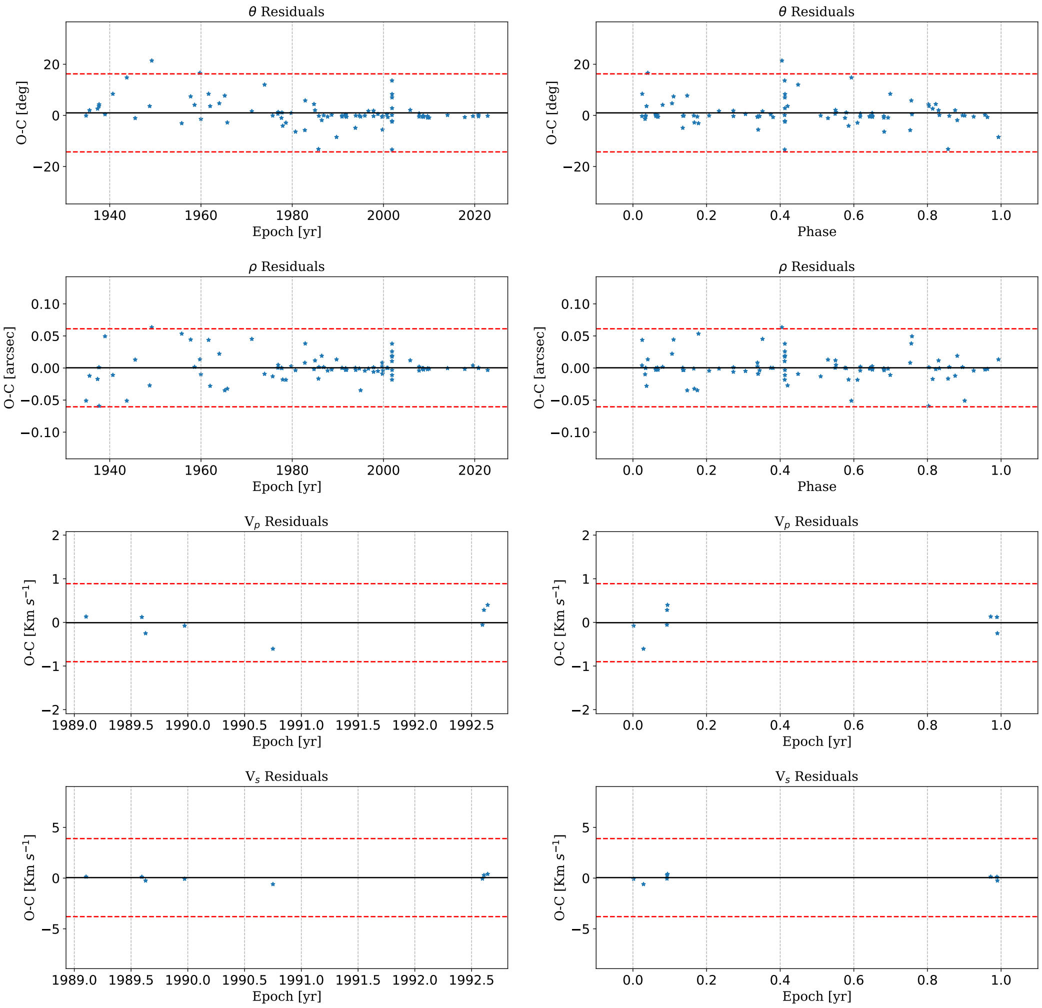

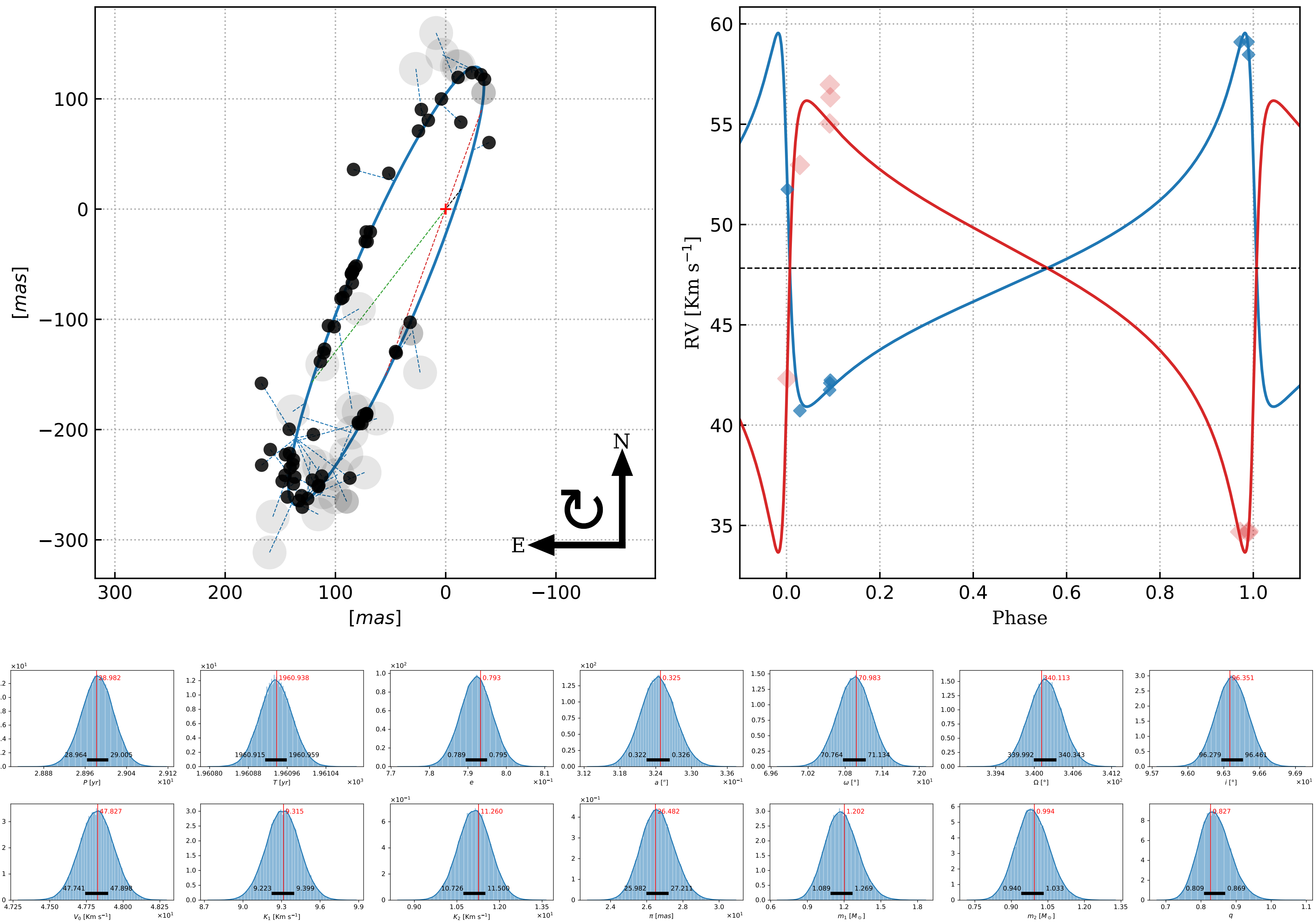
[mas]
100
0
−100
−200
−300
300
200
100
0
−100
N
E
RV [Km s^{-1}]
60
55
50
45
40
35
0.0
0.2
0.4
0.6
0.8
1.0
Phase
28.982
28.964
29.005
P [yr]
1960.938
1960.915
1960.959
T [yr]
0.793
0.789
0.795
e
0.325
0.322
0.326
a ["]
70.983
70.764
71.134
ω [°]
340.113
339.992
340.343
Ω [°]
96.351
96.279
96.461
i [°]
47.827
47.741
47.898
V$_0$ [Km s^{-1}]
9.315
9.223
9.399
K$_1$ [Km s^{-1}]
11.260
10.726
11.500
K$_2$ [Km s^{-1}]
26.482
25.982
27.211
π [mas]
1.202
1.089
1.269
m$_1$ [M$_\odot$]
0.994
0.940
1.033
m$_2$ [M$_\odot$]
0.827
0.809
0.869
q

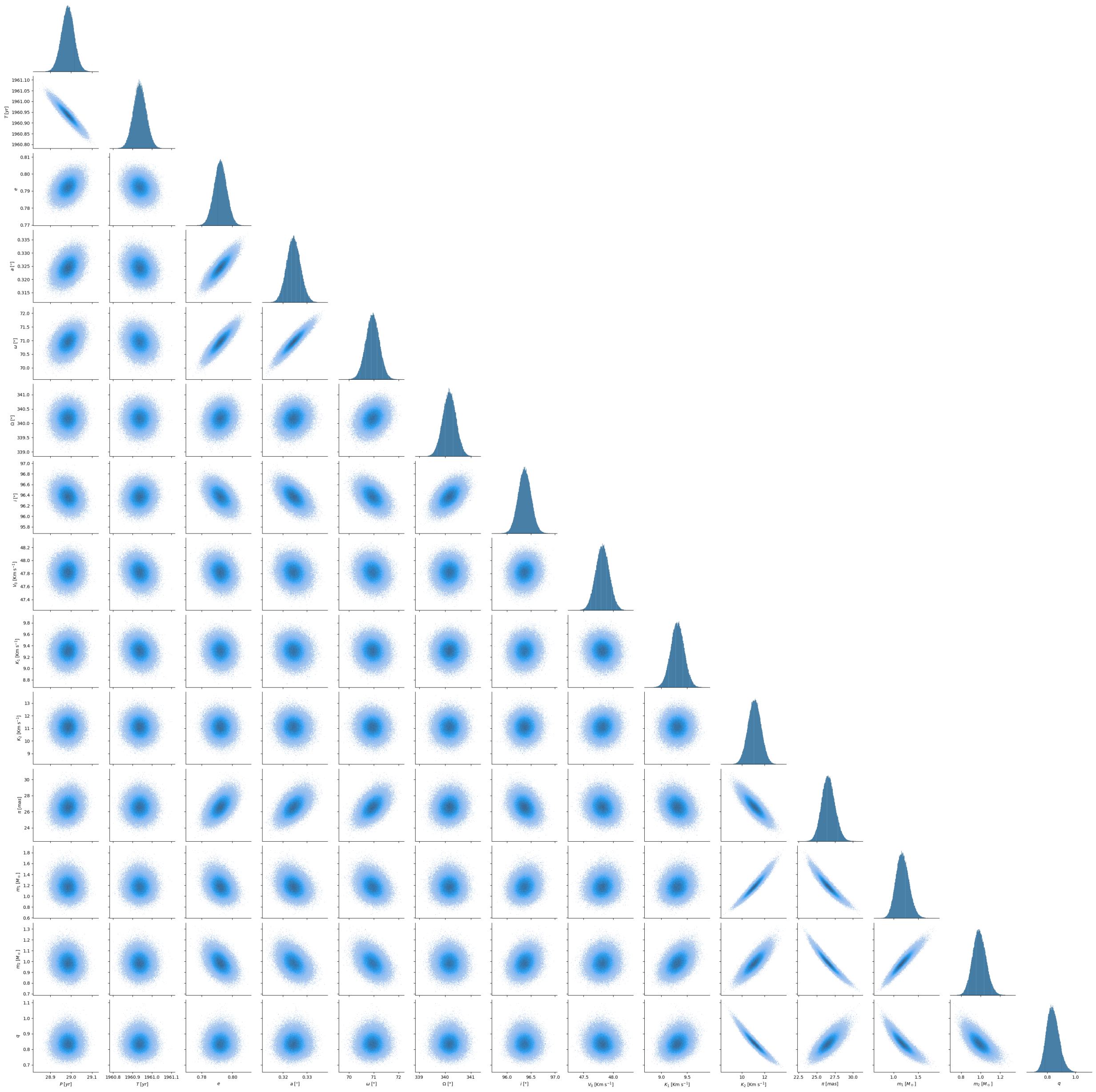

T [yr]
1961.10
1961.05
1961.00
1960.95
1960.90
1960.85
1960.80
e
0.81
0.80
0.79
0.78
0.77
a ["]
0.335
0.330
0.325
0.320
0.315
ω [°]
72.0
71.5
71.0
70.5
70.0
Ω [°]
341.0
340.5
340.0
339.5
339.0
i [°]
97.0
96.8
96.6
96.4
96.2
96.0
95.8
V_0 [Km s^{-1}]
48.2
48.0
47.8
47.6
47.4
K_1 [Km s^{-1}]
9.8
9.6
9.4
9.2
9.0
8.8
K_2 [Km s^{-1}]
13
12
11
10
9
π [mas]
30
28
26
24
m_1 [$M_\odot$]
1.8
1.6
1.4
1.2
1.0
0.8
0.6
m_2 [$M_\odot$]
1.3
1.2
1.1
1.0
0.9
0.8
0.7
q
1.1
1.0
0.9
0.8
0.7
28.9
29.0
29.1
P [yr]
1960.8
1960.9
1961.0
1961.1
T [yr]
0.78
0.80
e
0.32
0.33
a ["]
70
71
72
ω [°]
339
340
341
Ω [°]
96.0
96.5
97.0
i [°]
47.5
48.0
V_0 [Km s^{-1}]
9.0
9.5
K_1 [Km s^{-1}]
10
12
K_2 [Km s^{-1}]
22.5
25.0
27.5
30.0
π [mas]
1.0
1.5
m_1 [$M_\odot$]
0.8
1.0
1.2
m_2 [$M_\odot$]
0.8
1.0
q

WDS01376−0924=HIP 7580 | Prior Solution

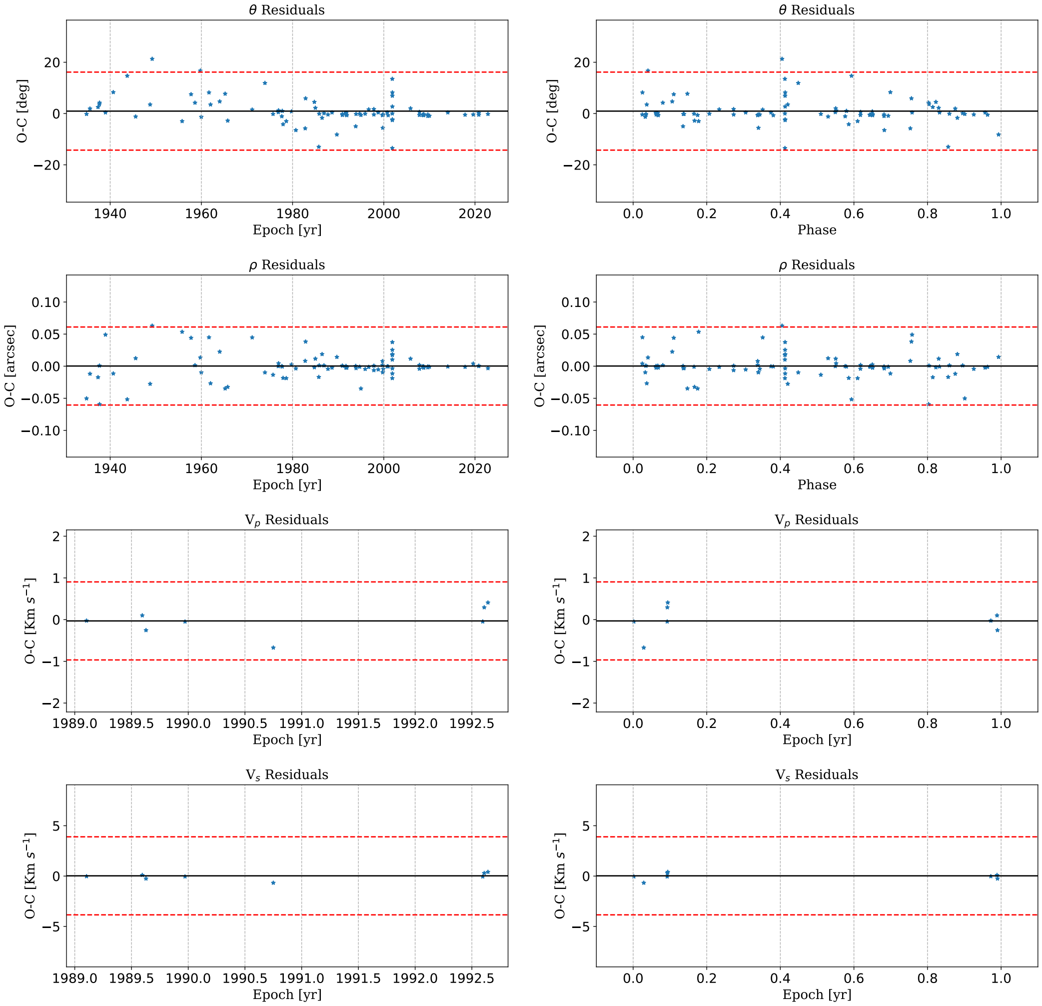

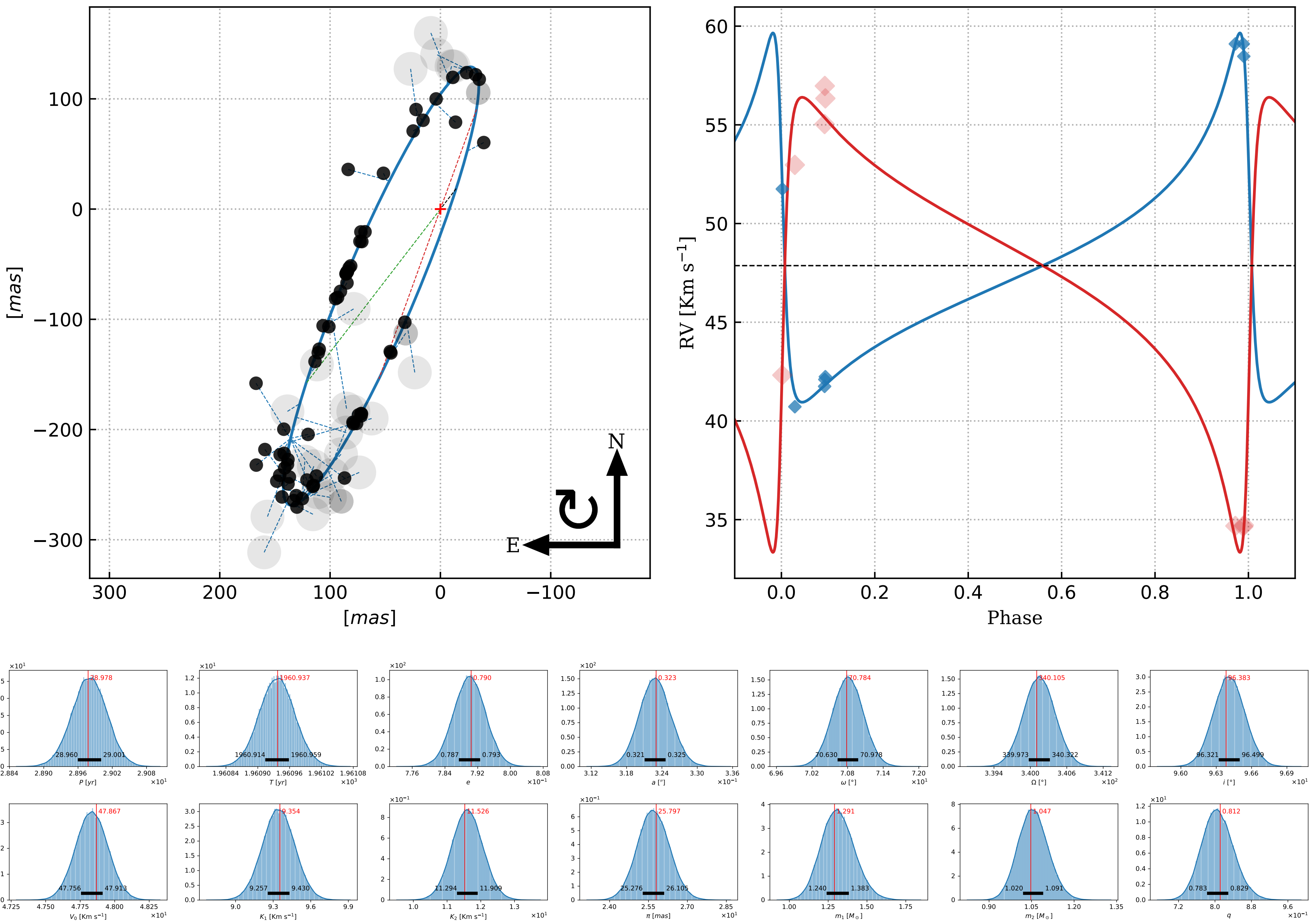
[mas]
[mas]
N
E
RV [Km s^{-1}]
Phase
P [yr] 28.978 28.960 29.001
T [yr] 1960.937 1960.914 1960.959
e 0.790 0.787 0.793
a ["] 0.323 0.321 0.325
ω [°] 70.784 70.630 70.978
Ω [°] 340.105 339.973 340.322
i [°] 96.383 96.321 96.499
V$_0$ [Km s^{-1}] 47.867 47.756 47.913
K$_1$ [Km s^{-1}] 9.354 9.257 9.430
K$_2$ [Km s^{-1}] 11.526 11.294 11.909
π [mas] 25.797 25.276 26.105
m$_1$ [M$_\odot$] 1.291 1.240 1.383
m$_2$ [M$_\odot$] 1.047 1.020 1.091
q 0.812 0.783 0.829

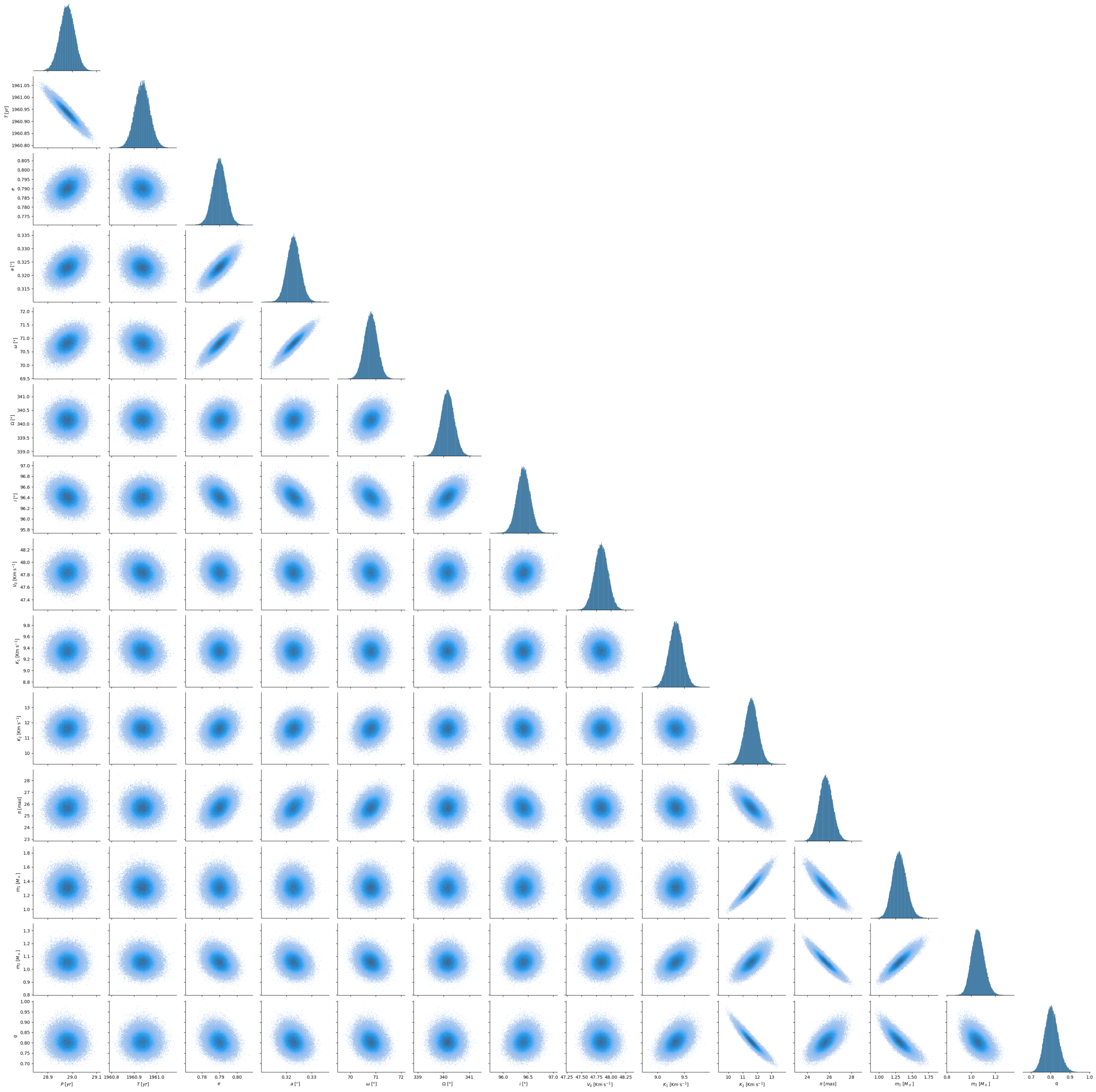T [yr]
1961.05
1961.00
1960.95
1960.90
1960.85
1960.80
e
0.805
0.800
0.795
0.790
0.785
0.780
0.775
a ["]
0.335
0.330
0.325
0.320
0.315
ω [°]
72.0
71.5
71.0
70.5
70.0
69.5
Ω [°]
341.0
340.5
340.0
339.5
339.0
i [°]
97.0
96.8
96.6
96.4
96.2
96.0
95.8
V_0 [Km s^{-1}]
48.2
48.0
47.8
47.6
47.4
K_1 [Km s^{-1}]
9.8
9.6
9.4
9.2
9.0
8.8
K_2 [Km s^{-1}]
13
12
11
10
π [mas]
28
27
26
25
24
23
m_1 [$M_\odot$]
1.8
1.6
1.4
1.2
1.0
m_2 [$M_\odot$]
1.3
1.2
1.1
1.0
0.9
0.8
q
1.00
0.95
0.90
0.85
0.80
0.75
0.70
28.9
29.0
29.1
P [yr]
1960.8
1960.9
1961.0
T [yr]
0.78
0.79
0.80
e
0.32
0.33
a ["]
70
71
72
ω [°]
339
340
341
Ω [°]
96.0
96.5
97.0
i [°]
47.25
47.50
47.75
48.00
48.25
V_0 [Km s^{-1}]
9.0
9.5
K_1 [Km s^{-1}]
10
11
12
13
K_2 [Km s^{-1}]
24
26
28
π [mas]
1.00
1.25
1.50
1.75
m_1 [$M_\odot$]
0.8
1.0
1.2
m_2 [$M_\odot$]
0.7
0.8
0.9
1.0
q

WDS02057−2423=HIP 9774 AaAb | No-prior Solution

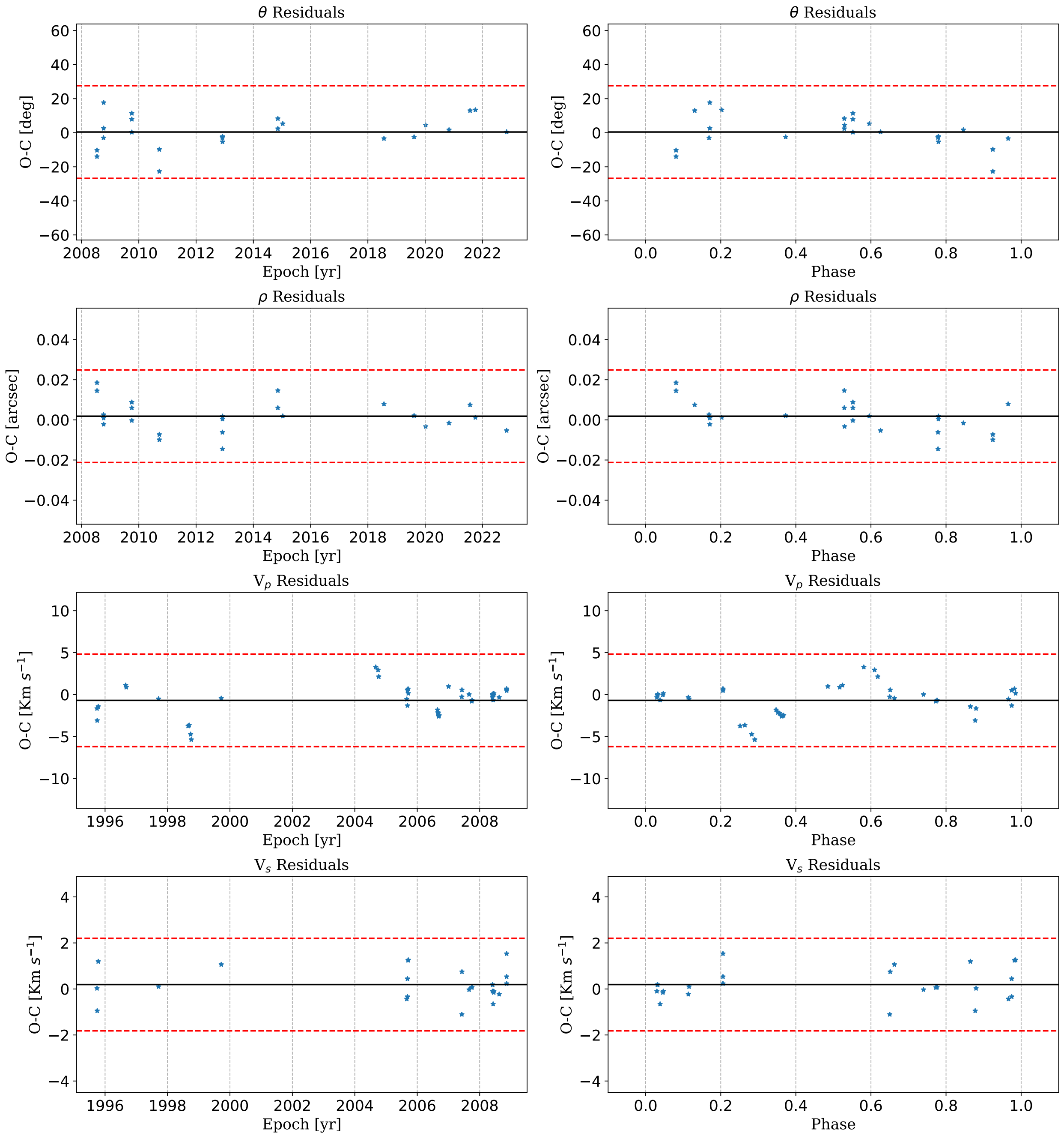

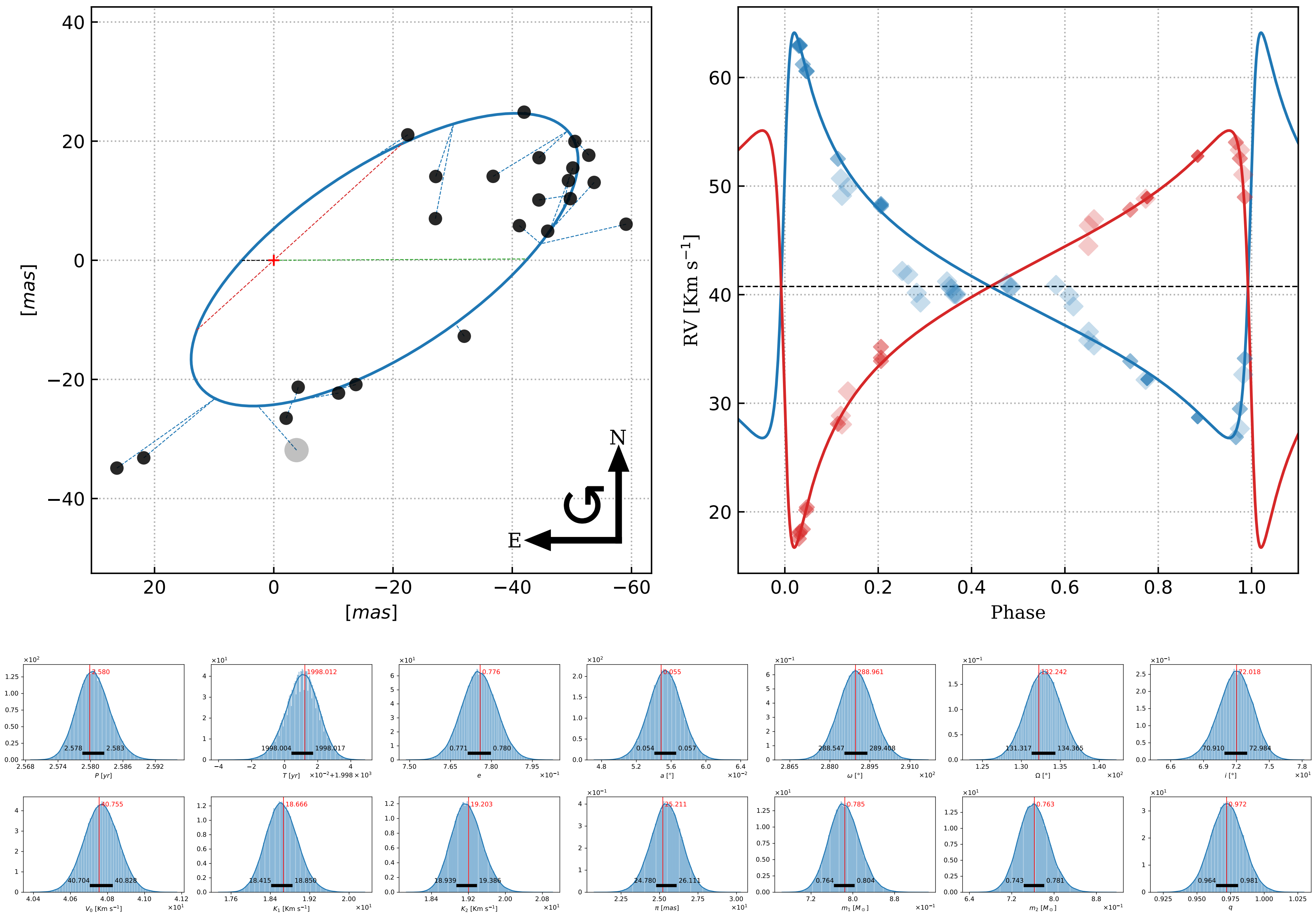

[mas]
[mas]
N
E
RV [Km s^{-1}]
Phase
P [yr] 2.580 2.578 2.583
T [yr] ×10^{-2}+1.998×10^{3} 1998.012 1998.004 1998.017
e 0.776 0.771 0.780
a ["] 0.055 0.054 0.057
ω [°] 288.961 288.547 289.408
Ω [°] 132.242 131.317 134.365
i [°] 72.018 70.910 72.984
V$_0$ [Km s^{-1}] 40.755 40.704 40.828
K$_1$ [Km s^{-1}] 18.666 18.415 18.850
K$_2$ [Km s^{-1}] 19.203 18.939 19.386
π [mas] 25.211 24.780 26.111
m$_1$ [M$_\odot$] 0.785 0.764 0.804
m$_2$ [M$_\odot$] 0.763 0.743 0.781
q 0.972 0.964 0.981

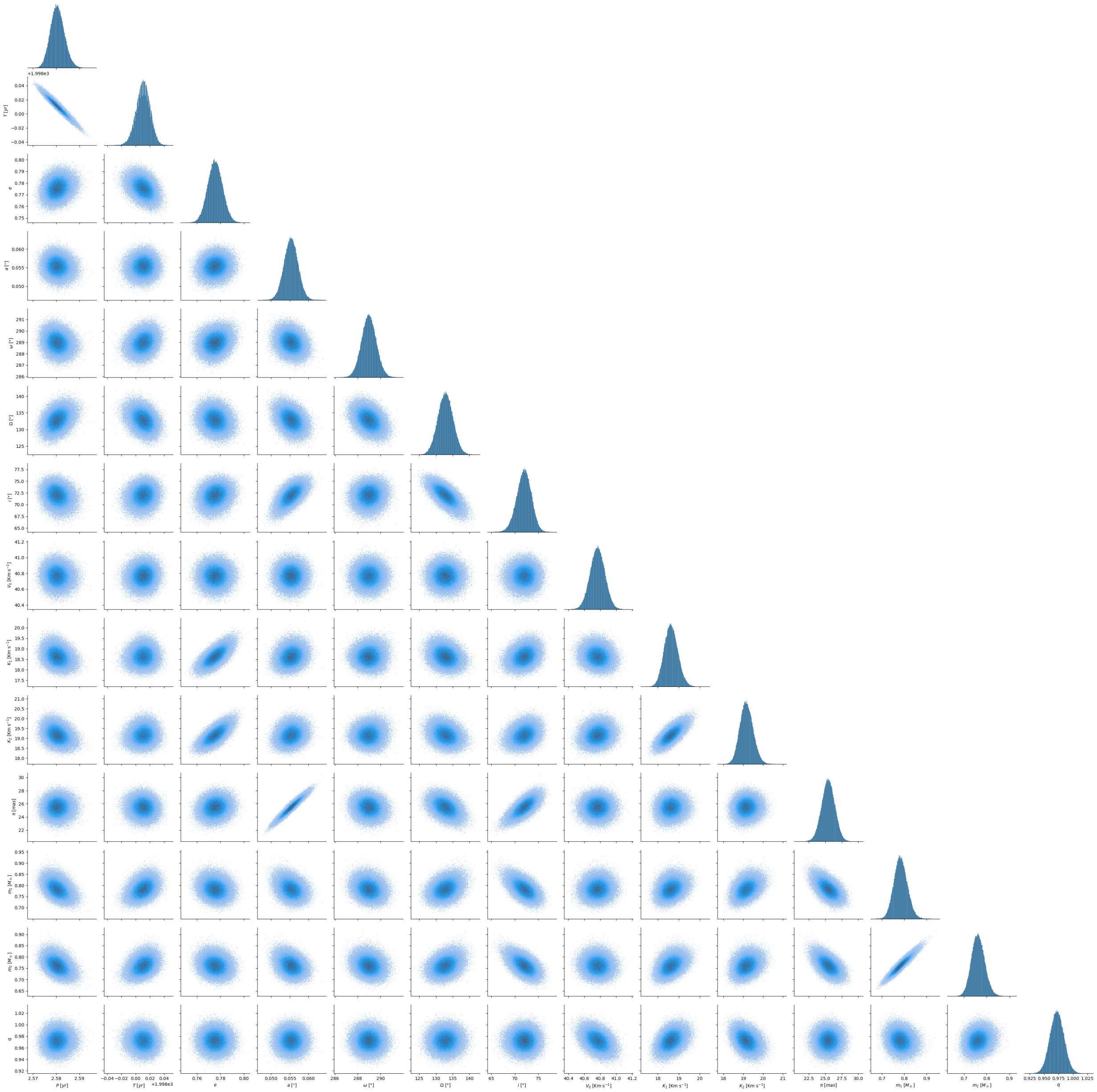
+1.998e3
$T\ [yr]$
0.04
0.02
0.00
−0.02
−0.04
e
0.80
0.79
0.78
0.77
0.76
0.75
$a\ ['']$
0.060
0.055
0.050
$\omega\ [°]$
291
290
289
288
287
286
$\Omega\ [°]$
140
135
130
125
$i\ [°]$
77.5
75.0
72.5
70.0
67.5
65.0
$V_0\ [\mathrm{Km\ s^{-1}}]$
41.2
41.0
40.8
40.6
40.4
$K_1\ [\mathrm{Km\ s^{-1}}]$
20.0
19.5
19.0
18.5
18.0
17.5
$K_2\ [\mathrm{Km\ s^{-1}}]$
21.0
20.5
20.0
19.5
19.0
18.5
18.0
$\pi\ [mas]$
30
28
26
24
22
$m_1\ [M_\odot]$
0.95
0.90
0.85
0.80
0.75
0.70
$m_2\ [M_\odot]$
0.90
0.85
0.80
0.75
0.70
0.65
q
1.02
1.00
0.98
0.96
0.94
0.92
2.57 2.58 2.59
$P\ [yr]$
−0.04 −0.02 0.00 0.02 0.04
$T\ [yr]$ +1.998e3
0.76 0.78 0.80
e
0.050 0.055 0.060
$a\ ['']$
286 288 290
$\omega\ [°]$
125 130 135 140
$\Omega\ [°]$
65 70 75
$i\ [°]$
40.4 40.6 40.8 41.0 41.2
$V_0\ [\mathrm{Km\ s^{-1}}]$
18 19 20
$K_1\ [\mathrm{Km\ s^{-1}}]$
18 19 20 21
$K_2\ [\mathrm{Km\ s^{-1}}]$
22.5 25.0 27.5 30.0
$\pi\ [mas]$
0.7 0.8 0.9
$m_1\ [M_\odot]$
0.7 0.8 0.9
$m_2\ [M_\odot]$
0.925 0.950 0.975 1.000 1.025
q

WDS02057−2423=HIP 9774 AaAb | Prior Solution

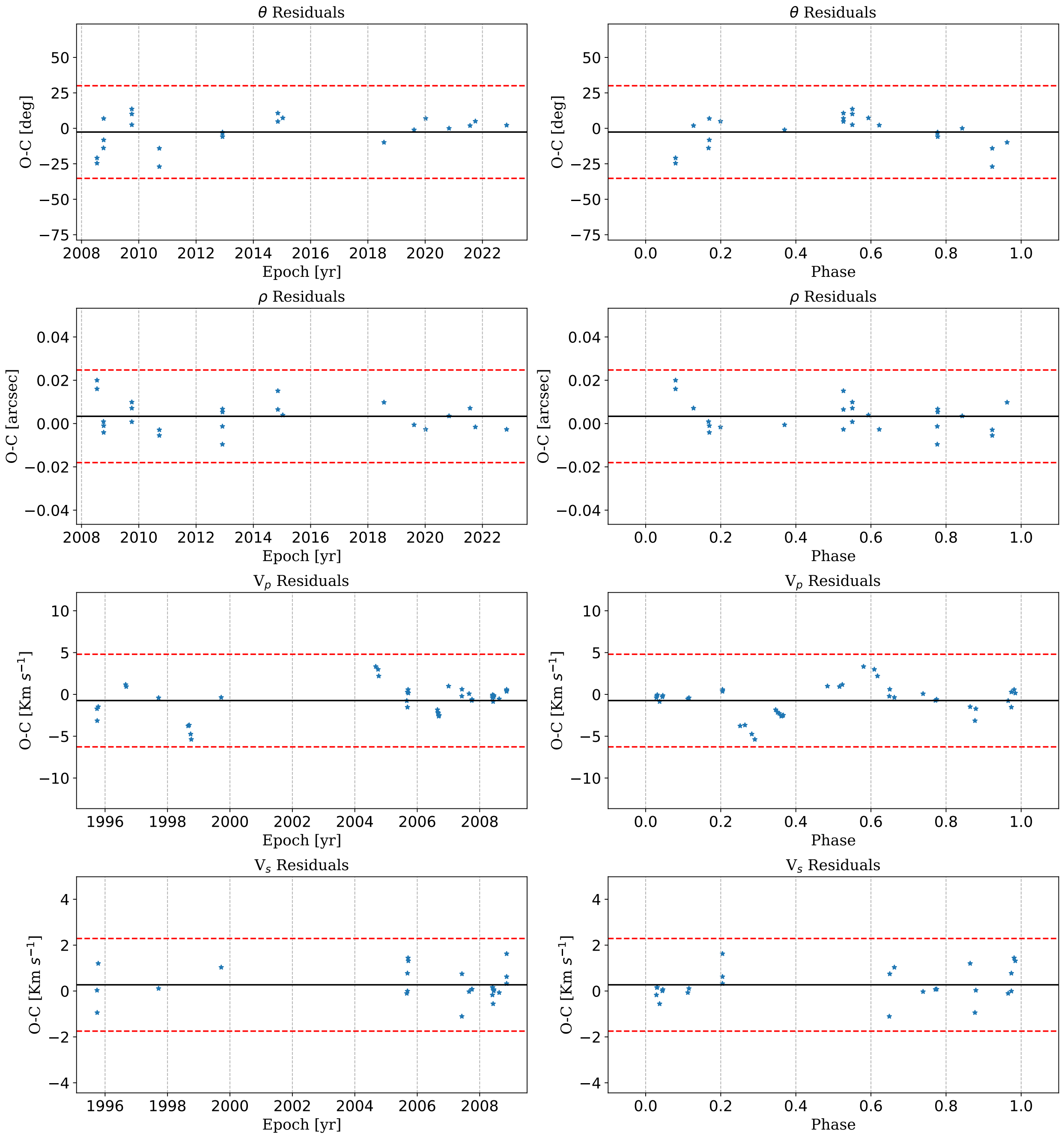

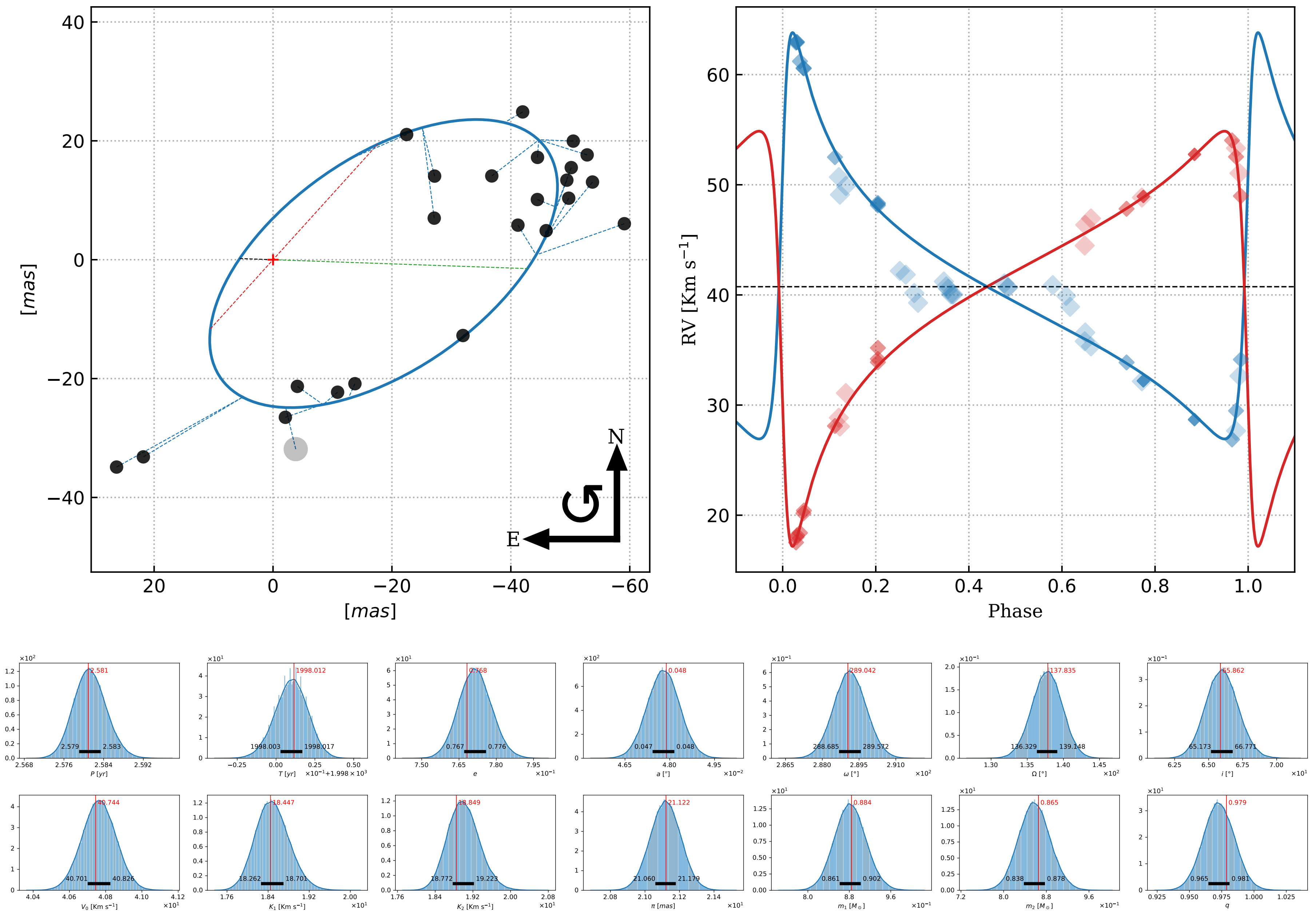
[mas]
[mas]
N
E
RV [Km s^{-1}]
Phase
P [yr]
T [yr]
e
a ["]
ω [°]
Ω [°]
i [°]
V_0 [Km s^{-1}]
K_1 [Km s^{-1}]
K_2 [Km s^{-1}]
π [mas]
m_1 [$M_\odot$]
m_2 [$M_\odot$]
q
2.581
1998.012
0.768
0.048
289.042
137.835
65.862
40.744
18.447
18.849
21.122
0.884
0.865
0.979

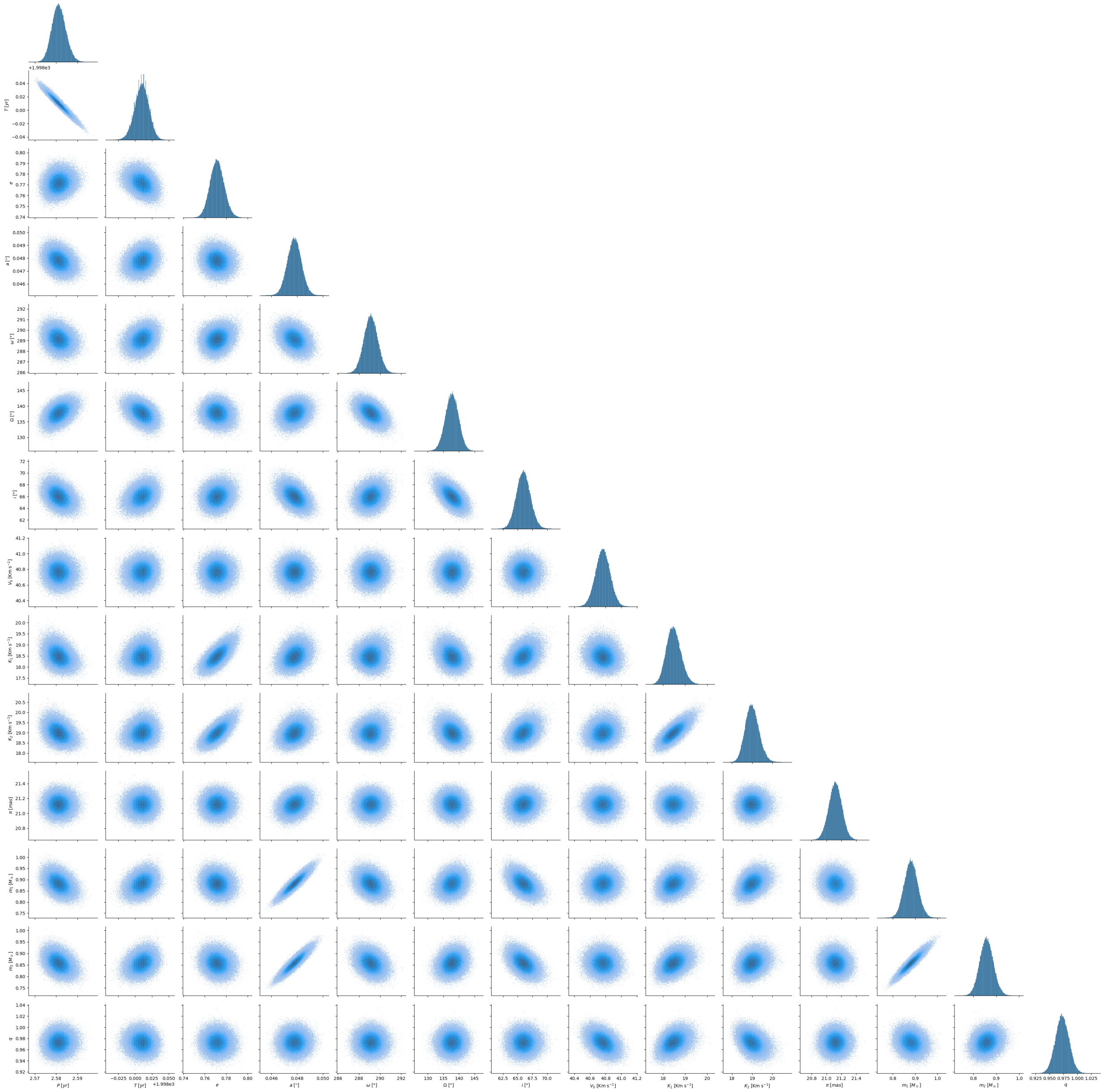

+1.998e3
T [yr]
0.04
0.02
0.00
−0.02
−0.04
e
0.80
0.79
0.78
0.77
0.76
0.75
0.74
a ["]
0.050
0.049
0.048
0.047
0.046
ω [°]
292
291
290
289
288
287
286
Ω [°]
145
140
135
130
i [°]
72
70
68
66
64
62
V_0 [Km s^{-1}]
41.2
41.0
40.8
40.6
40.4
K_1 [Km s^{-1}]
20.0
19.5
19.0
18.5
18.0
17.5
K_2 [Km s^{-1}]
20.5
20.0
19.5
19.0
18.5
18.0
π [mas]
21.4
21.2
21.0
20.8
m_1 [$M_\odot$]
1.00
0.95
0.90
0.85
0.80
0.75
m_2 [$M_\odot$]
0.95
0.90
0.85
0.80
0.75
q
1.04
1.02
1.00
0.98
0.96
0.94
0.92
2.57 2.58 2.59
P [yr]
−0.025 0.000 0.025 0.050
+1.998e3
T [yr]
0.74 0.76 0.78 0.80
e
0.046 0.048 0.050
a ["]
286 288 290 292
ω [°]
130 135 140 145
Ω [°]
62.5 65.0 67.5 70.0
i [°]
40.4 40.6 40.8 41.0 41.2
V_0 [Km s^{-1}]
18 19 20
K_1 [Km s^{-1}]
18 19 20
K_2 [Km s^{-1}]
20.8 21.0 21.2 21.4
π [mas]
0.8 0.9 1.0
m_1 [$M_\odot$]
0.8 0.9 1.0
m_2 [$M_\odot$]
0.925 0.950 0.975 1.000 1.025
q